LBL--17073

DE85 000569

APPLIED SCIENCE DIVISION ANNUAL REPORT ENVIRONMENTAL RESEARCH PROGRAM FY 1983

Elton J. Cairns
Head, Applied Science Division
and
Associate Director, LBL

Tihomir Novakov
Program Leader, Environmental Research Program

Report Coordinator
Maya Osowitt

Applied Science Division
Lawrence Berkeley Laboratory
University of California
Berkeley, California 94720

Prepared for the U.S. Department of Energy under Contract No. DE-AC03-76SF00098

CONTENTS

SCRUBBER CHEMISTRY RESEARCH

LAKE ECOTOXICOLOGY RESEARCH

TRACE ELEMENT ANALYSIS

ENVIRONMENTAL RESEARCH PROGRAM STAFF

ATMOSPHERIC AEROSOL RESEARCH

William Benner
Peter DeVroede
Ray Dod
Max Dunn
Lara Gundel
Anthony Hansen
Samuel Markowitz
Michael McKinney
Tihomir Novakov*†
Roland Otto
Hal Rosen
Richard Schmidt
Linda Wroth

APPLIED PHYSICS AND LASER SPECTROSCOPY RESEARCH

Nabil Amer†
Mark Cooper
Robert Gerlach
Richard Hall
William Imler
Marjorie Olmstead
Andrew Skumanich
Douglas Wake
Zafer Yasa

OIL SHALE RESEARCH

Ernest Blatchley
Jeremy Cantor
Christian Daughton‡
Richard Goodman‡
Gloria Harris-Winston
Joe Healy
Leon Hunter
David Jenkins‡
Bonnie Jones
Greg Langlois
Kumar Mehta‡
Peter Persoff
Rick Sakaji
Bob Selleck‡
Emelda Shields
Jerry Thomas†
Joan Tiernan

COMBUSTION RESEARCH

James Ang
Diana Brehob
Nancy Brown†
Mark Brosmer
Cam Carter
John Cavolowsky
Robert Cheng
Alexandre Chorin‡
John Daily
Edmund Dickson
Derek Dunn-Rankin
Christopher Edwards
Janet Ellzey
Carlos Fernandez-Pello
Fred Fisher‡
Michael Forsha
Cecile Grant
Ralph Greif
Jean Hertzberg
Kenneth Hom
Wei-Ming Huang
Frank Hurlbut
Claire Johnson‡
Kwi Lee
Trudy Lionel
Donald Lucas
Mehdi Namazian‡
Terry Ng
Clement Okoh
Antoni Oppenheim
Patrick Pagni
Richard Peterson
William Pitz
David Propper
Ola Rashed
Frank Robben
Robert Sawyer
Pauline Sherman§
Edward Stracke
Horton Stewart‡
Lawrence Talbot
Chang Tien
Steve Vosen
R. Brady Williamson
Eileen Wilner
Joan Woodard§

SCRUBBER CHEMISTRY RESEARCH

Kevin Brodbeck‡
Shih-Ger Chang†
David Littlejohn
Elizabeth Griffiths
Thuy Hoang
Scott Lynn
Robert Demyanovich

LAKE ECOTOXICOLOGY

Charles Blanchard
John Harte†
Don Levy
Gregory Lockett
Harvey Michaels
Joan Oldfather
John Rees
Ellen Saegebarth
Richard Schneider
Kathy Tonnessen

*Program Leader, †Group Leader, ‡University of California, Berkeley, §Participating Guest

TRACE ELEMENT ANALYSIS

Frank Asaro
Jon Bechtel
Charles Case
Robert Giauque
Ralph McLaughlin
Helen Michel
Anthony Nero
Amos Newton
Cindy Polansky
Mary Quinby-Hunt
Alexandre Quintanilha
Linda Sindelar
Rafael Zamora

ADMINISTRATIVE SUPPORT

Cynthia Coolahan
Gloria Gill
Linda Maio

Table 1. Quantum efficiency of photoreduction of ferric chelates.

	Φ (molecules/photon)		
	458 nm	488 nm	514 nm
Fe^{3+}EDTA	0.0127	0.0041 0.0053 0.0051 0.0053[a]	0.00118
Fe^{3+}citrate			
[citrate] = 0.1 *M*	--	0.2053 0.1787[a]	--
[citrate] = 2 m*M*	--	0.0795	--
Fe^{3+} oxalate	1.27	--	--
Fe^{3+}EDTA with citrate			
[EDTA] = 2.16×10^{-3} *M*	/		
[citrate] = 0.1 *M*	--	0.0309 0.0287	--
[citrate] = 0.01 *M*	--	0.0191	--
[citrate] = 2m *M*	--	0.0096	--
Fe^{3+}EDTA with oxalate			
[EDTA] = 2.16×10^{-3} *M*			
[oxalate] = 0.1 *M*	--	0.008	--

[a]NO introduced after photolysis.

determine whether NO has an effect on the chemistry of photolysis of ferric chelates.

Ferric chelate solutions were prepared such that the initial concentration of ferric ion was 7.2×10^{-4} *M* and the liquid concentrations varied from 2.16×10^{-3} to 0.1 *M*. The pH of the solutions was adjusted to 5.9 by adding NaOH and the ionic strength to 1 *M* by Na_2SO_4. The solutions were degassed in a photolysis cell, and one atmosphere of NO was added to the cell while solutions were agitated vigorously to ensure thorough mixing. In the cases when NO was added after photolysis, an atmosphere of inert Ar gas was introduced into the system over the solution prior to irradiation. The solutions were then irradiated with an Ar^+ laser at a selected wavelength. Ultraviolet and visible spectra of the solutions were recorded before and after photolysis on a Cary 219 spectrophotometer.

Table 1 shows that the quantum efficiency is greater at shorter wavelengths for all ferric chelates investigated and that Fe(III)(oxalate) has the largest quantum efficiency for the three wavelengths studied, followed by Fe(III)(citrate) and Fe(III)(EDTA). The quantum efficiency of Fe(III)(EDTA) is enhanced when citrate ion or oxalate ion is present, and increases with increasing citrate ion concentration. The quantum efficiency of Fe(III)(citrate) was found to be dependent on the citrate ion concentrations whereas the quantum efficiency of Fe(III)(EDTA) is independent of the EDTA concentrations.

Preliminary results showed that 0.5 molecules of EDTA were destroyed for every one molecule of ferric ion reduced. This was determined by adding an equivalent amount of ferrous ion to the excess EDTA in the photolyzed solution. Then the increase in concentration of the Fe(II)(EDTA)NO complex was measured, and from this, the amount of EDTA destroyed could be calculated.

The NO was found to have no effect on the chemistry of photolysis of Fe(III)(EDTA) solutions. The quantum efficiency of Fe(III)(EDTA) photoreduction at 488 nm was the same whether NO gas was introduced before or after the photolysis.

PLANNED ACTIVITIES FOR FY 1984

We will extend this study to other ferric chelates such as Fe(III)(NTA) and Fe(III)(IDA). The quantum efficiency of ferric chelates will be determined at wavelengths near the UV region. We will also investigate the mechanism of the photoreduction of ferric chelates. The potential of employing this previously unrecognized technology for the regeneration of flue-gas scrubbing liquors will be assessed.

techniques for measuring intermediate and product species formed during the oxidation of fossil fuels and for characterizing turbulence has been a major effort. The characterization and understanding of turbulence and high-temperature chemistry are of high priority in this program. Areas of application which dominate these studies are engine research, pollutant abatement in utilities, fire control, and ignition phenomena.

The Scrubber Chemistry Group has been investigating the chemical character of pollutants generated by the combustion of fossil fuels to develop new, efficient strategies for pollutant emission control. Current research has been directed toward understanding the kinetics and mechanisms of homogeneous and heterogeneous catalysis of the interactions of sulfur dioxide and nitrogen oxides, both among themselves and with other compounds. When this fundamental chemistry is understood, it will be applied to the development of an efficient, cost-effective scrubber for simultaneous desulfurization and denitrification of flue gases. The same knowledge can also be applied to improving the performance of lime/limestone desulfurization scrubbing systems, currently the type of scrubber most widely used by utilities.

Ecotoxicology is the science that seeks to determine the pathways, fate, and effects of toxic substances in the natural environment. The projects of the Lake Ecotoxicology Research Group focus on one particular type of natural environment, freshwater lakes. Research has proceeded in two converging directions: the development of laboratory microcosms for lake ecotoxicology and the study of acid precipitation in the western United States. The group has demonstrated that lake microcosms can be designed and operated to provide realistic toxic-substance test systems and has applied microcosms to analyze effects of acid precipitation. Field studies on acid precipitation and its effects in the Sierra Nevada and the Colorado Rockies have been another major focus of the group. Through a combination of microcosm technology and field work, it seeks to predict the chronology of acidification in the western United States.

Two major projects have occupied members of the Trace Element Analysis Group. The first is the continuation of the survey of instrumentation for environmental monitoring. Commercial publication of the survey is done through Wiley Interscience, which is handling the distribution of this work. Material devoted to water monitoring will be updated and published in 1984. The second project is the study of the relationship between massive repetitive life extinctions on the earth and asteroid (or other extraterrestrial) impacts. Studies of this relationship have concentrated on searches for unusually high iridium abundances in geochemical samples from rock layers known or expected to mark life-extinction horizons. Geochemical and other tests are made to determine if the iridium-rich rocks are of extraterrestrial origin and hence related to impacts. The nature of the sedimentation of the rocks, the worldwide extent of the extinction horizons, and the extent to which the extinctions are related to impacts are also studied.

During FY 1983, the research groups of the Environmental Research Program conducted the studies described in the short reports that follow. In many cases, more detailed papers have been or will be published in archival scientific journals.

Role of Graphitic Carbon Particles in Radiative Transfer in the Arctic Haze*

H. Rosen, A.D.A. Hansen, and T. Novakov

Aerosol particles can change the radiation balance of the earth, leading to a cooling or heating effect with the magnitude and sign of the temperature change largely dependent on aerosol optical properties, aerosol concentrations, and the albedo of the underlying surface.[1] A purely scattering aerosol will reflect energy that would normally be absorbed by the earth-atmosphere system back into space, leading to a cooling effect. Conversely, an absorbing component in the aerosol can lead to a heating of the earth-atmosphere system if the reflectivity of the underlying surface is sufficiently high. Most studies of the effects of aerosols on atmospheric radiative transfer on a global scale have assumed a dominantly scattering aerosol with only a small absorbing component, since this appears to be a good representation of naturally occurring aerosols.

Analysis of the optical properties of aerosols in urban locations, however, indicates that the absorbing component can be substantial, because of large concentrations in the aerosols of combustion-generated graphitic carbon particles. These particles have been identified on a molecular level by Raman spectroscopy.[2-4] If they can be transported on a global scale, then significant aerosol absorption should be observable, even in remote locations such as the Arctic. This was confirmed in previous papers,[5,6] where we reported finding substantial concentrations of graphitic carbon particles at ground level in the western Arctic.

ACCOMPLISHMENTS DURING FY 1983

If the large concentrations of graphitic particles found at Arctic ground-level stations also occur throughout the area's troposphere, they could have a significant impact on the Arctic radiation balance and climate.[7,8] During March and April, 1983, a series of flights, organized by the National Oceanic and Atmospheric Administration (NOAA), explored the vertical and horizontal distributions of the Arctic haze. One of the instruments on these flights was an aethalometer,[9] a soot meter developed at Lawrence Berkeley Laboratory and described in detail elsewhere in this annual report by Hansen *et al.* The aethalometer is capable of determining graphitic carbon concentrations in real time, using the calibration developed by Gundel *et al.*,[10] also described in this annual report.

The data from the flights have not yet been fully analyzed, but preliminary analysis of one flight in the Norwegian Arctic has been completed. This flight, northerly from Bodo, Norway, over Bear Island to northern Spitzbergen and back, took place on the morning of March 31, 1983. Data were taken during a slow descent from 7 km to 0.1 km at 74°N, 25°E. The graphitic carbon concentrations as a function of altitude are shown in Fig. 1. Also shown for comparison are the average ground-level concentrations found in Barrow for April, 1982, and the average ground-level concentrations found in various urban areas in the United States. It is clear from this figure that the vertical profile has considerable structure, with at least three layers located at approximately 1 km, 2.5 km, and 4.5 km. The concentrations within these layers are large, with the peak concentrations at 1 km only about a factor of 2.5 lower than those in New York City and a factor of 10 higher than ground-level concentrations measured at Barrow, Alaska (0.15 $\mu g/m^3$ in April, 1982). The flight profile also indicates a relatively clean region at low altitudes, which is consistent with the Barrow results at ground level and the limited ground-level measurements we've made in the Norwegian Arctic.

Recent modeling studies of the possible effects of the Arctic haze on the radiation budget of the Arctic indicate rather substantial changes in the heat balance if the optical depth due to absorption is sufficiently large.[7,8] One can calculate this optical depth from the results shown in Fig. 1 for various models of the Arctic aerosol. In these models, it is important to distinguish between graphitic particles mixed internally or externally with the other nonabsorbing components. Such differences, as shown by Ackerman and Toon,[11] can lead to significant changes in aerosol absorption. We will consider three examples:

*This work was supported by the Director, Office of Energy Research, Carbon Dioxide Research Division of the U.S. Department of Energy under Contract No. DE-AC03-76SF00098.

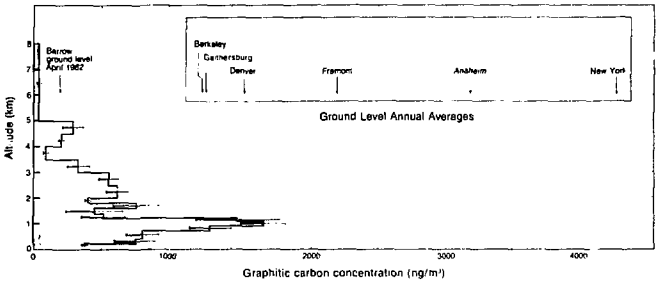

Figure 1. Graphitic carbon concentrations vs. altitude on March 31, 1983, at ~74°N 25°E expressed as nanograms per cubic meter. Shown for comparison are the annual average ground-level concentrations at various urban locations in the United States and the average ground-level values at the NOAA-GMCC observatory near Barrow, Alaska, for April 1982. (XBL 8312-4319A)

(1) Graphitic carbon particles internally mixed with all the major submicron aerosol components (i.e., sulfates, organics).

(2) Graphitic carbon particles internally mixed with only submicron organic aerosol components.

(3) Graphitic carbon particles externally mixed with the other aerosol components.

Of these three, the first two are the most likely combinations. For these, we treat the particles as homogeneous spheres and mix in the various components by volume mixing of dielectric constants.[12] In these calculations, the indices of refraction of graphitic carbon were chosen to be $1.94-0.66\,i$,[11] with a density of 1.5, and the index of refraction of the nonabsorbing components was taken to be 1.5. The relative concentrations of graphitic carbon, sulfates, and organic carbon are obtained from ground-level measurements in April at Barrow, Alaska, where detailed chemical analysis of the submicron aerosol has been completed. The particle size distribution for the submicron aerosol is assumed to be log-normal with $r_{gv} = 0.2\ \mu$ and $\sigma_g = 2$, which are obtained from Whitby[13] for the urban aerosol and are consistent with the results of Heintzenberg[14] for the Arctic aerosol. For the first two examples, Mie calculations yield absorption cross sections of 19 m^2 and 12 m^2 per gram of graphitic carbon, respectively. For the external mixture, we use the photoacoustic measurements of Roessler and Faxvog[15] and Szkarlat and Japar,[16] who obtain the average value of 8.3 m^2/g at 0.5 μ.

For these three examples, the optical depths due to absorption are respectively 0.052, 0.033, and 0.023. These optical depths are large enough to produce significant changes in the radiation balance over a highly reflecting surface.[7,8] This is illustrated by the calculations of Porch and MacCracken[7] and of Cess,[8] who have modeled the Arctic aerosol for an absorption optical depth of 0.021 (which is close to our minimum estimate), cloud-free conditions, a zenith angle of 72°, and a surface albedo of 0.8. For these parameters, they obtain a change in the noontime solar radiation balance at the top of the troposphere of about 20 W/m^2. When averaged over the day for March 15 at 70°N, the surface-atmosphere energy absorption would increase by about 7 W/m^2.[7,8] These changes are substantial: they would correspond to an increase in the energy absorbed by the earth-atmosphere system of approximately 5% of the incident solar flux at the top of the troposphere. Correspondingly larger changes would be expected for the internally mixed aerosol models.

PLANNED ACTIVITIES FOR FY 1984

These first estimates of the effects of graphitic carbon on the Arctic radiation balance are based on the flight profile shown in Fig. 1, which is obviously only over a small geographical region and in a narrow time frame. Similar vertical and horizontal profiles in other areas of the Arctic will be analyzed during FY 1984. The data analyzed so far represent about 2% of the flight time over the Arctic. These data will be compared to a wide range of meteorological variables (wind speed, wind direction, relative humidity) and physical parameters such as scattering coefficients, condensation nuclei counts, and net flux measurements. These comparisons should help to improve our understanding of the sources and optical properties of the Arctic haze.

REFERENCES

1. Paltridge, G.W. and Platt, C.M.R. (1976), *Radiative Processes in Meteorology and Climatology*, Elsevier, Oxford, England.
2. Rosen, H., Hansen, A.D.A., Dod, R.L., and Novakov, T. (1980), "Soot in Urban Atmospheres: Determination by an Optical Absorption Technique," *Science 208*, p. 741.
3. Rosen, H., Hansen, A.D.A., Gundel, L., and Novakov, T. (1978), "Identification of the Optically Absorbing Component in Urban Aerosols," *Appl. Opt. 17*, p .3859.
4. Lin, C.-I., Baker, M., and Charlson, R.J. (1973), "Absorption Coefficient of Atmospheric Aerosol: A Method for Measurement," *Appl. Opt. 12*, p. 1356.
5. Rosen, H., Novakov, T., and Bodhaine, B.A. (1981), "Soot in the Arctic," *Atmos. Environ. 15*, p. 1371.
6. Rosen, H. and Novakov, T. (1983), "Identification of Graphitic Carbon Particles in the Arctic Atmosphere," *Nature* (accepted for publication).
7. Porch, W.M. and MacCracken, M.C. (1982), "Parametric Study of the Effects of Arctic Soot on Solar Radiation," *Atmos. Environ. 16*, p. 1365.
8. Cess, R.D. (1983), "Arctic Aerosols: Model Estimates of Interactive Influences upon the Surface-Troposphere Radiation Budget," *Atmos. Environ.* (accepted for publication).
9. Hansen, A.D.A., Rosen, H., and Novakov, T. (1982), "Real-Time Measurement of the Absorption Coefficient of Aerosol Particles," *Appl. Opt. 21*, p. 3060.
10. Gundel, L.A., Dod R.L., Rosen, H. and Novakov, T. (1984), "The Relationship Between Optical Attenuation and Black Carbon Concentration for Ambient and Source Particles," *Science of the Total Environment*, in press.
11. Ackerman, T.P. and Toon, O.B. (1981), "Absorption of Visible Radiation in Atmosphere Containing Mixtures of Absorbing and Nonabsorbing Particles," *Appl Opt. 20*, p. 3661.
12. Chylek, P., Ramaswamy, V., Cheng, R., and Pinnick, R.G. (1981), "Optical Properties and Mass Concentration of Carbonaceous Smokes," *Appl. Opt. 20*, p. 2980.
13. Whitby, K.T. (1978), *Atmos. Environ. 12*, p. 135.
14. Heintzenberg, J. (1980), *Tellus 32*, p. 251.
15. Roessler, D.M. and Faxvog, F.R. (1979), "Opacity of Black Smoke: Calculated Variation with Particle Size and Refractive Index," *Appl. Opt. 18*, p. 1399.
16. Szkarlat, A.C. and Japar, S.M. (1981), "Light Absorption by Airborne Aerosols: Comparison of Integrating Plate and Spectrophone Techniques," *Appl. Opt. 20*, p. 1151.

Carbon-Oxygen Ratios in Ambient Particulate Matter*

W.H. Benner, L.A. Gundel, and T. Novakov

The partial oxidation of gaseous hydrocarbons observed in smog chamber studies[1] has been correlated with aerosol formation. Such gas-to-particle conversion in the troposphere is thought to contribute to haze formation. In general, the partial oxidation of gaseous hydrocarbons produces compounds that have carbonyl and acid functional groups. These groups reduce the vapor pressure of the precursor hydrocarbon and cause the gas-to-particle conversion. Our recent development[2,3] of a method sensitive enough to quantitate oxygen on filter samples or in extracts of filter samples of ambient particulate matter is directed toward understanding these reactions and their importance in haze formation. This article summarizes our initial determination of C/O ratios in the organic fraction of ambient particulate matter.

This work was supported by the Director, Office of Energy Research, Office of Health and Environmental Research, Physical and Technological Research Division of the U.S. Department of Energy under Contract No. DE-AC03-76SF00098 and by the National Science Foundation under Contract No. ATM 82-10343.

ACCOMPLISHMENTS DURING FY 1983

A high-volume sampler (~1100 lpm, 400 cm^2 filter) collected 24-hour samples of ambient or source particulate matter on prefired (775°C) quartz-fiber filters. A Soxhlet extractor was used to extract sequentially portions of each filter sample in benzene and then methanol-chloroform (1:2 vol/vol). Dessication of the samples over P_2O_5 for 24 hours pre-

cluded interference from adsorbed water vapor. The corrected pyrolyzable oxygen concentration (O_{pc}/cm^2) was calculated for each sample by subtracting the oxygen present in a sample as NO_3^- and $SO_4^=$ from the pyrolyzable oxygen concentration (O_p/cm^2); i.e., $O_{pc} = [O_p] - [O_{NO_3^-}] - [O_{SO_4^=}]$ blank value. Concentrations of NO_3^- and $SO_4^=$ were determined by ion chromatography.

Ambient samples collected in Berkeley were analyzed before extraction. Figure 1 shows that C and O_{pc} correlate strongly and that the C/O ratio ≈ 1 (atomic ratio ≈ 1.3). Since particulate C is a major component of ambient particulate matter, constituting 4–40% of the total suspended particulate mass,[4] it can be inferred that oxygen is also a major component. Comparison of the plot of O_p vs. C to the plot of O_{pc} vs. C shows that oxygen in NO_3^- and $SO_4^=$ makes up about 18% of the total O_p. Because oxygen-containing substances other than organics could be present in these samples, one cannot deduce the C/O ratio in the organic fraction from the data in Fig. 1. The major inorganic oxygen species are taken into account (NO_3^- and $SO_4^=$ are quantitated, carbonate is minimal in Berkeley samples, and silica and alumina are not detected), but OH groups on silica and oxygen attached to the black carbon could prejudice the conclusions.

The C/O ratio in the organic fraction was determined in two ways. First, the set of samples reported in Fig. 1 was reanalyzed after solvent extraction, and the extractable O_{pc} and extractable C values were calculated. Figure 2 shows that these

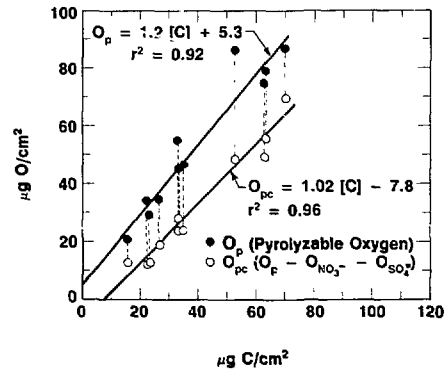

Figure 1. The determination of oxygen on filter samples of Berkeley ambient particulate matter. Filters analyzed before extraction. (XBL 838-2991A)

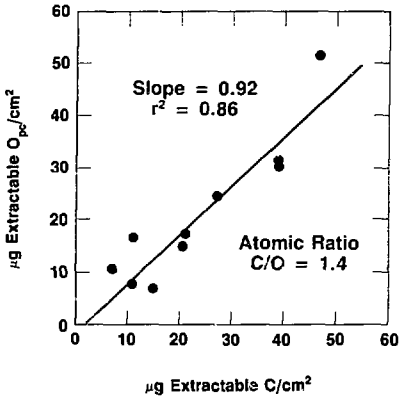

Figure 2. Determination of oxygen on filter samples of Berkeley ambient particulate matter. Filters analyzed before and after extraction and C and O_{pc} lost by extraction calculated. (XBL 838-2935A)

two values correlate strongly (r^2 = 0.86). Extraction removes the soluble organic material; and unless insoluble oxygen-containing particles are lost during the extraction procedure, these data suggest that the soluble organic fraction of the ambient particulate matter is highly oxygenated, having an atomic C/O ≈ 1.4.

The analysis of the Berkeley samples before and after extraction is presented in another way in Fig. 3, where O_{pc} on an extracted filter is plotted vs. O_{pc} on the same filter before extraction. Figure 3 shows that as much as 40% of the O_{pc} on a filter sample is insoluble. As long as none of this insoluble material is

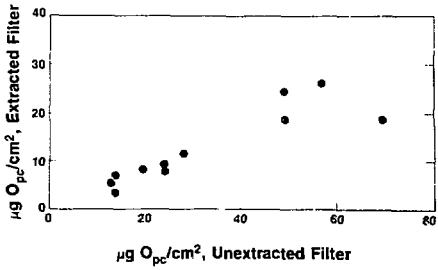

Figure 3. Determination of oxygen on filter samples of Berkeley ambient particulate matter. (XBL 838-2916A)

physically lost from a filter during extraction, the extractable C/extractable O_{pc} ratio of ~ 1.4 is a correct value.

To exclude the possibility that insoluble particulate oxygen was lost during extraction and thus prejudiced the calculated C/O ratios, a second set of samples was extracted and the filtered extracts analyzed for C and O_{pc}. Several filter samples of aged ambient particulate matter were collected in Riverside, California. Two samples that represent ambient particulate matter enriched with fresh vehicular emissions were collected downwind and immediately adjacent to a freeway in Berkeley, California. Another two filter samples were collected in the exhaust duct of a freeway tunnel and represent a composite of vehicle sources. An additional sample was collected in an enclosed parking garage dominated by diesel bus traffic. The solvent extracts of each sample were filtered through 0.5-μm Fluoropore filters to remove any particles and filter fibers dislodged from the filter during extraction. The extracts were then concentrated by evaporation under N_2 at room temperature, and, finally, the concentrate was analyzed after evaporation onto a piece of quartz-fiber filter.

Table 1. Analysis of solvent extracts of ambient particulate matter.

Sample	C/O (atom)
Ambient	
Riverside, CA, 16–17 June 1981	2.1
Riverside, CA, 17 June 1981	2.3
Riverside, CA, 16 June 1981[a]	1.6
Riverside, CA, 16–17 June 1981[a]	1.7
Source-enriched ambient	
Berkeley, CA, 30 August 1979	2.3
Berkeley, CA, 29 August 1979	2.9
Source	
Highway tunnel, 9 Feb. 1983, #5	6.4
Highway tunnel, 9 Feb. 1983, #6	5.4
Diesel bus, 12 Nov. 1978, #1	7.2

[a]Particulate diameter $\leq$ 1.5 μm.

Table 1 presents the C/O_{pc} ratios found in these extracts. The organic fraction of size-segregated samples (particles having a diameter of less than 1.5 μm) of aged ambient particulate matter were the most oxygenated (atomic C/O $\approx$ 1.6), and fresh source samples were the least oxygenated (atomic C/O $\approx$ 6). Ambient samples from Riverside and Berkeley showed nearly similar atomic C/O ratios of about 2.3, even though the Berkeley samples were enriched in source particulate matter. The data in Table 1 suggest that the aging of particles is associated with a decrease in C/O, i.e., an increase in oxygenation. The C/O_{pc} ratios determined from the analysis of filtered extracts and from the analysis of filters before and after extraction are not greatly different. But since these two procedures were performed on separate sets of samples, only the general conclusion that the organic fraction in age samples is highly oxygenated can be drawn.

PLANNED ACTIVITIES FOR FY 1984

The data base for oxygen content of ambient particulate matter will be expanded so that the influence of meteorology, aging, and source emissions on the composition of the ambient aerosol can be evaluated.

REFERENCES

1. Hidy, G.M., *et al.*, Eds., (1979), *The Character and Origins of Smog Aerosols*, Wiley, New York.
2. Benner, W.H. (1983), "The Determination of Pyrolyzable Oxygen in Ambient Particulate Matter," submitted to *Anal. Chem.*
3. Benner, W.H., Hansen, A.D.A., Gundel, L.A., and Novakov, T. (1984), "Determination of Organic Oxygen in Ambient Particulate Matter," *Science of the Total Environment*, in press.
4. Mueller, P.K., *et al.* (1982), "Atmospheric Particulate Carbon Observations in Urban and Rural Areas of the United States," *Particulate Carbon: Atmospheric Life Cycle*, G.T. Wolff and R.L. Klimisch, Eds., Plenum, New York, p. 343.

The Relationship Between Optical Attenuation and Black Carbon for Urban, Arctic, and Source Carbonaceous Particles*

L.A. Gundel, R.L. Dod, A.F. Berry, H. Rosen, and T. Novakov

Particulate material from ambient air and combustion sources usually appears black when collected on filters, because of the presence of light-absorbing graphitic or black carbon (BC).[1] In the atmosphere, light absorption by these particles can degrade visibility[2] and perturb the tropospheric radiation balance.[3,4] These effects are especially important in the Arctic haze, where significant amounts of black carbon have been found.[5] In this article, we describe a nondestructive and fast technique for measuring black-carbon concentration — the laser transmission method. This technique measures the attenuation of visible light (ATN) as it passes through a particulate sample on a filter.

The results of this study, as reported here, have been used to calibrate the laser transmission method and to provide a value for the specific attenuation, σ, which is the value of ATN per unit mass of black carbon. It is important to note that the calibration method is independent of knowledge of the exact optical properties of black carbon. Earlier work in this project[6] focused on particulate matter collected in urban locations and from combustion sources. Here we include studies of black carbon in the Arctic haze.

ACCOMPLISHMENTS DURING FY 1983

Samples of aerosol particles were collected on quartz-fiber filters that had been prefired at 800°C for 12 hours. Both high-volume (40 standard cubic feet per minute and low-volume (10–20 SCFM) samplers were used. One-third of the samples were size-segregated, with a particle cutoff of less than 2 μm. Ambient samples were collected in Berkeley (two sites) and Los Angeles, California; Warren, Michigan[6]; Vienna, Austria; and Ljubljana, Yugoslavia. Typical ambient sampling time was 24 hours.

A variety of combustion sources were sampled. A natural gas boiler (input of 290,000 Btu hr^{-1}) was sampled in its chimney. Propane soot was collected during an extensive intercomparison study.[7] A small diesel bus idling in a vacant parking garage was sampled 2 m from its exhaust pipe. Other samples, representing an average motor-vehicle population, were collected in the exhaust vents of the uphill bore of a highway tunnel and in a parking garage. The Arctic haze was sampled at Point Barrow, Alaska, using size-segregated (<2.5 μm) high-volume sampling at 40 SCFM for 1-week periods throughout the winter and spring of 1982–83.

The laser transmission method (LTM) measures the attenuation of visible light as it passes through the filter. ATN is defined as

$$\mathrm{ATN} = -100 \ln I/I_0 , \qquad (1)$$

where I_0 and I are the transmitted light intensities for the blank and the loaded filter respectively. Rosen *et al.*[1] and Yasa *et al.*[8] have shown that the light attenuation is due to the presence of black carbon. If ATN has a linear dependence on [BC], the concentration of black carbon, then

$$[\mathrm{BC}] = \mathrm{ATN}/\sigma , \qquad (2)$$

where σ is the specific attenuation for black carbon.

Attenuation was measured during the evolved gas analysis (EGA) procedure for determining [BC] and separately at room temperature by LTM. The two measurements of ATN agreed to within 3%. The limits of detection and quantitation for ATN are 6 and 20, respectively.

Temperature-programmed evolved gas analysis in oxygen[9] with continuous light transmission measurement was used to identify and quantify the black carbon. A thermogram of Arctic particles is shown in Fig. 1. [BC] was determined from the area of the thermogram peak that corresponds to the increase in light transmission during combustion. This carbon peak is usually centered between 425° and 500°C. Removal of soluble organic material by solvent extraction leads to thermograms in which isolation of this peak is straightforward. This procedure removes most of the organic carbon but leaves black carbon nearly uncharged, as shown by an average decrease in ATN for extracted samples of only 7%, for more than 100 samples. In this study, all BC determinations were performed on samples sequentially extracted by benzene and a methanol-chloroform mixture (1:2,v:v) in Soxhlet devices, in two 6-hour steps.[10] The limits of detection and

*This work was supported by the Office of Energy Research, Office of Health and Environmental Research, Physical and Technological Research Division of the U.S. Department of Energy under Contract No. DE-AC03-76SF00098 and by the National Science Foundation under Contract No. ATM 82-10343.

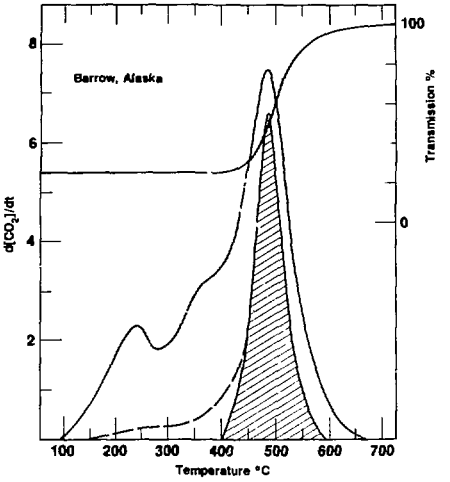

Figure 1. Thermogram of carbonaceous particles collected in the Arctic. Light transmission is shown by the *S*-shaped curve. The shaded area represents black carbon.
(XBL 8312-6902)

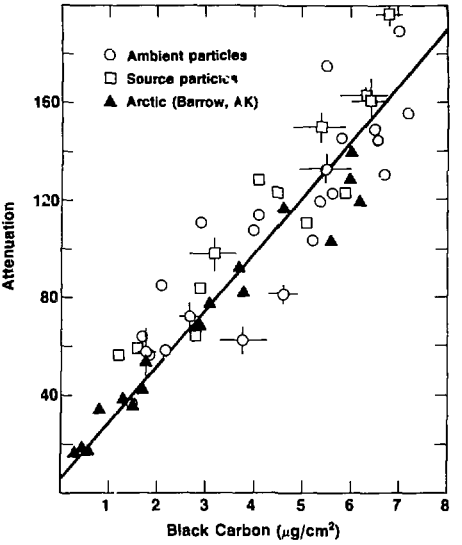

Figure 2. The relationship between attenuation and black carbon concentration for all data with ATN < 200 and BC < 8 $\mu g\ cm^{-2}$. (XBL 838-540)

quantitation for blank corrected samples are 0.6 and 2.0 μg BC cm^{-2}, respectively.

ATN and [BC] data are presented in Fig. 2 for all combustion-source, urban-air, and Arctic samples with ATN $\leq$ 200 and BC = 8 $\mu g\ cm^{-2}$. Within experimental error, all carbonaceous particles appear to follow the same relationship between ATN and [BC], regardless of their origin. If we combine all data with ATN $\leq$ 200 and [BC] $\leq$ 8 $\mu g\ cm^{-2}$,

$$ATN = (7.2 \pm 5.7) + (23.1 \pm 1.2)[BC], \quad (3)$$

with $r = 0.93$, where r is the correlation coefficient. [BC] can be predicted from Eq. (3) with an expected random error of 0.3 $\mu g\ cm^{-2}$ at ATN = 50, and 0.6 $\mu g\ cm^{-2}$ at ATN = 200, using the observed variances in [BC] and ATN. If the intercept of Eq. (3) is indistinguishable from zero, the slope of Eq. (3) is the specific attenuation, σ. If the non-zero intercept is real, it may indicate that σ is dependent on [BC] at low concentrations.

All data, regardless of sampling loading, can be fit to the equation:

$$ATN = -100 \ln [(1 - \alpha)e^{-\sigma[BC]} - \alpha],$$

which reflects the observation that a small fraction, α (~0.02), of the incident light is conducted along the quartz fibers without interaction with the particle deposit. Using this equation, we find that the specific attenuation is 23.9 ± 2.0 for all data, with α = 0.017 and r = 0.76.

PLANNED ACTIVITIES FOR FY 1984

We plan to investigate the dependence of the specific attenuation on [BC] at low concentrations, while calibrating the real-time ATN instrument for [BC]. We will also investigate the influence of particle size and composition on the specific attenuation.

REFERENCES

1. Rosen, H., Hansen, A.D.A., Gundel, L.A., and Novakov, T. (1978), "Identification of the Optically Absorbing Component in Urban Aerosols." *Appl. Opt. 17*, p. 3859.
2. Weiss, R.E., *et al.* (1979), "Studies of the Optical, Physical, and Chemical Properties of Light

Absorbing Aerosols," in *Proceedings, Conference on Carbonaceous Particles in the Atmosphere*, LBL-9037, p. 257.
3. Porch, W.M. and MacCracken, M.C. (1982), "Parametric Study of the Effects of Arctic Soot on Solar Radiation," *Atmos. Environ. 16*, p. 1365.
4. Cess, R.D. (1983), "Arctic Aerosols: Model Estimates of Interactive Influences upon the Surface-Troposphere Radiation Budget," *Atmos. Environ.*, in press.
5. Rosen, H., Novakov, T. and Bodhaine, B.A. (1981), "Soot in the Arctic," *Atmos. Environ. 15*, p. 1371.
6. Gundel, L.A., Dod, R.L., Rosen, H.J., and Novakov, T. (1983), "The Relationship Between Optical Attenuation and Black Carbon Concentration for Carbonaceous Particles," *Environmental Research Program, FY 1982 Annual Report*, LBL-15298, p. 4–10.
7. Gerber, H.E. and Hindman, E.E., Eds. (1982), *Light Absorption by Aerosol Particles*, Spectrum, Hampton, VA.
8. Yasa, Z., *et al.* (1979), "Photoacoustic Investigation of Urban Aerosol Particles," *Appl. Opt. 18*, p. 2528.
9. Dod, R.L., Rosen, H. and Novakov, T. (1979), "Optico-thermal Analysis of the Carbonaceous Fraction of Aerosol Particles," *Atmospheric Aerosol Research Annual Report, 1977–78*, LBL-8696, p. 2.
10. Appel, B.R., *et al.* (1979), "Analysis of Carbonaceous Material in Southern California Atmospheric Aerosols," *Environ. Sci. Technol. 13*, p. 98.

Primary Peroxides from Hydrocarbon Flames

P.M. McKinney, W.H. Benner, and T. Novakov

Hydrogen peroxide is an important oxidant for the aqueous-phase conversion of sulfur dioxide to sulfate in the atmosphere.[1,2] It has been assumed that this H_2O_2 originates from secondary photochemical reactions in the atmosphere; however, we have uncovered evidence that combustion is also a source of H_2O_2, as well as other, unknown peroxides.

ACCOMPLISHMENTS DURING FY 1983

Figure 1 shows the experimental setup, in which combustion is carried out in the bottom of a Pyrex chimney 4 inches in diameter and 40 inches long. The chimney and all Teflon and glass lines to the impinger are heated to prevent condensation. Water-soluble combustion products are collected by drawing approximately one-third of the air that flows through the chimney (6 liters per minute total) through a 1-micron Teflon filter and then through one or more impingers, which contain 20.0 mL of water. The soluble anions were quantitated by ion chromatography.

In a typical experiment, 0.05 mole of propane or butane, or 0.15 mole of natural gas, is burned under optional conditions, e.g., an intermittent flame, a diffusion flame, or a flame in which the fuel was premixed with air. Sulfate, nitrate, and sulfite were quantitated before and after the addition of micromolar concentrations of sulfite. Samples were analyzed for peroxide by a titrimetric procedure using potassium iodide.[3] The limit of detection of this method was approximately 1×10^{-5} *M* oxidant.

Peroxide was detected in samples collected during the intermittent combustion of propane and butane but not during the similar combustion of natural gas (Fig. 2). Diffusion and premixed flames from the three fuels produced no detectable peroxides in the impinger water. The addition of sulfite to

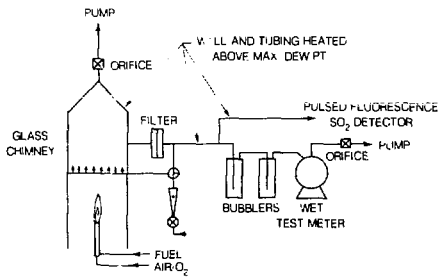

Figure 1. Apparatus for sampling primary oxidants. (XBL 834-173)

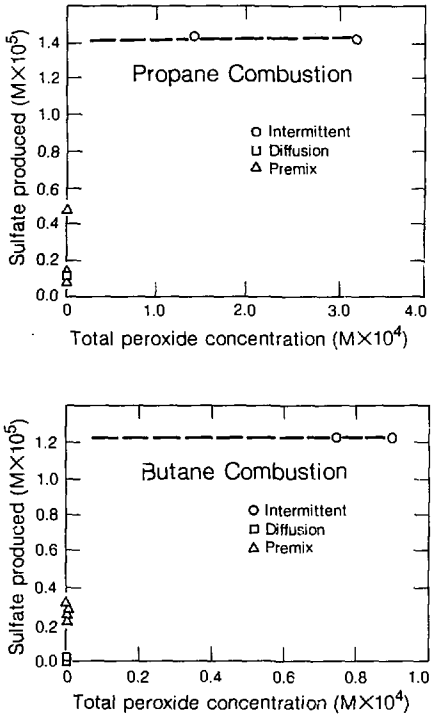

Figure 2. Sulfate produced vs. total peroxides.
(XBL 841-8319)

each sample resulted in sulfate formation in all but two samples, but sulfite oxidation was observed in at least one sample of each flame type. For the intermittent propane and butane samples, 14 μm and 12 μm sulfite were oxidized, respectively. Samples from the intermittent combustion of natural gas and from diffusion and premixed flames of the three fuels showed less oxidation of the added sulfite. A butane diffusion flame and an intermittent natural gas flame produced the least amount of sulfate. By modifying the sampling technique, combustion water was collected in an ice-cooled condenser. Oxidant concentrations as high as 0.02 *M* were observed in samples of intermittent propane flames.

Catalase, which selectively decomposes H_2O_2, was added to buffered impinger samples before peroxide analysis. These additions showed that more than 80% of the peroxide formed during the combustion of propane, and that 100% of the peroxide from butane was H_2O_2.

These simple experiments point out a fact apparently overlooked by many atmospheric chemists. Combustion can be a source of sulfite oxidants. This implies that primary oxidants could play an important role in the oxidation of SO_2 in fogs and clouds, thus helping to form acidic precipitation.

The importance of this finding depends on the amount of oxidant released by combustion sources. Table 1 presents the results of several filtered exhaust samples collected from three vehicles. Impinger water samples were analyzed before and after the addition of sulfite. All samples showed sulfite oxidation. Even before sulfite addition, a considerable fraction of the total aqueous sulfur was present as $SO_4^{=}$ (third column, Table 1). Because the production of primary sulfate during combustion

Table 1. Oxidation of exhaust SO_2 in impinger water.[a]

Source vehicle	ppm S(IV)	ppm S(VI)	$\frac{S(IV)}{S(IV)+S(VI)}$	Time (min)	ppm SO_4^{2-} in exhaust
Alfa 1	0.31	0.073	0.19	10	0.067
Alfa 2	2.43	0.81	0.25	15	0.40
Alfa 3	3.20	1.20	0.27	15	0.67
Audi	3.36	1.21	0.26	10	0.92
Truck[b]	0.40	0.13	0.24	15	0.13

[a] ppm SO_2 oxidized in exhaust = $\frac{\text{ppm S(VI)} \times 20(\text{mL } H_2O)}{2.5 \times \text{time(min)} \times \text{flow(L/min)}}$.

[b] Catalytic converter.

is small (99% of sulfur emissions are SO_2) and because primary sulfate would not have passed through the filter, it can be argued that the detected $SO_4^=$ came from the oxidation of SO_2 in the impinger water. (The SO_2 came from sulfur in the fuel). These results suggest that vehicles can be a source of primary oxidants.

PLANNED ACTIVITIES FOR FY 1984

We plan to further characterize combustion products and study the products of other fuels.

REFERENCES

1. Penkett, S.A., Jones, B.M.R., Brice, K.A., and Eggleton, A.E.J. (1979), "The Importance of Atmospheric O_3 and H_2O_2 in Oxidizing SO_2 in Cloud and Rainwater," *Atmos. Environ. 13*, p. 123.
2. Kunen, S.M. Lazrus, A.L., Kok, G.L., and Heikes, G.B. (1983), "Aqueous Oxidation of SO_2 by Hydrogen Peroxide," *J. Geophys. Rev. 88*, p. 3671.
3. Johnson, R.M. and Siddiqi, I.W. (1970), *The Determination of Organic Peroxides*, Pergamon Press, Oxford, England.

Non-Ammonium Reduced Nitrogen Species in Atmospheric Aerosol Particles*

R.L. Dod, L.A. Gundel, W.H. Benner, and T. Novakov

Particulate nitrogenous air pollutants have traditionally been considered to be limited largely to inorganic compounds containing ammonium and nitrate ions. This view was challenged about 10 years ago by results from the then-new technique of x-ray photoelectron spectroscopy (ESCA), which indicated that as much as half of the ambient particulate nitrogen could exist in forms more reduced than ammonium.[1] This nitrogen was later postulated to consist of amines, amides, and heterocyclic compounds and was given the collective name N_x.[2] Further indication of the existence of N_x in ambient particles has been found with total nitrogen combustion analysis, which often indicates more nitrogen than does wet chemical analysis for NH_4^+.[3] However, no direct method reported can identify or quantitate the N_x constituents.

We have developed an NO_x thermal evolved gas analysis (EGA) system that differentiates among nitrogenous species based on volatility and thermal stability in an oxygen atmosphere.[4] EGA, in conjunction with ESCA and ion chromatography, has been applied to the analysis of ambient aerosol particulate samples collected by filtration to confirm the existence of N_x and to identify characteristics that provide information regarding final speciation.

ACCOMPLISHMENTS DURING FY 1983

ESCA analysis of atmospheric particles has been described elsewhere.[5,6] The method analyzes for elemental composition as well as the oxidation states of those elements. Quantitation is achieved by comparing analyte photoelectron peak intensities to those for one or more independently determined species within the sample. The sample must be in vacuum, and its surface is analyzed to the escape depth of the photoelectrons (~ 20 angstroms). We have previously determined that ambient aerosol particles are usually resistant to vacuum degradation and have similar surface and bulk compositions. Concentrations of nitrogenous species were determined from ESCA spectra by reference to sulfur in the samples, which was independently determined by x-ray fluorescence and/or combustion analysis. Deconvolution of the reduced nitrogen peak was based on the peak position and on the form of the ammonium nitrogen peak in $(NH_4)_2SO_4$. All photoelectron spectra were taken with an AEI ES200 spectrometer modified by installation of a position-sensitive detector (Surface Science Laboratories Model 239G).

Evolved gas analysis (CO_2 and SO_2) has been used by Malissa, Puxbaum, and Pell to investigate collected aerosol particulate matter.[7] We have adapted this analytical technique to analysis of particles collected on quartz-fiber filters and have extended it to include visible light attenuation and evolved NO_x. Our system, shown in Fig. 1, uses an NDIR CO_2 detector (MSA LIRA 202S), and a chemi-

*This work was supported by the Office of Energy Research, Office of Health and Environmental Research, Physical and Technological Research Division of the U.S. Department of Energy, under Contract No. DE-AC03-76SF00098 and by the National Science Foundation under Contract No. ATM 82-10343.

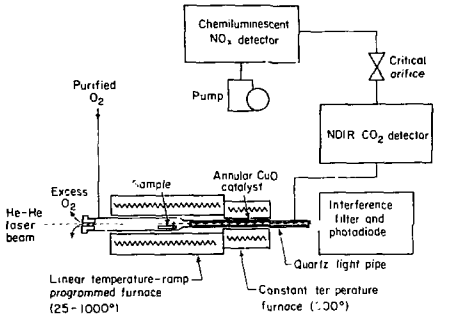

Figure 1. Schematic diagram of apparatus for thermal evolved gas analysis. (XBL 838-3111)

luminescent NO_x detector (ThermoElectron 14D/E) in series to determine analyte concentrations in a single low-volume gas stream. Detection limits of less than 1 ppm for CO_2 and less than 0.01 ppm for NO_x in the gas stream mean that, with a flow rate of 200–250 mL/min, the sample sizes required for quantitation with typical ambient particle samples are about 10 μg carbon and less than 1 μg nitrogen.

It has been shown that inorganic nitrogen ions in ambient aerosol particle samples can be identified from their ESCA spectra and can be further speciated to compounds with EGA.[4] We have shown that N_x can often be quantified by EGA[8] and have found that it is linked to organic material evolved during thermal analysis at temperatures above 250–300°C.

Investigation of a series of filter samples collected during a severe photochemical air pollution episode in Riverside, California, in June, 1981, gives further clues as to the composition of N_x. High-volume samplers were operated in parallel on top of a trailer on the University of California campus. One sampler collected total particulates; the particles collected on the second sampler were restricted to less than 1.5 μm by a size-segregating inlet and an impactor. Flow rates were equalized so that the only difference was in the particle sizes collected.

For each sample pair, substantially more nitrogen (and carbon) was present in the total-particulate sample than in the small-particle sample. Thermograms of a sample pair are shown in Fig. 2(a). When the large-particle contribution is determined by subtracting the fine-particle thermogram from that of total particulates [Fig. 2(b)], it becomes obvious that there is an apparent similarity of form between the CO_2 and NO_x thermograms of the large particles.

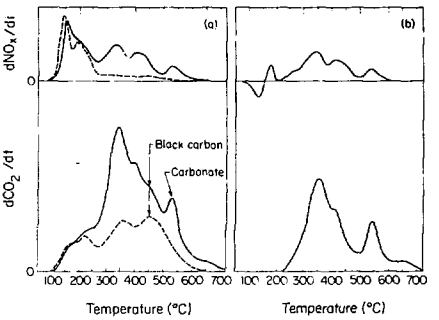

Figure 2. Evolved CO_2 and NO_x thermograms for ambient particles from Riverside, California, 17 June 1981. (a) Thermograms for total particle sample (solid lines) and small-particle (<1.5 μm) sample (dashed lines) collected in parallel. (b) Thermograms of large particles determined by difference between total-sample and small-particle thermograms. (XBL 838-3114)

This observation can be interpreted as an indication of chemical linkage between large-particle carbon and nitrogen. Such linkage could be caused by common existence in primary particles, by accretion of carbonaceous or nitrogenous species on large particles, or by some heterogeneous conversion of gaseous species on the surface of the particles. Although large and small particles may be different chemically, it seems unlikely that adsorption or conversion processes would be limited primarily to the large particles, which have a relative surface area less than that of the small particles.

PLANNED ACTIVITIES FOR FY 1984

Evidence that, at least under some circumstances, N_x is found primarily as a bulk component of the large aerosol particles suggests that further size-segregated sampling should be carried out. We intend to collect such segregated aerosol samples under a variety of atmospheric conditions. Analysis of these samples will be by the methods described above, with selected samples to be further analyzed by Fourier-transform infrared spectroscopy (FT-IR) for possible identification of at least some of the N_x species.

REFERENCES

1. Novakov, T., Mueller, P.K., Alcocer, A.E., and Otvos, J.W. (1972), "Chemical Composition of

Pasadena Aerosol by Particle Size and Time of Day. III. Chemical States of Nitrogen and Sulfur by Photoelectron Spectroscopy," *J. Colloid Interface Sci. 39*, p. 225.
2. Chang, S.-G. and Novakov, T. (1975), "Formation of Pollution Particulate Nitrogen Compounds by NO-Soot and NH_3-Soot Gas-Particle Surface Reactions," *Atmos. Environ. 9*, p. 495.
3. Spicer, C.W. (1977), "Photochemical Atmospheric Pollutants Derived from Nitrogen Oxides," *Atmos. Environ. 11*, p. 1089.
4. Dod, R.L. and Novakov, T. (1982), "Application of Thermal Analysis and Photoelectron Spectroscopy for the Characterization of Particulate Matter," in *Industrial Applications of Surface Analysis*, L.A. Casper and C.J. Powell, Eds., American Chemical Society, Washington, D.C., p. 397.
5. Novakov, T., Chang, S.-G. and Dod, R.L. (1977), "ESCA in Environmental Chemistry," in *Contemporary Topics in Environmental and Clinical Chemistry*, Vol. 1, D.M. Hercules, G.M. Hieftje, L.R. Snyder, and M.A. Evanson, Eds., Plenum, New York, p. 249.
6. Appel, B.R., *et al.* (1976), "An Intermethod Comparison of X-Ray Photoelectron Spectroscopic (ESCA) Analysis of Atmospheric Particulate Matter," *Intl. J. Environ. Chem. 4*, p. 169.
7. Malissa, H., Puxbaum, H. and Pell, E. (1976), "Zur Simultanen Relativkonduktometrischen Kohlenstoff- und Schwefelbestimmung in Stauben," *Z. Anal. Chem. 282*, p. 109.
8. Dod, R.L., Gundel, L.A. and Novakov, T. (1983), "Determination of Non-Ammonium, Non-Nitrate Nitrogen in Atmospheric Aerosol Particles," in *FY 1982 Annual Report: Environmental Research Program*, LBL-15298, p. 4-24.

Microencapsulation and Collection of Liquid-, Solid-, and Two-Phase Aerosols*

R.J. Otto

Work was started on the development of an advanced method for individual microparticle mass spectrometry based on the electrostatic accelerator of charged aerosol particles in the size range from 0.01 to 10 μm. An important first step in the research is the development of a collection method that will allow for the subsequent charging and acceleration of the aerosol particles. To this end, microencapsulation of the aerosol particles is being investigated as a new technique for preserving the physical and chemical properties of the particles for off-line analysis.

Microencapsulation has been used to fix cigarette smoke particles for size-distribution studies using electron microscopy.[1,2] Cigarette smoke is primarily a liquid-phase aerosol, and the normal procedure of collecting the particles on a Nuclepore filter for electron microscopy results only in the evaporation of the liquid phase, leaving a coating of tar on the filter and no visible particles in the micrographs. The mixing of gas-phase methyl-2-cyanoacrylate monomer (MCA, Eastman 910 adhesive) into a collection chamber containing smoke results in rapid condensation of the monomer on the smoke particles. The monomer then polymerizes and encapsulates the spherical liquid particles, which can then be filtered and will survive in the vacuum of an electron microscope. The polymeric reaction for MCA is an anionic initiated addition reaction catalyzed by water or hydroxyl groups.[3] The reaction is sufficiently rapid at 70°C that the particles can be collected immediately after mixing with the monomer. The term "encapsulation" implies the existence of a shell surrounding a liquid or solid core of material, which would be preferred. There is evidence, however, that true encapsulation does not occur with MCA, but rather that liquid particles are solidified by a polymer matrix, because of the solubility of the MCA monomer in the liquid phase.[1]

Aerosol microencapsulation can be broken down into three nearly sequential steps: mixing of the gas-phase monomer into the aerosol, condensation of the monomer on the aerosol surface, and polymerization of the monomer. Microencapsulation technology is being used for the controlled release of pesticides and drugs[4]; and although there are a large number of polymers used for this purpose, most of the work in this area has been with liquid suspensions. However, a number of these same polymers could be modified for encapsulation of aerosols. Control of the aerosol encapsulation

*This work was supported by the LBL Director's Program Development Fund and the U.S. Department of Energy under Contract No. DE-AC03-76SF00098.

process can be accomplished by selection of the polymerization reaction, by choice of initiator, and by control of the net rate of diffusion of the monomer to the surface of the aerosol, thereby controlling the amount of monomer deposited on the surface of the particle. Since temperature, pressure, and relative humidity affect the physical state of the aerosol, they would ideally be held constant during encapsulation.

Microencapsulation offers several advantages for use in preserving individual particles for off-line analysis. It effectively "freezes" both liquid-, solid-, and two-phase particles at the time of collection, preserving the particles' size distribution and isolating them from further chemical reactions with external reactants. It provides a uniform surface composition for all particles, which should result in uniform collection efficiency for particles of the same aerodynamic size but different chemical composition. Encapsulated hydrated aerosol particles will tend to be spherical, which should be the optimum shape for both their nonpreferential collection and acceleration. The ability to preserve the elemental composition of the liquid phase in the vacuum of the accelerator is also a distinct advantage. Another advantage is that the surface of the encapsulated particles could be modified to enhance their conductivity. The velocity of spherical conducting particles that have been electrostatically accelerated is proportional to the square root of the net charge on the particle. Since net charge is a function of particle radius, in-flight mass or size measurement can be achieved through measurement of the accelerated particles' velocity. Extremely thin high-purity gold or carbon coatings, similar to those used for scanning electron microscopy, could be applied to the encapsulated particles to make them uniformly conducting.

ACCOMPLISHMENTS DURING FY 1983

A collection method is being sought that will preserve both the physical and the chemical properties of the acrosol to be analyzed. To date, cigarette smoke and an aerosol of deionized water have been successfully microencapsulated with MCA using the batch method suggested by Holmberg.[1] The particle size distributions for these two aerosols was determined by scanning electron microscopy. Particle sizes ranged from 0.1 to 1.0 μm, consistent with previously reported size distributions.[1] Experiments are being done to optimize the amount of monomer used for encapsulation to ensure that it is not altering the size distribution of the aerosol. A less soluble monomer — isobutyl-2-cyanoacrylate — has also been successfully used as an alternative. Further work needs to be done on the optimum monomer partial pressure for encapsulation, the optimum temperature for polymerization, and the thickness of the polymer coating. A continuous-flow encapsulation process was also tested.

Collection by encapsulation is only the first step toward mass spectrometry of aerosol particles; the next is electrostatic acceleration. Graphitic carbon fibers are being studied for use as a collection and charging surface in the high-voltage end of the accelerator. Experiments have therefore been started to determine the relative collection efficiency of encapsulated cigarette smoke on a single fiber. The fiber was placed directly ahead of a Nuclepore filter, and the relative number of particles in each size bin, on the fiber, and on the filter was determined. In addition, the absolute collection efficiency for 0.30 and 2.00 μm polystyrene latex spheres (PSL) was determined. The predicted efficiency for the 0.30 and 2.0 μm particles on the 7-μm diameter fiber at a flow velocity were 0.20% and 22% respectively; the experimental values were 0.15% and 0.31% respectively. The minimum collection efficiency was expected to be at 0.30 μm for the sampling conditions. The collection efficiency for both the PSL and the encapsulated particles above and below the minimum were lower than expected by a factor of 10 to 100.

PLANNED ACTIVITIES FOR FY 1984

Further work on the relative and absolute collection efficiency of encapsulated particles as a function of particle size and chemical composition is planned. A monodisperse encapsulated microparticle generator needs to be built for this work. Microencapsulation of micrometer- and submicrometer-size aerosol particles with a polymer coating is a potentially useful technique for resolving some of the key issues in atmospheric aerosol science today. Both liquid and solid aerosol particles can be effectively frozen in their physical and chemical state at the time of encapsulation, preserving them for further analysis. However, microencapsulation of atmospheric aerosol particles is a relatively new and unexplored technique. Research into a few key aspects of microencapsulation should reveal its potential for a number of significant applications to hydrated and liquid-phase aerosols. Work on one or more of the following areas is planned to explore the usefulness of microencapsulation for: (1) preserving the physical and chemical characteristics of liquid and hydrated aerosols, fog, and cloud particles; (2) investigating the degree to which solid aerosol particles are hydrated; (3) determining the degree of internal

or external mixing of multicomponent aerosols; and (4) studying the physical and chemical heterogeneity of aerosol particles in a given size range.

REFERENCES

1. Holmberg, R.W. (1979), "Determination of Particle Size in Tobacco Smoke Inhalation Exposure Devices Using Methylcyanoacrylate Fixation and Scanning Microscopy," in *Tobacco Smoke Inhalation Bioassay Chemistry*, Oak Ridge National Laboratory Report ORNL-5424, p. 103.
2. Carter, W.L. and Hasegawa, I. (1973), "Fixation of Tobacco Smoke Aerosols for Size Distribution Studies," *J. Coll. Interface Sci. 53*, p. 134.
3. Mark, H.F., *et al.*, Eds. (1964), *Encyclopedia of Polymer Science and Technology*, Wiley/Interscience, New York, p. 338.
4. Scherr, H.B., Ed. (1982), *Controlled Release Pesticides*, ACS Symposium Series 53, American Chemical Society, Washington D.C.

The Aethalometer — An Instrument for the Real-Time Measurement of Optical Absorption by Aerosol Particles*†

A.D.A. Hansen, H. Rosen, and T. Novakov

Aerosol particles emitted from combustion sources contain many different carbonaceous compounds and structures. One of these components is carbon in a microcrystalline graphitic form,[1] which, because of its strong optical absorption, is called "black carbon." This material can only be produced by incomplete combustion: no secondary mechanisms for its production from airborne precursors are known. Since it is also inert to transformation in the atmosphere, it makes a good tracer for combustion emissions. Chemical techniques[2] for determining the black carbon content of aerosol samples collected on filters are generally complex and time consuming. In contrast, optical measurements are often simple and rapid. Because most ambient aerosols do not contain large amounts of other absorbing, noncarbonaceous particulate material, a measurement of optical absorption of the filter deposit corresponds very closely to the black carbon determination. These methods and results are discussed in detail by Gundel *et al.*[3] Here we describe an instrument that uses an optical technique to measure the concentration of aerosol black carbon in real time. We have named the instrument the *aethalometer*, from the Greek word "$\alpha\iota\theta\alpha\lambda o\upsilon\nu$," "to blacken with soot."

ACCOMPLISHMENTS DURING FY 1983

The aethalometer continuously measures the attenuation of a beam of light transmitted through a filter through which particle-laden air is being drawn.[4] At a constant airstream velocity, the rate of deposition of black carbon on the filter is proportional to its concentration in the aerosol and gives a corresponding rate of increase of optical attenuation. Measurement of this attenuation constitutes the basis of the method. The aerosol particles are retained on the filter and are available for subsequent analysis by other physical and chemical means. Some of these results are used for calibration of the instrument.

The optics and electronics can detect an increase in optical attenuation of 0.00075 units of optical density, corresponding to the deposition of 3 $\mu g/cm^2$ of black carbon on the filter. The minimum resolving time, t_{min}, is the time necessary to collect this minimum quantity, Q_{min}, of black carbon from the air stream, whose velocity at the filter face is denoted v. If the concentration of black carbon in the aerosol is C, then $t_{min} = Q_{min}/Cv$. Using quartz fiber as the filtering medium, the aethalometer can operate at filtering velocities of up to 5 m/sec, giving a minimum resolving time of 6 seconds for a black carbon concentration of 1 $\mu g/m^3$. A variable time base determines the actual interval over which the digitization and differentiation are performed. We may select longer base periods to improve the accuracy of the concentration measurement at the expense of its time resolution.

To avoid the effects of optical saturation, a maximum loading Q_{max} of 8 $\mu g/cm^2$ of black carbon on

*This work was supported by the Director, Office of Energy Research, CO_2 Research Division of the U.S. Department of Energy under Contract No. DE-AC03-76SF00098.

†Abridged from the text of a paper presented at the Second International Conference on Carbonaceous Particles in the Atmosphere, Linz, Austria, September, 1983; to be published in *Science of the Total Environment*, February 1984.

the filter is allowed before a filter change is required. At constant filtering velocity v and average aerosol black concentration C, this occurs after a time $t_{max} = Q_{max}/Cv$. At maximum flow rate with C equal to 1 $\mu g/m^3$, this time is approximately 4.5 hours. In situations that do not require maximum time resolution or sensitivity, the time between filter changes may be extended by reducing the air-flow rate.

The aethalometer is calibrated by performing quantitative chemical analysis for black carbon[3] on the quartz-fiber filter. The result is compared to the integral of the real-time output to give the calibration factor. This factor may be used for routine work; when the greatest accuracy is required, we chemically analyze each individual filter.

In previous ground-level studies[5] of the black carbon content of ambient aerosols, the aethalometer showed the time-dependent behavior of black carbon concentration. This time-resolution capability can be used to determine the spatial distribution of the aerosol. As part of the National Oceanic and Atmospheric Administration's "AGASP" project, the aethalometer was operated on board an aircraft flying over the Arctic in March and April, 1983. Figure 1 shows the output during a test flight when passing at 900 m altitude through a plume from agricultural burning. The time-base period was 4 seconds, giving a horizontal resolution of approximately 500 m and a measurement accuracy of approximately 5% of peak. Figure 2 shows the output during a descent profile from 6000 m altitude to sea level in the Norwegian Arctic. A 1-minute time-base period was used, and we obtained a vertical distribution of aerosol black carbon with a resolution of approximately 200 m.

In summary, we have developed and refined an instrument that is capable of yielding a highly sensitive measurement of the concentration of aerosol black carbon in *real time*. This measurement may be directly calibrated by chemical analysis and may be interpreted in terms of an aerosol absorption coefficient. The instrument has sufficient sensitivity to perform this measurement in remote locations with a time resolution of *minutes*, and within seconds in plumes. Its capabilities suggest applications in many

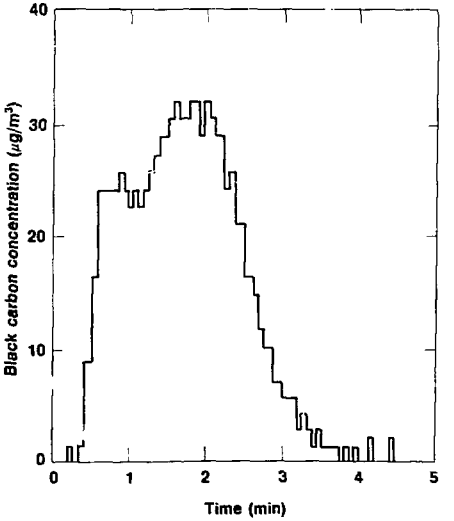

Figure 1. Aethalometer response during transit of a plume from agricultural burning over the Bahamas. The aethalometer time-base period of 4 seconds gives a horizontal resolution of approximately 500 m. (XBL 838-3120A)

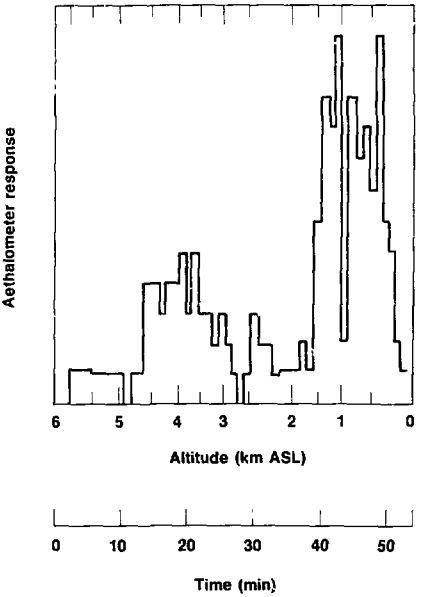

Figure 2. Aethalometer response during descent profile near Spitzbergen. A separate record of flow rate vs. altitude is also kept, which must be factored into these data to yield the aerosol black carbon concentration. The aethalometer time-base period is 1 min. (XBL 838-3118)

areas of atmospheric science as well as in combustion research.

PLANNED ACTIVITIES FOR FY 1984

The AGASP flight program demonstrated the considerable value of an instrument that can measure, in real time, aerosol black carbon concentrations as a direct indication of combustion emissions in a particular air mass. Work is in progress to reduce the large data set generated during the AGASP program and to correlate the results with measurement of other aerosol and meteorological parameters. The aethalometer as flown was a modification of the original prototype. We are using the experience gained in this flight program to design the next version; the objective is to improve the instrument's sensitivity (and hence its time resolution), while reducing its size, weight, and power requirements.

REFERENCES

1. Rosen, H., Hansen, A.D.A, Gundel, L., and Novakov, T. (1978), "Identification of the Optically Absorbing Component in Urban Aerosols," *Appl. Opt. 17*, p. 3859.
2. Wolff, G.T. and Klimisch, R.L., Eds. (1982), *Particulate Carbon: Atmospheric Life Cycle*, Plenum, New York.
3. Gundel, L.A., Dod, R.L, Rosen, H., and Novakov, T., "Role of Graphitic Carbon Particles in Radiative Transfer in the Arctic Haze," this annual report.
4. Rosen, H., and Novakov, T. (1983), "Optical Transmission Through Aerosol Deposits on Diffusely Reflective Filters: A Method for Measuring the Absorbing Component of Aerosol Particles," *Appl Opt. 22*, p. 1265.
5. Hansen, A.D.A., Rosen, H., and Novakov, T. (1982), "Real-Time Measurement of the Absorbing Component of Aerosol Particles," *Appl. Opt. 21*, p. 3060.
6. Hileman, B. (1983), "Arctic Haze" (editorial article), *Environ. Sci. Technol. 17*, p. 232A.

APPLIED PHYSICS AND LASER SPECTROSCOPY RESEARCH

N.M. Amer, S.-H. Chew, M.S. Cooper, R.W. Gerlach, A. Hitachi, W. Imler, M.A. Olmstead, A. Skumanich, D.R. Wake, D. Wei, and Z.A. Yasa*

The research philosophy of our group is to apply advanced laser spectroscopy and condensed-matter physics to energy and environmental problems. Lasers, because of their narrow linewidth and tunability, can provide unsurpassed sensitivity and specificity in detecting trace environmental contaminants. The advanced state of condensed-matter physics makes it possible to apply such knowledge to energy production and to test novel methods for energy conversion such as photovoltaic solar cells, superionic electrical energy storage devices, and the recovery and extraction of oil from abandoned wells and oil shale with lyotropic liquid-crystal emulsifiers.

Accomplishments During FY 1983

LASER PHOTOTHERMAL MEASUREMENTS AND CHARACTERIZATION†

Laser photothermal spectroscopies provide a powerful tool for detecting trace contaminants in air and water, as well as for investigating the fundamental properties of gaseous, liquid, and solid phases of matter. One goal of this project is to develop ultrasensitive, multiparameter, elemental, and molecular detectors for the characterization of trace constituents, with emphasis on remote sensing. Another is to maintain a state-of-the-art capability in photothermal detection by fully understanding the physics of these techniques. Concurrent with these efforts, we are actively developing new or modified laser systems compatible with our specific needs.

Direct Measurement of the Polarization Dependence of Si(111)2×1 Surface State Absorption Using Photothermal Displacement Spectroscopy‡

Upon cleavage at room temperature, the Si(111) surface reconstructs to a metastable 2×1 structure, with two surface atoms per surface unit cell. The exact nature of this reconstruction is still an open question. Early models for the 2×1 reconstruction centered around a buckling mechanism involving the raising and lowering of adjacent rows of surface atoms from their ideal bulk positions. Angle-resolved photoemission (ARPES), however, shows a strong dispersive band along the $\bar{\Gamma}-\bar{J}$ direction in the surface Brillouin zone, which is inconsistent with calculations based on the buckling model. Recently, low energy electron diffraction (LEED) and ion backscattering (IBS) data have revealed additional inconsistencies with this model.

An alternate model involving π-bonded chains along the $(\bar{1}10)$ direction of the Si(111)2×1 surface has been proposed. This model involves a major rearrangement of the atoms in the top few atomic layers. However, it has been shown that the energy barrier to this reconstruction is less than 0.03 eV/surface atom. Variations on this model, including dimerized and molecular chains, have also been proposed.

The polarization dependence of the surface state optical absorption is an important and straightforward test of semiconductor surface reconstructions, since it arises from symmetry considerations and is not critically dependent on calculations requiring accurate atomic positions, such as those required to simulate ARPES, LEED, and IBS data. Optical spectra of cleaved silicon with unpolarized light show a surface-sensitive peak near midgap, around 0.45–0.47 eV. Although the buckling and chain models predict a similar optical gap, the predicted polarization dependence of the optical absorption is quite different. For the chain model, the absorption is maximal for light polarized parallel to the chains (along $\bar{\Gamma}-\bar{J}$), whereas the buckling model predicts the maximum absorption to occur for light polarized perpendicular to the rows of atoms (along $\bar{\Gamma}-\bar{J}'$).

Using a new technique, photothermal displacement spectroscopy, we have measured the polariza-

*Group Leader.

†This work was supported by the Director, Office of Energy Research, Physical and Technological Research Division of the U.S. Department of Energy under Contract No. DE-AC03-76SF00098; and by the Defense Advanced Research Projects Agency under DARPA Contract No. 3343.

‡Complete version appeared in *Phys. Rev. Lett. 52*, p. 1148 (1984).

tion dependence of the Si(111)2×1 surface absorption. Unlike differential reflectivity and total internal reflection measurements, which require a difference spectrum between clean and oxidized surfaces, photothermal deflection spectroscopy measures the optical absorption directly. A peak absorption at ~ 0.46 eV was observed. As the polarization of incident light is rotated in a single domain region, determined from LEED to be reconstructed along the $[11\bar{2}]$ direction, the absorption is found to be highly peaked for light polarized in the $[\bar{1}10]$ direction (parallel to $\bar{\Gamma}-\bar{J}$). This result is predicted by the symmetric π-bonded chain model, but not by most variations on the chain model, or by the buckling model for this surface.

Photothermal displacement spectroscopy is based on optical detection of the thermal expansion of a sample as it is heated by absorption of light. An optical absorption spectrum is generated as an intensity-modulated, tunable light beam (the pump beam) is focused onto the sample. Following the absorption of light, the sample is locally heated and excited electrons decay nonradiatively. The illuminated portion of the surface is then displaced as the sample thermally expands. The resultant change in slope of the sample surface is detected through the deflection of a HeNe probe beam, as measured by a position-sensitive photodiode. The signal, detected by phase-sensitive methods, is directly proportional to the surface absorption coefficient of the sample. The volume of the sample probed is determined by the radius of the pump beam and the thermal diffusion length. In the experiments described here, the surface area probed had a diameter of ~300 μm.

The experimental configuration is shown in Fig. 1. A Kr^+ pumped F-center laser, tunable over the range 0.38–0.51 eV, serves as the pump beam. The beam is passed through a ZnSe Brewster-plate rotatable polarizer, focused by a 20-cm CaF_2 lens, and passed through a CaF_2 window into the ultrahigh vacuum (UHV) chamber and onto the sample surface. Silicon samples, 5 mm × 5 mm × 25 mm, p-type (ρ ~ 6 Ω-cm). were cleaved in ultrahigh vacuum along the $[11\bar{2}]$ direction, using a carbide blade and copper anvil. The pump and probe beams were aligned to probe a single-domain region of the surface as determined by LEED. The base pressure of the UHV chamber was ~4×10^{-10} torr.

As mentioned, a peak in the optical absorption at ~0.46 eV was observed (Fig. 2). For single-domain regions exhibiting sharp, unsplit (LEED) spots, a maximum absorption of 1.8%–2.35% was obtained for a $[\bar{1}10]$ polarization of the bump beam. After oxidation, the absorption signal was reduced to

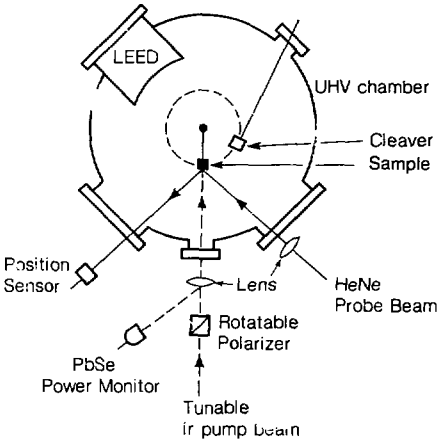

Figure 1. Experimental configuration for photothermal displacement spectroscopy. (XBL 8312-6935)

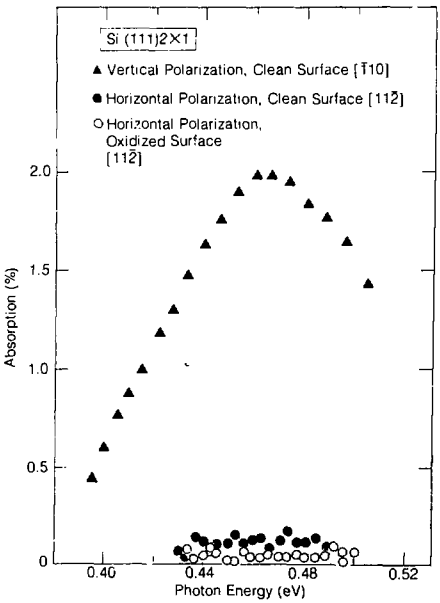

Figure 2. Si(111)2×1 surface state absorption spectrum. Saturation oxidation was obtained after ~ 1 hour at 10^{-7} torr. (XBL 8312-6937)

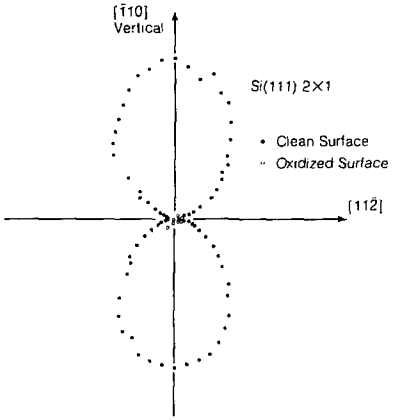

Figure 3. Polar plot of the polarization dependence of the Si(111)2×1 surface-state absorption at 0.468 eV.
(XBL 8312-6936)

less than 0.06% for all polarizations (Figs. 2 and 3). This conclusively shows that the absorption seen was due to surface states on the Si(111)2×1 surface.

The polarization of the infrared pump beam was rotated through 360° at a photon energy of 0.468 eV (Fig. 3). The sample region probed was determined by LEED to be single domain with the second-order spots occurring in the horizontal $[11\bar{2}]$ direction. The maximum signal was obtained with light polarized in the vertical direction (parallel to $[\bar{1}10]$). The signal decreases to less than 5% of the original for horizontal polarization. Spectra taken with horizontal $[11\bar{2}]$ polarization before and after oxidation are shown in Fig. 2.

As can be seen from Figs. 2 and 3, the polarization dependence of the Si(111)2×1 surface-state absorption is very strong, with the absorption of $[\bar{1}10]$ polarized light stronger than that of $[11\bar{2}]$ polarized light by at least 20:1. No rotation of the major axes relative to the cleavage direction was observed. These results are confirmed by differential reflectivity measurements. The polarization dependence of optical absorption between localized surface states should provide an unambiguous test of the validity of models proposed for the surface structure. If the chain model is correct, the observed direction of the strong surface-state absorption is then parallel to the chains; if the buckling model is correct, the measured direction is parallel to the buckled rows of atoms. The dependence of the absorption on polarization angle seen with photothermal displacement spectroscopy agrees with calculations for the symmetric π-bonded chain model. It is not consistent with any of the other models tested, including the π-bonded molecular chain, strongly dimerized chain, and buckling models.

Another interesting, though preliminary, result is the small blue shift of the surface peak with a smaller absorption signal. In the chain model, this could be interpreted as an increase in the surface optical gap as the chains are shortened by the disorder of the surface. Further study of this effect is in progress.

AMORPHOUS PHOTOVOLTAIC SEMICONDUCTORS*

Amorphous photovoltaic semiconductors, such as hydrogenated amorphous silicon (*a*-Si:H), hold promise for meeting Department of Energy cost and efficiency goals for thin-film solar cells prior to 1990. To achieve the higher conversion efficiencies required, it is necessary to better characterize the unique optical and transport properties of these materials. Photoacoustic and photothermal spectroscopies can be used to elucidate the optical and electronic properties of *a*-Si:H. Of particular interest is the investigation of the optical properties near the so-called bandgap. By combining luminescence studies, photoconductivity, and optical absorption, a full and accurate characterization of the de-excitation of these photoexcited amorphous semiconductors can be achieved.

Experiments investigating the optical properties of amorphous semiconductors are currently under way. These experiments are designed to yield new information on the details of the optical absorption, the nature of the bandgap, and the electronic and transport properties of this promising material.

The Effects of Compensation on Light-Induced Metastable Defects in *a*-Si:H†

Little attention has been given to the effects of compensation (doping with both *p* and *n* types) on the light-induced metastable defects in *a*-Si:H (Staebler-Wronski effect). By varying the degree of compensation, it is possible to isolate effects due to

*This work was supported by the Assistant Secretary for Conservation and Solar Energy, Office of Solar Energy, Photovoltaic Energy Systems Division, U.S. Department of Energy under Contract No. DE-AC03-76SF00098.

†Complete version appeared in *J. Non-Cryst. Solids 59–60*, p. 409 (1983).

Fermi-level motion from those due to the incorporation of dopants. Also, since gap-state optical absorption studies have shown that compensation removes Si dangling-bond defects, it is of interest to investigate the effects of compensation on the magnitude of the Staebler-Wronski effect. Using photothermal deflection spectroscopy to measure the optical absorption of the defect, we have shown that fully compensated films (equal doping concentrations of phosphorous and boron) exhibit the smallest increase ($\sim 10^{15}$ dangling-bond defects/cm^3) after illumination. Departure from full compensation, toward either phosphorus- or boron-rich material, results in a corresponding increase in the density of the light-induced defects.

In Fig. 4, we show that illumination enhances the gap-state absorption, while annealing restores it to the original value. This result is consistently reproducible when the illumination-anneal cycle is repeated several times. No detectable change is seen in the exponential (Urbach) edge.

Previous work has demonstrated that the magnitude of gap-state absorption in a-Si:H provides a direct measure of the density (N_s) and energy of the silicon dangling-bond defect. Using the same procedure for the light-induced change in the optical absorption, we measured the difference in defect density between the annealed and illuminated states (ΔN_s). Figure 5 shows the dependence of ΔN_s on the degree of compensation. It is clear that full compensation minimizes the Staebler-Wronski effect. When compared with undoped material, ΔN_s for the fully compensated films is an order of magnitude lower. As the relative concentration of boron to phosphorus deviates from unity, ΔN_s rises sharply. We determined the energy of the light-induced defect to be $\sim$1.25 eV below the conduction band, a value consistent with the defect being a silicon dangling bond.

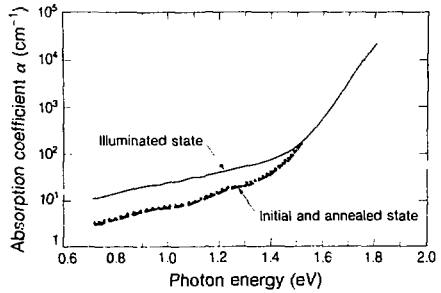

Figure 4. The effect of illumination on gap-state absorption in compensated a-Si:H (phosphorus: 10^{-3} and boron: 5×10^{-5}). Dotted spectrum is for second anneal.
(XBL 836-10266)

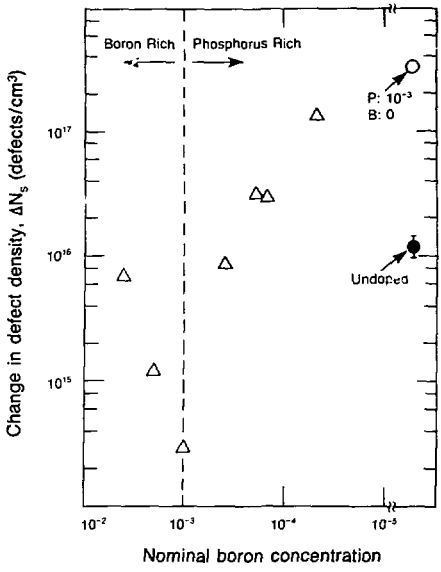

Figure 5. The dependence of ΔN_s on the degree of compensation. ΔN_s for typical undoped (O) and singly doped phosphorus (O) materials are shown for comparison.
(XBL 844-10440)

The results clearly show that the observed increase in dangling-bond density is not simply due to Fermi-level motion. If Fermi-level shifts were the only mechanism, one would expect ΔN_s to increase as full compensation is reached and the Fermi level reaches the midgap region. Furthermore, in the case of boron-rich material, since fewer dangling-bond states are occupied, ΔN_s would drop off. This is the opposite of what we observe experimentally.

The conclusion that Fermi-level shifts do not account for the increase in ΔN_s is supported by an earlier study of the effects of single doping and defects on the Staebler-Wronski effect. For singly doped material, ΔN_s increases as the dopant concentration increases. Also, the ratio $\Delta N_s/N_s$ was found to be independent of the doping level, thus indicating that the light-induced defects are related to dopants or doping-induced defects instead of Fermi-level shifts.

In addition, from the previous results on doping dependence, one would expect that, for fully compensated material, ΔN_s would be large due to the high doping level of phosphorus and boron. Yet this material yields the smallest ΔN_s. Evidence from photoluminescence and NMR studies indicates that boron and phosphorus form complexes during deposition. It is possible that these complexes, because they are in their "desired" bonding configurations, no longer contribute to the defect-creating mechanism.

These results have implications for solar-cell technology. Since the compensated material exhibits insensitivity to light-induced fatigue, it could be used as the outer layer of solar cells to avoid the reported degradation in efficiency.

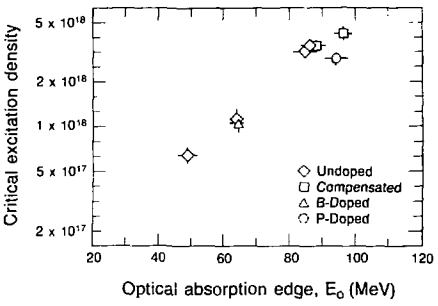

Figure 6. The critical transition density dependence on E_o, the optical absorption edge. (XBL 844-10441)

The Dependence of Recombination Kinetics on Photoexcitation Density in *a*-Si:H*

To evaluate the relative importance of the various centers in *a*-Si:H that may be involved in the process of carrier recombination, we have investigated the effects of defects and dopants on the monomolecular-to-bimolecular transition in the recombination kinetics of *a*-Si:H, using pulsed excitation. For this transition to be observed, the photoexcitition carrier density should exceed that which existed in the steady state, prior to the pulse. An additional requirement is that the recombination time τ must be less than the duration of the excitation pulse. By combining nanosecond-pulse excitation and the technique of photoinduced absorption, we have shown that early recombination in *a*-Si:H is strongly related to the width of the exponential absorption (Urbach) edge E_o; this result shows that Si dangling bonds do not play an important role in early recombination.

Photoexcitation was done with 2.2 eV, 4 nsec-wide, 1 μJ pulses. The *a*-Si:H films were deposited by rf glow discharge. Sample temperature was 10 K.

Figure 6 plots the critical excitation density (i.e., the density at which the mono-to-bimolecular transition occurs) as a function of the width of the exponential absorption edge. The undoped samples in this study covered a range of Si dangling-bond defect densities from $\sim 3 \times 10^{15}$/cm^3 at $\sim$50 meV to $\sim 10^{18}$/cm^3 at $\sim$85 meV. Over this range, the critical excitation density shifts by approximately an order of magnitude. Plotted on the same graph are a 10^{-4} boron-doped sample whose gap states are vacant and a 10^{-3} phosphorus-doped sample whose deep gap states are doubly occupied because of the position of the Fermi level in the gap. Also shown are two compensated samples with Si dangling-bond defect densities of 10^{16} and 10^{17}/cm^3.

Despite these disparate gap-state densities and occupancy factors, the data from these varied materials show a strong correlation between the critical excitation density and the width of the exponential bandtail, a correlation that reflects the extent of structural disorder in the material. A significant consequence is that deep gap states do not play a major role in early recombination in *a*-Si:H.

To explain qualitatively the results presented here, one can invoke the concept of multiple trapping. The recombination time can be written as

$$\log \nu\tau \approx (E_o/k_B) \log (b_t N_t / b_r N_r)^{1/T} \qquad (1)$$

where k_B is the Boltzmann factor, ν is the attempt-to-escape frequency, N_t is the total bandtail trap density, b_t is their capture coefficient, N_r is the total number of possible recombination centers, b_r is their capture coefficient, and T is the temperature. This relationship shows a recombination time dependent both on the exponential edge slope E_o and on the total bandtail trap density N_t. Preliminary numerical modeling using Eq. (1) yields qualitative agreement with the observed experimental results. Further work is in progress.

Optical Properties and Correlation Energy of Defects in *a*-Ge:H†

The optical absorption spectra of defect states provide information on the energy level and the den-

*Complete version appeared in *J. Non-Crystal. Solids 59-60*, p. 389 (1983).

†Complete version appeared in *J. Non-Crystal. Solids 59-60*, p. 249 (1983).

sity of defects in amorphous semiconductors. By using the sensitive technique of photothermal deflection spectroscopy to detect these weakly absorbing states, it has been shown that, in *a*-Si:H, the absorption is due to Si dangling-bond defects. The energy level of the defect was determined (~1.25 eV below the conduction band), and the defect density was found to depend on the deposition parameters and the level of doping. By extending this type of investigation to other tetrahedrally bonded semiconductors, a better understanding of defects in this class of materials should emerge. We have measured the gap-state absorption of undoped and doped hydrogenated amorphous germanium (*a*-Ge:H) and determined that the absorption is due to Ge dangling-bond defects. The defect energy level lies ~0.5 eV below the conduction band, and its correlation energy is estimated to be ~0.1 eV. Illumination appears to be much less efficient in creating defects than it is in *a*-Si:H.

In Fig. 7, we present the absorption spectra of undoped and singly doped *a*-Ge:H. As can be seen, there is significant subgap absorption. In the doped material, the magnitude of the absorption increases as the dopant concentration rises. Also, the slope of the exponential absorption (Urbach) edge increases with increasing dopant concentration.

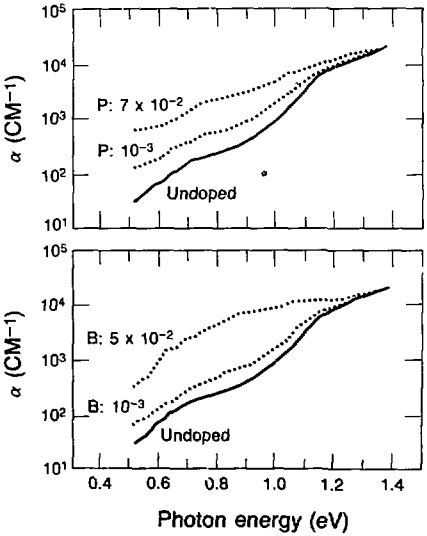

Figure 7. The gap-state absorption of doped and undoped *a*-Ge:H. (XBL 844-10401)

Previous work has shown that the magnitude of gap-state absorption in *a*-Si:H is a measure of dangling-bond-defect density (N_s). Employing the same procedure for *a*-Ge:H, we determine the density of defects in undoped material to be ~2 × 10^{17}/cm^3. This value is in good agreement with the ESR measurements, indicating that the absorption is due to a Ge dangling bond. In heavily doped material, the defect density is as high as ~6 × 10^{18} defects/cm^3. When compared with *a*-Si:H, for similar levels of doping, the number of defects is roughly the same. However, for the undoped case, the defect density in *a*-Ge:H is an order of magnitude higher than in *a*-Si:H, and the Urbach edge is broader.

In addition to measuring the defect density, optical absorption measurements enable the determination of the energy position of the defect. For *a*-Ge:H, the defect lies at ~0.5 eV below the conduction band. Furthermore, the correlation energy of the defect (U) can also be measured by comparing the singly and doubly occupied dangling bonds in undoped and doped material. U is found to be ~0.1 eV. This value is significantly smaller than the ~0.35–0.4 eV reported for the Si dangling-bond defect. A possible explanation for this striking dissimilarity is the weaker degree of localization in the case of *a*-Ge:H as compared with *a*-Si:H (correlation lengths of 11 Å for *a*-Ge:H and 4 Å for *a*-Si:H).

Finally, preliminary results indicate that the subgap absorption spectra were imperceptibly affected by illumination with unfiltered light from a quartz halogen lamp (~1 W/cm^2 for 1.5 hours). The implication is that intense illumination is much less efficient in creating defects in *a*-Ge:H than in *a*-Si:H.

LIQUID CRYSTAL RESEARCH*

The liquid-crystalline state of matter is characterized by a spontaneous anisotropic order and by fluidity. The anisotropic order leads to anisotropy in the physical properties of the medium, and the fluidity makes it easily susceptible to external perturbations in the form of electric or magnetic fields, temperature, or pressure. In addition, we have demonstrated that certain gaseous organic pollutants change the liquid-crystalline structure. This change,

*This work was supported by the Office of Energy Research, Physical and Technological Research Division of the U.S. Department of Energy under Contract No. DE-AC03-76SF00098.

which is readily detectable, is the basis for an inexpensive and sensitive (10^{-6}) personal dosimeter for some organic pollutants. Once their physical properties are well understood, the class of liquid crystals known as lyotropics potentially could be employed to recover oil efficiently from abandoned wells and from oil shale.

Observation of Macroscopic Collective Behavior and New Texture in Magnetically Doped Liquid Crystals[†]

A distinctive characteristic of liquid crystals is the anisotropic nature of their physical properties, as manifested when external fields are applied. The study of the effects of applied electric fields has contributed significantly to our understanding of the physics of liquid crystals and laid the foundation for many of their technological applications. To obtain analogous effects with magnetic fields, high field intensities ($\geq 10^3$ G) are required to overcome the typically minute anisotropy of the diamagnetic susceptibility ($\Delta\chi \simeq 10^{-7}$ cgs units) of liquid crystals. To circumvent this limitation, the liquid crystal matrix can be "doped" with ferromagnetic grains, which should, in principle, enable the liquid-crystalline molecular orientation to be coupled to weak external magnetic fields. It can be shown theoretically that, at a critical concentration of well-dispersed magnetic particles, the doped matrix should exhibit collective orientational distortion with an instability threshold occurring at a critical field value. Also, the coupling between the magnetic particles and the liquid crystal molecules, which is mechanical in nature, should result in a matrix with ferromagnetic behavior $|M(H=0) \neq 0|$.

Several attempts have been made at realizing this system experimentally, but none have achieved the predicted collective behavior of the doped matrix. Recently, however, we made the first reported observation of macroscopic collective behavior in a magnetically doped nematic liquid crystal. The behavior consists of a long-range uniform distortion of the molecular orientation of the entire sample when an external magnetic field as weak as < 1 G is applied [Fig. 8 (a),(b)]. At higher fields, the orientational distortion ceases to be uniform and is replaced by a field-induced "cellular" texture, with the "cells" having dimensions on the order of tens of micrometers [Fig. 8 (c)].

Our theoretical analysis of these results may be summarized as follows, beginning with the case of homeotropic alignment [Fig. 9 (a)]. For $\Theta_M << 1$, the free energy of the system can be written in the

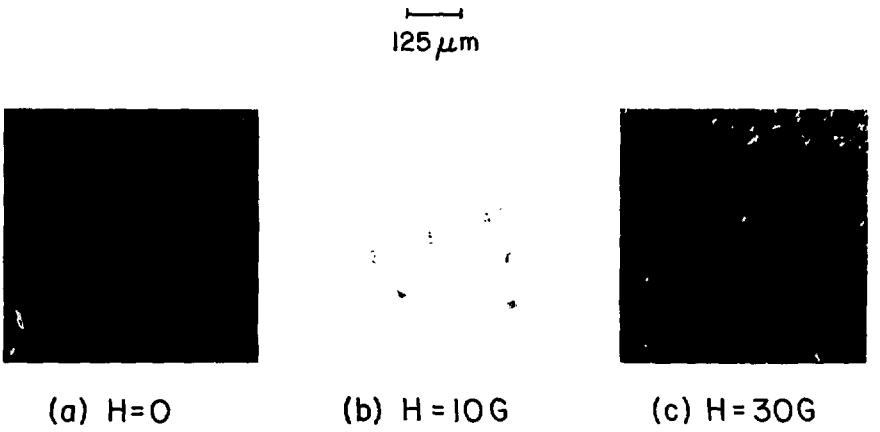

Figure 8. Magnetically doped, homeotropically aligned nematic matrix viewed with polarizing microscope: (a) no field; (b) uniform field-induced birefringence; (c) "cellular" texture. (XBB 839-8442)

[†]Complete version appeared in *Phys. Rev. Lett. 51*, p. 2298 (1983).

form:

$$F = \int_{-D/2}^{D/2} dz \left\{ \frac{1}{2} k_{33} (1 + K \sin^2 \Theta)(d\Theta/dz)^2 - MH \sin \Theta(z) \right\} \quad (2)$$

where $K = (k_{11} - k_{33})/k_{33}$; k_{11} and k_{33} are the splay and bend elastic constants, respectively; M is the matrix magnetization; and H is the strength of the externally applied magnetic field.

By minimizing the free energy using the Euler-Lagrange equation, it can be readily shown that the field-induced molecular distortion is given by

$$\Theta_M = (MH/8k_{33})D^2$$

where D is the matrix thickness.

The field-induced distortion of the doped matrix can be probed by measuring the corresponding induced change in birefringence. For small distortion $\Theta_M << 1$, it can be shown that the change in phase differences δ is given by

$$\delta = (2\pi/\lambda)(\frac{8}{15} D^5 (n_e - n_o)(\frac{M}{8k_{33}})^2 H^2 \quad (3)$$

where n_e and n_o are the extraordinary and ordinary indices of refraction of the nematic, respectively, and λ is the wavelength of the light used to measure the birefringence change.

The nematic liquid crystal used for this work was methoxybenzyledene butylaniline (MBBA). The magnetic particles were γ-Fe_2O_3 needles. To prevent clumping, these needles were coated with dimethyl octadecyl aminopropyl trimethoxysilyl chloride (DMOAP). The distortion induced by the external magnetic field was measured as a change in the phase difference of the ordinary and extraordinary rays. The external field was applied with a pair of Helmholtz coils such that $H \parallel n$ for both alignments.

Experimental Evidence for Collective Behavior

When observed between the crossed polarizers of a polarizing microscope, and upon the application of a weak external magnetic field ($H \leq 20$ G) such that $H \parallel n$, the entire doped matrix exhibited strong uniform birefringence, as shown in Fig. 8 (c). This effect was independent of the polarity of the applied field. That the entire sample (typically 0.5 cm across) became birefringent is evidence for collective behavior and indicates that single magnetic particles were homogeneously dispersed throughout the homeotropic nematic.

Distortion Dependence on External Magnetic Field

To gain a quantitative insight into the physics responsible for the observed orientational distortion, we studied the dependence of the field-induced birefringence on the strength of the applied field, the concentration of the magnetic dopant, and the thickness of the nematic matrix. The experimental results for the homeotropic alignment are shown in Figs. 9 and 10. A general feature of the dependence of δ on H is that the curves can be divided into two regimes:

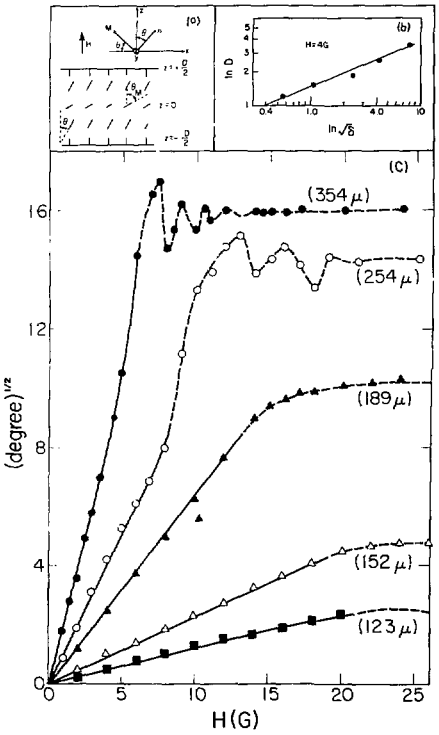

Figure 9. (a) The molecular geometry; (b) the phase difference dependence on sample thickness, $\delta \propto D^5$ as predicted by Eq. (3); (c) δ as a function of H for various thicknesses; filling factor = 16 *f*. (XBL 833-1405)

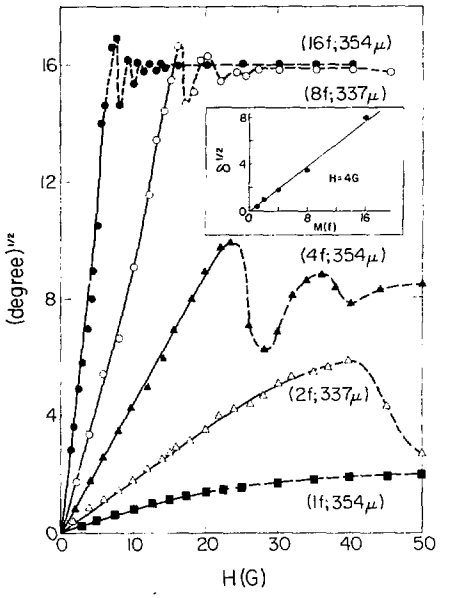

Figure 10. Phase difference versus field strength for various magnetic dopant concentrations. Inset shows $\delta \propto M^2$ as predicted by Eq. (3). (XB 833-1407)

(1) At low fields, there is a regime where δ, which is a measure of the nematic orientational distortion, varies monotonically with the strength of the applied field. Equation (3) predicts that $\delta \propto H^2$. As can be seen, for small distortions, the measured phase difference δ is indeed proportional to the square of the applied field. No critical field was observed. A second prediction of Eq. (3) is that the phase difference is proportional to the square of the matrix magnetization M. This was tested experimentally by varying the concentration of the magnetic grains. The results are shown in Fig. 10 and are in excellent agreement with the theoretical predictions. Finally, the theory predicts that $\delta \propto D^5$. Again, for small distortion, the experimental results agree remarkably well with this prediction.

(2) At higher fields, as the magnetic grains begin to flocculate into clumps, a saturation regime is reached where δ dependence on H saturates in an oscillatory fashion. When we examined this regime with a polarizing microscope, we found that its onset corresponds to the transformation of the nematic matrix from a uniformly birefringent state into a complex texture with a "cellular" topology, as seen in Fig. (8c). The texture response time to the application or removal of the magnetic field is < 1 sec. We tentatively ascribe this texture to a nonuniform distortion of the molecular orientation whose spatial geometry is analogous to that observed in the case of Williams domains.

NOVEL LASER SYSTEMS*

Our research activities sometimes require the development of new laser systems to meet a specific need. Of current interest is the generation of subpicosecond tunable laser pulses for use in probing elementary excitation in amorphous photovoltaic semiconductors. We also have a long-standing interest in waveguide laser technology because of the potential it offers for laser systems of high power, compactness, and ruggedness.

High-Average-Power, Widely Tunable, Passively Mode-Locked Dye Laser†

Passively mode-locked dye lasers have attracted interest because of the short pulsewidths obtained; their output power was low, however, and they were limited in tunability. We have eliminated both of these drawbacks by carefully optimizing cavity parameters. Thus, our laser generates pulses of approximately 200 femtoseconds, with an average power of $\gtrsim$ 100 mW, and is tunable over 570–630 nm, which covers most of the cw tuning range of the laser dye rhodamine 6G. At the repetition rate of 1/6 nanosecond, the peak power of the pulses corresponds to ~3 kW, making this laser a powerful tool for the study of ultrashort dynamics in linear and nonlinear optical phenomena with subpicosecond resolution.

The configuration of this cw Ar^+ laser–pumped dye laser is a conventional five-mirror-folded cavity for passive mode-locking, as shown in Fig. 11.

The overall cavity length corresponds to a round-trip time of 6 nsec, which corresponds to a pulse repetition rate of ~170 MHz. At this rate, double pulsing is avoided and the laser operates stably mode-locked with subpicosecond pulses at pump powers significantly above threshold. The R6G dye jet is kept near the center of the cavity,

*This work was supported by the Office of Energy Research, Physical and Technological Research Division of the U.S. Department of Energy under Contract No. DE-AC03-76SF00098.

†Complete version submitted to *Optics Letters*.

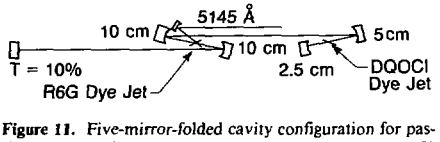

Figure 11. *Five-mirror-folded cavity configuration for passive mode-locking.* (XBL 844-10442)

maximizing the efficiency of single-pulsed operation. The folding angles are kept narrow, at optimum angles for effective astigmatic compensation. Thus, a good Gaussian mode is maintained. The radii of curvature of the folding mirrors are such that a smaller focal spot size is obtained at the mode-locker dye jet. This is thought to contribute to the wide tuning range, particularly for longer wavelengths. The saturable absorber is DQOCI, the absorption spectrum of which matches the gain spectrum of R6G. Stable mode-locking is obtained over the broad wavelength range of 570–630 nm, with pulsewidths of ~200 fsec, and the output mirror has a transmission of $T = 10\%$. This results in a highly efficient mode-locking operation for this laser, which achieves an output average power of ~150 mW, when cw-pumped with 2.5 W (5145 Å).

SPECIAL RESEARCH ACTIVITIES

Under this heading, we occasionally investigate interesting research problems which, while outside the mainstream of our research activities, would benefit from our particular expertise and the nature of our research tools.

To pursue such "extracurricular" activity, the research problem must be of significant scientific importance. A recent example, described below, is the application of Raman spectroscopy to test theoretical predictions regarding the effect of electrical excitation on living cells.

The Absence of Coherent Vibrations in the Raman Spectra of Living Cells[‡§]

Fifteen years ago, Frölich proposed that longitudinal electric vibrations in the 10^{11} to 10^{12} Hz frequency region might be coherently excited in living systems with metabolic energy. Frölich showed theoretically that when a critical rate of energy is supplied to a group of dipolar oscillators, such as the hydrogen bonds in a macromolecule, a Bose-like condensation of phonons can occur, resulting in the coherent excitation of the lowest longitudinal electric vibration of the system.

A variety of experiments have been interpreted as giving support to Frölich's theory. Among these is a set of Raman spectra from bacterial and mammalian cell suspensions. In these Raman scattering experiments, strong lines are reported to occur when cell populations are metabolically synchronized. This activity is reported to be absent in metabolically inactive or dead cells. To date, however, a molecular basis has not been established for any of these spectra.

We have demonstrated that many of the spectra reported can be closely reproduced by spurious Mie scattering from cell suspensions. We have further argued that these spectra cannot be explained in terms of Raman scattering from coherently vibrating intracellular molecules.

Figure 12 shows a simultaneous recording at a fixed wavenumber setting of the monochromator. Numerous intense lines were recorded from the monochromator's output as cell density fluctuations occurred at the laser beam. These lines were exactly correlated in time with the elastic light monitored by the photodiode. This Mie scattering declined in intensity with time as the settling and mixing of the yeast suspension proceeded.

In several of the reported spectra, there are very narrow lines, with linewidths smaller than the instrumental resolution. These spikes are of comparable amplitude to neighboring lines in the same spectra with normal linewidths. It is our experience that during a Raman scan, a clump of cells may cause either a noticeably false narrow line or a seemingly real line, of comparable amplitude and normal linewidth, depending upon the clump's transit time through the laser beam. Figure 13 shows a Raman scan of a settling yeast-cell suspension; part A shows false lines that disappear in part B, when the suspension has been well-mixed.

Figures 12 and 13 illustrate that Mie scattering can easily produce large false Raman lines throughout the range of the monochromator, including the 0–200 cm^{-1} region. Many of the low-frequency (< 200 cm^{-1}) lines reported could therefore also be due to Mie scattering.

The lines observed in the past have been attributed to coherently vibrating intracellular molecules. For nonresonant scattering, the power radiated from a molecule due to a Raman process is given classically by

$$I = \frac{16\pi^4\nu^4}{3c^4} \cdot \left[\frac{\partial\alpha}{\partial Q}\right]^2 Q^2 I_0 \qquad (4)$$

[‡]Complete version appeared in *Phys. Lett. 98A*, p. 138 (1983).

[§]Supported by an NIH National Research Service Award No. 1-T32-GM07379.

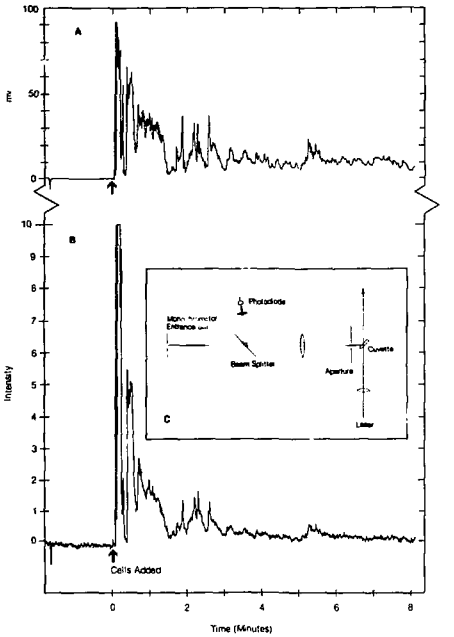

Figure 12. Mie scattering from a settling cell suspension. Changing cell density in the laser beam results in large elastic (Mie) scattering fluctuations. (A) Photodiode record of elastic light intensity entering monochromator. (B) Output of monochromator held at a fixed 1273 cm^{-1} setting; other parameters include 5 cm^{-1} instrumental bandwidth, 10^3 cps sensitivity, and 0.4 second time constant. (C) Optical configuration. Single-pass laser beam, 400 mW, 4880 A. The peak height of the 992 cm^{-1} benzene line under the same scattering conditions is 1.6×10^4 cps.

(XBL 844-8397)

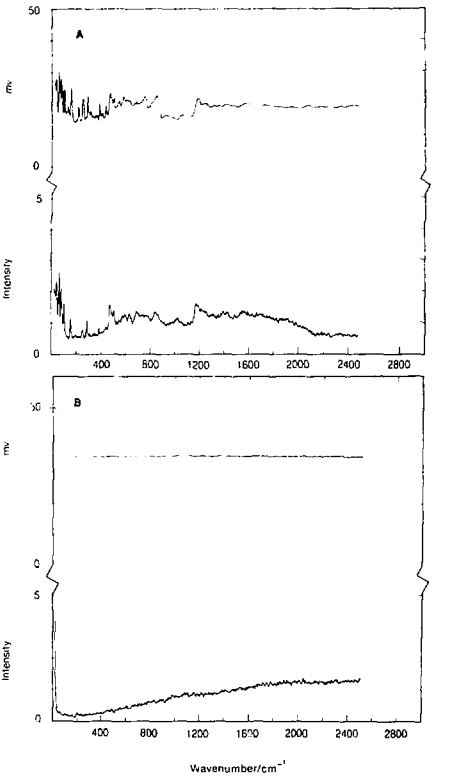

Figure 13. Raman scan of a settling cell suspension. Same conditions as Fig. 12, except that monochromator is scanned at 200 cm^{-1}/min. (A) False Raman lines and background fluctuations (lower trace) are correlated with photodiode record of elastic light fluctuations (upper trace). (B) Same sample, well mixed and scanned. False lines disappear. Benzene 992 cm^{-1} standard, 2×10^4 cps.

(XBL 844-1323)

where I_0 is the incident power per square centimeter, ν the exciting light frequency, α the molecular polarizability, and Q the normal mode coordinate. $\partial\alpha/\partial Q$ is essentially constant for small displacements from equilibrium and actually decreases at large displacements when the molecular vibration is strongly excited. Thus $\partial\alpha/\partial Q$ cannot contribute to large increases in Raman scattering from a coherently excited molecular vibration.

The quantum value for Q^2 is given by

$$Q^2 = \frac{(n + 1/2)h}{2\pi^2\nu_m} \qquad (5)$$

where ν_m is the molecular vibration frequency, and n the excitation number. The intensity of Raman scattering is therefore linear in n.

The lines above 200 cm^{-1} are in the range of local intramolecular vibrations, such as C-C stretching and bending modes. For such covalent bonds, the vibrational excitation number, n, cannot reach values on the order of 100 without the bond rupturing. With this rough limit on possible enhanced

scattering due to an excited vibration, we point out that the concentrations of specific components in the cell suspensions used would be too small to produce detectable lines, even if the molecules were coherently vibrating.

PLANNED ACTIVITIES FOR FY 1984

In laser spectroscopy, our goals will be to develop novel techniques and to exploit advanced applied physics concepts to the ultrasensitive measurements of minute optical absorption and vibrational spectra of gases, liquids, and solids. The emphasis will continue to be on unambiguous remote sensing of atmospheric constituents by laser photothermal spectroscopy and detection. Pulsed photothermal displacement spectroscopy will be studied, and extensions of this technique for the study of liquids will be devised. Nonlinear photoacoustic and photothermal spectroscopy of gases will be initiated.

Research on amorphous semiconductors will focus on the physics of defects in hydrogenated amorphous silicon and germanium. The elucidation of the nature of the metastable photoinduced defects in amorphous silicon will continue to be of interest. A new research direction is the physics of photovoltaic devices.

Another new activity is the investigation of the properties of semiconductor surfaces and interfaces. Processes at the liquid-semiconductor and gas-semiconductor interfaces will also be studied.

Finally, we will continue our research on laser physics and technology, with the goal of achieving widely tunable, high-average-power pulses a few femtoseconds wide. Another goal is to continue exploiting the waveguide laser configuration we have developed.

Quantification of Total and Organic Nitrogen in Oil Shale Wastewaters*

B.M. Jones, G.J. Harris, J.F. Thomas, and C.G. Daughton†

Nitrogenous organic compounds are responsible for much of the dark amber/brown color and noxious odor that characterize the wastewaters cogenerated with crude shale oil. The resistance of these waters to biological treatment has been attributed[1] to the numerous nitrogenous heterocyclic compounds that account for a large portion of the organic nitrogen. The importance of organic nitrogen in aqueous synfuel effluents has been underscored by the Environmental Protection Agency. To establish a data base and for baseline monitoring, it was recommended that nitrogenous organic compounds should be monitored in any stream unique to a particular synthetic fuel industry.[2] Individual compounds can be determined by gas-liquid chromatography with nitrogen-specific detection; but for the frequent performance assessment of waste treatment processes designed to remove nitrogenous organic compounds from an aqueous waste stream, a rapid and collective measurement is preferred.

The quantification of total and organic nitrogen in biological and agricultural samples has traditionally been accomplished using the time-consuming, wet-chemical Kjeldahl method. Total Kjeldahl nitrogen (TKN) is determined by digesting a sample in boiling H_2SO_4. The organic material is oxidized, and most forms of organically bound nitrogen are released as ammonia. The ammonia is separated from the digestate by distillation and quantified by acidimetric titrimetry or colorimetry. The procedure for organic Kjeldahl nitrogen (OKN) is identical to the TKN method, except that any endogenous ammonia is eliminated by distillation prior to sample digestion. The major failings of this method are the loss of volatile species such as aliphatic amines (during predistillation) and the incomplete recovery of nitrogen from many nitrogenous heterocycles (during digestion).

Within the last decade, a new approach, based on combustion followed by chemiluminescent detection (C/CL), has been developed for the quantification of total nitrogen. Aqueous samples containing organic and inorganic nitrogen species are combusted in an oxygen atmosphere at 1100°C to produce nitric oxide (NO), which is reacted with ozone to yield either nitrogen dioxide (NO_2) or electronically excited nitrogen dioxide (NO_2^*). The light emitted during relaxation of the metastable NO_2^* is then amplified by a photomultiplier tube (PMT) that is sensitive to long-wavelength light. A 650- to 900-nm bandpass filter eliminates chemiluminescent interference by unsaturated hydrocarbons, chlorine, and sulfur, all of which react with O_3 but emit light of shorter wavelengths. The principle of operation of a C/CL nitrogen analyzer (model 703C; Antek Instruments, Inc., Houston, TX) is summarized schematically in Fig. 1.

Organic nitrogen can be quantified *indirectly* by determining total nitrogen with the C/CL method and subtracting the concentrations of inorganic nitrogen species (i.e., NH_3, NO_2^-, and NO_3^-) determined by separate analyses. The *direct* determination of organic nitrogen by the C/CL method, however, has not been possible because the inorganic species cannot be separated from organic nitrogen

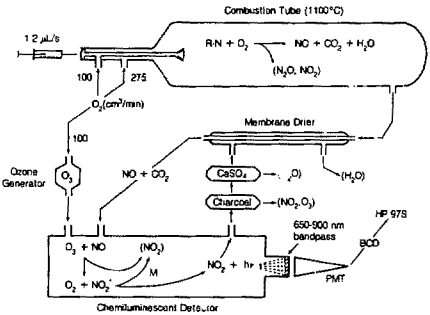

Figure 1. Reaction schematic for nitrogen quantificati by combustion/chemiluminescence (C/CL).

(XBL 8312-6910)

*This work was supported by the Assistant Secretary for Fossil Energy, Office of Oil Shale, Division of Oil, Gas, and Shale Technology of the U.S. Department of Energy under Contract No. DE-AC03-76SF00098.

†Sanitary Engineering and Environmental Health Research Laboratory, University of California (Berkeley), Richmond, CA.

prior to analysis. A sample pretreatment method that could effect a physical separation of inorganic from organic nitrogen would be extraordinarily valuable.

ACCOMPLISHMENTS DURING FY 1983

The C/CL method was evaluated for aqueous samples containing known concentrations of nitrogenous heterocycles. Oil-shale wastewaters were then analyzed for total nitrogen (TN). A technique employing chromatographic principles for separating inorganic from organic nitrogen was evaluated by determining the TN concentration of each of the two fractions. The results from the TN analyses were compared with the recovery of nitrogen using the ASTM adaptation of the Kjeldahl method[3] for total and organic nitrogen.

Water has been reported to depress quantification of nitrogen with C/CL by lowering the combustion burner-tip temperature, quenching the chemiluminescence, and contributing to two- and three-body reactions. A furnace at 1100°C mitigates the depression of burner-tip temperature, and a membrane dryer eliminates water from the gas stream that leaves the combustion tube. The slopes of standard curves for 2,4,6-trimethylpyridine (20 to 100 mg-N/L) in either toluene or water were virtually indistinguishable from those of standard curves for ammonium sulfate in water and 9-methylcarbazole in toluene. In addition, compounds dissolved in methanol (quinoline and 6-nitroquinoline) exhibited the same response as ammonium sulfate standards in water. These results indicate that water did not interfere with the combustion of the sample or with the detection of nitrogen by chemiluminescence; toluene or methanol could be used interchangeably with water, depending on the solubility of the analyte.

To validate whether the C/CL system would be applicable to quantification of nitrogen in oil shale process waters, we investigated the recovery of nitrogen from compounds reported to be both resistant to Kjeldahl digestion and prevalent in oil shale process waters (e.g., alkyl-substituted pyridines and quinolines). Most of the 52 compounds tested yielded 90% to 110% of their theoretical nitrogen contents (Fig. 2).[4] Compounds that contained the pyrazole nucleus exhibited exceptional resistance to quantitative liberation of nitrogen as NO; less than 15% of the nitrogen was recovered from pyrazole (Fig. 2), and the recovery of nitrogen did not exceed 50% from other compounds with the pyrazole nucleus (e.g., indazole and tetrazole). The important aspect of this structure appears to be a diaza N-N bond coupled with a N=C double bond in a 5-membered ring that is capable of tautomerizing (the nitrogens have an associated hydrogen). In contrast, complete recovery of nitrogen was obtained from 5-membered ring compounds with single-bonded N-N bonds (e.g., thiadiazole and 4-amino-2,3-dimethyl-1-phenyl-3-pyrazolin-5-one) and from 6-membered resonant rings with N-N bonds but with no associated hydrogen (e.g., pyridazine). Since pyrazoles have not been reported to occur in oil shale wastewaters, and since this was the only chemical class evaluated that yielded incomplete recoveries, C/CL would appear to be applicable to these waters.

Inorganic nitrate and nitrite salts yielded enhanced responses; apparent responses of 114% and 122%, respectively, were obtained. This phenomenon has been attributed to higher efficiencies of conversion to NO because of the higher oxidative states of these compounds. Since oil shale process wastewaters are generated in a reducing atmosphere, however, it is unlikely that oxidized nitrogen species would be present in large quantities.

To determine if oil shale process waters exerted a matrix effect on nitrogen quantification, a standard-additions study was designed to compare the results from TKN with those of TN using C/CL. Recovery of nicotinic acid spikes from a composite sample of nine wastewaters ranged from 98% to 103% for C/CL and from 102% to 104% for the Kjeldahl method.

For nine oil shale process waters and a composite, the values for TN by C/CL (n = 10) were compared with those for TKN (n = 3); each water was diluted to yield nitrogen concentrations between 30 and 75 mg-N/L. The difference in recoveries of nitrogen by the two methods ranged from −5.5% to +5.6%, and the relative standard deviation values for both were less than 3.5%.[4]

After a standard curve has been established with the C/CL nitrogen analyzer, each total nitrogen determination requires about 90 seconds. Some 42 samples can be prepared and analyzed in triplicate in 8 hours; in contrast, the Kjeldahl method, in our laboratory, requires 5 hours for three samples to be analyzed in triplicate.

We have also adapted a method that uses the principles of reverse-phase chromatography[5] to rapidly separate the large amounts of ammonia in oil

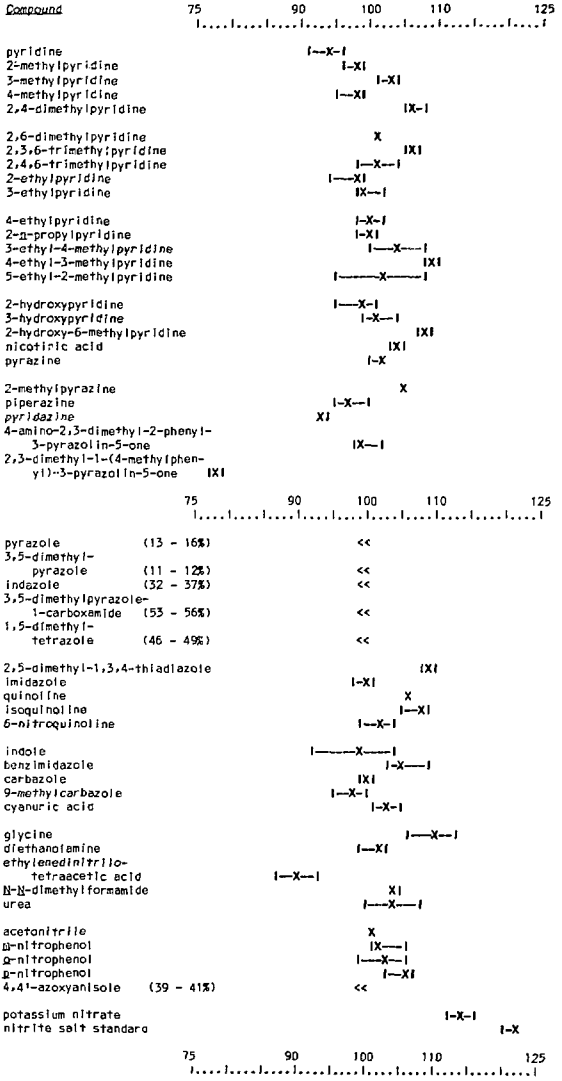

Figure 2. Percent recovery of nitrogen from standard solutions by C/CL nitrogen analysis, using an ammonium sulfate standard curve; mean (X) and range (|----|) are for three single-operator replications. (XBL 8310-12246)

shale process wastewaters from most of the organic nitrogen. The successful application of this method would allow an estimation of organic nitrogen by C/CL. To test the method's effectiveness, we analyzed the unfractionated filtered waters and two fractions (hydrophilic, HpF; lipophilic, LpF) from each of nine oil shale process waters and a composite sample. Each water was analyzed for TN (using the C/CL procedure) and for OKN (Fig. 3).

For the process waters analyzed, 8% to 24% of the OKN was sufficiently polar to remain with the ammonia in the HpF. The nitrogen content of the LpF was therefore an *underestimator* of the OKN. Furthermore, for each wastewater, the TN determined on the unfractionated sample exceeded the sum of the LpF-N and HpF-N as well as the sum of NH_3-N and OKN. This indicated that part of the LpF-N was irreversibly retained by the C-18 packing material during fractionation (this portion is called "residual-N" in Fig. 3), and that part of the nitrogen was not recovered by the Kjeldahl procedure. Some of the OKN was either steam-distilled or hydrolyzed to ammonia prior to OKN digestion, or a portion of the solutes was refractory to Kjeldahl digestion. Although LpF-N was not equivalent to OKN for these samples, reverse-phase fractionation of solutes, followed by TN analysis of the LpF by C/CL, may be the most rapid method available for obtaining an estimate of organic nitrogen in oil shale wastewaters.

PLANNED ACTIVITIES FOR FY 1984

Total nitrogen analysis by combustion coupled with chemiluminescent detection was demonstrated to be applicable to oil shale wastewaters. A rapid pretreatment technique (reverse-phase fractionation) followed by C/CL was shown to serve as an estimator of organic nitrogen in these complex wastewater samples. In FY 1984, this method will be more extensively evaluated and incorporated in our waste treatment research to assess the removal of organic nitrogen compounds. A detailed discussion of

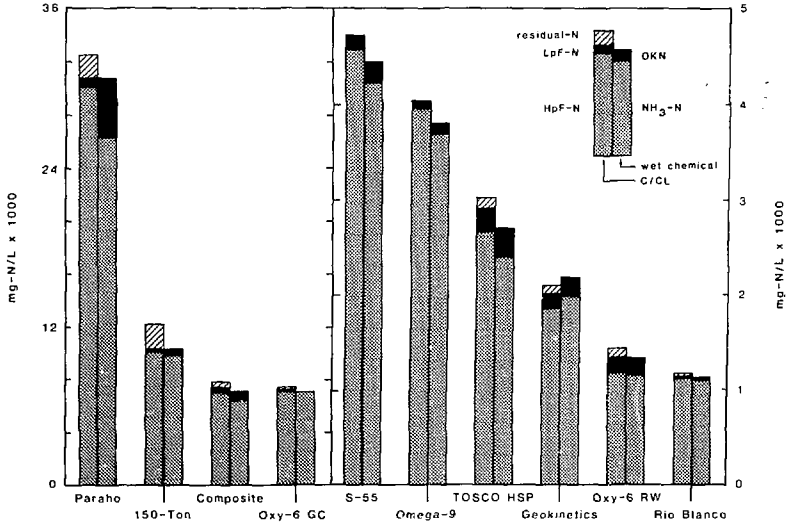

Figure 3. Nitrogen concentrations for oil shale process waters. For each pair of bars, the left member is total nitrogen (TN) as determined by C/CL, and the right member is total Kjeldahl nitrogen (TKN) as determined by the Kjeldahl method. The C/CL nitrogen values for the reverse-phase fractions (HpF and LpF) were evaluated as estimators of NH_3-N and organic Kjeldahl nitrogen (OKN), respectively. The cross-hatched areas are "residual-N" (i.e., that portion of the TN not accounted for by the sum of the two fractions); for S-55, the TN value was 111 mg-N/L less than the sum. (XBL 8310-12247)

theory and an operator's protocol will become available in the second edition of our analytical methods manual, *Quantitation of Oil Shale Wastewater Quality.*[6]

REFERENCES

1. Healy, J.B., Jr., Jones, B.M., Langlois, G.W., and Daughton, C.G. (1983), "Biotreatment of Oil Shale Wastewaters," in *Sixteenth Oil Shale Symposium Proceedings*, J.H. Gary, Ed., Colorado School of Mines Press, Golden, CO, p. 498.
2. Henschel, D.B., and Stemmle, J.T. (1983), *Environmental Monitoring Reference Manual for Synthetic Fuels Facilities*, EPA-600/8-83-027, Environmental Protection Agency, Washington, D.C.
3. American Society for Testing and Materials (1980), "Standard Test Method for Total Kjeldahl Nitrogen in Water," *1980 Annual Book of ASTM Standards*, Part 31, "Water," American Society for Testing and Materials, Phildelphia, PA, p. 743.
4. Jones, B.M. Harris, G.J., and Daughton, C.G. (1983), *Quantitation of Total, Ammoniac, and Organic Nitrogen in Oil Shale Process Waters by Kjeldahl Digestion and Combustion/ Chemiluminescence*, Lawrence Berkeley Laboratory Report LBID-765.
5. Daughton, C.G., Jones, B.M., and Sakaji, R.H. (1982), "Rapid Fractionation of Oil Shale Wastewaters by Reverse-Phase Separation," in *Quantitation of Oil Shale Wastewater Quality: A Manual of Analytical Methods*, C.G. Daughton, Ed., Chap. I, National Technical Information Service, DE-83-011034-A08, Springfield, VA; LBL-15816.
6. Daughton, C.G., Ed. (1982) *Quantitation of Oil Shale Wastewater Quality: A Manual of Analytical Methods*, NTIS DE-83-011034-A08; LBL-15816.

Biotreatment of Oil Shale Wastewaters Using Batch Cultures and Fixed-Film Reactors*

J.B. Healy, Jr., B.M. Jones, G.W. Langlois, J.F. Thomas, and C.G. Daughton†

Oil shale wastewaters originate during the retorting process from mineral dehydration, combustion, pyrolysis, input steam, and groundwater intrusion. Retorting pyrolyzes the complex polymeric kerogen to yield a wide variety of lower-molecular-weight organic compounds (e.g., shale oil) and by-products, many of which partition into the cogenerated wastewater. These process waters are particularly difficult to upgrade. Biological treatment is considered the most economical and efficient means of removing dissolved organic compounds from wastewaters. The primary objective of our biological treatment research is to optimize the microbial mineralization of the dissolved organic carbon (DOC) in oil shale wastewaters.

*This work was supported by the Assistant Secretary for Fossil Energy, Office of Oil Shale, Division of Oil, Gas, and Shale Technology of the U.S. Department of Energy under Contract No. DE-AC03-76SF00098.

†Sanitary Engineering and Environmental Health Research Laboratory, University of California (Berkeley), Richmond, CA.

Retort water from the modified *in-situ* retort No. 6 of Occidental Oil Shale Inc. (Oxy-6) has been the focus of most of the published research on oil shale wastewater biotreatment. Previous work in our laboratory has indicated that only 50% of the DOC in Oxy-6 retort water can be biooxidized; the remaining refractory DOC is hypothesized to comprise numerous nitrogenous heterocycles, each present at a low concentration.[1] The main focus of the biotreatment research presented in this article was the determination of whether the large quantity of biorefractory organic carbon in this retort water was characteristic of process waters from other oil shale operations, and if so, whether it could be rendered biodegradable under more specialized conditions. This work has been described extensively elsewhere.[2,3]

ACCOMPLISHMENTS DURING FY 1983

Aerobic bacterial oxidation was evaluated for removal of DOC from nine wastewaters from surface, modified *in-situ*, true *in-situ*, and simulated *in-situ* oil shale retorting processes: Oxy-6 gas condensate, Rio Blanco sour water, and Oxy-6, 150-Ton (run 13), TOSCO HSP, S-55, Omega-9, Geokinetics-9, and Paraho retort waters. Extensive acclimations for metabolically competent microbiota were completed after several months of serial enrichments using each water as a sole source of carbon,

nitrogen, and energy. Before biotreatment, each water was diluted with an equal volume of inorganic orthophosphate buffer that contained essential trace elements.[2] Samples were analyzed for DOC by a method that uses UV-peroxydisulfate oxidation coupled with coulometric titration.[4] Total nitrogen analyses were made by the chemiluminescence method described by Jones *et al.* in the preceding article.

Preliminary experiments have indicated that extensive losses of DOC can occur simply by volatilization. Such losses can be up to 30% and can be easily mistaken for biologically mediated removal. Biodegradation was therefore assessed in closed flasks that contained sufficient headspace to ensure aerobic conditions. Biological removals of DOC ranged from 9% for Oxy-6 gas condensate to 49% for Oxy-6 retort water (Fig. 1). Sample fractionation by a reverse-phase separation method[4] indicated that most of the mineralized DOC resided in the hydrophilic fraction (HpF); this supported the hypothesis that polar compounds were more easily biodegraded than those in the lipophilic fraction (LpF). Total removal of DOC from any of the waters did not exceed the amount of carbon in the respective HpF's.

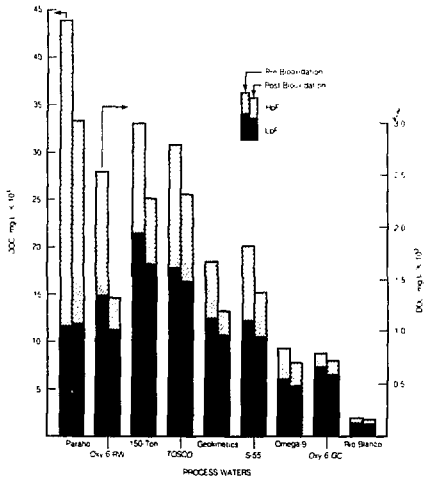

Figure 1. Biooxidation of nine oil shale process wastewaters; each water was diluted to lower the ammonia concentration below 1500 mg-N/L; each DOC value is given on the basis of raw water. (XBL 834-9136)

The extent of DOC removal could not be correlated with total organic carbon, chemical oxygen demand, ammonia concentration, pH, alkalinity, or changes in color or odor. These properties vary widely among these waters, making generalizations about biotreatability difficult. Further dilution of the waters rarely increased removal efficiencies, suggesting that the remaining material was metabolically refractory rather than inherently toxic. The amount of organic nitrogen in the LpF did not change significantly after biotreatment, and the molar ratio of LpF-DOC to LpF-nitrogen was similar for all nine waters. Molar C:N ratios ranged from 7 to 12, indicating that the biorefractory, malodorous, colored solutes were predominantly nitrogen heterocycles.

Defined culture media containing N-heterocycles as sole sources of C and N were used to investigate the refractory nature of the LpF. Mixed microbial cultures adapted to mineralize one of a series of three structurally related alkylpyridines were able to degrade the other two congeners at concentrations of 200 mg/L in a defined medium.[2] Twenty-six nitrogen heterocycles, each supplied to a mixture at a trace level (250 μg/L), were partially degraded (37%) by an acclimated culture. Higher levels of these same compounds (25 mg/L for each compound), however, may have exerted a toxic effect because only 9% of the DOC was mineralized.

The extracellular fluid that remained after extensive biotreatment of Oxy-6 retort water (i.e., spent retort water) was used for enrichment cultures at pH values of 7.4 and 9.1. Over 200 enrichment cultures, including cultures previously adapted to representative N-heterocycles, failed to remove much of the DOC from this spent water. The greatest additional DOC removal achieved was only 5% (on the basis of the DOC originally present in the raw retort water).

There are at least three possible causes for the refractory nature of spent water: (1) the N-heterocycles are inherently recalcitrant to catabolism; (2) the large overall concentration of heterocycles comprises numerous compounds that are each present at a low concentration, resulting in insignificant rates of utilization; and (3) the synthesis of the requisite catabolic enzymes may be repressed by the presence of more easily metabolized ammoniac nitrogen or may be sequentially regulated by the numerous heterocycle substrates. These points have been discussed with regard to the published literature on heterocycle degradation, with emphasis placed on means of enhancing biodegradation.[2]

Fixed-film bioreactors were investigated as means of overcoming these possible causes of biorecalcitrance. All fixed-film biological treatment

(FFBT) processes have a thin film of actively growing microorganisms attached to a solid support over which the wastewater is passed. Four characteristics distinguish FFBT from dispersed-phase systems such as activated sludge: (1) a greater concentration of biomass, (2) a spatially organized succession of diverse ecological habitats, (3) tolerance to shock loadings of toxic materials, and (4) the possibility for solutes to concentrate at the surface of the solid support by adsorption, thereby increasing the concentrations available to the cells. This greater spectrum of environmental conditions can facilitate the biodegradation of refractory molecules that may require the combined effects of different types of metabolism (e.g., anaerobic and aerobic; sequential cometabolism).

The restricted availability of oil shale process wastewaters limited our biotreatment studies to investigating FFBT using small laboratory-scale columns. Glass columns (25 cm × 2.5-cm i.d.) were positioned vertically and packed with one of four solid support materials: Calgon F-400 granular activated carbon (GAC), TOSCO II spent shale, Arco raw shale, or glass beads. These columns were fed air (1.0 cm^3/min) and raw Oxy-6 retort water (2 mL/min) that had been diluted twofold with phosphate buffer.[2] Each stream was introduced through a separate line in a downflow mode. This design permitted the influent to "trickle" through the solid support.

The biofilm in each column was established from three inoculum sources: activated sludge, a culture that had been enriched on 50% Oxy-6 retort water for several years, and a soil suspension. The entire column effluent was recycled back to the feed reservoirs for 5 days before switching to a fresh reservoir of medium. After recycle of the first sixteen 1-liter reservoirs, the average DOC removals were 80%, 62%, and 58% for the GAC, raw-shale, and glass-bead columns, respectively; all were greater than the 50% DOC removal that is typical of batch shake-flask biotreatment. Removals by the glass-bead and raw-shale columns were attributed solely to biodegradation since neither material was expected to adsorb a significant amount of organic material. These enhanced removals of an additional 8% to 12% of the DOC were therefore at the expense of DOC that was refractory in batch treatment.

The removals in the GAC column were probably the result of mutual physicochemical removal and biodegradation since saturation of the GAC sorptive capacity was unlikely during the time period in which the data were collected. There are major difficulties in distinguishing biodegradation from physicochemical removals. Furthermore, it has not been established if these two mechanisms are simply complementary or whether they can act synergistically to yield enhanced removals. Such synergistic removal (whether it occurs at all is highly controversial) might occur in GAC-packed FFBT reactors by the acclimation of bacteria to adsorbable compounds that are normally refractory.

PLANNED ACTIVITIES FOR FY 1984

Extensive microbial enrichments on nine oil shale process wastewaters failed to yield a culture that could mineralize more than 50% of the DOC from any sample. All wastewaters appeared to contain large quantities of material refractory to biodegradation. The inherent recalcitrance of N-heterocycles and their low concentrations were offered as explanations. Although FFBT was able to remove some of the DOC in Oxy-6 retort water that would normally remain after exhaustive shake-flask treatment, more than 32% of the DOC still remained. Despite major difficulties in distinguishing biodegradation from physicochemical removal, GAC may be the most effective of the solid supports tested.

Work planned for FY 1984 includes further investigation of FFBT using GAC. A column duplicating the GAC recycle-column will be operated in single-pass mode with biologically spent retort water fed at a reduced flow rate. This feed water will consist of biotreated 50% Oxy-6 retort water medium that will be amended (2% vol/vol) with untreated 50% Oxy-6 retort water medium as a supplemental source of carbon and energy. Removal of DOC beyond the amount required to saturate the sorptive capacity of the GAC would indicate that biodegradation of refractory material is occurring. Other GAC columns will be operated as fluidized beds under both aerobic and anaerobic conditions.

Further evidence will be sought to establish that N-heterocycles are the major class of metabolically refractory compounds in retort waters. The mechanisms causing N-heterocycles in retort water to resist biodegradation will be investigated using a mixture of pure compounds in batch cultures. The effects of ammonia as a preferred N-source in the presence of N-heterocycles will also be studied.

REFERENCES

1. Jones, B.M., Sakaji, R.H., and Daughton, C.G. (1982), "Physicochemical Treatment Methods for Oil Shale Wastewater: Evaluation as Aids

to Biooxidation," in *Fifteenth Oil Shale Symposium Proceedings*, J.H. Gary, Ed., Colorado School of Mines Press, Golden, CO, p. 581.
2. Healy, J.B., Jr., Jones, B.M., Langlois, G.W., and Daughton, C.G. (1983), "Biotreatment of Oil Shale Wastewaters," in *Sixteenth Oil Shale Symposium Proceedings*, J.H. Gary, Ed., Colorado School of Mines Press, Golden, CO, p. 498.
3. Healy, J.B., Jr., Jones, B.M., Langlois, G.W., and Daughton, C.G. (1983), *Removal of Dissolved Organic Carbon from Oil Shale Retort Water Using Fixed-Film Bioreactor Columns*, Lawrence Berkeley Laboratory Report LBID-788.
4. Daughton, C.G., Ed. (1982), *Quantitation of Oil Shale Wastewater Quality: A Manual of Analytical Methods*, National Technical Information Service, DE-83-011034-A08, Springfield, VA; LBL-15816.

Prediction of Atmospheric Emissions Resulting From Codisposal of Oil Shale Wastes*

P. Persoff, L. Hunter, J.F. Thomas, and C.G. Daughton†

Mixing two waste streams from oil shale processing (spent shale and process wastewater) for waste disposal is called codisposal. Codisposal of wastewater (retort water and gas condensate) with spent shale would be advantageous for the oil shale industry because the spent shale must be moistened to control dust and facilitate compaction. For each barrel of oil produced, 1.2 barrels of moisturization water would be needed; wastewater production is generally about 0.4 barrels per barrel of oil. Currently, retort water would be difficult to discharge or reuse. Codisposal could solve the immediate problem of retort water disposal.

Although codisposal would contribute to satisfying the water requirement for spent shale compaction, it might adversely affect air quality. Both retort water and gas condensate contain malodorous and possibly mutagenic organic compounds that are difficult to remove by conventional treatment processes. During transportation to the disposal site and compaction, the moisturized spent shale would still be warm (85°C when leaving the plant and cooling only to 65°C on hot days). Atmospheric emissions would occur over a large area and would not be amenable to end-of-pipe control. Two goals of this project are to identify and quantify atmospheric emissions during codisposal and to determine the mechanism of such releases so that better waste management techniques can be devised.

ACCOMPLISHMENTS DURING FY 1983

Heterocyclic nitrogenous compounds comprise a significant fraction of organic solutes in oil shale retort waters. These compounds are thought to be responsible for much of the objectionable odor and difficulty of biological treatment.[1] This year, a preliminary estimate of certain N-heterocycles that could be emitted during codisposal was made. The following assumptions, generalized from published commercial development plans, were made: (1) spent shale moisture content is 15%, wt/wt (moisture provided by Oxy-6 gas condensate[2]); (2) spent shale temperature is constant (85°C); (3) spent shale is delivered to the disposal site at a dry density of 0.865 Mg/m^3 and compacted in 0.5-m "lifts" to 1.36 Mg/m^3; (4) spent shale lifts remain uncovered for 24 hours before another lift is emplaced; (5) there is no aqueous leaching of N-heterocycles from spent shale; and (6) there is no significant removal of N-heterocycles by sorption on spent shale.[3]

Emissions calculated by the method reported here are directly proportional to the concentrations of individual species in the moisturizing water, providing the stated assumptions are met, and they can also be adjusted for changes in the assumptions. Therefore, although the results presented here represent a worst case (moisturizing with raw process water), the method could be used to calculate emissions from moisturizing with process water pretreated by steam stripping or biological treatment (see accompanying articles).

Three modes of emission were considered: (1) expulsion of interstitial gas from voids during shale compaction, (2) transport via fugitive dust, and (3) diffusion through the compacted spent shale to the

*This work was supported by the Assistant Secretary for Fossil Energy, Office of Oil Shale, Division of Oil, Gas, and Shale Technology of the U.S. Department of Energy under Contract No. DE-AC03-76SF00098.

†Sanitary Engineering and Environmental Health Research Laboratory, University of California (Berkeley), Richmond, CA.

atmosphere. The first mode was estimated by multiplying the volume of interstitial gas that would be expelled during compaction (calculated from the spent shale density before and after compaction[4]) by the gas-phase concentrations of the N-heterocycle species (calculated using a reported chemical analysis of gas condensate[2] with vapor-pressure data from handbooks,[5,6] and UNIFAC activity coefficients[7]). The volume of gas expelled during compaction was calculated as 0.536 m^3 per barrel of syncrude recovered. Emission via fugitive dust was calculated using a published value of 2 g fugitive dust emitted during spent shale disposal per barrel of syncrude recovered[8] and assuming that the dust contained 15% moisture of the same composition as the moisturizing water. Emissions by diffusion were calculated using a standard mathematical solution to the diffusion equation[9] and a new expression for effective diffusivity (Eq. (2), below) in a waste disposal pile. Because diffusion was found to be the major mode of emission, and because the method of calculation is new, this article will concentrate on the expression of effective diffusivity for volatile compounds in a waste codisposal situation.

A compound in soil, or in a solid waste, can escape to the atmosphere by volatilization. Resistance to mass transfer occurs in both phases—the soil and the atmosphere. If the wind speed at the ground surface is at least 2 cm/sec, then resistance in the atmosphere is negligible,[10] and volatilization can be modeled as a diffusive or diffusive-advective process, depending on whether soil water is evaporating. Mathematical models for volatilization from soil have recently been reviewed.[10] In addition, nonsteady-state diffusion of pesticides from soil under various boundary conditions has been modeled using classical diffusion equations,[11] an effort that serves as a precedent for the present work. Diffusion of lindane through soil was characterized by an experimentally measured effective diffusivity; no attempt was made to predict the value of the effective diffusivity from fundamental physical and chemical parameters.[11] This analysis has been extended[12] to include the effects of steady-state advection caused by water evaporation as well as nonsteady-state diffusion; a formula was presented by which the effective diffusivity could be derived from the following fundamental parameters: diffusivity in air, diffusivity in water, volume fraction of air, volume fraction of water, Henry's law constant (which gives the air-water partition coefficient), and sorption isotherm data (which gives the soil-water partition coefficient). This formula, however, was not used to fit experimental data to the model; rather, a value of effective diffusivity was calculated from experimental data.

For diffusion models to be truly predictive, a method to calculate the effective diffusivity from data that are known or can be calculated is needed. Such a formula is presented here, requiring as input data the fundamental parameters listed in the preceding paragraph and also a diffusion hindrance factor for each phase in which diffusion occurs. Hindrance, h, is the product of tortuosity and the pore-constriction factor. Tortuosity refers to the fact that diffusion to the atmosphere does not follow a straight line, but must go around solid particles. Tortuosity is conventionally assigned a value of $\sqrt{2}$ or $\sqrt{3}$ on the assumption that the concentration gradient follows a zig-zag path in two or three dimensions.[13] Pore constriction is less well characterized.

Compacted, codisposed solid and liquid wastes from oil shale processing represent a matrix of three phases: solid, liquid, and gas. Any solute present in the wastes would eventually distribute itself among the three phases. The distribution would be determined by the Henry's law constant and the adsorption isotherm for each solute. At time zero, the three phases can be considered uniform in composition throughout the pile and in equilibrium with one another. The surface of the pile represents a constant-concentration boundary condition, while the bottom of the pile represents a zero-flux boundary condition. This problem of one-dimensional diffusion without advection has been solved for a single phase. The solution[9] is:

$$\frac{C - C_0}{C_1 - C_0} = 1 - \frac{4}{\pi} \sum_{n=0}^{\infty} \frac{(-1)^n}{2n + 1} \times \exp\left\{-D(2n + 1)^2 \pi^2 t / 4l^2\right\} \cos \frac{(2n + 1)\pi x}{2l} \quad (1)$$

where C is the concentration of solute (ML^{-3}) in the single phase at the point represented by x; C_0 is the initial uniform concentration (ML^{-3}) throughout the pile in the single phase; C_1 is the boundary concentration (= 0 for codisposed oil shale wastes; ML^{-3}); D is the molecular diffusivity (L^2T^{-1}) of the solute in the single phase; t is time (T); x is dimensionless height in the pile = h/l; h is the height (L) of the point above the bottom of the pile; and l is the height (L) of the pile.

In a three-phase matrix, the solute can diffuse through any of the three phases and can also be transferred between phases as necessary to maintain

chemical equilibrium among the phases. For example, as solute in the gas phase leaves the pile and enters the atmosphere, a disequilibrium is created between the interstitial liquid and gas phases. Liquid-phase solute will then evaporate to restore equilibrium.

Equation (1) can be used to model diffusion through a three-phase matrix if the concentration and diffusivity are appropriately redefined. If C represents the total concentration of solute in all three phases (ML^{-3}), then the effective diffusivity, D_e, must be used:

$$D_e = \frac{\dfrac{e_1 r_1 D_1}{h_1} + \dfrac{e_2 r_2 D_2}{h_2 H_{12}} + \dfrac{e_3 r_3 D_3}{h_3 H_{12} H_{23}}}{e_1 r_1 + \dfrac{e_2 r_2}{H_{12}} + \dfrac{e_3 r_3}{H_{12} H_{23}}} \qquad (2)$$

where subscripts 1, 2, and 3 represent the gas, liquid, and solid phases, respectively; D_i is the molecular diffusivity of the solute in phase i; e_i is the volume fraction occupied by phase i; r_i is the mass density of phase i; h_i is the diffusion hindrance factor in phase i; $H_{12} = x_1/x_2$; $H_{23} = x_2/x_3$, and x_i is the mass fraction of the solute in phase i. It is evident from the form of Eq. (2) that the effective diffusivity is weighted by the volume fraction, mass density, and the diffusivity (corrected for hindrance) of the solute in each phase.

Experimental measurement of the hindrance in two-phase systems (solid-gas and solid-liquid) has given values ranging from 1 to more than 6, with values falling in the range 2.7 to 3.0 for sand.[13] There appear to be no data available on individual-phase hindrance factors for three-phase systems in which diffusion can occur in either the gas or liquid phase. If one considers diffusion in the solid phase, separate solid particles do not constitute a continuous flow path; the pore-constriction factor is therefore infinite. This simplifies calculation in that only diffusion in the two remaining phases needs to be considered. Experimental measurement of effective diffusivity for two compounds suffices to calculate hindrance for the gas and liquid phases, and these values can then be used to calculate effective diffusivity for other compounds. Furthermore, empirical relationships among compacted density, moisture content, and hindrance can be established by experiment, which may lead to a theory for estimating hindrance.

Equations (1) and (2) were used to estimate the fraction of compound that would be lost during 24 hours by diffusion through codisposed wastes at constant temperature. The compounds considered were those N-heterocycle species (or isomer groups) that have been identified in Oxy-6 gas condensate.[2] Results of these calculations are shown in Table 1. The gas- and liquid-phase diffusivities were estimated using the Wilke-Lee and Hayduck-Laudie equations.[10] A value of 1.73 was taken for the hindrance factor of both the gas and liquid phases. Analysis of sorption data available for 2,4,6-trimethylpyridine on spent shale[3] showed that removal by sorption would not significantly reduce the amount of that solute in the liquid phase; this was assumed to apply to N-heterocycles in general.

Calculation of emissions that could occur by all three modes (Table 2) shows that diffusion would be the major mode of atmospheric release of N-heterocycles during codisposal of oil shale wastes and that release via particulates would be negligible. The large proportion of material lost during compaction and 24 hours of diffusion results from the large activity coefficients calculated by UNIFAC and the assumption that nothing partitions to the solid phase. Both points need to be confirmed experimentally.

Table 1. Estimated loss of nitrogenous heterocycles *via* diffusion.

Compound	Diffusivity, m^2/sec: Gas phase ($\times 10^{-5}$)	Liquid phase ($\times 10^{-9}$)	Effective ($\times 10^{-7}$)	Henry's law constant[a]	Fraction lost from disposal pile in 1 day[b]
pyridine	1.36	3.21	0.461	4.75	0.14
methyl-pyridines	1.21	2.83	1.21	14.54	0.23
dimethyl-pyridines	1.10	2.55	3.25	44.85	0.38
2,4,6-tri-methyl-pyridine	1.01	2.33	8.13	135.15	0.60
quinolines	1.02	2.47	0.734	10.35	0.18
pyrrole	1.47	3.55	0.281	2.59	0.11

[a]Henry's law constant = (vapor pressure of pure compound) × (activity coefficient)/(total pressure).

[b]See Ref. 9, p. 59, for graphical method of calculation. Hindrance of both phases was taken as 1.73; if it were taken as 3.0, then the values in this column would be reduced by approximately 24%.

Table 2. Summary of emission rates of nitrogenous heterocycles resulting from three modes of emission.[a]

Compound	Mass of compound placed in codisposal (kg/day)	Mass emission rate (kg/day): By diffusion[b]	By expulsion	In particulates
pyridine	140	21	1.5	0.0002
methyl-pyridines	209	47	7.4	0.0003
dimethyl-pyridines	448	148	54.6	0.0007
2,4,6-tri-methyl-pyridine	669	224	289.6	0.0010
quinolines	93	16	2.2	<0.0002
pyrrole	47	5	0.3	0.00007

[a]Assuming 50,000 bbl/day oil production rate, 1.4 tons of spent shale produced per barrel of syncrude, 15% moisture in disposal pile, and spent shale moisturized with untreated Oxy-6 retort water (analysis reported in Ref. 2).

[b]Calculated using fraction lost by diffusion as calculated in Table 1.

PLANNED ACTIVITIES FOR FY 1984

A report presenting this work in greater detail will be prepared.[14] Bench-scale laboratory simulations of the codisposal process will be attempted. Diffusive emissions will be quantified by dynamic headspace sampling and analysis. Variables to be studied include compacted density, moisture content, and temperature. Equation (2) will be verified experimentally, and the effects of advection resulting from evaporation of water will be included in Eq. (1). Adsorption isotherms will be determined for N-heterocycles on various spent shales.

REFERENCES

1. Healy, Jr., J.B., Jones, B.M., Langlois, G.W., and Daughton, C.G. (1983), "Biotreatmemt of Oil Shale Wastewaters," in *Sixteenth Oil Shale Symposium Proceedings*, Colorado School of Mines Press, Golden, CO, p. 498.
2. Leenheer, J.A., Noyes, T.I., and Stuber, H.A. (1982), "Determination of Polar Organic Solutes in Oil-Shale Retort Water," *Environ. Sci. Technol. 16*, p. 714.
3. Routson, R.C. and Li, S.W. (1980), "Collidine Sorption on a Silt Loam and a Spent Shale," *Soil Sci. 130*, p. 233.

4. Magic Circle Energy Corp. (1982), *Commercial Oil Shale Production from the Utah Cottonwood Wash Project,* prepared for the Bureau of Land Management, U.S. Department of the Interior.
5. Perry, J. and Chilton, C.H., Eds. (1973), *Chemical Engineer's Handbook,* 5th ed., McGraw-Hill Book Co., New York, p. 3-49 through 3-61.
6. Weast, R.C., Ed. (1974) *Handbook of Chemistry and Physics,* 55th ed., CRC Press, Cleveland, OH, pp. D-170 through D-186.
7. Arbuckle, W.B. (1983), "Estimating Activity Coefficients for Use in Calculating Environmental Parameters," *Environ. Sci. Technol. 17,* p. 537.
8. Crawford, K.W., *et al.* (1977), *A Preliminary Assessment of the Environmental Impacts from Oil Shale Developments,* Environmental Protection Agency report EPA/600/7-77/069 (National Technical Information Service no. PB-272 283), Springfield, VA.
9. Crank, J. (1975), *Mathematics of Diffusion,* 2nd ed., Clarendon Press, Oxford, England.
10. Lyman, W.J., Reehl, W.F., and Rosenblatt, D.H., Eds. (1982), *Handbook of Chemical Property Estimation Methods,* Chapters 11, 16, and 17, McGraw-Hill Book Co., New York.
11. Mayer, R., Letey, J., and Farmer, W.J. (1974), "Models for Predicting Volatilization of Soil-Incorporated Pesticides," *Soil Sci. Am. Proc. 38,* p. 563.
12. Jury, W.A., Grover, R., Spencer, W.F., and Farmer, W.J. (1980), "Modeling Vapor Losses of Soil-Incorporated Triallate," *Soil Sci. Soc. J. 44,* p. 445.
13. Thibodeaux, L.J. (1979), *Chemodynamics,* John Wiley and Sons, New York, p. 246.
14. Persoff, P., Hunter, L., and Daughton, C.G., *Atmospheric Emissions from Codisposed Oil Shale Wastes,* Lawrence Berkeley Laboratory report (forthcoming).

Volatile Emissions from Codisposal of Spent Shale and Retort Wastewaters*

L. Hunter, P. Persoff, J.F. Thomas, and C.G. Daughton†

A major problem in the commercialization of the oil shale resources of Colorado, Utah, and Wyoming is the development of environmentally acceptable practices for the disposal of the two major by-products of the surface retorting process: retorted (spent) shale and cogenerated retort wastewater. Spent shale would be disposed and compacted in layered "lifts" at on-site dumpsites. To achieve the desired degree of compaction for the physical stability of the lifts, it is necessary to wet the spent shale to an optimal water content of about 15%. Because of the limited water resources of the oil shale region, process wastewaters would have to supply at least part of this moisturizing water. This codisposal strategy would also eliminate the problem of contaminated wastewater disposal. For codisposal to be acceptable, however, it must meet a number of criteria for minimizing negative environmental effects. Our area of interest is the evaluation of volatile emissions that may occur during the dumping, compacting, and weathering of the codisposed materials. With no pretreatment of the wastewater, these emissions would comprise large quantities of ammonia and a wide variety of organic compounds. Our primary goals are to (1) identify the mechanisms that control the release of volatile compounds, (2) identify some of the components that could contribute to the hazardous or malodorous nature of these emissions, and (3) quantify the release of volatiles to the atmosphere. A preliminary report discusses this research in more detail.[1]

*This work was supported by the Assistant Secretary for Fossil Energy, Office of Oil Shale, Division of Oil, Gas, and Shale Technology of the U.S. Department of Energy under Contract No. DE-AC03-76SF00098.

†Sanitary Engineering and Environmental Health Research Laboratory, University of California (Berkeley), Richmond, CA.

ACCOMPLISHMENTS DURING FY 1983

The first task has been the design of laboratory simulations to gauge the possible extent of the volatilization problem and test the accuracy of a predictive model that is being developed. We have been looking at the feasibility of gas chromatography for direct headspace analysis of retort waters and retort-water/spent-shale mixtures.

Headspace was analyzed by flame ionization detection, using a 6-m packed column containing SP 2100 silicone stationary phase (10%) on Supelcoport (80/100 mesh) support. The column was programmed from 40°C to 240°C in a series of steps

designed to sharpen component peaks and minimize run time. Since resolution of the anticipated complex mixture of peaks into individual components could not be expected with this type of packed column, these initial efforts were intended to provide an overall comparison of the headspace components from nine wastewaters currently under study.

The usefulness of direct headspace analysis was demonstrated on a sample of Paraho retort water that had been equilibrated with its headspace in a sealed container at 65°C for 90 min. A 2-mL headspace sample gave a complex chromatogram (Fig. 1). Distinct differences in the behavior of two groups of peaks (designated *H* and *P*) were noted when the samples were maintained at 65°C for various times. The *P* peaks showed a rapid build-up in size within the first 15 minutes, whereas the *H* peaks showed a gradual increase over several hours (Fig. 2). This behavior was surprising since the chromatographic responses suggested that the *H* groups comprised nonpolar, highly volatile components (i.e., narrow, nontailing peaks), and the *P* groups comprised polar compounds (i.e., tailing peaks). One would normally expect highly volatile, nonpolar compounds (possibly hydrocarbons) to equilibrate more rapidly with the headspace. The presence of substantial amounts of surface-active agents in the retort water may be the cause of this anomalous behavior. Under the prevailing alkaline conditions of retort waters, longer-chain fatty acids could lead to micelle formation. Nonpolar solutes would accumulate preferentially within the micelles. Their subsequent transfer to the headspace would be a two-stage process: diffusion from micelle to solution (continuous phase) and then equilibration with headspace. Equilibration would be especially slow if the compounds' solubilities were low, such as those for hydrocarbons.

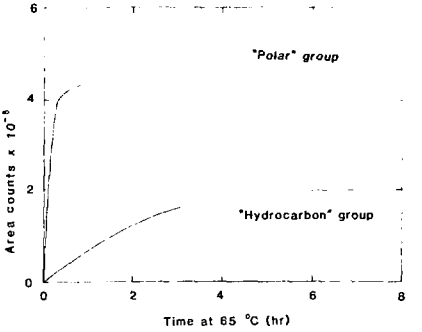

Figure 2. Effect of time at temperature (65°C) on Paraho headspace components—comparison of *P* (polar) and *H* (hydrocarbon) peaks. (XBL 836-10419A)

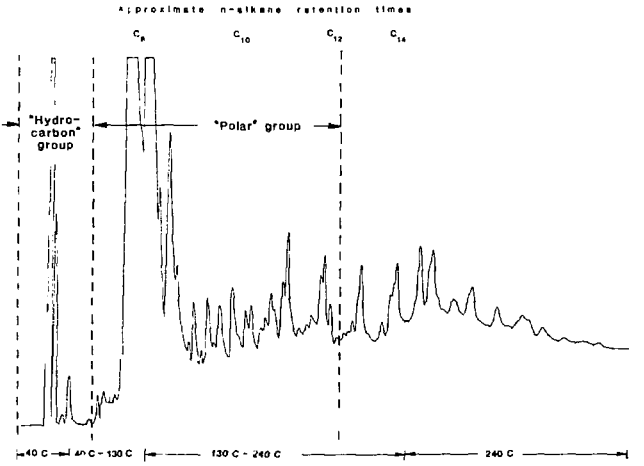

Figure 1. Chromatogram of headspace (65°C for 90 min) above Paraho retort water. (XBL 836-10420A)

Nine different wastewaters were compared on the basis of their *H* and *P* groups (Fig. 3). Among the differences observed were the very high *H* level in Paraho and the high *P* level in TOSCO HSP.

Preliminary headspace experiments with retort-water/spent-shale mixtures have demonstrated that spent shale can substantially alter the headspace composition. Diluted Paraho retort water and spent shale (L-2; Lawrence Livermore National Laboratory) were heated in sealed containers for 90 min at 65°C. The headspace chromatograms for the mixture and for the spent shale and retort water alone are shown in Fig. 4. Among the changes effected by the presence of the spent shale were: (1) a substantial reduction in the *H* group, (2) an increase in the major peaks of the polar *P* group, and (3) a large increase in the series of small peaks riding on the *P* group "tail." These differences appeared to be caused in part by rate changes; the *H* group, for example, would eventually have increased to its former size over a longer heating period.

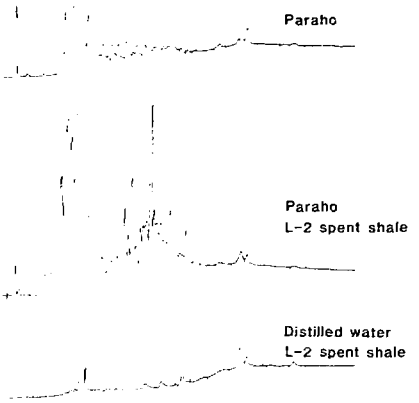

Figure 4. Effect of spent shale (L-2) on headspace components from Paraho retort water. (XBL 836-10460A)

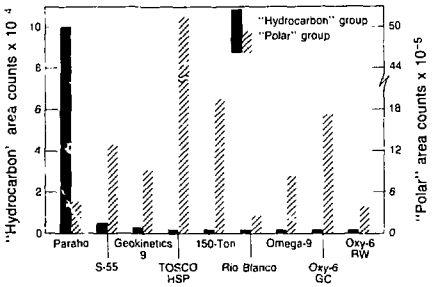

Figure 3. Comparison of *H* and *P* groups in headspace (65°C for 90 min) for nine retort wastewaters. (XBL 836-10421A)

PLANNED ACTIVITIES FOR FY 1984

Headspace analysis of retort waters and retort-water/spent-shale (codisposed) mixtures will be continued. Fused-silica capillary gas chromatography will be used to identify and quantify individual volatile components. Attention will focus primarily on heterocyclic nitrogenous compounds, which may be major contributors to the malodorous and possibly hazardous nature of volatile emissions from the codisposal process.

REFERENCE

1. Persoff, P., Hunter, L., and Daughton, C.G. (1983), *Volatilization from Codisposed Oil Shale Wastes: Preliminary Estimate of Emissions During Compaction and Characterization of Headspace over Retort Waters*, Lawrence Berkeley Laboratory Report *LBID-786*.

Physicochemical Treatment of Oil Shale Wastewaters by Steam Stripping*

R.H. Sakaji, J.F. Thomas, and C.G. Daughton†

For waters containing high concentrations of volatile species, pretreatment by steam stripping before codisposal has been proposed. Stripping removes volatile solutes from a wastewater by passing a gas through the water. In a commercial operation, this process is accomplished by flowing the gas and liquid streams countercurrent to each other through a column packed with inert material. The packing material increases the interfacial contact between the phases. The petroleum industry uses steam as a stripping gas to remove carbon dioxide, hydrogen sulfide, ammonia, and other volatile solutes from refinery wastewaters. Steam stripping can also remove ammonia as well as carbon dioxide from oil shale wastewaters because the elevated temperature concomitantly reduces both the pK of the ammonium ion-ammonia gas equilibrium and the solubility of ammonia gas. The stripping of these compounds by steam involves: (1) conversion of ionic species, such as ammonium, bicarbonate, and carbonate, into their neutral, gaseous forms, (2) diffusion of the dissolved gases from the bulk solution to the liquid-steam interface; and (3) transfer of the dissolved gas through the liquid-steam interface into the steam phase.

The objectives of treating oil shale wastewaters by stream stripping include: (1) removal of biorefractory organic compounds; (2) removal of organic or inorganic solutes that may be toxic to microorganisms used in subsequent treatment processes; (3) reduction of the high alkalinity (caused by carbonate and ammonia) to allow the pH to be adjusted downward; (4) equalization of wastewater flow to downstream treatment units to maintain constant organic and inorganic loading rates (this prevents shock loads to downstream treatment units); (5) removal of volatile compounds that could cause nuisance atmospheric emissions (e.g., malodors) during codisposal; and (6) reduction in the volume of wastewater that ultimately needs to be managed by concentrating the solutes in a small volume of condensed steam. If steam stripping partially or fully meets these objectives, it may prove to be one of the only treatments used by developers.

ACCOMPLISHMENTS DURING FY 1983

For the steam stripping process to meet these treatment goals, the scientist or engineer must understand how variables such as temperature, pressure, and composition affect the wastewater matrix and interact with variables such as stripping-column packing size, wastewater and steam flow rates, and column height. Although determining optimum performance characteristics appears to be an elementary problem, reported variabilities in stripper performance indicate that design and operation of steam strippers is a complex task.

A major variable that determines solute removal efficiencies is the quantity of gas used to strip a given volume of wastewater. To simplify our examination of the steam stripping process, we decided not to vary the bed height, operating temperature, or size of packing material during a series of experimental runs. The only process variables that were changed were the gas and liquid flow rates. These two rates are combined into a dimensionless quantity called the G/L ratio which is the quotient of the gas (i.e., steam) flow rate divided by the liquid (i.e., wastewater) flow rate. The rationale for examining the removal efficiencies for a given solute as a function of the G/L ratios has been outlined.[1] When the size of packing material, temperature, and bed height are held constant, the gas and liquid flow rates determine the degree to which a solute can be separated from a wastewater.

Published studies have shown that steam stripping can be effective for removing dissolved gases such as carbon dioxide and ammonia from oil shale process wastewaters. Oxy-6 retort water has been stripped with hot gas in a column packed to a height of 2.07 m and operated at 104.4°C with a G/L ratio of 0.70 (kg/kg); removal of 97.2% of the ammonia was achieved under these conditions.[2] Oxy-6 retort water has also been stripped with steam in a 1.5-m column operated at 110.0°C, but with a lower G/L ratio of 0.40 (kg/kg); 96% of the ammonia was removed.[3]

These results compare favorably with design calculations used to predict the length of column required to achieve 99% removal of ammonia. The design calculations for several oil shale process wastewaters are summarized in Table 1.[1] In general, these design calculations indicate that a steam stripper containing at least 2.04 m of packing and

*This work was supported by the Assistant Secretary for Fossil Energy, Office of Oil Shale, Division of Oil, Gas, and Shale Technology of the U.S. Department of Energy under Contract No. DE-AC03-76SF00098.

†Sanitary Engineering and Environmental Health Research Laboratory, University of California (Berkeley), Richmond, CA.

Table 1. Height of a packed bed required to achieve 99% removal of ammonia from oil shale wastewaters.

Wastewater	Height of packing (m)	
	Calculation A[a]	Calculation B[b]
Paraho	1.89	0.52
150-Ton (run 13)	2.04	0.58
Oxy-6 gas condensate	1 89	0.52
S-55	1.89	0.55
Omega-9	1.77	0.49
TOSCO HSP	1.80	0.52
Geokinetics-9	1.77	0.49
Oxy-6 retort water	2.04	0.58
Rio Blanco sour water	2.04	0.58
Composite[c]	1.86	0.52

[a]Values for calculation A were derived from empirical correlations for H_G and H_L, which are heights of transfer units based on gas- and liquid-phase ammonia compositions, respectively.[7,8]

[b]Values for calculation B were derived using empirical correlations to calculate the H_G and H_L values.[8]

[c]Equal volumes of each of the nine waters.

operated at 110°C with a G/L ratio of 0.10 should remove 99% of the ammonia from these wastewaters. The height of the columns calculated empirically (Calculation A of Table 1) are qualitatively consistent with the results presented above.

When the temperature decreases, the solubility of ammonia increases. This necessitates a higher G/L ratio or a longer packed bed to achieve 99% removal. When the column temperature in the first of the two previous examples[2] was decreased, a higher G/L ratio and a longer packed bed were required to approach the desired degree of separation. Since the packed-bed height was close to that calculated empirically (2.04 m), the G/L ratio had to be increased to achieve the ammonia removal of 97.2%. In the second steam stripping study,[3] a shorter column of 1.5 m was used, which meant that a higher temperature (110°C) and higher G/L ratio were required to achieve the 96% removal of ammonia. Although the results of these two studies are qualitatively consistent with the design calculations, neither study used a G/L ratio near 0.10, which is considered the minimum G/L ratio required to achieve 99% removal of ammonia (at 110°C).

An anomaly noted by some researchers[2] is that although Omega-9 and 150-Ton (run 17) wastewaters contain equivalent concentrations of ammonia, these two wastewaters behaved differently when stripped with hot gas at 104.4°C. At a G/L ratio of 1.44 (kg/kg), the ammonia removal from Omega-9 retort water was essentially complete. In marked contrast, at a G/L ratio of 1.74 (kg/kg), only 76.6% of the ammonia was removed from the 150-Ton retort water. In the petroleum industry, the ammonia that remains after such exhaustive treatment is called "fixed" ammonia.

The objectives of our steam stripping project include: (1) determining the optimum operating conditions for different oil shale wastewaters and attempting to delineate which variables are critical to the efficient operation of the stripping process; (2) elucidating the physical and chemical factors that make certain oil shale process wastewaters difficult to strip; and (3) producing stripped wastewaters for subsequent use in our biological treatment and co-disposal research.

To meet the objectives of this treatment process, a pilot-scale steam stripper was designed and constructed in FY 1981.[4] Since the stripper could not be operated on a continuous basis (because of design limitations and shortage of wastewaters), the ability to achieve reproducible operating conditions for the duration of a run was critical. Because of the unique design of both the gas generation and sample collection systems, most of FY 1983 was devoted to troubleshooting, modifying, and testing the stripper. The design theory, design calculations, and operating procedures are all being documented in a manual of operations. Part of FY 1983 also was spent validating the analytical methods being used to quantitatively assess treatment performance. The methodology for quantifying total dissolved carbon and dissolved organic carbon by UV-peroxydisulfate oxidation coupled with coulometric titration has been validated.[5] Detailed protocols for total dissolved carbon, dissolved organic carbon, and dissolved inorganic carbon are available.[6] Ammonia was assayed using a colorimetric phenate method. Dissolved inorganic carbon (DIC), which was used as a measure of CO_2, was determined by coulometric titrimetry; dissolved organic carbon (DOC) was determined by UV/peroxydisulfate oxidation coupled with coulometric titrimetry.

Before treatment performance could be quantitatively assessed, we needed the ability to reliably sample the pilot plant effluent streams. To verify the accuracy of a sampling process, mass balance calculations must be performed to show that all the material fed into the reactor is recovered. The ability to achieve and calculate mass balances was one of

th· primary criteria used to design our steam stripper. The use of steam for stripping was preferred to air because it can be condensed after passage through the wastewater and thereby be easily separated from the noncondensable stripped gases. Since steam-stripping research within the petroleum industry indicates a preferred operating temperature of 110°C, the system must also operate under pressure.

With our stripper, wet steam is generated by a 6-kW flash evaporation unit and dried and superheated in a 6-kW steam drier. The dry steam (i.e., liquid water is absent) is injected at the bottom of the packed stripper bed. The temperature of the effluent gas streams, superheated steam, and wastewater influent are monitored and controlled remotely. The temperature gradient between the steam entering the column and the overheads condenser can be preset. This gradient governs the flow rate of steam. The ratio of steam to liquid flow rates governs the removal of the dissolved gases from the wastewater stream. While holding the liquid flow rate and packed-bed height constant, the rate of steam flow is ultimately determined by the temperature differential between the steam and the overheads condenser. Increasing the steam-to-liquid ratio will increase the absolute removals, but economic operation necessarily requires low ratios. The wastewater feed is injected at the top of the packed bed. This configuration results in countercurrent flow of the steam and liquid streams. The stripped wastewater is pooled in a bottoms collector, and the steam and stripped gases are collected in an overheads condenser.

The wastewater is preheated prior to injection into the column so that column operation approaches isothermal conditions; wrapping the column with heating tape and fiberglass insulation minimized heat losses to the surroundings. The heating tapes and insulation also minimized condensation of the stripping gas in the packed bed.

The stripping column is made of a 4.88-m × 5.08-cm i.d. Pyrex beaded-glass tube packed with 0.64-cm Intalox ceramic saddles (Norton Industries, Irvine, CA). The internal diameter of the packed-bed column was selected to minimize "wall effects" caused by nonuniform flow. The internal diameter of the column was selected by choosing a ratio of packing material diameter to inside column diameter of a least 1 to 8.

For the first series of stripping runs, a composite sample of oil shale wastewaters was used. This composite was made from equal volumes of Oxy-6 gas condensate and Oxy-6, S-55, TOSCO HSP, Geokinetics-9, Paraho, and Omega-9 retort waters. The packed-bed height and bed temperature were held constant (3.81 m and 110°C, respectively) over a series of five runs that used G/L ratios ranging from 0.079 to 0.93. Because these wastewaters are in short supply, the bottoms and overheads from a given run were recombined with any unused influent and used in the subsequent run.

The results of these runs are summarized in Fig. 1. As the G/L ratio was increased, the removals of ammonia, DIC, and DOC also increased. Removal of DIC was the most easily achieved: it was greater than 90% for each G/L ratio. In contrast, DOC was very difficult to remove; even at high G/L ratios, the removal of DOC was less than 11%. Of the two dissolved inorganic species, the removal of ammonia was the most dependent on the G/L ratio. The removal of ammonia was low at low G/L ratios, and it increased only to 55% at the high ratio of 0.93.

The difficulty in removing ammonia indicates that the theory and practice of steam stripping are not well developed. A packed-bed height greater than 3.81 m is required to achieve a removal that would still be significantly less then the 99% removal predicted by design calculations. The empirical correlations used in calculating bed heights[7,8] are apparently inadequate for the design of packed-bed strippers.

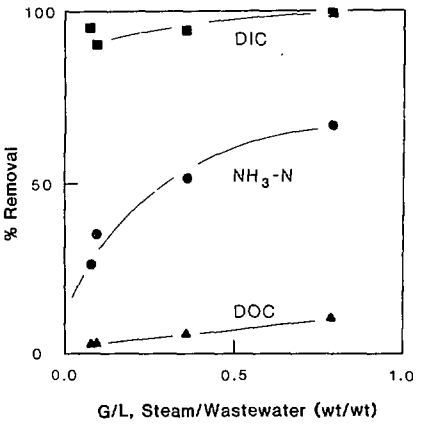

Figure 1. Percent removal vs. gas-to-liquid ratio for a composite oil shale wastewater; packed-bed height = 3.81 m and temperature = 110°C. (XBL 8310-12128A)

The poor removals of ammonia could be attributed to several factors, including: (1) interferences and inconsistencies in the analytical methodology (e.g., the ammonia measured in these samples may have been a combination of ammonia and organic amines or other bases), or (2) the ammonia may be "fixed" by the wastewater matrix (i.e., chemical interaction between other solutes prevents the formation of free ammonia gas). Since a composite water was used, it is not known if these problems were a result of an individual water or of interactions between waters.

PLANNED ACTIVITIES FOR FY 1984

Design theory predicts that a packed-bed height of 2.04 m should be adequate to achieve 99% removal of ammonia from oil shale wastewaters. Demonstrated poor removals of ammonia from these wastewaters indicates a discrepancy between design theory and actual practice. Ammonia removal from a composite wastewater, using a G/L ratio of 0.93, was well below the 99% removal that would have been expected from using a G/L ratio almost an order of magnitude lower. These results clearly demonstrate the need for further study to elucidate those chemical and physical factors that play a role in the removal of ammonia from oil shale wastewaters.

Objectives for FY 1984 include: (1) determining which process wastewaters are difficult to treat by steam stripping, (2) elucidating the major physical and chemical factors that affect the stripping process, (3) determining the cause of "fixed" ammonia, and (4) trying to alleviate the problem of "fixed" ammonia by chemical addition (e.g., pH adjustment).

The steam stripper will also be used to generate stripped wastewaters for further study. The effluent (bottoms) will be used in our codisposal research to examine whether stripping of volatile solutes eliminates the subsequent release of nuisance, malodorous compounds. Effluents will also be subjected to biotreatment studies to determine if biorefractory or toxic compounds are removed by the stripping process.

REFERENCES

1. Sakaji, R.H. and Daughton, C.G. (1983), *Physicochemical Treatment of Oil Shale Wastewaters by Steam Stripping*, Lawrence Berkeley Laboratory Report LBID-814.
2. Hines, A.L., Pedram, E.O., Punnoose, S., and Poulson, R.E. (1982), "Hot Gas Stripping of Oil Shale Retort Waters," in *Fifteenth Oil Shale Symposium Proceedings*, J.H. Gary, Ed., Colorado School of Mines Press, Golden, CO, p. 468.
3. Pearson, F., *et al.* (1980), *Steam Stripping of Shale Oil Wastewater—Phase I*. Sanitary Engineering Research Laboratory Report UCB-SERL Report 80-8, University of California, Berkeley.
4. Sakaji, R.H., Jones, B.M., Thomas, J.F., and Daughton, C.G. (1982), "Processes for the Physico-Chemical Treatment of Oil Shale Wastewaters," in *Energy and Environment Division Annual Report FY 1981*, LBL-13500, p. 4-57.
5. Langlois, G.W., Jones, B.M., Sakaji, R.H., and Daughton, C.G. (1984), "Coulometric Quantitation of Carbon in Oil Shale Wastewaters via UV-Peroxydisulfate or High-Temperature Oxidation," *ASTM J. Test. Eval.*, in press.
6. Daughton, C.G., Ed. (1982), *Quantitation of Oil Shale Wastewater Quality: A Manual of Analytical Methods*, LBL-15816 (National Technical Information Service No. DE 83011034), Chapters II and III.
7. Sherwood, T.K. and Holloway, F.A.L. (1940), "Performance of Packed Towers—Experimental Studies of Absorption and Desorption," *Trans. Am. Inst. Chem. Eng. 36*, p. 21.
8. Onda, K., Takeuchi, H., and Okumoto, Y. (1968), "Mass Transfer Coefficients Between Gas and Liquid Phases in Packed Columns," *J. Chem. Eng. (Japan) 1*, p. 56.

COMBUSTION RESEARCH

Premixed Turbulent Combustion*

R.K. Cheng, S.U. Choi, T.T. Ng, F. Robben, and L. Talbot

The objective of this research is to investigate the interaction between fluid dynamic turbulence and chemical reaction in turbulent combustion flows. The goal is to improve the physical understanding of turbulent combustion processes and to provide more reliable data for the development of theoretical models of turbulent combustion.

Our research is concentrated on the experimental study of premixed turbulent combustion — where the fuel and the oxidizer are thoroughly mixed before combustion takes place. Compared to diffusion-controlled combustion, where the mixing and burning of fuel and air occur simultaneously, the study of premixed combustion may be considered somewhat more fundamental because the governing equations do not include the mixing variables.

In these experiments, velocity is measured by laser Doppler anemometry (LDA) and density by Rayleigh scattering; the data are used to determine statistical correlations in two simplified and idealized flow configurations. The statistical measurements are complemented by high-speed schlieren movies showing qualitative features of the flame structures.

The first of these experimental configurations consists of combustion embedded in a turbulent boundary layer over a strongly heated wall. The isothermal turbulent boundary layer flow is a classical fluid mechanical problem for which there have been many experimental and theoretical investigations. The wealth of information from these studies on turbulence properties provides the necessary background for the present investigation of the effects of combustion. An appealing feature of this boundary-layer configuration is that, by adjusting the wall temperature, a wider range of fuel-to-air equivalence ratios can be studied than is possible in stabilized flame configurations.

The second experimental configuration consists of rod-stabilized unconfined flames propagating in turbulent flow. This so-called "V-flame" has similarities to the flame configuration found in many practical combustors. The configuration is relatively free of geometric and flow constraints so that the fundamental properties of the flame-turbulence interaction can be studied in more detail. Experimental studies of this flame can be compared with theoretical predictions of turbulent combustion, such as that developed by Bray *et al.*[1]

*This work was supported by the Director, Office of Energy Research, Office of Basic Energy Sciences, Chemical Sciences Division of the U.S. Department of Energy under Contract No. DE-AC03-76SF00098.

ACCOMPLISHMENTS DURING FY 1983

Reacting Turbulent Boundary Layer

Previously reported velocity fluctuations and covariance measured by a two-color LDA system in isothermal, heated, and reacting turbulent boundary layers have been analyzed to obtain the joint probability density function (jpdf) of two velocity components and the third moment of the velocity fluctuations.[2] The experimental conditions for these studies are free-stream velocity, U_∞, of 19 m/s, wall temperature, T_w, of 1000 K, and ethylene/air equivalence ratio of 0.35.

As previously reported, conditional analysis of the data show that the reduction in the Reynolds stress (the velocity covariance) by combustion is due mainly to a significant decrease in the contribution from the so-called burst event. The burst event is part of a cycle in the development of large-scale turbulent structures in the turbulent boundary layer, and is also the major mechanism of turbulence production. This cycle in the reacting layer consists of the inrushing of high-momentum cold reactants from the outer flow and the bursting of low-momentum hot products from the wall region. Compared to the jpdf obtained in the heated layer, the jpdf of the reacting layer shows a significant reduction in axial and transverse momentum in the fluid associated with the burst event. The reduction of the transverse momentum indicates that ejection of fluid from the wall becomes less energetic.

The difference in the contributions to Reynolds stress from the burst and inrush events, ΔS, across the reacting boundary layer at six axial locations is shown in Fig. 1. To show the correlation between the change in Reynolds stress contributions and the combustion reaction, ΔS is plotted with the distance from the wall y, normalized by the thermal boundary

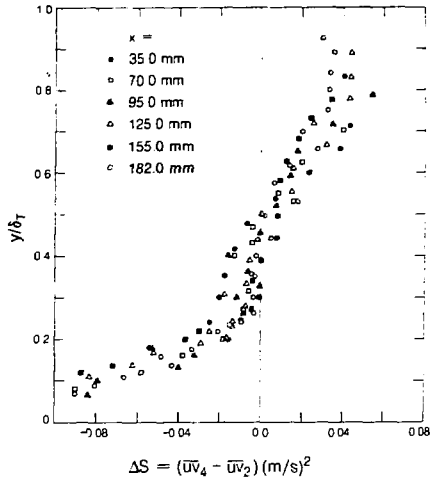

Figure 1. Reynolds stress contributions from burst and inrush modes, $\overline{uv}_4 - \overline{uv}_2$, at six axial locations, x, across a reacting turbulent boundary layer. (XBL 841-9471)

layer thickness δ_t, instead of the velocity boundary layer thickness δ_u. At $y/\delta_t > 0.6$, ΔS is positive, meaning that the contribution from the burst event is higher than that from the inrush event. At about $y/\delta_t = 0.5$, the contribution from the inrush event exceeds that from the burst event and ΔS becomes negative. This position corresponds to the position of the maximum mean density gradient and suggests that the reductions in the contribution from the burst event occur mostly in the hot burned products near the wall region.

The two-point Rayleigh scattering technique is being used to determine the statistical spatial character of the thermal and flame structures. This technique simultaneously measures the density fluctuations at two points separated by an adjustable distance. The data are analyzed to obtain spatial and temporal scales of the density fluctuation, their jpdf's, and higher-order moments.

Preliminary measurements of the density cross correlation at two points separated in the spanwise (z) direction, orthogonal to the axial and transverse planes, have been obtained across the heated and reacting boundary layers at two axial locations. The separation between the two points, Δz, has been varied from 0.0 to 12.0 mm. The spatial correlation coefficient in the heated layer at four distances from the wall is shown in Fig. 2. The integral length scale can be derived from the area under these curves. This length scale, l_z, varies from about 2.7 mm close to the heated wall, to about 3.0 mm in the outer region of the thermal layer. The integral time scale deduced from the space-time correlation coefficient also shows an increase with distance from the wall. Further analysis of the spatial and time scales in the reacting layer is being carried out.

Rod-Stabilized V-Shaped Flame

One important but unresolved issue in the study of premixed turbulent flames is the true nature of the Reynolds stress and the magnitude of the so-called "flame-generated turbulence." Our previous studies show that the Reynolds stress and turbulence intensity increase within the turbulent flame brush. However, the sign of the Reynolds stress is inconsistent with that predicted by the mean-gradient-transport assumption commonly used in modeling.[3]

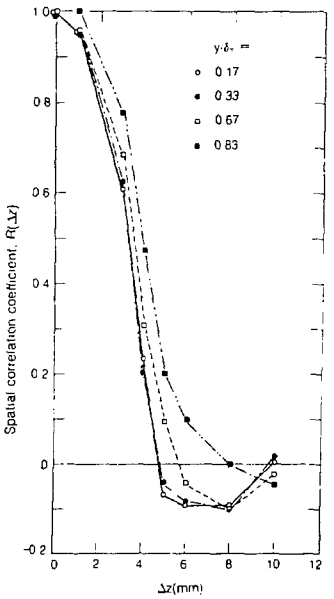

Figure 2. Spatial correlation coefficient of density for two points as a function of the separation Δz in the spanwise direction, at four positions within a heated turbulent boundary layer. (XBL 841-9472)

For these experimental conditions, it has been shown that the turbulent flame consists of a fluctuating wrinkled flame sheet, often referred to as a wrinkled laminar flame.[4] We have attributed the increase in Reynolds stress and turbulent intensity to the effects caused by intermittent velocity measurements in the burned products and the unburned reactants, which are separated by the fluctuating thin flame front. An intermittency model is therefore more suitable for describing the flame turbulence. In this model, the turbulence parameters are expressed with the use of an intermittency factor and the corresponding conditioned mean and fluctuation velocities in the reactants and in the products.

A two-color LDA technique has been developed to determine the turbulence fluctuation and Reynolds stress in the premixed flames. These data are useful for comparison with either Lagrangian or Eulerian turbulent-flame models. To sample conditionally in the reactants, the flow is seeded with a silicone oil aerosol which is evaporated and burned quickly at the flame front.[5] Consequently, the LDA measurements refer only to the unburned reactants. To measure the velocity unconditionally in both the unburned reactants and the burned products, aluminum oxide seed particles were used. A conditional analysis method has been developed to deduce the conditioned quantities in the products from the unconditioned data. This technique has been used to study two methane-air and two ethylene-air flames.[6,7]

Within the flame brush, the apparent increase in turbulence intensity and Reynolds stress is due mainly to the intermittency effects. In addition, the conditioned fluctuation intensities in the products are generally higher than those in the reactants, indicating production of turbulence by the flame. Conditioned and unconditioned Reynolds stress profiles are compared in Fig. 3. Inside the flame brush (10.0 mm $> y >$ 20.0 mm) the conditional Reynolds stress in the reactants remains unchanged. In contrast, the unconditioned Reynolds stress, $-\overline{uv}$, increases to 0.3 $(m/s)^2$. Since the unconditioned Reynolds stress is positive and since the local mean velocity gradients, $\delta U'/\delta y$ and $\delta V'/\delta x$, are both negative, the mean gradient transport model, $-\overline{uv} = \epsilon(\delta U'/\delta y + \delta V'/\delta x)$, would imply that the eddy viscosity ϵ is negative.

However, the sign and magnitude of $-\overline{uv}$ is consistent with the predictions of the intermittency model. In Fig. 4, separated states for unburned reactants and burned products are shown quite distinctly on the double-peaked unconditional jpdf of the two velocity components. The peak on the left is associated with the products and the one on the right is

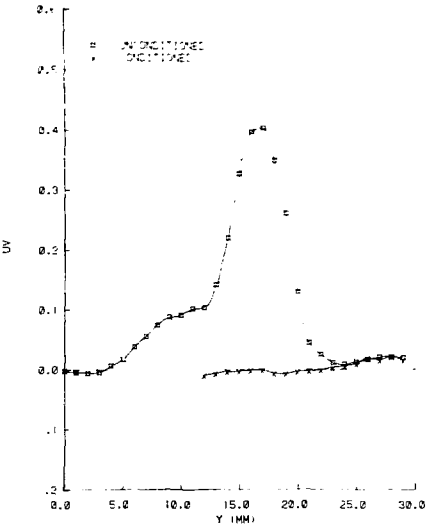

Figure 3. Comparison of unconditioned Reynolds stress, $-\overline{uv}$, and conditioned Reynolds stress in the reactant, $-\overline{uv}_r$, for an ethylene/air V-shaped turbulent flame. Profiles taken at x = 60 mm above the flame stabilizer. (XBL 837-10666)

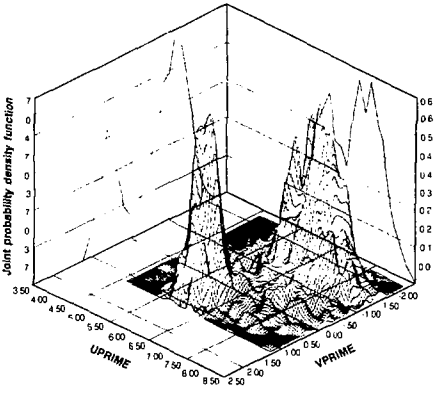

Figure 4. Unconditional joint probability density function (jpdf) of two velocity components obtained at the position of maximum $-\overline{uv}$ shown in the profile of Fig. 3. (x = 50 mm, y = 16 mm). Also shown as projections are the probability density function (pdf) of the transverse velocity fluctuations (left) and the pdf of the axial velocity fluctuations. (XBL 8310-12099)

associated with the reactants. According to the intermittency model, the major contribution to Reynolds stress is proportional to the product of ΔU and ΔV, where ΔU is the difference in the conditioned mean axial velocities and ΔV is the same parameter for the transverse velocities. Since ΔU and ΔV in our flames are of opposite signs, their contribution to $-\overline{uv}$ is negative. The model also shows that the contribution to the axial and transverse turbulence fluctuations are proportional to ΔU and ΔV, respectively.

PLANNED ACTIVITIES FOR FY 1984

Reacting Turbulent Boundary Layer

The two-point Rayleigh scattering technique will be used to measure spatial and temporal cross-correlations in the axial and transverse directions. These results will yield a more complete description of the thermal and flame structures. Among the quantities that can be deduced are the periodicity of the passage of these structures, which can then be compared with those reported in other investigations of isothermal boundary layers. Such comparison should show whether or not the thermal and flame structures scale with the same free-stream variables as large turbulence structures.

Rod-Stabilized V-Shaped Flame

The conditional turbulence statistics will be further analyzed to compare with a theoretical one-dimensional Eulerian turbulent-flame model, such as that of Bray *et al.*[1] Also, comparison of the turbulence intensities in the products with calculations using two-dimensional vortex dynamic models[8] will help to determine the mechanism responsible for the production of turbulence across the flame. The experimental measurements will be extended to include comparative studies of propane- and hydrogen-air flames in both open and enclosed configurations.

REFERENCES

1. Bray, K.N.C., Libby, P.A., Masuya, G., and Moss, J.B. (1981), "Turbulence Production in Premixed Turbulent Flames," *Combust. Sci. Technol., 25*, p. 127.
2. Cheng, R.K. and Ng, T.T. (1983), "The Influence of Combustion on Reynolds Stress in a Strongly Heated Turbulent Boundary Layer," in preparation.
3. Cheng, R.K. and Ng, T.T. (1983), "Velocity Statistics in Premixed Turbulent Flames," *Combust. Flame 52*, p. 185.
4. Namazian, M., Talbot, L., Robben, F., and Cheng, R.K. (1982), "Two-Point Rayleigh Scattering Measurements in a V-shaped Turbulent Flame," in *Nineteenth Symposium (International) on Combustion*, p. 487, The Combustion Institute, Pittsburgh, PA.
5. Hertzberg, J.R. (1984), "A Laser Tomographic Study of a Laminar Flame in a Kármán Vortex Street," to be published in *Combust. Sci. Technol.*
6. Cheng, R.K. (1983), "Conditional Sampling of Turbulence - ..nsities and Reynolds Stress in Premixed Turbulent Flame," submitted to *Combust. Sci. Technol.*; LBL-16938.
7. Cheng, R.K., Talbot, L. and Robben, F. (1983), "Conditional Velocity Statistics in Premixed CH_4-Air and C_2H_4-Air Turbulent Flames," submitted to *Twentieth Symposium (International) on Combustion*, Ann Arbor, MI, Aug. 7–11, 1984; LBL-17220.
8. Ashurst, W.T. and Barr, P.K. (1983), "Stochastic Calculation of Laminar Wrinkled Flame Propagation via Vortex Dynamics," *Combust. Sci. Technol. 34*, p. 227.

Fluid Mechanics of Combustion*

A.F. Ghoniem, A.J. Chorin, C.-C. Hsiao, and A.K. Oppenheim

The studies summarized below on the fluid-mechanical features of combustion are based primarily on the numerical modeling techniques we have developed, as described last year.[1]

ACCOMPLISHMENTS DURING FY 1983

In fulfillment of the objectives set forth for this year, we have published a theoretical study of the generation of pressure waves by accelerating flames[2] and a manual on numerical modeling of turbulent combustion based on the random-vortex method.[3] Moreover, we have completed the numerical analysis of the formation and inflammation of a turbulent jet[4,5] and developed a methodology for interpreting the experimentally observed fluid-mechanical properties of prominent flame propagation phenomena, *the aerodynamics of flames*.[6] Progress made in the latter two topics is reported here.

Turbulent Jet

Upon gaining a good insight into the formation of a turbulent jet, as reported last year (Ref. 1, Fig. 4), we studied two cases of its inflammation. In the first case, we explored the consequences of igniting the jet at the center of the orifice from which it is issued; in the second, we calculated the flame spread following the initiation of combustion across its full cross section.

To provide an illustration of the results we obtained, displayed here in Fig. 1 is the solution of the second case, representing, in effect, the propagation of a turbulent torch as it ignites a combustible atmosphere into which it is injected. The flame evidently establishes itself at the outer contour of the "vortex fluid"—the region of concentrated vorticity whose structure is dominated by large-scale eddies. When this region is compared with that obtained in the case of a nonreacting jet (Fig. 4 of Ref. 1), it appears that, although on the whole they are quite similar, the expansion due to the combustion process

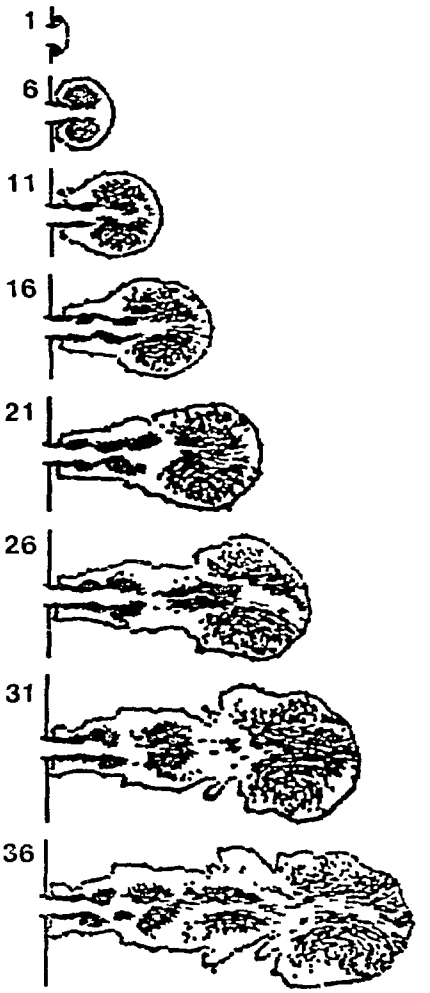

Figure 1. Development of vorticity field and progress of the flame front associated with formation of a turbulent torch generated by a jet of hot combustion products in a combustible atmosphere. Numbers denote time expressed in nondimensional units of $u_i t/d_i$ where u_i is the inlet velocity, d_i the width of the orifice, and t the time.
(XBL 8312-2493)

*This work was supported by the Office of Energy Research, Basic Energy Sciences Division, and the Office of Energy Conservation and Utilization Technology of the U.S. Department of Energy under Contract No. DE-AC03-76SF00098, by the National Science Foundation under Grant CPE-8115163, and by NASA-Lewis Research Center under Grant NAG 3-131.

causes vortex blobs to spread apart, impeding thereby the development of a coherent structure. Nonetheless, the recirculation induced by these eddies is of major importance in consolidating the field of combustion products and in keeping the flame front at the outer boundary of the vortex structure.

Aerodynamics of Flames

The understanding of the basic features of turbulent flow and flame propagation, attained from the results of our numerical modeling studies, led to the development of a fluid-mechanical interpretation founded upon classical aerodynamics. It is based on the premise that the salient properties of flame propagation phenomena, in particular those involving the kinematics of the front and its feedback effect on the flow field, are incompressible and inviscid—an apparent paradox, considering that combustion is associated with significant changes in density while its sustenance depends intrinsically upon transport processes.

Nonetheless, we have been able to demonstrate that a number of experimentally observed phenomena can be explained rationally upon the introduction of some quite drastic idealizations—namely, the assumptions that the unburnt and burnt media are incompressible, the former behaving moreover as an inviscid fluid, while the flame front acts as an interface associated with a step change in density, its ratio corresponding to that of the temperature produced by the exothermicity of the combustion process. These assumptions have three consequences: (1) the continuity, momentum, and energy conservation equations are decoupled; (2) the flow field can be considered as essentially a potential; and (3) its prominent features can be determined by an appropriate solution of the Laplace equation, subject to given initial conditions. Under such circumstances, the flame front acquired the character of a Stefan-like interface, whose motion is evaluated numerically by the use of SLIC (Simple Line Interface Calculation)—a code especially adapted for this purpose by Chorin.

The solution provides information on the consequences of three properties of the flame front: (1) rotary flow in its immediate vicinity, (2) self-advancement at a prescribed "normal burning speed," and (3) expansion due to the exothermicity of combustion. On this basis, we have been able to reveal kinematic features of a number of experimentally observed fluid mechanical phenomena. For example, Fig. 2 displays an aerodynamic solution pertaining to experimental records reported last year.[7] The fact that the solution can reproduce so well the salient features revealed by experimental observations demonstrates the commanding influence of the three elementary properties specified above.

Figure 2. Results of an aerodynamic analysis of the propagation of a laminar flame in a flame duct. Left, the initial phase following ignition at a point on the center line; right, the final phase of approach to the closed end.
(XBL 8312-2494)

PLANNED ACTIVITIES FOR FY 1984

Both the numerical modeling of turbulent combustion and the aerodynamic theory of flames are to be pursued further. The modeling will be aided significantly by arrangements to use a Cray computer at the NASA-Ames Research Center. Work on the aerodynamic theory will be centered upon the development of analytical techniques for treating the kinematic properties of flames.

REFERENCES

1. Ghoniem, A.F., Chorin, A.J., and Oppenheim, A.K. (1983), "Numerical Modeling of Turbulent Combustion," in *Energy and Environment Division Annual Report, FY 1982*, LBL-15300, p. 4-55.
2. Guirguis, R.H., Kamel, M.M., and Oppenheim, A.K. (1983), "Self-Similar Blast Waves Incorporating Deflagrations of Variable Speed," in *Shock Waves, Explosions, and Detonations*, J.R. Bowen, N. Manson, A.K. Oppenheim, and R.I. Soloukhin, Eds., Vol. 87 of *Progress in Astronautics and Aeronautics*, American Institute of Aeronautics and Astronautics, New York.
3. Ghoniem, A.F., Marek, C.J., and Oppenheim, A.K. (1983), "Modeling Interface Motion of Combustion (MIMOC)," NASA Technical Paper 2132.
4. Chen, D.Y., Ghoniem, A.F., and Oppenheim, A.K. (1983), *Experimental and Theoretical Study of Combustion Ignition*, NASA CR-168139 (DOE/NASA/0131-1).
5. Ghoniem, A.F., Chen, D.Y., and Oppenheim, A.K. (1984), "Formation and Inflammation of

a Turbulent Jet," to be presented at the American Institute of Aeronautics and Astronautics. 22nd Aerospace Sciences Meeting.
6. Ghoniem, A.F., and Oppenheim, A.K. (1983). "Acrodynamic Features of Turbulent Flames." American Institute of Aeronautics and Astronautics. Paper AIAA-83-D470.
7. Dunn-Rankin, D., and Sawyer, R.F. (1983). "Flame Propagation." in *Energy and Environment Division Annual Report, FY 1982*. LBL-15300, p. 4-65; see especially Figs. 1 and 2.

Optical Study of a Perturbed Premixed Flame*

J.R. Hertzberg, M. Namazian, L. Talbot, and F. Robben

In order to demonstrate some aspects of the interaction of large-scale turbulence with a flame front, an otherwise laminar flame sheet was perturbed by the regular vortices generated in the wake of a rod. The response of the flame to this regular perturbation, which has some aspects of turbulent flow, was visualized using a high-speed cinematographic technique, and some major characteristics were determined.

ACCOMPLISHMENTS DURING FY 1983

The combustor configuration for the laminar, premixed V-shaped flame consisted of a 5-cm-diameter open jet of ethylene-air mixture with a 1-mm-diameter rod flameholder transverse to the flow, as described in other papers in this annual report. The otherwise laminar flow was perturbed by the wake of a second rod, 3 mm diameter, placed slightly upstream and to one side of the flameholder.[1] For the Reynolds numbers used, the wake is known as a Kármán vortex street and consists of a regular series of alternating vortices.

A laser-illuminated, tomographic technique was used to visualize the flame front,[2] as described in the following. The premixed, combustible mixture was seeded with a translucent aerosol of silicone oil droplets. These droplets evaporate and burn quickly at the flame, so that the disappearance of the droplets marks the flame front. By illuminating the flow with a sheet of light from an argon ion laser, sufficient light is scattered from the aerosol to be photographed with a high-speed movie camera.

The photograph shown in Fig. 1 is an example of the results. The flame forms the sides of the V and the flameholder is at the apex. The vortex street is generated by a rod slightly below and to the left of the flameholder; thus the wrinkled, perturbed flame front is on the left side of the V, while the right side is undisturbed. The outer boundaries of the bright region delineate the turbulent interface between the seeded jet flow and a shielding, annular surrounding flow.

Figure 2 shows the motion of the flame during one cycle of the vortex street. Regions A, C, and D show the passage of a counterclockwise vortex through the flame. B shows the velocity defect in the center of the street, and F shows the action of a clockwise vortex. The clockwise vortex forms a cusp that convects downstream with the flow velocity,

Figure 1. Example of laser tomography; flame forms sides of V. Flow speed = 1 m/s. (XBB 839-8041)

*This work was supported by the Air Force Office of Scientific Research under Contract No. F-44620-76-C-0083. Additional equipment and facility support was provided by the Chemical Sciences Division of the U.S. Department of Energy under Contract No. DE-AC03-76SF00098.

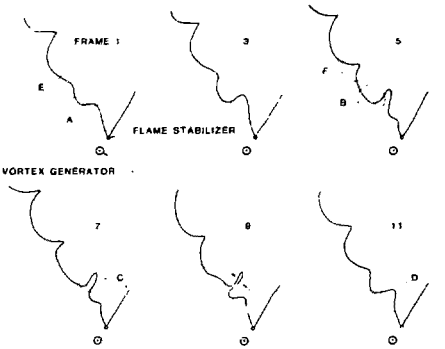

Figure 2. Flame motion during perturbation by vortex street. (XBL 841-142)

while the effect of the counterclockwise vortex is damped. This damping may be due to the stabilizing influence of the velocity defect in the center of the vortex street.[3]

PLANNED ACTIVITIES FOR FY 1984

The tomographic technique will be extended to fully turbulent V-shaped flames and the results correlated with previously obtained density and velocity statistics.[4,5] In addition, tomographic, Rayleigh scattering, and laser Doppler velocimetry studies of the flameholder region will evaluate the effect of flameholder fluid mechanics on these flames.

REFERENCES

1. Namer, I. (1980), *An Experimental Investigation of the Interaction Between a Kármán Vortex Street and a Premixed Laminar Flame.* Ph.D. dissertation, University of California, Berkeley.
2. Boyer, L. (1980), "Laser Tomographic Method for Flame Front Movement Studies," *Combust. Flame 39* p. 321.
3. Hertzberg, J.R., Namazian, M., and Talbot, L. (1984), "A Laser Tomographic Study of a Laminar Flame in a Kármán Vortex Street," to be published in *Combust. Sci. Technol.*
4. Namazian, M., Talbot, L., Robben, F., and Cheng, R.K. (1982), "Two-Point Rayleigh Scattering Measurements in a V-Shaped Flame," *Nineteenth Symposium (International) on Combustion*, The Combustion Institute, p. 487, Pittsburgh, PA.
5. Cheng, R.K. and Ng, T.T. (1983), "Velocity Statistics in Premixed Turbulent Flames," *Combust. Flame 52*, p 185.

Density Fluctuations in Premixed Turbulent Flames*

M. Namazian, L. Talbot, and F. Robben

The structure of turbulent flames is quite complex and not well understood in spite of numerous theoretical and experimental studies. The density fluctuations in several relatively simple turbulent flames have been determined using the two-point Rayleigh scattering technique. A number of the characteristics have been compared with the predictions of some simple modeling assumptions and shown to be in good agreement. This work[1] is a continuation of previous studies on the velocity and density of turbulent flames,[2,3] and in particular of the initial two-point Rayleigh scattering measurements.[4]

*This work was supported by the Air Force Office of Scientific Research under Contract No. F-44620-76-C-0083. Additional equipment and facility support was provided by the Chemical Sciences Division of the U.S. Department of Energy under Contract No. DE-AC03-76SF00098.

ACCOMPLISHMENTS DURING FY 1983

Figure 1 shows a schematic diagram of the flame configuration and optics. The positions of the two-point density measurements were separated in three orthogonal (x, y, and z) directions. Here, only the y-direction measurements will be reported.

For each flame condition, profiles in the y (transverse) direction were taken at 20, 40, 60, and 80 mm above the flameholder. For each profile, the separation of the two points was varied in about 8 steps from 0.0 to 10.0 mm. The mean, variance, correlation coefficient, and probability density functions of the measured data were compared with a wrinkled laminar flame model.

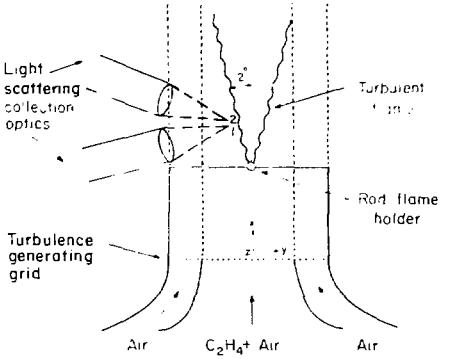

Figure 1. Schematic of the experimental apparatus for two-point Rayleigh scattering measurements. (XBL 823-8761)

According to this model, the turbulent flame brush consists of a thin laminar reaction front that fluctuates in shape and location. Figure 2 shows the coordinate system used to describe the motion and the density profile ρ of the reaction front in one spatial dimension. The y axis is fixed in the laboratory frame with $y = 0$ at the center of the turbulent flame brush. The moving ξ axis is attached to the instantaneous flame, with $\xi = 0$ fixed at the center. On the vertical axis, ζ indicates either the density ρ or the probability density function Q. The mean density $\overline{\rho}(y)$, the instantaneous density $\rho(y)$, the pdf of the instantaneous flame $Q(y)$, and the unburned (ρ_u) and burned (ρ_b) densities are also shown.

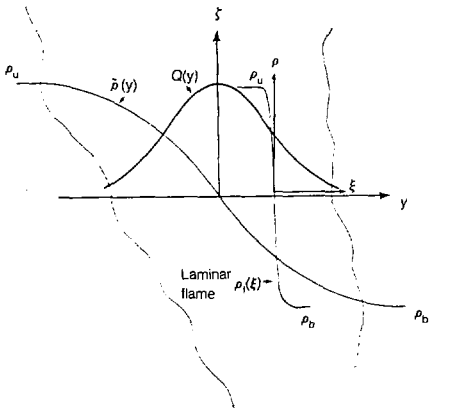

Figure 2. Coordinate system of the wrinkled laminar flame model with moving ξ axis attached to the center of the laminar reaction front and the stationary y axis fixed to the center of the turbulent flame brush. (XBL 841-375)

An analytic expression for obtaining $Q(y)$ from the mean turbulent flame profile can be found if a thin reaction front is assumed, i.e., the laminar flame thickness δ_f is much less than the turbulent flame brush thickness. In this case, there are only burned or unburned states within the flame, and the probability of finding burned gas at the point y will be given by

$$p_b(y) = \int_{-\infty}^{y} Q(y')dy' . \qquad (1)$$

The mean density at point y is then given by

$$\overline{\rho}(y) = \rho_u p_u(y) + \rho_b p_b(y)$$

$$= \rho_u - (\rho_u - \rho_b)p_b(y), \qquad (2)$$

since $p_u(y) = 1 - p_b(y)$. By differentiating Eq. (2) with respect to y, $Q(y)$ may be found:

$$Q(y) = -\left[\rho_u/(\rho_u - \rho_b)\right](d/dy)\left[\overline{\rho}(y)/\rho_u\right] \qquad (3)$$

From Eq. (3), $Q(y)$, the probability that the flame center is located at y, can be found from the measured $\overline{\rho}(y)$. The instantaneous flame profile $\rho_f(\xi)$ is assumed to be the same as the laminar flame profile and is obtained directly by Rayleigh scattering measurements of a laminar flame at the same equivalence ratio.

Equation (2) for the mean density can be generalized to include the effect of a finite instantaneous flame thickness, and equations for the variance, correlation coefficient at two separated points, and the pdf of the density can be found.

In Fig. 3, the mean flame density profile $\overline{\rho}(y)$ and the pdf of the reaction front $Q(y)$ as calculated from Eq. (3), are shown. A two-point Rayleigh method was also used to directly measure $Q(y)$ and is shown by the circles and the dashed line through them. There is good agreement with the result derived from Eq. (3). The directly measured $Q(y)$ was determined by measuring the fraction of the

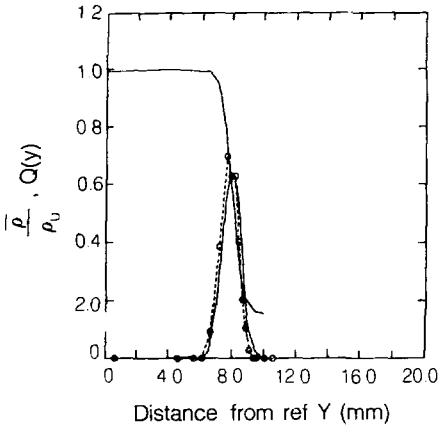

Figure 3. Measured mean density profile $Q(y)$ and measured (solid line) and calculated (points and dashed line) probability density function of the reaction front position inside the flame brush at 20 mm above the flameholder. (XBL 841-376A)

time that the front was found between two measurement points, as a function of the location of the two measurement points across the flame brush. The separation between the sampling points was 1.2 mm, while the laminar flame thickness was about 1.0 mm. Similar results were obtained for other stations and flame conditions.

Figure 3 shows good agreement between the two methods for determining $Q(y)$. Even better agreement was found for the stations further away from the flameholder where the turbulent flame brush is thicker; at these more remote points, the thin instantaneous flame approximation made in deriving Eq. (3) is more fully satisfied.

Good agreement with the model predictions is also obtained for the two-point correlation coefficient, as indicated in Fig. 4. The data are plotted as a function of distance δ between the two sample points, with one of the points always kept at the center of the turbulent flame.

The experimental and predicted values of the density pdf are shown in Fig. 5 for the center of the flame brush at different axial locations. The experimental measurements include photomultiplier noise, and thus are somewhat different from the model predictions, which did not include noise.

In all cases, the model predictions are in relatively good agreement with the measured intermediate state densities. In particular, the decrease in the intermediate states with distance from the flameholder predicted by the model is in agreement with the experimental measurements. This decrease in the intermediate states at distances further away from the flameholder is due to the increase in the flame brush thickness, while the laminar flame thickness remains constant, which decreases the probability that the measurement point will fall within the laminar flame region. It is clear that the finite instantaneous flame thickness is responsible for the intermediate-state density. In these experiments,

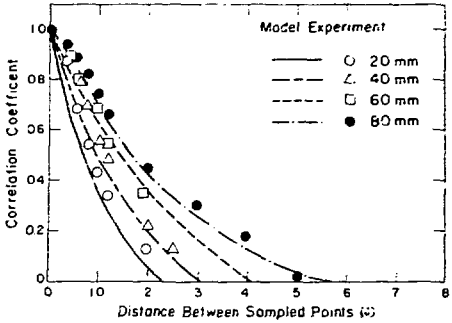

Figure 4. Measured and calculated correlation coefficient of the density fluctuations at two points separated by δ, with one of the points fixed at the center of the flame brush, plotted against δ. (XBL 841-378A)

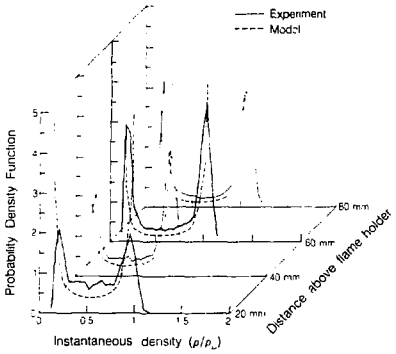

Figure 5. Measured and calculated density pdf (probability density function) for the center of flame 1 at different axial locations above the flameholder. (XBL 8401-6751)

both the spatial resolution and the time response of the measurement technique were adequate to call for, at most, a small correction.

PLANNED ACTIVITIES FOR FY 1984

The two-point Rayleigh data will be further analyzed and compared with other available models. The density fluctuations along a line (256 points along a 10-mm line) will be measured using a newly developed diagnostic technique called LARS, Linear Array for Rayleigh Scattering. This system will have a maximum 10-kHz line-sampling rate for the linear array and will produce a computer-displayed space-time image of the density fluctuations.

REFERENCES

1. Namazian, M., Talbot, L. and Robben, F. (1983), "Density Fluctuations in Premixed Turbulent Flames," submitted to Twentieth Symposium (International) on Combustion to be held at the University of Michigan, August 1984; LBL-17466.
2. Bill, R.G., Jr., *et al.* (1981), "Flame Propagation in Grid-Induced Turbulence," *Combust. Flame 43*, p. 229.
3. Bill, R.G., Jr., Namer, I., Talbot, L. and Robben, F. (1982), "Density Fluctuations of Flames in Grid-Induced Turbulence," *Combust. Flame 44*, p. 277.
4. Namazian, M., Talbot, L., Robben, F., and Cheng, R.K., (1983), "Two-point Rayleigh Scattering Measurements in a V-Shaped Turbulent Flame," in *Nineteenth Symposium (International) on Combustion*, p. 487, The Combustion Institute, Pittsburgh, PA.

Theoretical Studies of Unimolecular and Bimolecular Combustion Reactions*

N.J. Brown, J.A. Miller,† and O.M. Rashed

The radical species HO_2 plays an important role in the oxidation of all hydrocarbons. We have investigated the high-pressure-limit unimolecular dissociation of HO_2 using a molecular dynamics approach. Thermal unimolecular dissociation and the reverse recombination reaction in the gas phase represent an important class of elementary processes in complex systems, particularly combustion. Recombination reactions typically are the most important sources of heat in flames, and the dissociation of weakly bonded free radicals provides important mole-number (i.e., number of moles per unit mass) increases in combustion systems. Such mole-number increases typically accelerate the oxidation process either by satisfying a thermodynamic requirement or by feeding chain-branching reactions, or both. For these reasons, it is desirable to understand this class of reactions. Our current research has been concerned with unimolecular reactions in the low pressure limit where collisional energy transfer to and from the dissociating molecule determines the rate coefficient.

Another radical species which plays an important role in hydrocarbon oxidation schemes is OH. We are investigating the bimolecular reaction between OH and H_2, which is largely responsible for the formation of H_2O in combustion systems and which also makes significant contributions to the heat release in combustion. It is a radical-shuffling reaction, since it is a reaction between a radical and stable species that produces a different radical and stable species.

ACCOMPLISHMENTS DURING FY 1983

A collaborative study with Dr. J.A. Miller on the low-pressure-limit unimolecular dissociation of HO_2 has been completed. A paper[1] describing this work has been submitted for publication. In this study, we investigated the properties of He-HO_2 collisions in which the HO_2 is excited to energies near, but below, the dissociation limit. We have used a molecular dynamics approach with the statistical sampling of the phase space treated by orthant sampling and Monte Carlo techniques, described by us in an earlier paper.[2] In a master-equation formulation of the dissociation process, the natural independent parameters are the two good constants of the motion of the

*This work was supported by the Director, Office of Basic Energy Sciences, Chemical Sciences Division of the U.S. Department of Energy under Contract No. DE-AC03-76SF00098.

†Combustion Research Facility, Sandia National Laboratories, Livermore, CA.

both the spatial resolution and the time response of the measurement technique were adequate to call for, at most, a small correction.

PLANNED ACTIVITIES FOR FY 1984

The two-point Rayleigh data will be further analyzed and compared with other available models. The density fluctuations along a line (256 points along a 10-mm line) will be measured using a newly developed diagnostic technique called LARS, Linear Array for Rayleigh Scattering. This system will have a maximum 10-kHz line-sampling rate for the linear array and will produce a computer-displayed space-time image of the density fluctuations.

REFERENCES

1. Namazian, M., Talbot, L. and Robben, F. (1983), "Density Fluctuations in Premixed Turbulent Flames," submitted to Twentieth Symposium (International) on Combustion to be held at the University of Michigan, August 1984; LBL-17466.
2. Bill, R.G., Jr., *et al.* (1981), "Flame Propagation in Grid-Induced Turbulence," *Combust. Flame 43*, p. 229.
3. Bill, R.G., Jr., Namer, I., Talbot, L. and Robben, F. (1982), "Density Fluctuations of Flames in Grid-Induced Turbulence," *Combust. Flame 44*, p. 277.
4. Namazian, M., Talbot, L., Robben, F., and Cheng, R.K., (1983), "Two-point Rayleigh Scattering Measurements in a V-Shaped Turbulent Flame," in *Nineteenth Symposium (International) on Combustion*, p. 487, The Combustion Institute, Pittsburgh, PA.

Theoretical Studies of Unimolecular and Bimolecular Combustion Reactions*

N.J. Brown, J.A. Miller,† and O.M. Rashed

The radical species HO_2 plays an important role in the oxidation of all hydrocarbons. We have investigated the high-pressure-limit unimolecular dissociation of HO_2 using a molecular dynamics approach. Thermal unimolecular dissociation and the reverse recombination reaction in the gas phase represent an important class of elementary processes in complex systems, particularly combustion. Recombination reactions typically are the most important sources of heat in flames, and the dissociation of weakly bonded free radicals provides important mole-number (i.e., number of moles per unit mass) increases in combustion systems. Such mole-number increases typically accelerate the oxidation process either by satisfying a thermodynamic requirement or by feeding chain-branching reactions, or both. For these reasons, it is desirable to understand this class of reactions. Our current research has been concerned with unimolecular reactions in the low pressure limit where collisional energy transfer to and from the dissociating molecule determines the rate coefficient.

Another radical species which plays an important role in hydrocarbon oxidation schemes is OH. We are investigating the bimolecular reaction between OH and H_2, which is largely responsible for the formation of H_2O in combustion systems and which also makes significant contributions to the heat release in combustion. It is a radical-shuffling reaction, since it is a reaction between a radical and stable species that produces a different radical and stable species.

ACCOMPLISHMENTS DURING FY 1983

A collaborative study with Dr. J.A. Miller on the low-pressure-limit unimolecular dissociation of HO_2 has been completed. A paper[1] describing this work has been submitted for publication. In this study, we investigated the properties of He-HO_2 collisions in which the HO_2 is excited to energies near, but below, the dissociation limit. We have used a molecular dynamics approach with the statistical sampling of the phase space treated by orthant sampling and Monte Carlo techniques, described by us in an earlier paper.[2] In a master-equation formulation of the dissociation process, the natural independent parameters are the two good constants of the motion of the

*This work was supported by the Director, Office of Basic Energy Sciences, Chemical Sciences Division of the U.S. Department of Energy under Contract No. DE-AC03-76SF00098.

†Combustion Research Facility, Sandia National Laboratories, Livermore, CA.

in the average properties of the vibrational energy transfer for the various ensembles considered are consequences of changes in the high-energy exponentials, i.e., in the tails of the distributions. We have also determined total vibrational energy transfer cross sections by removing a singularity in the differential cross sections for near-zero energy transfer. The total cross sections are weak functions of the initial molecular energy, molecular angular momentum and heat-bath temperature, and are somewhat larger than Lennard-Jones cross sections.

We have made considerable progress on our molecular dynamics study of the H2 + OH → H_2O + H reaction. In this study, we are using the analytical fit of Schatz and Elgersman[4] of the Walsh-Dunning[5] potential energy surface for this system. We discovered spurious wells in the asymptotic region of this surface which were giving rise to anomalous long-lived trajectories at low values of the translational energy. The potential energy surface was modified by using a cubic spline function and a Morse function with the proper asymptotic behavior to remove the spurious wells at large internuclear separations while retaining the favorable description at short distances. A plot of potential energy as a function of distance between the center of mass of the H_2 and OH is shown for a fixed geometry for the old (upper trace) and new (lower trace) surface in Fig. 3.

The objective of this study is to determine the effect of the initial reactant energy distribution on reactivity and energy transfer characteristics. Preliminary results of trajectory calculations reveal that reactivity increases with translational energy, as shown in Fig. 4. Reactivity is also much more dependent on the initial rotational energy of OH than of H_2.

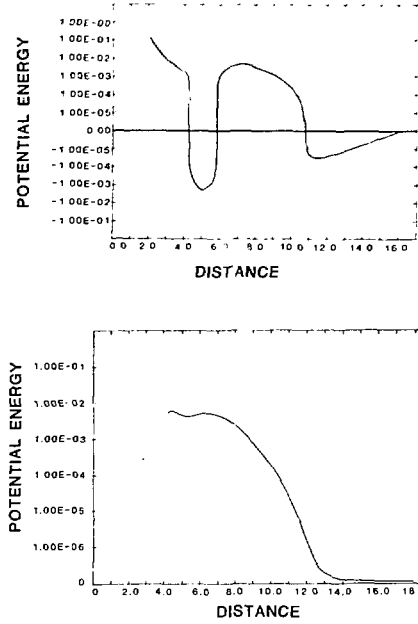

Figure 3. Potential energy in hartrees of the H_2/OH system as a function of the distance between the center of mass of the two molecules (in atomic units) for a fixed geometry. (XBL 842-823)

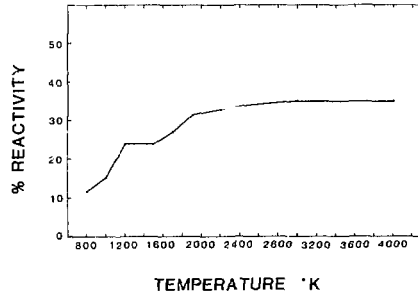

Figure 4. Reaction probability for H_2 + OH → H_2O + H as a function of translational temperature in Kelvins. (XBL 842-824)

PLANNED ACTIVITIES FOR FY 1984

Extensive calculations will be performed for the H_2/OH system. Results will be analyzed in terms of reactivity and energy transfer characteristics with special attention given to the effect of reagent rotation. New work will be initiated on a study of the high-pressure-limit unimolecular kinetics of three- and four-atom systems. Ignition chemistry will be investigated using molecular-beam mass spectroscopy. The initial effort in our ignition studies will focus on combustion chemistry of the methane/oxygen system initiated by flash photolysis.

REFERENCES

1. Miller, J.A. and Brown, N.J. (1982). "The Dynamics of Unimolecular Dissociation of HO_2: Phase Space Sampling, Microcanonical Rate Coefficients and Rotational Effects." *J. Phys. Chem. 86*, p. 772.
2. Brown, N.J. and Miller, J.A. (1983). "Collisional Energy Transfer in the Low Pressure Limit Unimolecular Dissociation of HO_2." accepted for publication. *J. Chem. Phys.*
3. Melius, C.F. and Blint, R. J. (1979). *J. Chem. Phys. Lett. 64*, p. 183.
4. Schatz, G.C. and Elgersman, H. (1981). *Chem. Phys. Lett. 73*, p. 21.
5. Walsh, S.P. and Dunning, T.H. (1980). *J. Chem. Phys. 72*, p. 1303.

Measurement of Sulfur Dioxide in the Post-Combustion Environment*

D. Lucas and N.J. Brown

Our research is directed toward the development and characterization of techniques to quantify pollutant emissions from combustion systems. Current emphasis is placed upon the measurement of sulfur dioxide, thought to be the primary combustion-generated pollutant responsible for acid deposition.

Sulfur is present in gaseous fuels, fuel oil, and coal. Although the amount of sulfur in gaseous fuels is quite low, the sulfur content in heavier oils ranges from 0.5 to 5%, while in coal, sulfur can account for up to 10% of the mass. The kinetic mechanisms of sulfur-containing compounds in combustion are not well understood. Concentrations of intermediate species during various stages of the combustion process have not been determined, and the rates of many elementary reactions involved in the combustion of sulfur-containing compounds have not been measured. Measurements of the concentrations of the products of combustion of fuels with a known sulfur content indicate that the principal sulfur containing product is sulfur dioxide.

Sulfur dioxide is emitted to the atmosphere with other products of combustion and is a sulfate precursor. If the relationship between stack emissions and acid deposition is to be fully understood, it is crucial that sulfur dioxide concentrations be measured reliably under exhaust-stack conditions. Techniques for accomplishing this have been investigated in our most recent research.

*This work was supported by the Director, Office of Energy Research, Office of Health and Environmental Research, Physical and Technological Research of the U.S. Department of Energy under Contract No. DE-AC03-76SF00098.

ACCOMPLISHMENTS DURING FY 1983

In-Situ Measurements of Sulfur Dioxide

Sulfur dioxide has been measured in a high-temperature combustion environment by ultraviolet absorption spectroscopy and by Tunable Atomic Line Molecular Spectroscopy (TALMS).[1] The TALMS technique was pioneered at LBL by Dr. T. Hadeishi and his co-workers, who used it to measure SO_2 under ambient conditions.[2] The TALMS technique has been used by Cuellar and Brown[3-5] and by Brown *et al.*[6] to measure diatomic species in combustion environments.

In this study, sulfur dioxide is measured in cells heated to a fixed temperature and in the post-flame region of a flat flame burner using stoichiometric and lean methane/air mixtures doped with SO_2. The post-flame region of the atmospheric methane/air flame was shown to have negligible temperature and concentration gradients and is thus ideal for optical measurements.

TALMS is an *in situ*, line-of-sight technique that uses a Zeeman-tuned atomic emission lamp as the light source. In these experiments, the Zn line at 213.8 nm ($^1S_0$ $^1P_1$ transition) is used with the light parallel to the magnetic field. Detection of SO_2 is accomplished by magnetically tuning one of the Zeeman components into resonance with a specific absorption in SO_2 while using the other component as the reference signal. The two components are very close in frequency (20 GHz), but differ in polarization, with the $\Delta M = +1$ transition right circularly polarized, and the $\Delta M = -1$ transition left circularly polarized. Both beams traverse an identical optical path, thus permitting good correction of the signal in highly scattering or absorbing systems, such as those encountered in flames and other combustion systems. The high selectivity of the technique greatly reduces the possibility of interference by

other molecules that absorb in the same spectral region.

Due to the complexity of the ultraviolet absorption spectrum of SO_2 in the 200.0 to 220.0 nm region, it is not possible to identify the particular transition responsible for the TALMS signal. The dependence of signal strength on magnetic field is shown in Fig. 1. The maximum TALMS signal occurs at a magnetic field strength of 14.5 kG, and this value is used for all subsequent measurements. Data obtained at 1500 K show the same dependence of signal strength on magnetic field as that obtained at 300 K, confirming that the same transition is measured in the flame system as under ambient conditions.

The sensitivity of the TALMS technique varies with the temperature of the sample. For a 7-cm path length at 1 atmosphere, the mininum detectable concentration is 40 ppm at 300 K, and 2000 ppm at 1500 K. Density differences due to combustion reduce the sensitivity by a factor of 5, and broadening of the absorption features at the higher temperatures further reduces this sensitivity by an additional order of magnitude. The ultraviolet absorption spectrum of SO_2, measured as a function of temperature in the 300 to 1500 K range, is shown in Fig. 2. The discrete absorption features gradually broaden as the temperature increases, and the underlying continuum becomes even more absorbing. This broadening is largely due to redistribution of the rotational level populations at the elevated temperatures, with the result that fewer molecules are in the particular state probed by the Zn line.

The TALMS signal is linear with SO_2 concentrations below 20,000 ppm, while the absorbance at approximately the same wavelength is linear at concentrations as high as 30,000 ppm. This indicates that the fall-off in the TALMS signal is not attributable to self-absorption or deviations from Beer's law, but is inherent to the TALMS technique. The nonlinear region can be avoided by the proper choice of path length. The range of concentrations that can be measured by the TALMS technique make it an attractive method for measuring SO_2 at utility sites where emission levels must be monitored.

Fluorescence Measurements of Sulfur Dioxide

Another method for measuring SO_2 uses pulsed fluorescence in the 190–230 nm region. In combustion exhausts, with high concentrations of combustion products, the signal from such an instrument must be corrected for the effects of third body quenching of the SO_2 fluorescence. These effects are

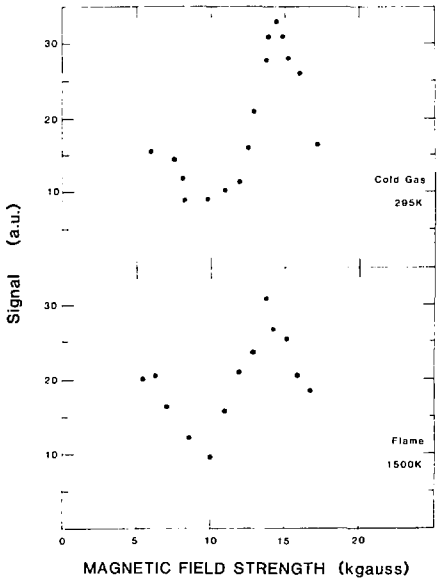

Figure 1. The SO_2 TALMS signal as a function of magnetic field. (XBL 83?-11799)

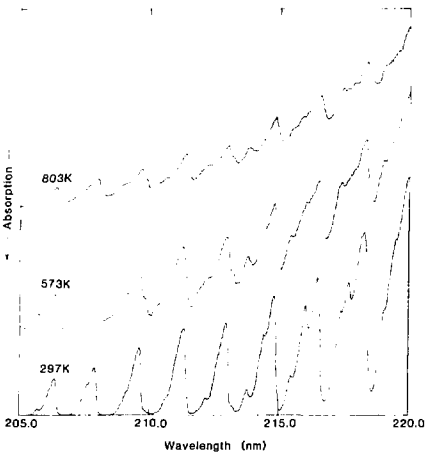

Figure 2 Absorption spectra of SO_2 in the 205 to 220 nm region as a function of temperature. (XBL 839-11803)

being measured in a popular commercial device, a Thermo Electron Model 40, by metering known concentrations of the various gases into a mixture of SO_2 in nitrogen. When the SO_2 concentration is low and the optical path relatively short, the signal S obtained in the presence of the third body relative to the unperturbed signal S_o is

$$S/S_o = 1/(1 + \Phi M_i)$$

where Φ is the Stern-Volmer quenching coefficient and M_i is the mole fraction of the third-body species.

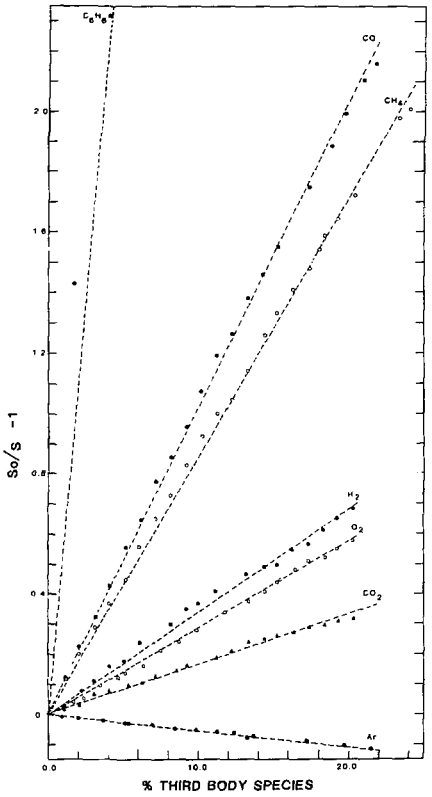

Figure 3. Relative quenching of SO_2 by combustion products. (XBL 8312-7532)

A plot of $S_o/S - 1$ as a function of the third-body mole fraction at a constant SO_2 concentration should yield a straight line with a slope of Φ. Such plots for species of interest in combustion are shown in Fig. 3. It should be noted that rich combustion, where the concentrations of CO and unburned hydrocarbons may be significant, has the largest quenching effects.

PLANNED ACTIVITIES FOR FY 1984

Research concerned with the measurement of SO_2 in the post-combustion environment will be completed. Research concerned with the measurement of NO using the TALMS techniques in methane/air flames of varying stoichiometry will also be completed.

REFERENCES

1. Lucas, D., and Brown, N.J. (1983), "Optical Measurement of SO_2 in Combustion Environments," presented at the Oak Ridge National Laboratory–Department of Energy Conference on Analytical Chemistry in Energy Technology, Knoxville, TN, October 11–13, 1983; LBL-16741.
2. Koizumi, H., Hadeishi, T., and McLaughlin, R. (1979), "Detection of Small Molecules by Magnetically Tuned Frequency-Modulated Atomic Line Sources," *Appl. Phys. Lett. 34* (6), p. 382.
3. Cuellar, E., and Brown, N.J. (1981), "Combustion Diagnostics by Tunable Line Molecular Spectroscopy," in *First Specialists Meeting (International) of the Combustion Institute, Bordeaux, France*, p. 545; LBL-12127.
4. Cuellar, E., and Brown, N.J. (1982), "Detection of S_2 by Magnetic Tuning of a Chromium(I) Atomic Emission Line," *J. Phys. Chem. 86* (11), p. 1966.
5. Cuellar, E., and Brown, N.J. (1983), "The Measurement of NO in Methane/Air Flames by Tunable Atomic Line Molecular Spectroscopy," accepted for publication in *AIAA, Progress in Aeronautics and Astronautics*; LBL-16468.
6. Brown, N.J., Cuellar, E., and Lucas, D. (1983), "Measurement of Nitrogenous and Sulfurous Combustion Emissions," in *Advanced Techniques in Synthetic Fuels Analysis*, C.W. Wright, W.C. Weimor, and W.D. Felix, Eds., Technical Information Center, U.S. Department of Energy, Oak Ridge, TN; LBL-14366.

Combustion Characteristics of Unvented Space Heaters*

T. Lionel and N.J. Brown

The use of unvented combustion heaters as home heating devices has increased dramatically in the last few years. There are several reasons for this upsurge: these heaters can be purchased at a relatively low cost, they are portable, and they are quite efficient, thus offering some distinct advantages over central heating home furnaces. However, there are two major problems associated with the use of unvented combustion heaters, namely, fire safety and the direct emission of combustion products into the room of origin.

The kerosene-burning combustion heater is the most popular type commercially available. It is currently anticipated that by 1985 kerosene fuel consumption will increase to 10% of the total amount of oil used for space heating, largely as a measure to achieve energy conservation. Since kerosene heaters mix the hot products of combustion directly with room air, they have high thermal efficiencies. Moreover, because they can be used for localized space heating, kerosene heaters, compared to central heating systems, offer residential dwellers a rather substantial decrease in home heating expenses.

Emissions of CO, NO, SO_2, CO_2, CH_2O, and particulates have been detected in environmental chamber studies of the heaters.[1-3] Emissions of CO, CH_2O, gaseous hydrocarbons, and particulates are all indications of incomplete combustion. These emissions could be reduced by enhancing the completeness of combustion, which would also improve the overall efficiency.

The purpose of this research is to gain an understanding of the combustion associated with unvented kerosene heaters, which will allow us to modify the combustion process in order to achieve an optimum conservation of energy. An understanding of the combustion of wick-supported kerosene burning with air entrainment accomplished through free convection is being emphasized. A number of diagnostics useful in assessing the combustion characteristics of unvented kerosene heaters and other direct-combustion devices have been developed. These techniques will be used to assess the effect of changing various experimental parameters (e.g., fuel dispersion, mixing characteristics, and ventilation) on the overall combustion characteristics. Concentration and temperature profiles, heat release rates, and thermal losses will be monitored under a host of experimental conditions to ascertain conditions optimizing the combustion process.

*This work was supported by the Assistant Secretary of Conservation Renewable Energy, Office of Energy Conservation Technology of the U.S. Department of Energy under Contract No. DE-AC03-76SF00098.

ACCOMPLISHMENTS DURING FY 1983

Major effort has been devoted to the preparation of an experimental apparatus to monitor the combustion characteristics of prototype kerosene heaters. There are two main tasks in meeting this objective. The first is associated with the construction of an exhaust and sampling manifold which can be interfaced with the burner. The second task involves setup, calibration, and interfacing of analytical instrumentation to the sampling manifold. The experimental apparatus is shown schematically in Fig. 1.

Oxides of nitrogen are measured with a chemiluminescence analyzer which has been calibrated and successfully interfaced. Oxygen, nitrogen, and gaseous species containing carbon are measured with a programmable gas chromatograph that has a column-switching capability. A fluorescent SO_2 detector has been calibrated and will be used to measure SO_2 concentrations in the heater exhaust. Sample extraction is accomplished with quartz microprobes, which are connected to the instruments with heated Teflon lines. Additional diagnostic information is obtained from a fine particulate collection filter and a thermocouple probe. Fuel consumption is measured gravimetrically with a triple-beam balance. Fuel uniformity is important throughout these experiments, and to assure this, fuel was purchased in large quantities. This kerosene fuel (Union 76 K-1) was analyzed with mass spectroscopy to determine its elemental composition; in addition to a sulfur content of 0.04% sulfur by weight, it had the kerosene carbon-hydrogen ratio of 6.38.

Preliminary results of our characterization studies indicate that burning in the radiant-type kerosene heaters occurs between two concentric perforated metal cylinders that entrain air flowing through the center of the heater. The results of temperature mapping are shown in Fig. 2. Temperature and exhaust composition measurements indicate a great lack of uniformity along a radial profile due to dilution by the central air column. Neither CO_2 or CO, nor significant concentrations of the nitrogen oxides are found in the center section in or above

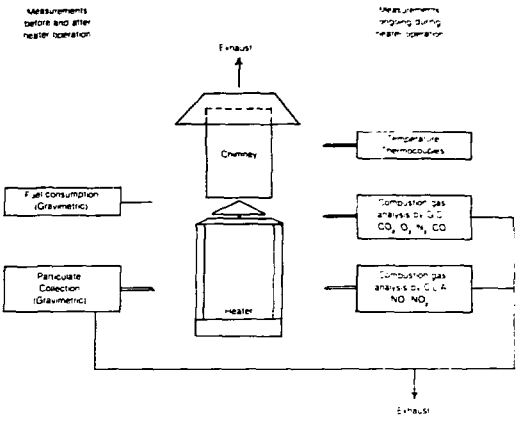

Figure 1. Heater testing apparatus. (XBL 841-413)

the heater. However, in the exhaust flow and directly above the wick, NO is increased fivefold and CO by two orders of magnitude. Changes in the concentrations of CO and O_2 are inversely proportional when measured above the wick. A large amount of particulates is produced, and care must be taken to minimize their effect on the sample measurement.

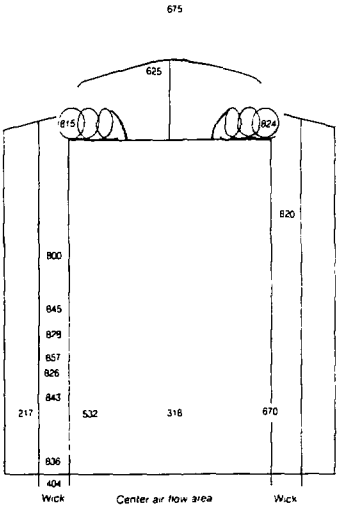

Figure 2. Kerosene heater temperature profile (°C). (XBL 841-412)

Experiments are currently under way to characterize the combustion of two or more heaters as a function of fuel dispersion and air entrainment. Heat-release rates, composition profiles, and temperature profiles are measured. These studies will aid us in isolating important characteristics of kerosene burning that are deserving of further study. New diagnostics will be developed and connected as needed. A search of the relevant scientific literature has been accomplished; however, to keep it current will require an ongoing effort throughout the duration of the research.

PLANNED ACTIVITIES FOR FY 1984

Combustion characterization studies will continue. Initially, they will be concerned with investigating combustion in commercially available kerosene heaters and involve monitoring heat-release rates, products of combustion, and temperature as a function of fuel dispersion and air entrainment. Thereafter, the research will focus on isolating the characteristics of wick-supported kerosene burning which result in complete combustion, e.g., low concentrations of CO, gaseous hydrocarbons, and particulates. Fuel dispersion will be investigated by examining the effects of wick material, wick length, wick cross-sectional area, and wick aging. Air entrain-

ment under conditions of free convection will be investigated for the purposes of improving fuel/air mixing and extending residence times in the combustion section to achieve complete burnout of carbon containing species.

A series of experiments with commercially available catalysts is planned with the objective of using the catalysts to reduce exhaust concentrations of NO and to enhance the completeness of combustion. There are potential problems associated with the use of catalysts because of the sulfur content of the fuel. Sulfur is a notorious catalyst poisoner, and this work will thus be dependent upon the results of a review of commercially available low cost catalytic materials. When the need arises, new gas-phase diagnostics will be developed in our characterization studies. Research associated with the investigation of venting configurations for the heaters will be initiated late in the grant year. These studies will be undertaken to determine the reliability of venting and its effect on overall efficiency. New venting configurations will be designed and investigated for effectiveness and heat losses.

REFERENCES

1. Traynor, G.W., *et al.* (1983), "Pollutant Emissions from Portable Kerosene-Fired Space Heaters," *Environ. Sci. Technol. 17*, p. 369.
2. Traynor, G.W., Apte, M.G., Dillworth, J.F., and Grimsrud, D.T. (1983), "Indoor Air Pollution from Portable Kerosene-Fired Space Heaters," presented at Hazardous Heat: A Symposium on the Health and Safety of Kerosene Heaters, Hempstead, NY, November 8, 1982; LBL-15612.
3. Leaderer, B.P., (1982), "Air Pollutant Emissions from Kerosene Space Heaters," *Science 218*, p. 1113.

Controlled Combustion*

N.J. Brown, T.D. Bui, M. Forsha, K. Hom, F.C. Hurlbut, D. Lucas, A.K. Oppenheim, T. Parker, R.B. Peterson, D.T. Pratt, R.F. Sawyer, and H.E. Stewart

The main objective of this program is to gain fundamental understanding of the chemical and physical processes that govern the evolution of exothermic energy in the course of combustion, as well as the effects of its deposition in the reacting medium. Basic problems encountered in this connection and the methodology adopted for their solution were described in last year's annual report.[1] The fundamental knowledge we seek is necessary for the development of controlled combustion systems. For power plant and internal combustion engine technologies, such systems offer the prospect of simultaneously maximizing thermal energy conversion efficiency, minimizing pollutant emissions, and optimizing tolerance to a wide variety of fuels. Currently, major emphasis is placed on revealing the life history of active radicals and the role they play in the development and sustenance of the exothermic process of combustion.

ACCOMPLISHMENTS DURING FY 1983

Over the past year, as before, the principal effort has been directed at investigating the ignition process. Our studies consisted of three phases:

(1) Experiments involving the use of the molecular-beam mass spectrometer we have developed for this purpose;
(2) development of analytical techniques for studying the thermochemistry of ignition; and
(3) experimental investigation of high-temperature liquid-fuel jet ignition.

Progress made in each of these phases is reported here in turn.

Molecular Beam Spectrometry

Significant progress has been made in understanding the effects of transient combustion events on molecular-beam sampling, in particular, the influence of beam overrun on the distribution of molecules arriving at the detector—a feature associated with the fact that, in the course of ignition, hotter, and thus faster, constituents of the beam are formed later than its colder, and thus slower, por-

*This work was supported by the Office of Energy Research, Basic Energy Sciences, Engineering, Mathematics, and Geosciences Division and the Office of Utilization Technology of the U.S. Department of Energy under Contract No. DE-AC03-76SF00098, by the National Science Foundation under Grant CPE-8115163, and by NASA-Lewis Research Center under Grant NAG 3-137.

tions. Experimental measurements have been made of molecular beams produced by photolysis of NO_2 in Ar and by flash-ignited mixtures of CH_4 and O_2, using a chopped time-of-flight (TOF) technique. These measurements yield data on time-resolved temperature profiles and information on the time resolution achievable in a combustion system.

Preliminary calculations concerned with TOF distribution in steady-state systems have shown that the ultimate time resolution in a molecular-beam system is not significantly affected by the high temperatures attained in the course of combustion events.[2] This is because the beam velocity increases when the source temperature rises, resulting in less time for spread in the distribution of molecules before they reach the detector. Accordingly, the experimental results we obtained indicate that the TOF data are not significantly affected by the Mach number—an important conclusion for combustion studies where the source conditions change rapidly.

A mixture of 0.08 CH_4, 0.15 O_2, 0.07 NO_2, and 0.70 Ar initially at 300 torr was ignited by two flash lamps discharging a total of 630 joules in ~120 μsec. Results obtained by chopping the resultant molecular beam at 1.6 kHz with a narrow slotted wheel are shown in Fig. 1(a); displayed there is the signal of mass 40, evidently due to argon in the sample. The upper trace was recorded in the course of photolysis, while the lower is the signal obtained from the same mixture at room temperature. The shift in the peak arrival time is a measure of the temperature of the sampled gas. Various flash-lamp trigger delays were used so that data taken at different times in the combustion process were recorded. The resulting temperature profile is shown in Fig. 1(b). The initial temperature rise is due to flash energy absorbed by the sample, while the subsequent increase is produced by combustion. Average pressure recorded simultaneously with the mass signal is presented in Fig. 1(c).

Experimental measurements are most clearly and comprehensively interpreted by expressing them in the form of an orthographic projection such as Fig. 2, which displays the results calculated for the combustion process of Fig. 1.[3] The abscissa and ordinate of the horizontal plane represent, respectively, the detector and source times. The vertical coordinate expresses the relative number of molecules arriving at the detector. The source temperature profile used in generating the figure, shown on the left vertical plane, is the same as that of Fig. 1. Displayed on the right vertical plane is a plot of peak arrival times for each TOF curve as a function of the detector time. The deviation of the slope of this

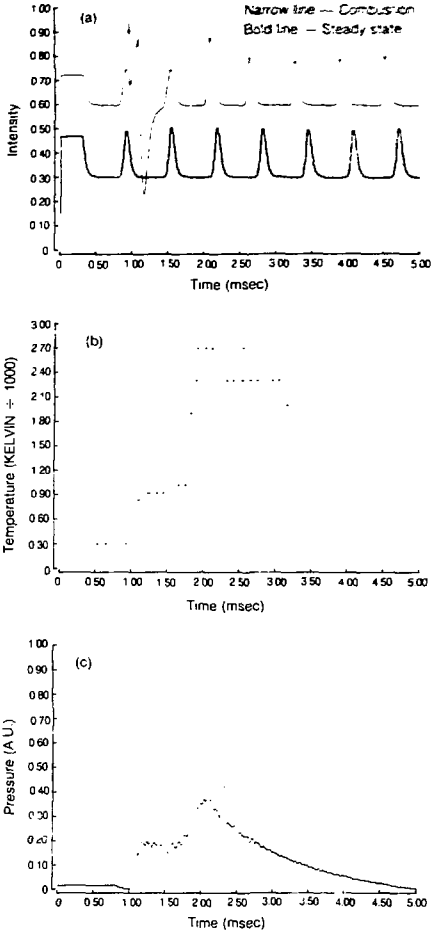

Figure 1. Results of mass spectroscopy of a molecular beam sampled in the course of combustion in a mixture of 0.08 CH_4, 0.15 O_2, 0.07 NO_2, and 0.70 Ar initially at 300 torr, ignited by two flash lamps discharging a total of 830 joules in ~120 μsec. (a) Argon signal measured during combustion under steady-state conditions (arrow denotes instant of flash lamp discharge). (b) Measured temperature profile for flash-ignited combustion. (c) Reaction-cell pressure measured in the course of combustion.

[(a) XBL 8312-4848; (b) XBL 8312-4850; (c) XBL 8312-4849]

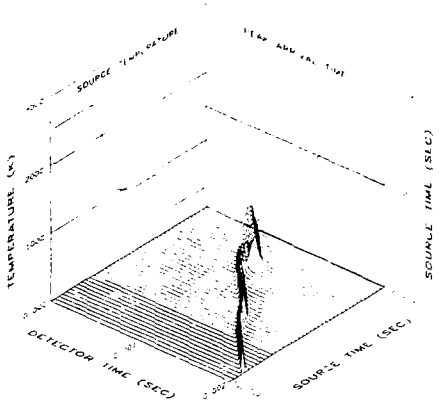

Figure 2. Beam overrun calculated on the basis of the temperature profile of Fig. 1. (XBL 8312-4847)

curve with respect to the diagonal manifests the effect of the overrun. A critical situation arises when this slope becomes infinite, indicating that adjacent portions of the beam arrive simultaneously at the detector. Negative slopes signify that the detector measurement is no longer a single-valued function of the time at which the molecules leave the source. It is evident that there is a certain amount of beam overrun present during both photolysis and combustion. However, it is not as severe in combustion as in photolysis because, immediately prior to ignition, the temperature is higher and its subsequent growth is slower. Thus, although the time-resolved mass measurements may be meaningless for photolysis, for combustion they can yield reliable data, provided that the effect of the overrun is properly taken into account.

Thermochemistry

Due principally to the efforts of Professor W.C. Gardiner of the University of Texas, with whom we have established a collaborative program of studies, as well as to worldwide interest in combustion chemistry, great strides were made last year in acquiring chemical kinetic rate data pertaining to the generation of intermediate species and active radicals occurring in the course of pyrolysis and oxidation of heavier hydrocarbon molecules—information of particular relevance to combustion of most commercial fuels.

In order to apply these data to any concrete problem, one must integrate the kinetic rate equations that describe the destruction and formation of all the chemical species participating in the reaction under study. As it is well known, these equations exhibit the awkward phenomenon of "stiffness"—a circumstance that has a perplexing effect upon any numerical technique used for their integration. Although a number of mathematical schemes have been devised for proper treatment of stiff equations, their utility is quite limited, primarily because most of them are not only implicit, but also multi-step in nature. Thus, the task of combining these equations with those describing the fluid mechanical aspects of the problem is, in most cases, awkward and difficult.

Having encountered these difficulties, it became imperative for us to face this issue head on. Our first step was to review the situation. This has been done in collaboration with Professor T.D. Bui of Concordia University, combined with a series of seminars delivered by Professor D.T. Pratt of the University of Washington. The outcome has been presented in reports[4,5] to be published in the *International Journal of Computational and Applied Mathematics*. This effort revealed a number of recently developed implicit methods that offer good promise for treating the integration of chemical kinetic rate equations in a manner much more compatible with numerical techniques used for the solution of the equations of fluid mechanics than the currently employed implicit, multi-step schemes.

At the same time, we have devised a novel method of approach, based on the fact that the kinetic rate equations are autonomous with respect to time. This allows the independent variable of time to be eliminated, thereby transforming the equations into the domain of dependent variables, the so-called phase space, and the solution is reduced to the task of determining integral curves in this space by a relatively straightforward procedure. We expect to avoid problems associated with stiffness by a judicious choice of parameters to be adopted as independent variables for numerical integration. The most important advantage of this technique is that it is fully compatible with numerical methods we developed recently for treating the fluid mechanical aspects of combustion, as described in an accompanying article.[6]

Jet Ignition

Our program of jet ignition studies was concerned at the outset primarily with the use of flame or plasma jets for initiating combustion in lean fuel-air mixtures. We then became involved, under the

support of a grant from the NASA–Lewis Research Center, in an investigation of the ignition of a high-temperature fuel spray in compressed air, as it occurs in a diesel engine.

Prime motivation for this work stems from the advent of the adiabatic diesel engine—a system that provides unique conditions for combustion. At the moment of injection, compressed air in this engine is at a thermodynamically supercritical state for the fuel, which concomitantly can be preheated by the high temperature of the cylinder walls. Ignition delay is thereby cut down drastically, reducing significantly the tendency to knock. By thus eliminating virtually the major criterion of fuel quality, the tolerance of the engine to a wide variety of fuels is significantly expanded. Moreover, under such circumstances the spray becomes a jet of vapor packets that lend themselves to deeper penetration and better mixing with air, thus enhancing the achievement of a more homogeneous combustion process than that occurring in the diffusion flame of a conventional diesel engine—a feature of great advantage in curbing production of particulates and pollutants.

Specifically, we are studying ignition of liquid fuel jets in air at thermodynamically supercritical conditions, using pure hydrocarbons, in particular n-dodecane and n-heptane—the major ingredients of diesel fuels—as test media. So far, our experiments have been carried out using a high-pressure bomb situated in a high-temperature furnace, both fitted with suitable windows for optical insight into the test space along its axis. Fuel was supplied by a conventional Roosa-Master injector actuated by an electronically controlled pump system, while adequate instrumentation was provided for time-resolved measurements of pressure and temperatures in various locations of the fuel and air system, including the tip of the injector as well as the combustion chamber, the motion of the injector pintle being concomitantly monitored by a displacement transducer. The results were recorded by a fully computerized data processing system we developed especially for this purpose.

On the basis of the experience thus gained, we designed a shock tube using a tailored interface technique, capable of furnishing proper conditions for tests of supercritical-fuel jet ignition with excellent accessibility for optical measurements. The construction of this apparatus is currently under way. The test time we expect to have available behind the reflected shock wave, at the supercritical state of 20 atm and 900 K, should be on the order of 20 msec. The test section, of about 4 inches square cross section, will be fitted with five 3.5-inch-diameter, 2-inch-thick window frames that can accommodate either quartz disks for optical techniques or opaque ceramic support for a heater-equipped fuel injector, as well as a pressure transducer. The most attractive aspect of this facility is that it lends itself to the application of laser tomographic techniques whose impressive potential as a diagnostic tool for combustion studies has been revealed over the last few years by a number of research laboratories.

PLANNED ACTIVITIES FOR FY 1984

The next objectives in each of the three phases of our research on controlled combustion are as follows:

(1) To modify the molecular-beam mass spectrometer by drastically changing its configuration from cross-axes to in-line; we expect this to enhance detection of species down to the range of 100 ppm, thus providing suitable means for measuring radical concentrations—the ultimate purpose of the apparatus.

(2) To continue work on the development of new techniques for the integration of chemical kinetic rate equations, in a manner fully compatible with the random-walk methods we have developed for numerical modeling of combustion systems.

(3) To build and instrument the shock-tube apparatus for experimental study of fluid-mechanical and thermodynamic features of jet ignition.

REFERENCES

1. *Energy and Environment Division Annual Report, FY 1982*, LBL-15300 (1983), p. 4–59.
2. Lucas, D., Peterson, R., Hurlbut, F.C., and Oppenheim, A.K. (1983), "Effects of Transient Combustion Phenomena on Molecular Beam Sampling," to be published in *J. Phys. Chem.*; LBL-15799.
3. Peterson, R., Lucas, D., Hurlbut, F.C., and Oppenheim, A.K. (1983), "Molecular Beam Overrun in Sampling of Transient Combustion Processes," to be published in *J. Phys. Chem.*; LBL-16713.
4. Bui, T.D. (1983), "A Study of Numerical Methods for Combustion Kinetics," *Int. J. Computat. Appl. Math.*, in press; LBL-16769.
5. Bui, T.D., Oppenheim, A.K., and Pratt, D.T. (1983), "Recent Advances in Methods for

Numerical Solution of O.D.E. Initial Value Problems," *Int. J. Computat. Appl. Math.*, in press; LBL-16943.

6. Ghoniem, A.F., Chorin, A.J., Hsiao, C.-C., and Oppenheim, A.K. (1984). "Fluid Mechanics of Combustion," this annual report.

Residual Fuel Combustion in Diesel Engines*

D.D. Brehob, F. Robben, D.J. Ruzicka,† and R.F. Sawyer

The quality of residual fuels available for marine and locomotive applications and for stationary power generation have become further degraded as a result of the energy crisis. Because of the increased demand for the higher quality distillate fuels, oil refiners have adjusted the distillate yield from crude oil by using more intensive refining techniques such as vacuum distillation, visbreaking, and fluidized catalytic cracking. The resulting residual fuels have poorer combustion quality and contain a higher loading of various impurities such as metallic compounds, unfilterable catalytic fines, and other impurities.

Two studies of residual fuels in diesel engines have been carried out. One was aimed at determining the fuel parameters that correlate with engine combustion performance so that ignition and combustion problems can be predicted based on a fuel analysis.[1] The other evaluated the potential for improvement in residual fuel combustion characteristics by using water emulsification.[2]

ACCOMPLISHMENTS DURING FY 1983

Correlation Study of Residual Fuel Combustion

Six residual fuels were evaluated in a small CFR (Coordinated Fuel Research) indirect-injection diesel engine. Although this engine is much smaller than commercial engines burning residual fuel, with suitable modifications to the test procedure, good advantage can be taken of the CFR's flexibility and its less expensive operating costs. The following parameters were measured to assess the performance of the fuels: cylinder pressure, thermal efficiency, ignition delay, torque, exhaust hydrocarbons, carbon monoxide, and particulate concentrations. Fuel line pressure and temperature, engine coolant temperature, and inlet air pressure and temperature were controlled and monitored.

The residual fuels were provided by the Chevron Research Company in Richmond, California. In addition to selecting samples representative of residual fuels from various crudes and refining processes, Chevron performed standard chemical analyses on these fuels. Complete specifications and descriptions of the fuels are given elsewhere.[1] The objective of this program was to determine the degree of correlation between engine performance and existing fuel parameters. A summary of the results appears in Table 1. Engine performance (mean effective pressure, thermal efficiency) and particulates correlated well with the Conradson carbon number. A lesser degree of correlation was observed with the asphaltene content of the fuels.

Water Emulsification of Residual Fuels

Transamerica Delaval, Inc. of Oakland, California conducted an evaluation of water-emulsified residual fuels for the Maritime Adminstration of the Department of Transportation. The fuels were tested in a six-cylinder, 450 RPM, turbocharged diesel engine that developed 2500 kW at full load. The DSR-46 engine is used for stationary power generation and marine applications. The fuel emulsions were prepared by pumping the heated residual fuel and water through a commercial emulsification unit, as shown in Fig. 1.

Delaval operated the engine, measured exhaust NO_x concentration and thermal efficiency, and performed a post-test wear and deposit analysis. LBL installed a dilution tunnel (schematic in Fig. 2) at the test site for filter collection of exhaust particulates. Two devices were used to analyze the filters for mass loading[3] and elemental composition[4] of the particulates.

The following parameters were investigated:

(a) Fuel: Distillate reference fuel and three residual fuels of different viscosity grades.

*This work was supported by the U.S. Department of Energy, through the LBL Director's Research Fund, under Contract No. DE-AC03-76SF00098.

†On leave from Central Institute for Industrial Research, Oslo, Norway.

Table 1. Combustion quality versus fuel properties.[a]

Engine performance parameters	Fuel Parameters					
	C/H	Aliphatics	Aromatics	Asphaltenes	Conradson carbon number	Asphaltenes + aromatics + polar compounds
Ignition delay	×××	××	×	×	×	×
Mean effective pressure[b]	×			×××	×××	××
Thermal efficiency	××			×	×	××
Emission: HC	×××			×	××	
CO	×××			×	×	
Particulate	×			×××	×××	

[a]Key: ××× — good correlation
×× — some correlation
× — poor correlation

[b]Mean effective pressure is proportional to engine power.

(b) Percent water in fuel: 0%, 4%, 8%, and 12%.
(c) Water droplet size: 2–5, 5–10, and 10–20 micrometer size ranges.
(d) Engine load: 50%, 75%, and 100% load.

The water emulsified fuels exhibited a statistically significant 10–15% reduction in NO_x emission and a trend toward lower thermal efficiency (1–2%) with 12% water addition. The reduction of NO_x is expected to be independent of the method of introducing the water into the combustion chamber. A decline in particulate loading is also expected as theory indicates that microexplosions[5] can occur in the fuel droplets, thereby enhancing atomization. However, no statistical differences in particulate mass were observed as a result of the water content or droplet size. The particulate measurements proved to be repeatable and were similar to results obtained with a different collection technique.

PLANNED ACTIVITIES FOR FY 1984

Further study of the combustion characteristics of residual fuels in a diesel engine is planned. High-speed movies will be taken of the combustion chamber in a special, single-cycle diesel test engine which has a square piston and transparent cylinder walls. These photographs will allow comparative studies of the atomization, ignition, and combustion of various residual diesel fuels to be carried out.

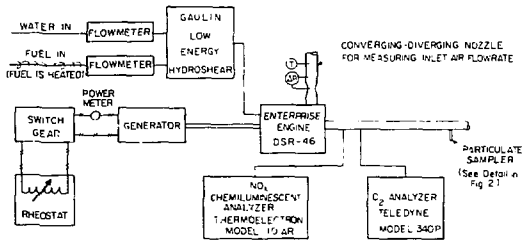

Figure 1. Schematic of test engine and associated measurement equipment. (XBL 829-6481)

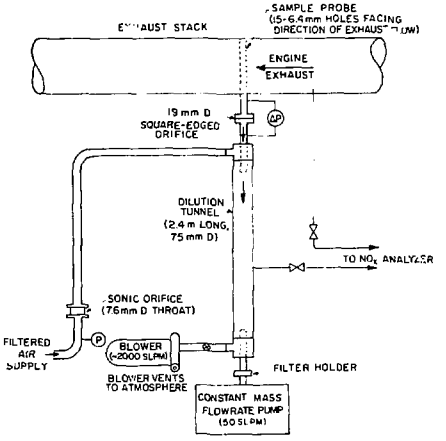

Figure 2. Schematic of diesel particulate sampler.
(XBL 829-5512)

REFERENCES

1. Ruzicka, D.J., Robben, F., and Sawyer, R.F. (1982), *Combustion of Residual Fuels in a CFR Diesel Engine*, LBL-17013.
2. Brehob, D.D., *et al.* (1983), "Performance of Water Emulsified Residual Fuels in a Medium-Speed Diesel," ASME Paper No. 83-*DGP-10*; *LBL-14987*.
3. Jaklevic, J.M., Gatti, R.C., Goulding, F.S., and Loo, B.W. (1981), "A beta-Gauge Method Applied to Aerosol Samples," *Environ. Sci. Techn. 15*, p. 680.
4. Jaklevic, J.M., Loo, B.W., and Goulding, F.S. (1977), "Photon Induced X-Ray Fluorescence Analysis Using an Energy Dispersive Detector and Dichotomous Sampler," in *X-Ray Fluorescence Analysis of Environmental Samples*, Chap. 1, p. 3, T.G. Dzubay, Ed., Ann Arbor Science, Ann Arbor, MI.
5. Dryer, F.L. (1977), "Water Addition to Practical Combustion System Concepts and Application," *Sixteenth Symposium (International) on Combustion*, p. 279, The Combustion Institute, Pittsburgh, PA.

Coal-Fueled Diesel Engines*

F. Robben, D. D. Brehob, N. Dickson, M. Namazian, A. Sarsten,† R. F. Sawyer,‡ and P. Sherman†

Diesel engines provide energy for a wide variety of applications in the United States. For railroad and marine transportation, diesels currently consume about 2.5% of the nation's oil supply. The potential for using diesel engines in the cogeneration of electrical power, using the normally wasted exhaust heat for industrial and commercial process steam, could involve as much as 10% of current oil consumption. Another 5% of oil consumption is consumed by high-speed diesels in trucks, farm, and construction equipment. A significant savings of oil would be made if a coal-based fuel replaced the oil used in these engines. A very promising coal-based fuel is a coal-water slurry suspension of finely pulverized coal. This results in the most efficient use of coal and preserves the advantages and safety of a liquid fuel. Though the small diesel engine applications are problematic, the larger engine uses are closer to feasibility.

To operate on coal-water slurry fuel, major changes in existing diesel engine design are necessary. The fuel injection and combustion systems must be completely redesigned. The sliding surfaces of the cylinder rings, pistons, and valves will be subject to greatly increased abrasive wear; these parts must be built with more wear-resistant materials, such as hard ceramics, and incorporate designs that minimize the deposition and accumulation of abrasive ash in critical areas. These combustion and materials problems are technologically sophisticated and require improved understanding of the underlying physical phenomena in order to develop the necessary ideas and designs.

Extensive research and development of coal-fueled diesel engines was carried out in Germany from 1930 to 1944.[1] This work achieved many

*This work was supported by the Assistant Secretary for Energy Technology, Heat Engine Section, U. S. Department of Energy under Contract No. DE-AC03-76SF00098.

†On leave from the Department of Mechanical Engineering, Norwegian Institute of Technology, Trondheim.

‡On leave from the Department of Aerospace Engineering, University of Michigan, Ann Arbor.

advances and demonstrated the practical operation of a number of prototype engines by different industries. The most advanced program, at I. Bruenner MFG, resulted in production plans for a smaller, high-speed engine. However, following World War II, the low cost of petroleum removed the economic incentive for its production, and no further significant development has been carried out until recently.

In the present project, which has just begun, experimental investigation of the injection and combustion of coal-water slurry in a special single-cycle diesel test engine is being carried out.

ACCOMPLISHMENTS DURING FY 1983

A review of the economic and technical issues related to diesel engines fueled by coal-water slurry has been prepared.[2] This review evaluated the early German development and discussed some technical ideas that could improve engine performance.

A special, one-cycle test engine has been modified for diesel operation and is being used for studies of coal-water slurry injection, ignition, and combustion. This engine, shown schematically in Fig. 1, has a 9-cm-square piston and two quartz cylinder walls so that high-speed movies and other optical measurements can be made of the entire combustion region. A fast-acting clutch-brake assembly operates the engine for only a few revolutions, and the injection pump uses a solenoid-actuated control so that only one injection stroke is obtained in a test sequence. Cylinder and injection pressures are recorded, and shadow photography is used to visualize the injection and combustion process.

The injection pump is operated with oil, and a small syringe fills the injection line with coal-water slurry before each measurement, as shown in Fig. 1. The present injector is a single orifice of approximately 0.38 mm, and no injector valve is used. Satisfactory operation of this injection system on the engine with diesel oil has been difficult to achieve, because of the unwanted introduction of air into the injection line after each injection cycle. Careful bleeding of the injection line has given reasonably good injection. On the other hand, the introduction and injection of coal water slurry has not been as difficult as anticipated, and satisfactory injection patterns have been achieved. Fig. 2 shows a high speed flash photograph of a coal-water slurry spray into atmospheric pressure air.

An electrically heated air reservoir allows the inlet air to the engine to be heated up to 250°C and pressurized up to 3 atm. By this means, the conditions in highly turbocharged engines can be simulated at a relatively low compression ratio. This gives a larger combustion chamber volume at top dead center so that the injected fuel spray is less likely to strike the piston.

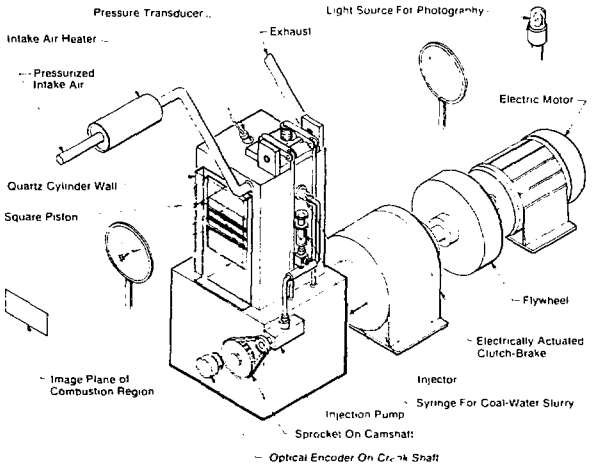

Figure 1. Single-cycle, square-piston diesel test engine. (XBL 841-8333)

Figure 2. An example of coal-water slurry injected into air at atmospheric pressure. The orifice diameter is 0.38 mm, injection pressure about 100 bar. (XBB 841-437)

The ignition and combustion of diesel No. 2 oil has been achieved at a compression ratio of 16:1 with about 2.0 atm intake air pressure and 20°C intake air temperature. Satisfactory injections of coal-water slurry into the engine has not yet been achieved.

PLANNED ACTIVITIES FOR FY 1984

The major aim of these experiments is to determine the conditions necessary to achieve ignition and combustion of a coal-water slurry. The ignition delay will be determined as a function of the temperature and pressure of the air in the combustion chamber, and as a function of the injection conditions and fuel parameters. The phenomenological behavior of the injection and combustion will be determined from high-speed movie photographs of the combustion chamber and from the pressure record. The experimental results will be compared with a computer model being developed.

The degree of agglomeration of the coal particles during combustion is a major factor in coal-water slurry operation, affecting both the rate of combustion and the abrasive wear caused by the particles. Particulate samples collected from the exhaust will be analyzed to assess the agglomeration, degree of combustion, and other morphological characteristics of the exhausted particulates.

An optical system for flash-illuminated microphotography of the spray during injection and combustion will be used to determine the spray particulate size, droplet breakup, water evaporation, and agglomeration of the coal particles. Spatial resolution of 5 μm should be attainable and would yield valuable information on injection and combustion phenomena.

We want to expand the research activity to a five-year program aimed at designing and constructing a laboratory coal-fueled diesel test engine. This would be divided into two major activities, combustion and materials wear, with a third, smaller component for technology assessment and review. As an example of a proposed combustion task, the injection of superheated coal-water slurry to enhance the atomization of the spray, through flash boiling of the water, and to accelerate ignition and combustion, would be explored. Practical injection and combustion techniques must be developed and tested; for instance, common rail injection systems with electronically controlled injection valves, high-turbulence pre-combustion chambers, and hot-wall combustion chambers. Suitable materials for the cylinder liners, piston rings, valves, and injectors must be found. Techniques for minimizing particulate deposition on critical wearing surfaces need to be found and evaluated. The use of highly cleaned coal as a means of reducing wear needs to be explored.

Coal-fueled diesel engines offer a technically feasible, long-range method of effectively using coal in heavy transportation and in stationary power. Railroad fuel consumption alone presently costs about $4 billion annually. An effective research program to further evaluate the technical and scientific issues underlying coal-fueled diesel engines is justified.

REFERENCES

1. Soehngen, E. E. (1976), *Development of Coal-Burning Diesel Engines in Germany*, Energy Research and Development Administration Report FE/WAPO/3387-1, Department of Energy, Washington, D.C.
2. Robben, F. (1983), *Coal-Fueled Diesel Engines*, SAE Paper No. 831747, Society of Automative Engineers, Warrendale, PA.

Lean Limit Combustion Under Reciprocating Engine Conditions*

R.F. Sawyer and D. Dunn-Rankin

Operation of homogeneous-charge, reciprocating internal combustion engines under lean conditions offers the possibility of improved efficiency, reduced emissions, and broadened fuel tolerance. Important fundamental processes impeding the development of such engines include ignition of lean mixtures, flame propagation, and quenching of combustion during expansion. Lean-limit combustion is being studied in a square-piston apparatus that allows the observation of combustion events under conditions simulating engine operation.

ACCOMPLISHMENTS DURING FY 1983

An experimental study of the combustion of lean, premixed gases in a square cross-section enclosure fitted with a reciprocating piston was conducted.[1] The compression-expansion (CE-1) facility is pneumatically driven and simulates the compression-expansion phase of an internal combustion operation (Fig. 1). Two borosilicate glass windows provide full optical access to the enclosure. A line igniter produces an approximate two-dimensional flame front. Flame location and shape are obtained from high-speed schlieren and shadowgraph motion pictures. Pressure measurements and piston location records are simultaneously acquired and computer-logged. Mass burning rate is calculated from flame location, piston location, and pressure.

The experiments concentrate on lean methane/air mixture behavior. Situations being investigated are (1) compression followed by combustion and (2) compression-expansion-combustion. Compression-combustion experiments investigate the effect of equivalence ratio and ignition time on combustion at pressures higher than atmospheric. A piston-generated "roll-up vortex" is observed from the movies. The mass burning rate is not noticeably affected by flame interaction with the "roll-up vortex." A typical flame propagation is shown in Fig. 2. As the mixture ratio becomes leaner and flame velocities decrease, the time to peak pressure increases, and the peak pressure decreases.

*This work was supported by the Office of Utilization Technology, Division of Transportation Programs of the U.S. Department of Energy under Contract No. DE-AC03-76SF00098.

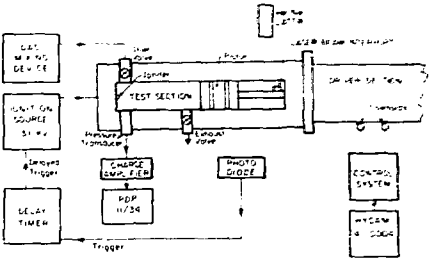

Figure 1. Schematic of experimental apparatus. (XBL 841-460)

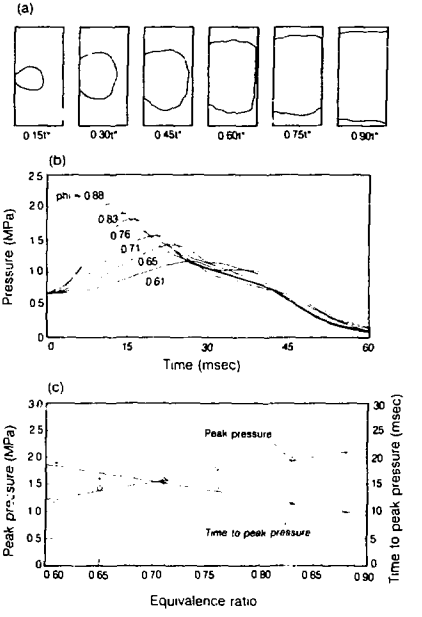

Figure 2. Effect of equivalence ratio ("phi") in compression-combustion. Compression time = 15 ms, ignition time = 80 ms. (a) Typical flame propagation; $t^* =$ total combustion time. (b) Chamber pressure for various equivalence ratios. (c) Peak pressure and time to peak pressure. (XBL 841-459)

Compression-expansion-combustion experiments explore the phenomenon of flame propagation during piston expansion. Three types of flame propagation are observed (Fig. 3). In Type 1, flames propagate rapidly enough to burn the mixture before the piston is fully expanded. In Type 2, flames begin to propagate as in Type 1, but the mass burning rate decreases as the chamber expands. And in Type 3, the flame is quenched during the expansion. Equivalence ratio is the most significant factor in determining flame propagation behavior. Piston-generated fluid motion does not play a major role in these experiments.

The quench process is of particular interest because it defines the lean limit for engine operation. The Type 3 flame cannot generate enough thermal energy during the expansion process to make up for the energy removed by the piston motion. Consequently, when the piston reaches the halfway point, the flame is quenched. The quenching process is likely to be due to bulk quench, as the adiabatic flame temperature of the unburned mixture is below 1600 K at quenching. This work is in agreement with earlier studies of quenching under laminar expansion-combustion without the initial compression.

PLANNED ACTIVITIES FOR FY 1984

An explanation of the flame shape in these experiments is sought. A constant-volume plexiglass combustion chamber, with the same dimensions as the CE-1 apparatus, has been constructed for laser Doppler measurements of combustion-induced flows

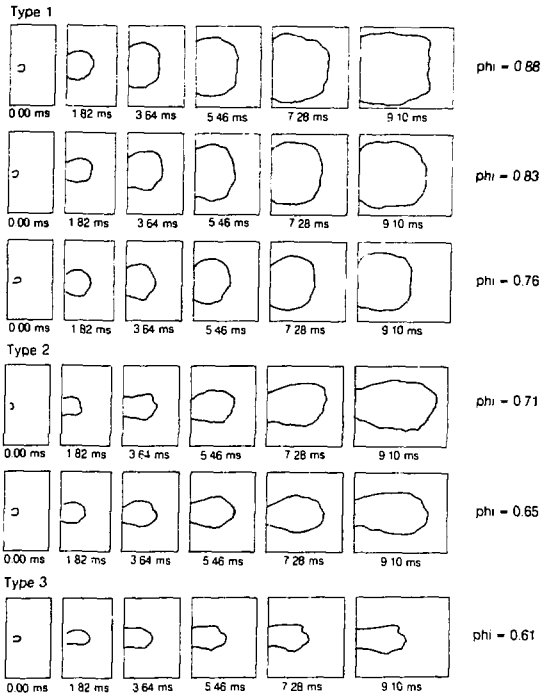

Figure 3. Flame propagation in compression-expansion-combustion for various equivalence ratios ("phi"). (XBL 841-458)

thought to be important to flame propagation and flame shape.

Lean combustion will be observed using the crank-driven compression-expansion apparatus (CE-2). This facility has been modified for a high compression ratio, up to 22:1 compared to the typical 8:1 compression of the CE-1 apparatus. An advantage of lean combustion in reciprocating engines is the potential for operation at higher compression ratios. Studies of lean combustion will be conducted in which compression ratio is an experimental parameter.

REFERENCE

1. Dunn-Rankin, D. and Sawyer, R.F. (1983). "Combustion of Lean Mixtures under Simulated Internal Combustion Engine Conditions." presented at the Fall Meeting of the Western States Section/The Combustion Institute, October 17, 1983, University of California, Los Angeles; LBL-16745.

Heat and Mass Transfer with Combustion*

S.R. Vosen, R. Greif, and C. Westbrook†

A major goal of this research has been the experimental and theoretical determination of the unsteady heat and mass fluxes during compression and combustion. This is not only of considerable practical importance, but of fundamental interest since the results elucidate basic aspects of combustion phenomena. The research has now reached the point that critical comparisons are being made between experiment and theory.

Measurements had previously been carried out during combustion in a shock tube in the end-wall region behind the reflected shock wave.[1,2] This was desirable because during the pre-ignition period, the free-stream temperature and pressure are constant, and the phenomena during this period are well understood. When ignition occurs, the effects of combustion are clearly displayed, providing a useful basis for appraisal.[1,2]

Studies were then made in a relatively long constant-volume chamber.[3-5] The system was a single-pulse compression-expansion apparatus[6] with the piston fully withdrawn. This system provided full optical access to the phenomena and showed the importance of equivalence ratio, buoyancy, and wall effects on flame propagation and heat transfer. Measurements have also been made during piston compression and expansion in nonreacting gases[7-9] and in methane-air flames.[10] Here we report on a comprehensive experimental and theoretical study of heat and mass transfer in reacting gases.

ACCOMPLISHMENTS DURING FY 1983

Direct and comprehensive comparisons have now been made between the experimental data and numerical calculations for the variation of heat flux with respect to time during combustion. These results clarify basic combustion phenomena relative to kinetics, quenching, equivalence ratio, and pressure effects and point the way for further research.

Measurements were made in a constant-volume combustion system. The system was specifically designed and constructed for this study and provided good optical accessibility to its interior. The measurements consisted of pressures, wall temperatures, and schlieren films for the combustion of premixed methane and air in the constant-volume chamber. The experiments were performed over a range of equivalence ratios, f, varying from 0.7 to 1.2 and a range of pressures at the time of quenching, p_q, varying from 1 to 4 atmospheres. The unsteady heat flux at the wall was determined from wall-temperature measurements. These were made with a thin-film resistance thermometer connected as the active element in a direct-current bridge. The change in temperature changed the resistance of the film, which caused an imbalance in the bridge. The resulting variable voltage was recorded and provided the data for determining wall temperature.

The results for the unsteady wall heat flux at a pressure of 1.1 atmospheres are presented in Fig. 1. The characteristic flux, q_c, is the heat release rate in an undisturbed flame, and the characteristic time, t_c, is the thermal diffusivity divided by the square of the flame speed.[10] These quantities are tabulated in

*This work was supported by the Assistant Secretary for Conservation and Renewable Energy, Office of Transportation Programs, Division of Transportation Energy Conservation of the U.S. Department of Energy under Contract No. DE-AC03-76SF00098.

†Lawrence Livermore National Laboratory, Livermore, CA.

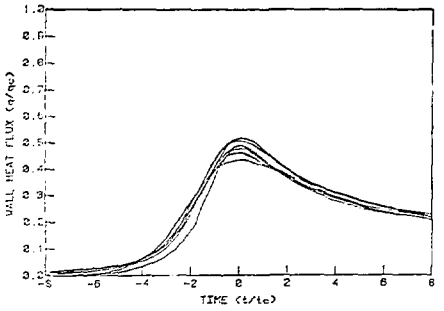

Figure 1. Experimental results—wall heat flux versus time. (XBL 842-851)

Table 1. The heat flux, q_w, varies considerably with respect to equivalence ratio; refer, for example, to the values of the maximum flux $q_{w,max}$ in Table 1. From Fig. 1 (also refer to the values of $q_{w,max}/q_c$ in Table 1), it is seen that the effects of the equivalence ratio are successfully brought together through the utilization of the dimensionless variables q_w/q_c and t/t_c.

Numerical results were also obtained for the unsteady heat transfer. The calculations were based on finite-difference formulations of the conservation equations governing reacting and diffusing gas mixtures. Two models were used. One, the detailed kinetics model, employed 86 chemical reactions (Westbrook *et al.*[11]); the other used a single-step, global reaction (Westbrook and Dryer[12]) in which the reaction-rate constants were chosen to give good agreement with the flame speed. The two predictions for heat flux differed by less than 10% in their maximum flux for several test cases. Accordingly, the single-step kinetics model, which requires much less computer time and gives good agreement with the detailed model, was used for all the calculations. The dimensionless results for the calculations are shown in Fig. 2, and the ranges of both the experimental data and the numerical calculations are shown in Fig. 3. The agreement between the two results is good, with the single-step kinetics model successfully predicting the heat flux over the range of equivalence ratios from 0.7 to 1.20.

The study of Isshiki and Nishiwaki[13] is pertinent to the present work. They carried out experiments in hydrogen-oxygen flames and used a simplified thermal model to obtain the following equation for maximum heat flux:

$$q_{w,\max} = \frac{2k_o \Delta T_f}{(\pi \alpha_o t_f)^{1/2}} \left(\frac{p_q}{p_o}\right)^{1/2} \qquad (1)$$

where t_f is the total time required for quenching as determined from wall temperature measurements and ΔT_f is the temperature difference across the flame. Isshiki and Nishiwaki[13] obtained good agreement between their experimental values of the maximum heat flux and the values from Eq. (1).

A comparison between the work of Isshiki and Nishiwaki[13] and the present study has been made. Using the characteristic heat flux q_c and the characteristic time t_c, along with the experimentally determined relationship $t_f = 2t_q^{\ddagger}$ we obtain

$$\frac{q_{w,\max}}{q_c}\left[\frac{t_q}{t_c}\right]^{1/2} = \left[\frac{2}{\pi}\right]^{1/2} \approx 0.80 . \qquad (2)$$

$^{\ddagger}t_q$ is the time required for the heat flux to rise from 50% to 100% of its maximum value. Values are tabulated in Table 1.

Table 1. Experimental and numerical results.

				Experimental		Experimental		Numerical	
p_q (Atmos)	ψ	t_c (msec)	q_c $\left[\frac{MW}{m^2}\right]$	t_q (msec)	$q_{w,max}$ $\left[\frac{MW}{m^2}\right]$	$\frac{t_q}{t_c}$	$\frac{q_{w,max}}{q_c}$	$\frac{t_q}{t_c}$	$\frac{q_{w,max}}{q_c}$
1.10	0.7	.416	.499	.85	.20	2.03	.40	----	----
1.12	0.8	.238	.771	.56	.28	2.41	.36	2.28	.463
1.17	0.9	.153	1.07	.24	.45	1.60	.42	----	----
1.19	1.0	.100	1.38	.20	.51	2.00	.37	2.15	.363
1.18	1.1	.095	1.43	.19	.61	2.06	.43	----	----
1.17	1.2	.119	1.21	.22	.53	1.90	.44	2.26	.385

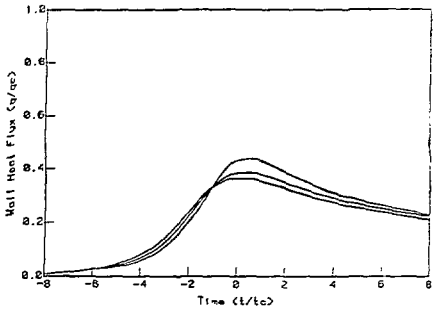

Figure 2. Numerical results, single-step kinetics, for wall heat flux. (XBL 842-852)

To obtain Eq. (2), the wall temperature is taken to be equal to the initial temperature.

For the present experiments (Table 1), we have

$$\frac{q_{w,\max}}{q_c}\left[\frac{t_g}{t_c}\right]^{1/2} = 0.57 \pm 10\%. \qquad (3)$$

The agreement between the results of our experiments (Eq. (3)) and the results of Isshiki and Nishiwaki (Eq. (2)) is quite good. Isshiki and Nishiwaki showed that Eq. (2) successfully correlated their data for the maximum heat flux. Thus the results of this work have been shown to reduce to the results of Isshiki and Nishiwaki and, more importantly, also provide a basis for correlating the quenching time and the heat flux independently.

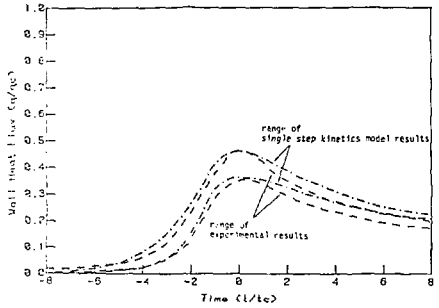

Figure 3. Comparison of experimental results and single-step kinetics model. (XBL 842-853)

Specifically, from Table 1, we have the approximate relations $q_{w,\max}/q_c = const = 0.4$, and $t_g/t_c = const = 2.0$.

A length scale for quenching has also been determined by assuming that the maximum wall heat flux is related to the closest approach of the flame to the wall; that is,

$$\delta_T \equiv \frac{\Delta T_f k_u}{q_{w,\max}}. \qquad (4)$$

Experimental and theoretical quenching studies have shown that the Peclet number based on the quenching distance is a constant or, at most, a function of the gas kinetics. The Peclet number based on the unburned gas properties is given by:

$$Pe_u = \rho_u S_u \frac{c_{pu}}{k_u}\delta_T = \frac{q_c}{q_{w,\max}}\frac{k_w}{k_u} \qquad (5)$$

From the experimental results for $q_{w,\max}/q_c$ (Table 1) and $k_u/k_w \propto (T_u/T_w)^{0.881}$ we have,

$$Pe_u = 2.4 \pm 10\%. \qquad (6)$$

Note that $T_u = T_o(p_u/p_o)^{(\gamma-1)/\gamma}$. In the experiments, k_u/k_w proved to be nearly constant, varying from 1.03 to 1.05.

The Peclet number may also be obtained from the numerical calculations, using $q_{w,\max}/q_c$ tabulated in Table 1. The calculations used $T_w = T_u$ so that $k_w = k_u$. The result is

$$Pe_u = 2.5 \pm 12\%. \qquad (7)$$

Thus, the experimental data and the calculations both predict the same value for the Peclet number within the experimental uncertainty. Note that the Peclet number is expressed as a heat-flux ratio (Eq. (5)). Hence, this agreement is a consequence of the good agreement, previously discussed, between the calculations and the data for the heat flux.

The results discussed here are for pressures near atmospheric. At elevated pressures, the wall phenomena are more complex because of the substantial wall boundary layer at this condition. Preliminary results for elevated pressures are available and the work is continuing.

PLANNED ACTIVITIES FOR FY 1984

Detailed studies with respect to variations in both pressure and equivalence ratio will be carried

out. The work will also be extended to different fuels. This should permit critical appraisals of our understanding of flame-wall interactions over a broad range of conditions.

REFERENCES

1. Heperkan, H.A. (1980). *An Experimental and Theoretical Study of Heat Transfer with Combustion*, Ph.D. Dissertation, University of California, Berkeley; LBL-10868.
2. Heperkan, H., and Greif, R. (1982). "Heat Transfer During the Shock-Induced Ignition of an Explosive Gas," *Int. J. Heat Mass Transfer 25*, p. 267.
3. Woodard, J.B. (1982). *An Experimental and Theoretical Study of Heat Transfer in Constant Volume and Compression-Expansion Systems Including the Effects of Flame Propagation*, Ph.D. Dissertation, University of California, Berkeley; LBL-14097.
4. Woodard, J.B., Hirvo, D.H., Greif, R., and Sawyer, R.F. (1981). "Wall Heat Transfer and Flame Propagation in a Constant Volume Duct," presented at the Western States Section/The Combustion Institute Fall Meeting, October 19-20, 1981, Tempe, AZ; LBL-13021.
5. Woodard, J.B., Hirvo, D.H., Greif, R., and Sawyer, R.F. (1982), *Flame Propagation, Wall Heat Transfer, and Their Interaction in Lean Premixed Gases*, LBL-13950.
6. Oppenheim, A.K., *et al.* (1976), "A Cinematographic Study of Combustion in an Enclosure Fitted with a Reciprocating Piston," presented at the Conference on Stratified Charge Engines, London, England, November 23-24.
7. Nikanjam, M. (1977). *An Experimental and Theoretical Study of Unsteady Heat Transfer During Piston Compression*, Ph.D. Thesis, Department of Mechanical Engineering, University of California, Berkeley, California.
8. Nikanjam, M., and Greif, R. (1978). "Heat Transfer During Piston Compression," *J. Heat Transfer 100*, p. 527.
9. Greif, R., Namba, T., and Nikanjam, M. (1978). "Heat Transfer During Piston Compression Including Side Wall and Convection Effects," *Int. J. Heat Mass Transfer 22*, p. 901
10. Vosen, S.R. (1983). *Unsteady Heat Transfer During the Interaction of a Laminar Flame with a Cold Wall*, Ph.D. Dissertation, University of California, Berkeley, California.
11. Westbrook, C.K., Adamczyk, A.A., and Lavoie, G.A. (1981). "Numerical Study of Laminar Flame Wall Quenching," *Combust. Flame 40*, p. 81.
12. Westbrook, C.K. and Dryer, F.L. (1981). "Simplified Reaction Mechanisms for the Oxidation of Hydrocarbon Fuels in Flames," *Combust. Sci. Technol.* , p. 31.
13. Isshiki, N. and Nishiwaki, N. (1974). "Basic Study of Inside Convective Heat Transfer of Internal Combustion Engines," in *Proceedings of the Fifth International Heat Transfer Conference*, Vol. 2, p. 344, Japan Society of Mechanical Engineering, Tokyo.

Tests and Criteria for Fire Protection of Cable Penetrations*

R.B. Williamson, F.L. Fisher, and F.W. Mowrer

The spread of fire in nuclear reactors depends critically on the barrier qualities of the cable penetrations of fire-resistant walls and floor/ceiling assemblies. The new American Society for Testing and Materials standard, E-814,[1] is now available for the evaluation of "penetration fire stops." This new fire test is similar to the earlier ASTM E-119,[2] except that it is written specifically to cover assemblies such as cable and pipe penetration devices in fire-rated construction. The new standard calls for the pressure differential in the test furnace to be measured and specifies who shall establish the pressure differential. The ASTM E-119 fire endurance test method has been used for some 70 years to qualify unpenetrated walls and floor/ceiling assemblies; but when such assemblies contain cable penetrations, special attention is required, and the new standard, E-814, addresses the problem. The validation of E-814 and the concept of requiring positive pressure in the test furnace have been the focus of this project for the past 5 years.

*This work was supported by the U.S. Nuclear Regulatory Commission through Sandia National Laboratories, Albuquerque, New Mexico under Contract No. 50-9723 and through the U.S. Department of Energy under Contract No. DE-AC03-76SF00098.

One method of controlling the potential spread of fire in nuclear reactors is to construct fire-resistant wall and floor/ceiling assemblies that define fire areas or zones. An overriding consideration in the safe operation of nuclear reactors is that all systems and associated circuits used for safe shutdown be free from fire damage. This objective is achieved in part by identifying the "redundant" systems necessary for safe shutdown and then making certain that the two systems will not be subject to damage from the same fire. This can be accomplished by locating redundant systems in different fire areas separated by fire-rated barriers.

The actual fire conditions represented by the E-119 test method are termed "post-flashover"—those in which a fire fully involves a compartment; the test itself, however, is conducted in a furnace not closely controlled by the standard. Under actual conditions, as opposed to laboratory test furnaces, post-flashover fires are characterized by a positive pressure differential between the upper half of the fire compartment and the unexposed face of the wall and floor/ceiling assemblies making up its boundaries. The initial phase of this post-flashover period is also characterized by excess amounts of pyrolyzed fuel. The existence of positive pressure and excess pyrolyzates is clearly proven by the flames that commonly emerge from the doors and windows of both actual and laboratory post-flashover fires.

ACCOMPLISHMENTS DURING FY 1983

A new concept was discovered during the research that may have far-reaching consequences for the evaluation of all penetrations of fire-resistive barriers. The concept is to evaluate penetrations through walls or floor/ceiling assemblies in a true post-flashover compartment fire exposure. Many of the problems associated with the E-119 test are due to the tests being conducted in furnaces, not compartments. Thus if we return to an actual compartment geometry and create a true post-flashover compartment fire, the pressure differentials, excess pyrolyzates, and other characteristic features of post-flashover fires will automatically be accomplished.

This was the last year for the study of cable penetrations, and a report[3] was prepared that summarizes our research on this subject. This report gives a detailed analysis of how to evaluate the fire resistance of cable penetrations using the new fire test standard, ASTM E-814,[1] and how this relates to other standards, such as IEEE 635. Our research has focused on three areas of testing previously identified as having particular significance for the performance of penetration seals under actual fire conditions, namely:

(1) The temperature exposure history in terms of intensity and duration.
(2) The static pressure differential across the face of the penetration seal.
(3) The presence of excess pyrolyzates that can burn on the unexposed side of the test specimen.

For primarily historical reasons, the new ASTM E-814 standard test for penetration seals in the United States uses the same temperature exposure conditions as the ASTM E-119 test procedure. The E-814 procedure refers to the issue of static pressure differential, but it does not dictate a specific pressure differential as a test condition, nor does it address the issue of excess pyrolyzates. Our opinions on these issues are summarized below.

On the basis of both theoretical and experimental analysis, it appears that a static pressure differential of approximately 12.5 pascals would be an appropriate specification for rooms with typical ceiling heights. But in rooms with significantly higher ceilings or where a mechanically induced pressure differential exists, larger pressure differentials may be appropriate and necessary to assure the desired performance of a penetration seal in a real fire. The rationale behind this recommendation is discussed more completely in the final report of this project.[3] Because positive pressure differentials do exist in actual compartment fires, they should be integrated more specifically into the penetration test procedure. As demonstrated by our experiments, a consideration of the pressure differential can mean the difference between passing and failing the penetration seal test. Under positive pressure, the seal is attacked by hot fire gases that tend to locate openings and cracks in the seal and enlarge them through pyrolitic degradation. Conversely, with negative pressure, cool ambient air is drawn through the back face of the seal, thus decreasing the severity of the exposure.

The issue of excess pyrolyzates has been considered by the ASTM standards group only in a peripheral way. While it is widely recognized that excess pyrolyzates are produced in almost all post-flashover fires, the ASTM standards specify a hose stream test rather than one in which excess pyrolyzates are introduced into the test furnace. The philosophy underlying this approach is that the mechanical durability of a seal under the hose stream test is an adequate indication of what its performance would be with excess pyrolyzates in the furnace.

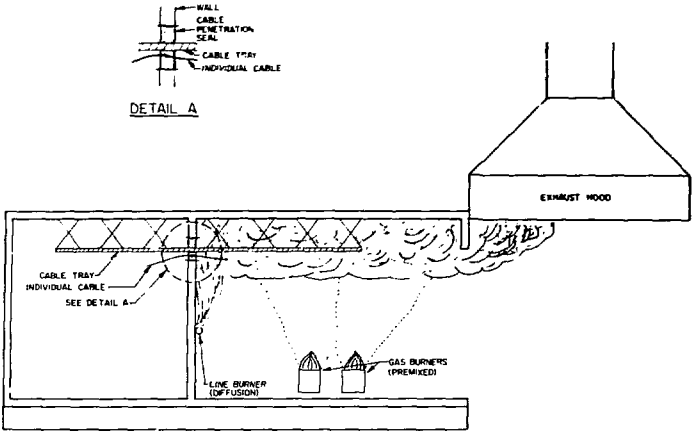

Figure 1. Schematic of a new type of fire test for cable penetrations in walls. (XBL 842-819)

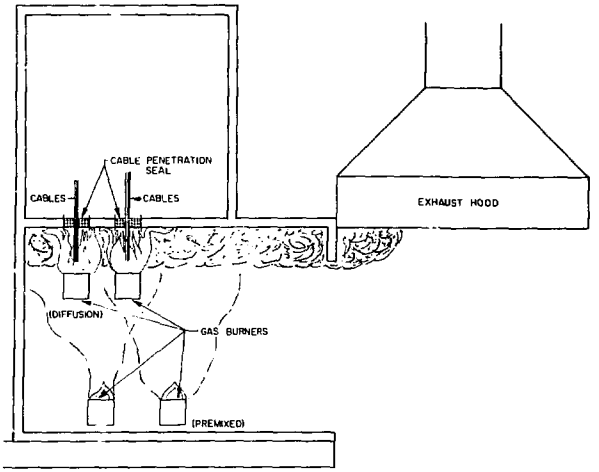

Figure 2. A similar fire-test facility with a floor/ceiling assembly. (XBL 842-820)

This philosophy may have some merit, since the hose stream test imposes a considerable orthogonal load on a penetration seal and is likely to find weaknesses and openings in the seal. On the other hand, the introduction of excess pyrolyzates in conjunction with positive pressure would have a more direct bearing on the fire performance of the seal. In particular, the "F" rating[1] of seals might be seriously altered with excess pyrolyzates because combustible gases will be pushed through any seal openings or cracks. With positive pressure alone, hot products of combustion may thermally degrade the seal, but they are noncombustible for the most part and thus will not burn upon reaching the back face of the seal. In addition, the burning of adjacent combustible materials may be prevented by the vitiated gases from the test furnace.

Finally, it is the authors' opinion that one unknown aspect of all fire-resistive construction is the passage of toxic smoke from the fire to the unexposed side of the wall or floor/ceiling assembly. Figures 1 and 2 show schematic representations of a test geometry that would allow the assessment of the penetration of the assembly by flame and heat as well as gaseous products from the fire. Figure 1 shows a side elevation through a fire test facility with a roomlike fire exposure chamber and a closed chamber on the unexposed face of the assembly, in this case a wall with a cable penetration seal. Figure 2 shows a similar facility with a floor/ceiling assembly. We propose that such a test arrangement would allow for direct flame exposure to the penetration seal as well as for the development of realistic pressure profiles through the selection of soffit height in the fire compartment. Additional pressure differentials can be developed by depressurizing the unexposed compartment. We propose that CO_2 could be monitored on both sides of the test assembly to measure potential passage of toxic products under fire conditions. There is currently an effort in several European laboratories to use CO_2 measurements in this way, and the concept appears to have merit.

There are other advantages to this method which make it superior to the traditional fire-resistance furnace for the evaluation of cable penetrations. Since the gas flow to the burners can be measured separately, the contribution of the fire-stop material to the fire can be quantitatively assessed through oxygen-consumption calorimetry in the exhaust stack. The cable can also be burned in a calibration test that is the same as the penetration seal test without the penetration seal. The calibration test would also give a baseline for the gas penetration of the wall or floor/ceiling assembly.

Furthermore, the fire-exposure chamber shown in Figs. 1 and 2 is open to clear observation of the fire environment and the behavior of the cable tray support system and similar structures. In the floor/ceiling test, the upper chamber could have electrical cabinets over the penetration seals to reproduce the actual conditions found in many reactor control rooms. Finally, since it could reasonably be argued that this is not a traditional fire-resistance test, the standard time-temperature curve would not have to be used. It would be more reasonable to represent a range of fuel release rates in the compartment with different opening heights and widths to achieve a range of time-temperature curves that would be representative of actual fire conditions.

PLANNED ACTIVITIES FOR FY 1984

Research concerned with the fire protection of cable penetrations was completed during 1983.

REFERENCES

1. *1983 Annual Book of ASTM Standards*, Vol. 4.07, p. 817, American Society for Testing and Materials, Philadelphia, PA.
2. *1983 Annual Book of ASTM Standards*, Vol. 4.07, p. 337, American Society for Testing and Materials, Philadelphia, PA.
3. Williamson, R.B., Fisher, F.L. and Mowrer, F.W. (1983), "Tests and Criteria for Fire Protection of Cable Penetrations," final report for this project, to be submitted to *Fire Safety Journal*.

Fire Safety of Electrical Cabinets*

R.B.Williamson, F. L. Fisher, and F. W. Mowrer

The principal objective of this research was to assess the susceptibility of components within electrical cabinets to damage from fire, especially with regard to nuclear power plants. Fire originating outside the cabinet was the main concern, although the possibility of an interior fire spreading to adjacent cabinets, and even to the surrounding room, was found to constitute a potential problem where cabinets are naturally ventilated. Two experiments in which prototype cabinets were exposed to ignition sources representative of design-basis fire scenarios were performed, and a report on the results was written.[1]

ACCOMPLISHMENTS DURING FY 1983

The two experiments mentioned, one conducted on October 29, 1982, and the other on February 14, 1983, used the cabinet illustrated in Fig. 1(a). In the first experiment, the cabinet contained only thermocouple wire and leads, while in the second, the cabinet was modified and outfitted with an array of insulated cable, as shown in Fig. 1(b). During the second experiment, the rate of heat release of the cables in the cabinet, smoke production, flame height, and other characteristics were assessed quantitatively, while damage to the cables within the cabinet was evaluated qualitatively. Figures 2(a) and 2(b) show the rate of heat release for these two experiments, as calculated from the oxygen consumption.

These two experiments demonstrated the potential for serious fires in electrical cabinets resulting from a "typical" transient ignition source. The direct damage to the cabinets and their contents suggests a need for greater scrutiny of this fire problem, especially if redundant safety systems are located within the same or adjacent cabinets. The flashover that occurred in the room surrounding the cabinet during the second experiment is considered to have important safety implications for both new and operating reactors. Figures 3–5 show the extent of the fire in the second experiment. Figure 3 shows the fire spreading to a 32-gallon waste container and the surface of the electrical cabinet at 2:35 (2 minutes, 35 seconds) after ignition. Figure 4 shows the heavy smoke produced by the burning cables in the cabinets at 12:39. Finally, Fig. 5 shows the full extent of the burning at 15:12, just before a light spray of water was applied.

The ignition source and the location of ventilation openings in the electrical cabinets have been identified as two parameters upon which the potential for damage depends. Other parameters include the construction and materials of the cabinets, as well as the nature of the contents themselves.

The location of ventilation openings and the construction of electrical cabinets has been a responsibility of the operators of nuclear plants. In general, the specifications for electrical cabinets have focused on the expected power load in each cabinet and compliance with the test procedures required by the NRC for licensing. The number and location of ventilation openings generally follow the National Electrical Manufacturers Association (NEMA) practice and no special attention to potential fire problems appears to be given. A number of A/E firms that design reactors have, however, specified "fire resistive paint" for the cabinets in nuclear power projects. This has usually meant an intumescent paint, such as those manufactured by the Albi Corporation, for example.

An intumescent paint is designed to form an insulating layer on a substrate when exposed to fire, and the use of such a paint might be very effective in preventing the penetration of a small exterior fire into the cabinet. There are two possible mechanisms by which an intumescent paint could prevent fire penetration into the cabinet: (1) the insulation formed on the exposed face of the cabinet could limit the heat build-up in the cabinet interior and thereby decrease the chimney effect; (2) the grille could be sealed off from direct flame impingement by the paint.

Finally, in discussions with engineers concerned with control-room equipment in nuclear reactors, it became evident that there is a tendency to use natural ventilation in electrical cabinets containing safety-related circuits and components. This is because any ducted, fan-operated ventilation system would have to be classified as a safety-related system, and, as such, it would require special attention and be more costly than natural ventilation. This use of natural ventilation means that safety-related circuits and components may be particularly susceptible to accidental fires of transient materials stored near the ventilation openings.

*This work was supported by the U.S. Nuclear Regulatory Commission through Sandia National Laboratories, Albuquerque, New Mexico under Contract No. 45-5967 through the U.S. Department of Energy under Contract No. DE-AC03-76SF00093.

a)

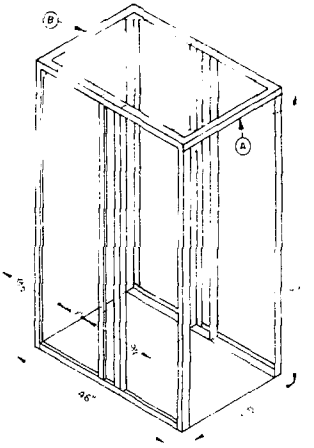

NOTE VENT HOLES CLOSED DURING EXPERIMENT

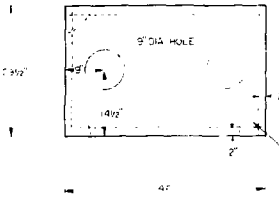

ISOMETRIC VIEW OF FRAMING

FRAMING OF 1/4"x1 1/2"x 2" ANGLES

MEMBERS (A)(B)(B)' ETC., ALL OTHERS ALUMINUM

6"x6" BRACKETS

TOP & SIDES 1/32" SHEET STEEL

DOORS & GRILLES 1/8" SHEET ALUMINUM

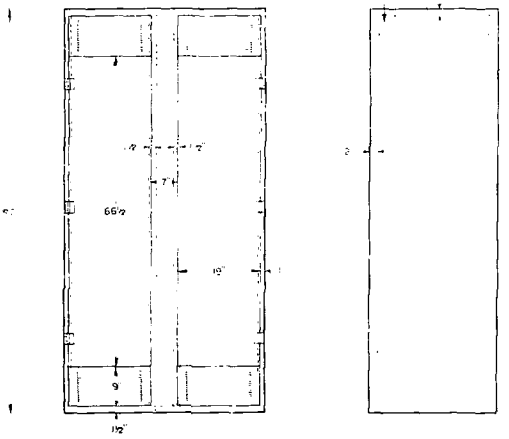

PLAN VIEW OF EXTERIOR LAYOUT

% OPENING OF GRILLES

AREA OF FRONT = 4002 sq in

AREA OF GRILLES = 224 sq in

% OF TOTAL AREA = 5.6 %

Figure 1(a). Electrical cabinet used in the first experiment (October 29, 1982). (XBL 842-818)

b)

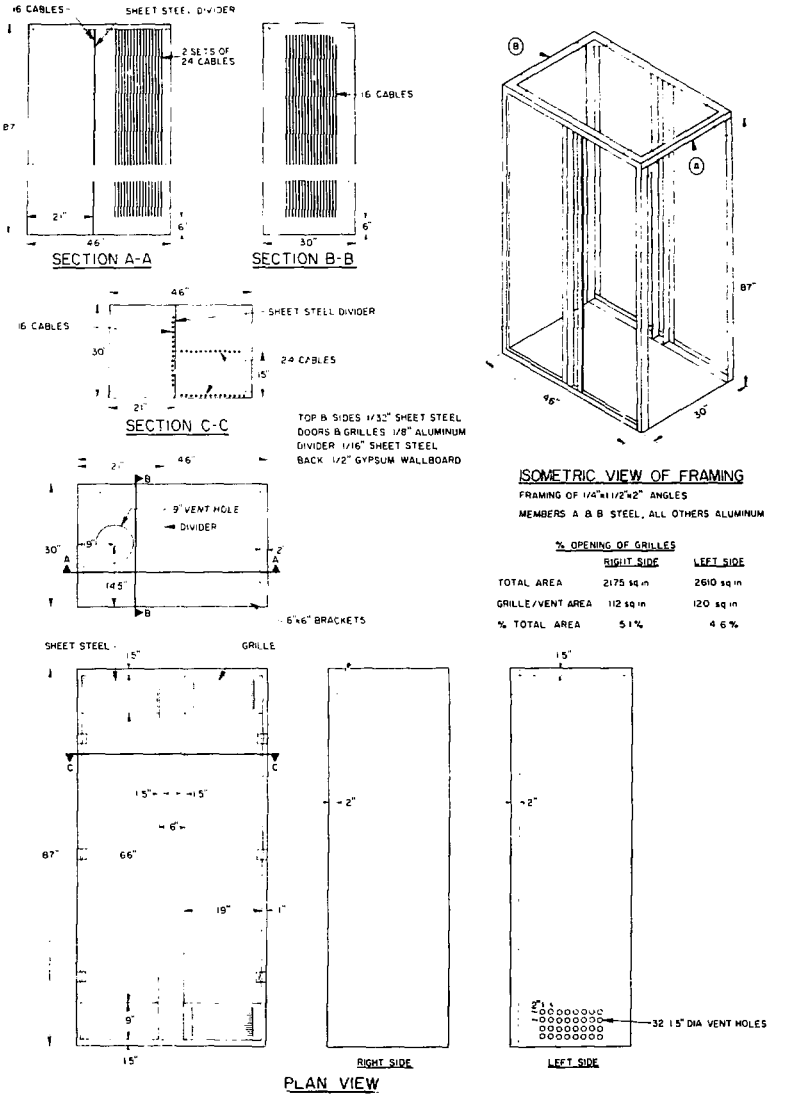

Figure 1(b). Electrical cabinet with cable, as used in the second experiment (February 14, 1983). (XBL 842-817)

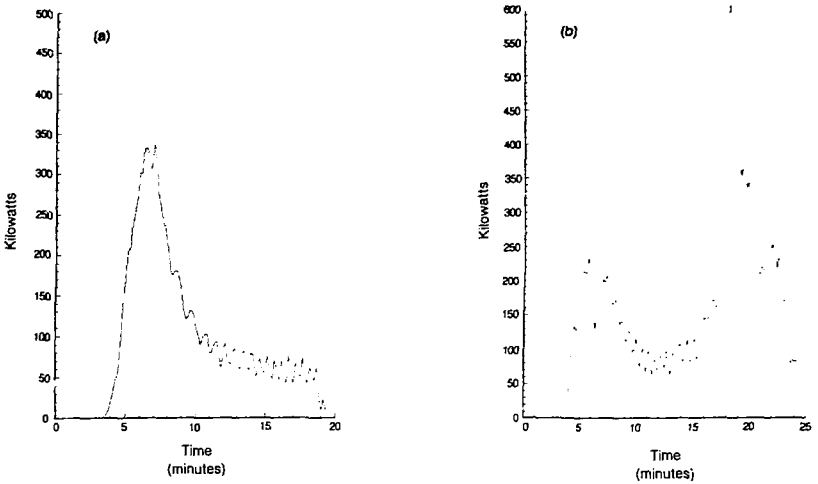

Figure 2. (a) The rate of heat release during the first experiment, calculated from oxygen consumption. Three minutes of "baseline" data were collected before ignition. (b) Rate of heat release, calculated from oxygen consumption during the second experiment. (a) XBL 842-816; (b) XBL 842-815

Figure 3. At 2:35 after ignition, the fire has spread to a 32-gallon waste container and the surface of the electrical cabinet (Feb. 14, 1983). (XBB 842-1386)

Figure 4. Heavy smoke produced by the cables burning in the cabinet at 12:59 (Feb. 14, 1983). (XBB 842-1387)

Figure 5. *Extent of burning at 15:12 after ignition, before a light spray of water was applied to the outside of the cabinet (Feb. 14, 1983).* (XBB 842–1388)

PLANNED ACTIVITIES FOR FY 1984

It is planned to continue the evaluation of the susceptibility of the contents of electrical cabinets to fire damage and to perform an assessment of the experiments conducted during the previous project period in order to determine the likelihood of similar events occurring under actual operating conditions. Special attention will be paid to the electrical cabinets having safety-related equipment necessary for the safe shutdown of a nuclear facility.

A further task will be to determine the locations and intensities of "credible" control-room fire scenarios. Special attention will be paid to "trash" fire scenarios like those used in the experiments conducted in the previous report period, but other scenarios, such as full involvement of an unoccupied room in the control-room fire zone, will also be explored.

REFERENCES

1. Williamson, R.B., Fisher, F.L., and Mowrer, F.W. (1983), "Fire Safety of Electrical Cabinets," Report to Sandia National Laboratories, Albuquerque, NM.

Development of Fixed Ferrous Catalysts for Simultaneous Desulfurization and Denitrification of Flue Gas in Aqueous Solutions*

S. G. Chang and K. Brodbeck

Ferrous ion can be used as a catalyst in a wet flue gas clean-up process to improve the efficiency of nitric oxide (NO) and sulfur dioxide (SO_2) removal. Organic chelates are required in this type of process to stabilize and promote the catalytic activity of ferrous ion. However, the ferrous ion and organic chelates can be consumed in the scrubbing process as a result of coprecipitation with reaction products and of reaction with active species downstream in the process. If ferrous ion and organic chelates could be immobilized onto a solid particulate surface and if these immobilized ferrous chelates could retain the required catalytic properties, the resulting scrubber system could provide important advantages over one employing mobile ferrous catalysts. These advantages include a simpler process design for species separation, reduction of water, energy, and catalyst consumption, and lower operating costs.

ACCOMPLISHMENTS DURING FY 1983

A polymeric material (Chelex 100), a crosslinked polystyrene divinylbenzene porous lattice with attached imminodiacetate multidentate functional groups, was employed as a solid substrate to bind ferrous ion. The thermodynamic properties (equilibrium constants, enthalpy, and entropy) of the coordination of NO to the ferrous ion on Chelex 100 were determined.

These experiments were performed in a bench-scale flue-gas scrubber system. A known amount of distilled water and Chelex 100 were transferred to an absorber in the system. After removal of dissolved oxygen by purging N_2 gas through a sinter glass plate located at the bottom of the absorber, a known amount of $Fe(NH_4)_2SO_4$ was added to the solution. The concentration of Fe(II) ranged between 3×10^{-2} *M* and 2×10^{-1} *M*. The pH and ionic strength of the solution were adjusted to 5–7 pH with oxygen-free NaOH solution and to 0.5 *M* with Na_2SO_4 solution. A mixture of NO and N_2 of known NO concentration (850–960 ppm) was bubbled through a NaOH solution to absorb NO_2 impurities in the gas. This NO_2-free mixture of NO and N_2 gas was then bubbled through the sinter glass plate into the solution containing Fe(II)-Chelex 100, and the NO concentration in the outlet gas was measured with a Thermoelectron model 14A chemiluminescent NO_x analyzer. The gas flow rates were 685–735 mL/min. Absorption of NO was carried out until the NO concentration in the outlet gas became equal to that in the inlet gas, i.e., until equilibrium was reached. The experiments were performed at 25, 40, and 55°C.

The equilibrium constant of the coordination of NO with Fe^{2+} on Chelex 100 has been calculated to be 1.8×10^4, 1.0×10^4, and 5.8×10^3 L/mole at 25, 40, and 55°C, respectively. The enthalpy and entropy of this reaction is $\Delta H^\circ = -7.3$ kcal/mole and $\Delta S^\circ = -5.0$ e.u.

PLANNED ACTIVITIES FOR FY 1984

We will study the stability of Chelex 100 under flue-gas scrubbing conditions. The rate of oxidation of NO and Fe(II) on Chelex 100 by O_2 and the reaction rate constant of NO on Fe^{2+} – Chelex 100 with $HSO_3^-/SO_3^=$ will be determined. This study will be extended to other porous particulate materials as solid supports for the Fe(II) catalyst.

*This work was supported by the Assistant Secretary for Fossil Energy, Office of Coal Research, Advanced Environment Control Division of the U.S. Department of Energy under Contract No. DE-AC03-76SF00098 through the Pittsburgh Energy Technology Center, Pittsburgh, PA.

Binding of Nitric Oxide to Ferrous Chelate Complexes*

D. Littlejohn and S.G. Chang

While techniques for control of sulfur dioxide in power-plant flue-gas emissions are fairly well developed, methods for control of nitrogen oxides (NO_x) are still being studied.[1] A major problem is that most of the NO_x, which is typically present in hundreds of parts per million (ppm), is in the form of nitric oxide (NO), which has low solubility in water.[2] One answer is to use a compound in the scrubbing solution to enhance the solubility of NO in solution. Ferrous chelate complexes are one class of compounds that have this capability: they reversibly form ferrous chelate nitrosyls on exposure to NO.[3] The chelate used can have considerable influence on the binding ability of the complex. There is some uncertainty about the stoichiometry of the nitrosyl complexes.

ACCOMPLISHMENTS DURING FY 1983

The method used to prepare the ferrous nitrosyl complexes has been described previously.[4] The frequency of the N-O stretch, ν_{NO}, can provide some information on the character of the bond between NO and the complex. This can be obtained from infrared and Raman spectra of the nitrosyl complexes. Solutions of Fe(II)(EDTA)NO and Fe(II)(NTA)NO were prepared to obtain the Raman shifts of NO bound to the complexes. They are listed below, along with $Fe(II)(H_2O)_5NO$ and nitric oxide.

Compound	ν_{NO}
$Fe(II)(H_2O)_5NO$	1765 cm^{-1}
Fe(II)(EDTA)NO	1784 cm^{-1}
Fe(II)(NTA)NO	1797 cm^{-1}
NO gas	1877 cm^{-1}

Since NO^+ has $\nu_{NO} \approx 2100$ cm^{-1},[5] the ferrous nitrosyl complexes listed show close to neutral NO character.

*This work was supported by the Assistant Secretary for Fossil Energy, Office of Coal Research, Advanced Environment Control Division of the U.S. Department of Energy under Contract No. DE-AC03-76SF00098 through the Pittsburgh Energy Technology Center, Pittsburgh, PA.

The stoichiometry of NO bound to Fe(II) was found to be 1:1 in our earlier studies,[3] done at low NO concentrations. Other workers have reported different values, using indirect methods.[6] We have extended our NO absorption studies to higher concentrations. The technique used involved preparing a ferrous chelate solution under vacuum. Then NO stored under a known pressure in a standarized volume was expanded into the bulb containing the ferrous chelate solution. The pressure drop due to absorption of NO by the solution was recorded. The number of moles of NO absorbed was compared with the number of moles of Fe(II) in solution, after correcting for the amount of free NO in solution. The following stoichiometry was observed for the following ligands, with Fe(II) = 0.02 *M*, NO pressure ≈ 650 torr, and pH ≈ 3.5:

Ligand	Fe:NO
H_2O	1:0.6 ± 0.1
IDA	1:1.0 ± 0.
EDTA	1.,.0 ± 0.1
NTA	1:1.15 ± 0.1

The value obtained for H_2O is in reasonable agreement with the equilibrium constant obtained by temperature-jump measurements.[4] The results obtained for IDA and EDTA ligands do not agree with results obtained by electrochemical means.[6] However, the pressure-measurement technique is more direct and less prone to interference, and we believe that the stoichiometries of the EDTA and IDA complexes are 1:1 only under the given conditions. It does appear that the NTA complex can form both a mononitrosyl and a dinitrosyl complex, Fe(II)(NTA)NO and $Fe(II)(NTA)(NO)_2$, as indicated by the observed overall stoichiometry. The aquoferrous complex does not bind NO well enough that not all the ferrous ions are bound to NO at these conditions. It would require NO pressures substantially higher than 1 atm to obtain 1:1 stoichiometry. With the exception of the NTA result, these results confirm the values obtained at lower NO concentrations.[3]

PLANNED ACTIVITIES FOR FY 1984

We plan to investigate other ligands that form ferrous nitrosyl complexes to determine their stoichiometry. In some instances, mixtures of ligands appear to enhance the binding ability of Fe(II) above that of either ligand separately. The

stoichiometry of these systems will also be studied. By using different pressures of NO to vary the concentration of dissolved NO, it should be possible to determine the equilibrium constant for the binding of the second NO to Fe(II)(NTA)NO.

REFERENCES

1. Yaverbaum, L.H. (1979). "Nitrogen Oxides Control and Removal, Recent Developments." Noyes Data Corp., Park Ridge, N.J.
2. Chang, S.G., Littlejohn, D., and Lin, N.H. (1982). "Kinetics of Reactions in a Wet Flue Gas Simultaneous Desulfurization and Denitrification System." in *Flue Gas Desulfurization*, ACS Symposium Series 188, American Chemical Society, Washington, D.C.
3. Lin, N.H., Littlejohn, D., and Chang, S.G. (1982). "Thermodynamics of the Coordination of NO to Fe(II)NTA in Aqueous Solutions." *I&EC Proc. Design Dev. 21* p. 725.
4. Littlejohn, D. and Chang, S.G. (1982). "Kinetic Study of Ferrous Nitrosyl Complexes." *J. Phys. Chem. 86* p. 537.
5. Feltham, R.E. (1980). "Coordinated Nitrosyl Complexes." Inorganic Chemistry Seminar, University of California, Berkeley, October 24, 1980.
6. Ogura, K. and Watanabe, M. (1982). "Nitrosylmetallochelates—II. Composition of Fe-NO-Aminocarboxylic Acid Complexes in Solution." *Electrochim. Acta 27* p. 111.

The Effect of Citrate Buffer Additive on the Absorption of NO by Ferrous Chelates*

E. Griffiths, T. Hoang, and S.G. Chang

In a wet flue gas simultaneous denitrification and desulfurization system where ferrous chelates are added in the scrubbing liquor to promote the solubility of nitric oxide, nitrosyl ferrous chelates are formed.[1-3] The reaction between the complexed NO and $HSO_3^-/SO_3^=$ ions is too slow to affect significantly the rate of absorption of sulfur dioxide.[4] One must, instead, depend upon the buffering capacity of the solution for absorbing SO_2 and upon subsequent reactions for removing it from the solution. Since the pH of the solution in the scrubber is advantageously kept in the range 5-7, and since the acid constants of chelates commonly used for the complexation with ferrous ion, such as NTA, EDTA, and IDA, cannot provide buffering in this pH range, the buffering must be provided by adding some other soluble base to the scrubbing solution. There has been substantial commercial experience with scrubbing SO_2 from stack gas with a solution containing a soluble base. Sodium citrate is an example of a base that has been employed in the citrate process developed by the U.S. Bureau of Mines. This is a regenerable flue-gas desulfurization process, where the dissolved SO_2 is reacted with H_2S to form elemental sulfur. It has also been demonstrated in our laboratory that hydrogen sulfide (H_2S) can reduce NO in the nitrosyl ferrous chelates and regenerate ferrous chelate catalysts. The development, therefore, of a regenerable flue-gas denitrification and desulfurization process, based on the addition of both ferrous chelates and H_2S in a wet scrubber and with sodium citrate as a buffer, sounds very promising. With this approach, a salable form of sulfur is produced and costs may be reduced as a result.

*This work was supported by the Assistant Secretary for Fossil Energy, Office of Coal Research, Advanced Environment Control Division of the U.S. Department of Energy under Contract No. DE-AC03-76SF00098 through the Pittsburgh Energy Technology Center, Pittsburgh, PA.

ACCOMPLISHMENTS DURING FY 1983

We have determined the equilibrium constants of NO with Fe(II)citrate and Fe(II)IDA as a function of pH and temperature. We have also studied the effect of citrate ions on the absorption capacity of NO by Fe(II)EDTA, Fe(II)NTA and Fe(II)IDA.

Solutions of these ferrous chelates, at *0.01 M*, were prepared under oxygen-free conditions. The solutions were adjusted to the desired pH by NaOH and ionic strength 1 *M*, using Na_2SO_4. The NO, obtained from the Matheson Co., was a mixture of 2.55% NO in N_2 with NO_2 impurity of less than 255 ppm. The experiments proceeded by bubbling a mixture of NO and N_2 of known NO concentration through a NaOH solution to absorb any NO_2 impurity in the gas, and then through the ferrous chelate solution. The NO concentration in the outlet gas was measured with a Thermoelectron model 14A chemiluminescent NO_x analyzer. Equilibrium was attained when the NO concentration in the outlet gas

became equal to that of the inlet gas.[5,6] The gas flow rates were 600–810 mL min^{-1}. The experiments were performed at 25 and 55°C.

The equilibrium constants of $Fe(II)(cit^{3-})NO$ were determined to be $4.9 \times 10^4\ M^{-1}$ at 25°C and $1.3 \times 10^4\ M^{-1}$ at 55°C in the pH range 4–6.5. At a pH > 6.5, the absorption of NO increased linearly until at pH ≈ 8.5, it leveled out and the equilibrium constants became $2.1 \times 10^5\ M^{-1}$ at 25°C and $1.15 \times 10^5\ M^{-1}$ at 55°C. Studies of ratio dependency showed that, for every one mole of ferrous ion, only one mole of citrate ions was bound to it. So the absorbing species must have been $Fe(II)(cit^{3-})$ when $4 < pH < 6.5$, and $Fe(II)(cit^{3-})OH^-$ at pH > 6.5.

The equilibrium constants of $Fe(II)(IDA^{1-})_nNO$ were $1.9 \times 10^5\ M^{-1}$ at 25°C and $5 \times 10^4\ M^{-1}$ at 55°C. Ratio-dependent studies showed n equal to one. At pH > 8, the absorption of NO decreased, which may be attributed to the formation of a new complex, $Fe(II)(IDA^{2-})_x$, where x is undetermined.

When 0.1 M citrate ions were added to a solution of 0.01 M $Fe(II)IDA^{1-}$, the equilibrium constant became that of $Fe(II)(cit^{3-})NO$ in the pH range 4–5.2. At pH > 5.2, the equilibrium constant increased with increasing pH, similar to the behavior observed for $Fe(II)(cit^{3-})(OH)NO$, although the latter only occurred at pH ≥ 6.5. The formation of $Fe(II)(cit^{3-})(OH)NO$ complex could not account for the strong absorption of NO. It is proposed that a mixed chelate, such as $Fe(II)(cit^{3-})(IDA^{1-})NO$, is formed at 25°C. Experiments were performed at pH > 7.5 to see if the absorption of NO would change when the second hydrogen ion of IDA was ionized. Precipitation occurred, whereas the $Fe(II)(cit^{3-})(OH)NO$ complex was soluble up to pH 9.5. At 55°C, the absorption of NO was that of $Fe(II)(cit^{3-})(OH)NO$ at high pH.

Effectively, citrate ions acted as a masking agent, decreasing the value of the stability constant of Fe(II)IDA. This new stability constant is referred to as a conditional stability constant.[7]

In the presence of 0.1 M citrate ions, the absorption of NO by Fe(II)NTA decreased when pH > 5 at 25 and 55°C. This is due to the decrease in the concentration of Fe(II)NTA available, because of the reduced stability constant. The absorption of NO by Fe(II)EDTA at 25 and 55°C was unaffected by the addition of 0.1 M citrate ions, because the conditional stability constant was still large.

This study showed that the addition of citrate ions could enhance NO absorption [Fe(II)(IDA^{1-})], decrease it [Fe(II)(NTA)], or have no effect [Fe(II)EDTA].

PLANNED ACTIVITIES FOR FY 1984

We plan to study the effect citrate ions have on the absorption of NO by other ferrous/nonferrous chelates as a function of pH and temperature. We also hope to verify by polarography the existence of the $Fe(II)(cit^{3})(IDA^{1-})$ complex, as proposed in the explanation of the experimental results observed here.

REFERENCES

1. Yaverbaum, L.H. (1979), *Nitrogen Oxide Control and Removal, Recent Developments*, Noyes Data Corporation, Park Ridge, N.J.
2. Martin, A.E., Ed. (1981), *Emission Control Technology for Industrial Boilers*, Noyes Data Corporation, Park Ridge, N.J.
3. Chang, S.G., Littlejohn, D., and Lin, N.H. (1982), "Kinetics of Reactions in a Wet Flue Gas Simultaneous Desulfurization and Denitrification System," in *Flue Gas Desulfurization*, ACS Symposium Series 188, American Chemical Society, Washington, D.C.
4. Chang, S.G., Littlejohn, D., and Griffiths, E. (1982), "The Reaction of Ferrous Nitrosyl Complexes with Sulfite and Bisulfite Ions," LBL-15298, p. 4.
5. Hishinuma, Y., *et al.* (1979), "Reversible Binding of NO to Fe(II)(EDTA)," *Bull. Chem. Soc. Japan 52*, p. 2863.
6. Lin, N.H., Littlejohn, D., and Chang, S.G. (1982), "The Thermodynamic and Kinetics of the Coordination of NO to Fe^{2+}(NTA) in Aqueous Solutions," *I & EC Process Res. Dev., 21*, p. 725.
7. Ringbom, A. (1963), *Complexation in Analytical Chemistry*, Wiley-Interscience, New York.

Reaction of Ferrous Nitrosyl Complexes with Sulfite and Bisulfite Ions*

D. Littlejohn and S.G. Chang

Several methods are being developed to control the emission of the acid rain precursors sulfur dioxide (SO_2) and nitrogen oxides (NO_x).[1-3] Coal-fired power plants emit SO_2 in flue gases in concentrations as high as thousands of parts per million (ppm) and NO_x in concentrations of hundreds of ppm before treatment. Since nitric oxide (NO), which has low solubility in water, is the major constituent of NO_x, control strategies based on aqueous solutions cannot effectively remove it without conversion to NO_2 or the addition of a compound to enhance its solubility.[1-3] One class of compounds that enhance the solubility of NO is that of the ferrous chelates, which reversibly form ferrous chelate nitrosyls on exposure to NO.[4] These compounds can be regenerated by reaction with dissolved SO_2 in the form of bisulfite ions (HSO_3^-) or sulfite ions ($SO_3^=$), which will be collectively referred to as S(IV). The kinetics and products of this reaction need to be understood to effectively use this technique in a flue-gas scrubbing system.

ACCOMPLISHMENTS DURING FY 1983

We have extended our previous studies[5] on the kinetics and reaction products of this system. The gaseous products and major anion products have been determined. A plausible mechanism for production of these compounds has been developed.

The kinetics of this reaction system have been fairly well established. The reaction appears to be first order in S(IV) from pH 4 to 8 and first order in Fe(II)(L)NO at high pH (where $SO_3^=$ is present).

Our work indicates that a substantial amount of the NO in the complex is converted into the gaseous species N_2O and N_2. Figure 1 shows the fraction of N in NO converted to N_2O and N_2, and the N_2O:N_2 ratio, as a function of pH for Fe(II)(NTA)NO = 0.02 *M* and S(IV) = 0.20 *M* at 25°C. Figure 2 shows the fraction of N in NO converted to N_2O and N_2, and the N_2O:N_2 ratio as a function of

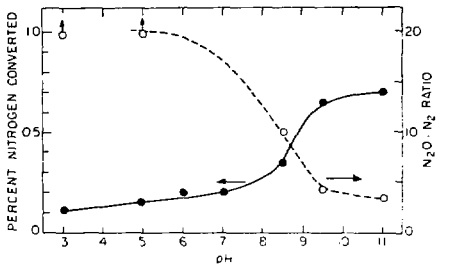

Figure 1. The fraction of N in NO converted to N_2O and N_2, and the N_2O:N_2 ratio, as a function of pH for Fe(II)(NTA)NO = 0.02 *M* and S(IV) = 0.20 *M* at 25°C. (XBL 838-6246)

Fe(II)(NTA)NO concentration for pH = 8 and $[SO_3^=]$:[Fe(II)(NTA)NO] ≈ 10 at 25°C. The amount of nitrogen converted into gaseous products did not change greatly over the temperature range of 25 to 50°C, although the N_2O:N_2 ratio does drop slightly with an increase in temperature. Neither the fraction of nitrogen converted nor the N_2O:N_2 ratio changes appreciably over a range of $[SO_3^=]$:[Fe(II)(NTA)NO] ratios of 2:1 to 20:1 at pH 8 and 25°C. Similar results are observed with Fe(II)(EDTA)NO + S(IV).

The remainder of the nitrogen in NO is converted into nitrogen-sulfur compounds such as hydroxylamine disulfonate (HADS), hydroxylamine monosulfonate (HAMS), aminetrisulfonate (ATS), and aminedisulfonate (ADS). The mechanism for

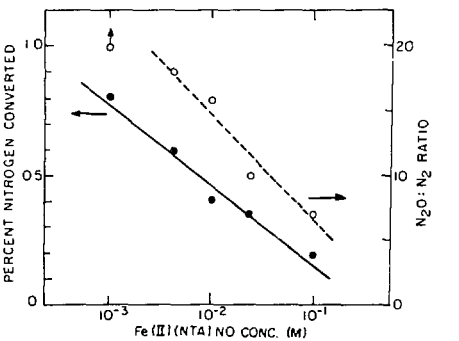

Figure 2. The fraction of N in NO coverted to N_2O and N_2, and the N_2O:N_2 ratio as a function of FE(II)(NTA)NO concentration for pH = 8 and $[SO_3^{2-}]$:[Fe(II)(NTA)NO] ≈ 10 at 25°C. (XBL 838-6245)

*This work was supported by the Assistant Secretary for Fossil Energy, Office of Coal Research, Advanced Environment Control Division of the U.S. Department of Energy under Contract No. DE-AC03-76SF00098 through the Pittsburgh Energy Technology Center, Pittsburgh, PA.

production may be similar to that of the reaction of NO_2^- with HSO_3^-,[6] involving an intermediate such as nitrososulfonic acid. HADS has been determined by conversion to nitrosodisulfonate with photometric measurement and by Raman spectroscopy. The other nitrogen-sulfur compounds have been observed by Raman spectroscopy.[7]

The S(IV) consumed in the reaction is converted into either nitrogen-sulfur compounds or sulfate ion. A small amount of the S(IV) may be converted into dithionate in some cases.

The ferrous ion in the complex is not inert in this reaction. Shortly after addition of the S(IV) species, the solution color changes from green to red. The rapidity of the change is affected by the ligand, reactant concentration, and solution pH. The spectrum of the reddish solution has a structure very similar to that of ferric ion complexes.[8] In reactions involving $Fe(II)(H_2O)_5NO$, the Fe(II) concentration can be determined using 1,10-phenanthroline.[5] (With other nitrosyl complexes, the ligand interferes with this technique.) Measurements indicated there was a substantial reduction in Fe(II) concentration after the addition of S(IV), indicating conversion to Fe(III). The oxidant responsible for the conversion has not been determined, but it could be an intermediate such as $^-ONSO_3^-$ from the reaction of NO with $SO_3^=$.

PLANNED ACTIVITIES FOR FY 1984

We plan to develop a polarographic system to quantitatively determine the amount of Fe(III) formed with time in reaction mixtures, regardless of the ligand used. We also plan to look for intermediates such as the nitroxyl radical (HNO or NOH)[9] that may be present in the reaction mixture. This information should provide insight into the reaction mechanism that occurs in mixtures of ferrous nitrosyl complexes and S(IV).

REFERENCES

1. Yaverbaum, L.H. (1979). *Nitrogen Oxides Control and Removal, Recent Developments*, Noyes Data Corp., Park Ridge, N.J.
2. Martin, A.E., Ed. (1981). *Emission Control Technology for Industrial Boilers*, Noyes Data Corp., Park Ridge, N.J.
3. Chang, S.G., Littlejohn, D., and Lin, N.H. (1982). "Kinetics of Reactions in Wet Flue Gas Simultaneous Desulfurization and Denitrification System," in *Flue Gas Desulfurization*, ACS Symposium Series 188, American Chemical Society, Washington, D.C.
4. Lin, N.H., Littlejohn, D., and Chang, S.G. (1982). "The Thermodynamics and Kinetics of the Coordination of NO to Fe^{2+}(NTA) in Aqueous Solutions," *I&EC Process Res. Dev. 21*, p. 725.
5. Littlejohn, D., Griffiths, E., and Chang, S.G. (1983). "The Reaction of Ferrous Nitrosyl Complexes with Sulfite and Bisulfite Ions," *Energy and Environment Division Annual Report, FY 1982*, LBL-15300, p. 4-88.
6. Oblath, S.B., Markowitz, S.S., Novakov, T., and Chang, S.G. (1982). "Kinetics of the Initial Reaction of Nitrite Ion in Bisulfite Solutions," *J. Phys. Chem. 86*, p. 4853.
7. Littlejohn, D. and Chang, S.G. (1983). "Identification of Species in a Wet Flue Gas Desulfurization and Denitrification System by Laser Raman Spectroscopy," to be published in *Environ. Sci. Tech.*
8. Huie, R.E. and Peterson, N.C. (1983). "Reactions of S(IV) with Transition-Metal Ions in Aqueous Solutions," in *Trace Atmospheric Constituents, Advances in Environmental Science and Technology*, Vol. 12, John Wiley & Sons, New York.
9. Bonner, F.T. and Pearsall, K.A. (1982). "Aqueous Nitrosyliron(II) Chemistry. 1. Reduction of Nitrite and Nitric Oxide by Iron(II) and (Trioxodinitrato)iron(II) in Acetate Buffer. Intermediacy of Nitrosyl Hydride," *Inorg. Chem. 21*, p. 1973.

Reaction of Nitric Oxide with Amine Sulfonates*

D. Littlejohn and S. G. Chang

Several nitrogen-sulfur compounds—including HADS (hydroxylamine disulfonate), HAMS (hydroxylamine monosulfonate), hydroxylamine, ATS (amine trisulfonate), ADS (amine disulfonate), and sulfamic acid—have been found in power-plant flue gas scrubbing liquors.[1,2] It is important to understand the chemistry of these compounds to see what effect they have on scrubber operation.

Several studies have shown that NO reacts with amines,[3] including hydroxylamine.[4,5] No reports of NO reacting with the nitrogen-sulfur compounds mentioned above have been found. It was decided to make a systematic investigation of the reactivity of the nitrogen-sulfur compounds with NO, to enhance our understanding of the chemistry of systems in which these compounds are present.

ACCOMPLISHMENTS DURING FY 1983

Experimental Procedure

Mildly alkaline or neutral pH solutions of the nitrogen-sulfur compounds were prepared and degassed. Known amounts of $KClO_4$ were added to the solutions as a reference so that Raman spectroscopy could be used to monitor changes in concentration of the compounds. One atmosphere of NO was added to the vessel containing the solution and the solution was stirred vigorously to enhance transfer of the NO into solution. Solution samples were examined periodically by Raman spectroscopy to observe any changes in concentration of the nitrogen-sulfur compounds and any appearance of new compounds. Gas samples were withdrawn periodically and analyzed by gas chromatography (GC) to determine if N_2O or N_2 were being produced by the solution.

Results

The rate of reaction under these conditions was found to be negligible for HADS, ATS, ADS, and sulfamic acid. The results obtained for hydroxylamine were in agreement with previous studies.[4,5] The reaction products observed were N_2O and N_2. The reaction mechanism proposed by Cooper *et al.*[4] is:

$$NO + NH_2OH \rightarrow HNO \text{ (or NOH)} + NHOH \text{ (or } NH_2O)$$

$$NHOH + NO \rightarrow N_2O + H_2O$$

$$HNO + NH_2OH \rightarrow N_2 + 2H_2O$$

This was confirmed and expanded upon by Bonner *et al.*[5]

We also observed a significant rate of reaction between NO and HAMS. The solution was at neutral pH to prevent occurrence of alkaline hydrolysis of HAMS.[6] Raman spectra of the reaction mixture indicated the disappearance of HAMS and the appearance of $SO_4^{=}$ in an amount proportional to the loss of HAMS. No other products were observed. Gas chromatographic (GC) analysis of the gas over the solution indicated the presence of N_2O and N_2. Since, in the GC output, the NO peak interfered with the N_2 peak, a gas sample was run on a mass spectrometer to quantify the amount of N_2 present. It was found that the amount of N_2O and N_2 observed is proportional to the amount of HAMS lost. The N_2:N_2O ratio was equal to or slightly greater than 1 at approximately neutral pH.

Proposed Mechanism

The structure of HAMS does not differ too greatly from that of hydroxylamine. In analogy to the NO + NH_2OH mechanism, we propose that the reaction occurs by:

$$NO + NHOH(SO_3^-) \rightarrow NOH \text{ (or HNO)} + NOH(SO_3^-)$$

$$NOH(SO_3^-) + NO \rightarrow N_2O + SO_4^{=} + H^+$$

$$NOH + NHOH(SO_3^-) \rightarrow N_2 + SO_4^{=} + H_2O + H^+$$

This produces only the observed products, and in the proportions observed. A decrease in pH was noted during the reaction, which is in agreement with this

*This work was supported by the Assistant Secretary for Fossil Energy, Office of Coal Research, Advanced Environment Control Division of the U.S. Department of Energy under Contract No. DE-AC03-76SF00098 through the Pittsburgh Energy Technology Center, Pittsburgh, PA

mechanism. There are other reactions involving the nitroxyl radical (NOH) that can occur, such as dimerization and subsequent production of N_2O (Ref. 5):

$$2\ NOH \rightarrow N_2O + H_2O$$

These reactions, as well as the relative rates of the above reactions, the concentrations of the reactants, and the pH of the solution, can affect the N_2O:N_2 ratio. It would be difficult to obtain individual rate constants for the above reactions because of the small concentrations of the intermediates and the difficulty in isolating one reaction so it can be studied without interference from the others.

PLANNED ACTIVITIES FOR FY 1984

We plan to extend the pH range over which the reaction can be studied. It may also be possible to use isotopic tracers to investigate the reaction mechanism in more detail.

REFERENCES

1. Yaverbaum, L.H. (1979), *Nitrogen Oxides Control and Removal, Recent Developments*, Noyes Data Corp., Park Ridge, N.J.
2. Chang, S.G., Littlejohn, D., Lin, N.H. (1982), "Kinetics of Reactions in a Wet Flue Gas Simultaneous Desulfurization and Denitrification System," in *Flue Gas Desulfurization*, ACS Symposium Series 188, American Chemical Society, Washington, D.C., and references therein.
3. Drago, R.S. and Paulik, F.E. (1960), "The Reaction of Nitrogen (II) Oxide with Diethylamine," *J. Amer. Chem. Soc. 82*, p. 96.
4. Cooper, J.N., Chilton, J.E., Powell, R.E. (1970), "Reaction of Nitric Oxide with Alkaline Hydroxylamine," *Inorg. Chem. 9*, p. 2303.
5. Bonner, F.T., Dzelzkalns, L.S., Bonucci, J.A. (1978), "Properties of Nitroxyl as Intermediate in the Nitric Oxide–Hydroxylamine Reaction and in Trioxodinitrate Decomposition," *Inorg. Chem. 17*, p. 2487.
6. Ackermann, M.N. and Powell, R.E. (1966), "Alkaline Hydrolysis of Hydroxylamine-N-Sulfonate," *Inorg. Chem. 5*, p. 1334.

Photoregeneration of Flue-Gas Scrubbing Liquors*

S.G. Chang and E. Griffiths

Untreated flue gases from coal-fired power plants contain substantial amounts of sulfur dioxide (SO_2) and nitric oxide (NO). A number of control strategies to reduce the concentrations of these pollutants to acceptable levels are being developed. One promising technique is to add ferrous chelate catalysts to flue-gas scrubbing liquors: this substantially increases both the solubility of NO and the reaction rates of NO with bisulfite (HSO_3^-) and sulfite ($SO_3^=$). Under these conditions, the efficiency of removing NO and SO_2 in a flue-gas wet scrubber can be improved. However, ferrous chelates in scrubbing liquors are subject to oxidation by residual oxygen, forming ferric chelates, which are inactive. To be economically attractive, a scrubbing solution must be cost-effectively regenerable with little or no loss of active ingredients. One of several methods we are investigating to accomplish this is photoreduction of ferric chelates in scrubbing liquors to regenerate the desired ferrous chelates.

ACCOMPLISHMENTS DURING FY 1983

The quantum efficiency of photoreduction of Fe(III)(EDTA), Fe(III)(citrate), Fe(III)(oxalate) and mixtures of these complexes has been determined at 458, 488, and 514 nm Ar^+ laser lines (Table 1). These quantum efficiencies are calculated from the number of ferrous ions produced as a result of photolysis divided by the number of photons absorbed by ferric chelates during irradiation. The concentration of ferrous ion was determined by *colorimetric* analysis at 630, 570, and 590 nm for Fe(II)(EDTA)NO, Fe(II)(citrate)NO, and Fe(II)(oxidate)NO respectively, which were produced as a result of the coordination of ferrous chelates with NO. Nitric oxide was added into the system either before or after the solutions were irradiated to

*This work was supported by the Assistant Secretary for Fossil Energy, Office of Coal Research, Advanced Environment Control Division of the U.S. Department of Energy under Contract No. DE-AC03-76SF00098 through the Pittsburgh Energy Technology Center, Pittsburgh, PA.

Table 1. Quantum efficiency of photoreduction of ferric chelates.

	Φ (molecules/photon)		
	458 nm	488 nm	514 nm
Fe^{3+}EDTA	0.0127	0.0041 0.0053 0.0051 0.0053[a]	0.00118
Fe^{3+}citrate			
[citrate] = 0.1 *M*	--	0.2053 0.1787[a]	--
[citrate] = 2 m*M*	--	0.0795	--
Fe^{3+} oxalate	1.27	--	--
Fe^{3+}EDTA with citrate			
[EDTA] = 2.16×10^{-3} *M*	/		
[citrate] = 0.1 *M*	--	0.0309 0.0287	--
[citrate] = 0.01 *M*	--	0.0191	--
[citrate] = 2m *M*	--	0.0096	--
Fe^{3+}EDTA with oxalate			
[EDTA] = 2.16×10^{-3} *M*			
[oxalate] = 0.1 *M*	--	0.008	--

[a]NO introduced after photolysis.

determine whether NO has an effect on the chemistry of photolysis of ferric chelates.

Ferric chelate solutions were prepared such that the initial concentration of ferric ion was 7.2×10^{-4} *M* and the liquid concentrations varied from 2.16×10^{-3} to 0.1 *M*. The pH of the solutions was adjusted to 5.9 by adding NaOH and the ionic strength to 1 *M* by Na_2SO_4. The solutions were degassed in a photolysis cell, and one atmosphere of NO was added to the cell while solutions were agitated vigorously to ensure thorough mixing. In the cases when NO was added after photolysis, an atmosphere of inert Ar gas was introduced into the system over the solution prior to irradiation. The solutions were then irradiated with an Ar^+ laser at a selected wavelength. Ultraviolet and visible spectra of the solutions were recorded before and after photolysis on a Cary 219 spectrophotometer.

Table 1 shows that the quantum efficiency is greater at shorter wavelengths for all ferric chelates investigated and that Fe(III)(oxalate) has the largest quantum efficiency for the three wavelengths studied, followed by Fe(III)(citrate) and Fe(III)(EDTA). The quantum efficiency of Fe(III)(EDTA) is enhanced when citrate ion or oxalate ion is present, and increases with increasing citrate ion concentration. The quantum efficiency of Fe(III)(citrate) was found to be dependent on the citrate ion concentrations whereas the quantum efficiency of Fe(III)(EDTA) is independent of the EDTA concentrations.

Preliminary results showed that 0.5 molecules of EDTA were destroyed for every one molecule of ferric ion reduced. This was determined by adding an equivalent amount of ferrous ion to the excess EDTA in the photolyzed solution. Then the increase in concentration of the Fe(II)(EDTA)NO complex was measured, and from this, the amount of EDTA destroyed could be calculated.

The NO was found to have no effect on the chemistry of photolysis of Fe(III)(EDTA) solutions. The quantum efficiency of Fe(III)(EDTA) photoreduction at 488 nm was the same whether NO gas was introduced before or after the photolysis.

PLANNED ACTIVITIES FOR FY 1984

We will extend this study to other ferric chelates such as Fe(III)(NTA) and Fe(III)(IDA). The quantum efficiency of ferric chelates will be determined at wavelengths near the UV region. We will also investigate the mechanism of the photoreduction of ferric chelates. The potential of employing this previously unrecognized technology for the regeneration of flue-gas scrubbing liquors will be assessed.

Detection of N-S Complexes in Lime/Limestone Flue-Gas Desulfurization Scrubbers by Laser Raman Spectroscopy*

S. G. Chang and D. Littlejohn

The lime/limestone system is the most widely used type of FGD (flue gas desulfurization) scrubber in the utility industry for the control of sulfur dioxide (SO_2) emission in power-plant flue-gas at present. There are two types of lime/limestone systems: wet and dry. In a wet system, flue gas is passed through an aqueous slurry of lime or limestone to absorb SO_2. The calcium sulfite and sulfate precipitated as a result of chemical reactions are separated from the scrubbing liquors, which can be recycled. In a dry system, the lime/limestone slurry, a pelletized lime/coal mixture, or both are sprayed into boilers. The SO_2 formed during combustion reacts with the limestone to form calcium sulfite and sulfate salts. The majority of calcium salts remain in the ash bed and are discharged from the boiler along with the bottom ash.

The sludge produced from both wet and dry systems is generally disposed of by ponding or landfill. This sludge should not be harmful if it is composed of fly ash, calcium sulfite, and calcium sulfate, and its disposal should not cause any damage to biological systems. However, power-plant flue gas frequently contains several hundred ppm of nitrogen oxides (NO_x) in addition to up to several thousand ppm of SO_2. In principle, NO_x and SO_2 can interact to yield various N-S complexes. Some of these complexes are toxic and should not be allowed to contaminate sludges to be disposed. Thus, chemical characterization of FGD scrubbing liquors and sludges is needed.

ACCOMPLISHMENTS DURING FY 1983

We have analyzed both liquid and solid samples of several power-plant lime/limestone scrubbers by laser Raman spectroscopy (LRS). The advantages of LRS include a rapid and simple analysis procedure, simultaneous and unambiguous identification of a large number of species, and the ability to analyze a sample *in situ*. Unlike the case with infrared spectra, water does not interfere significantly with Raman spectra.

The Raman system employed in this study utilized a Coherent Innova 90 argon ion laser as excitation source and a Spex Ramalog spectrometer. Spectra were generally obtained using the 514 nm argon ion line as the exciting light. Liquid samples were contained in capillary tubes, while solid samples were ground to fine powders and were laid on a flat glass plate for Raman analysis. Quantitative information of chemical species in samples was obtained from their relative Raman scattering efficiencies with respect to the efficiencies of a known amount of $KClO_4$ that was added to the samples.

Examples of these Raman spectra are shown in Figs. 1–3. Figure 1 shows the Raman spectra of a scrubbing liquor for a pilot-plant scrubber at the Arapahoe power plant in Denver, Colorado; Fig. 2, the spectra of a solid precipitate obtained from a wet lime/limestone FGD scrubber for a power plant in Indiana; and Fig. 3, the spectra of a water extract of solid particulates from a spray-drying lime/limestone scrubber. A Raman shift at 1085 cm^{-1}, assigned to hydroxylamine disulfonate, $HON(SO_3)_2^{2-}$, was detected in all three samples. The 941 and 935 cm^{-1} wavelengths are due to $KClO_4$ and ClO_4^-, respectively. The assignments of the peaks and the quantitative determination of species in these samples are tabulated in Table 1.

From the results obtained, we conclude that N-S complexes can indeed be produced in substantial quantity in some wet and dry lime/limestone FGD scrubbers.

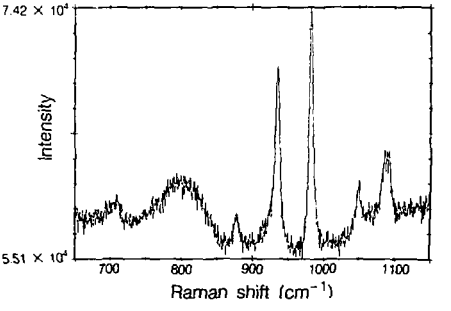

Figure 1. The Raman spectrum of a scrubbing liquor for a pilot plant scrubber at the Arapahoe power plant in Denver, Colorado. (XBL 844-1570A)

*This work was supported by the Electric Power Research Institute through the U.S. Department of Energy under Contract No. DE-AC03-76SF00098.

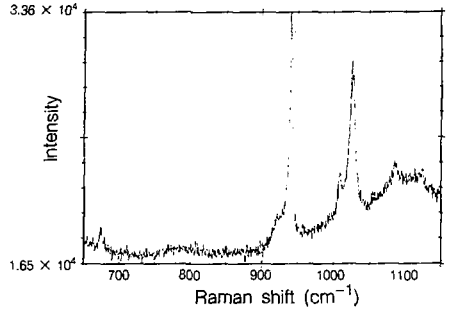

Figure 2. The Raman spectrum of a solid precipitate obtained from a wet lime/limestone FGD scrubber of a power plant in Indiana. (XBL 844-1571A)

PLANNED ACTIVITIES FOR FY 1984

We will make quantitative determinations of N-S complexes in both scrubbing liquors and solid precipitates of many more lime/limestone FGD scrubbers in the nation by laser Raman spectroscopy. These results will be compared with those of the Radian Corporation (Austin, Texas) and the Brown and Caldwell Corporation (Emeryville, California), using the ion chromatographic technique. We will also investigate the chemistry of N-S complexes in lime/limestone FGD systems, including their solubility, reactivity, and formation kinetics and mechanisms as influenced by the impurities and operating conditions of FGD systems.

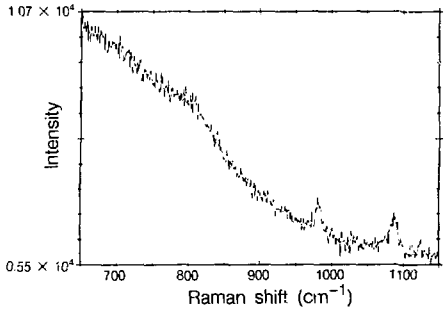

Figure 3. The Raman spectrum of a water extract of solid particulates from a spray-drying lime/limestone scrubber. (XBL 844-1572A)

Table 1. Characterization of chemical species in lime/limestone FGD systems by laser Raman spectroscopy.

	Raman lines (cm^{-1})									
Samples	1086	1050	1026	1009	982	941	935	877	710	674
Arapahoe scrubbing liquor	HADS ($6\times10^{-3}M$)	NO_3^- (6.7×10^{-3})			$SO_4^=$ (3×10^{-2})		IO_4^- ($\times10^{-2}$)	?	$S_2O_6^{2-}$ (5.8×10^{-3})	
IPU solid PPT	HADS		$2CaSO_4\text{-}H_2O$		$CaSO_4\text{-}2H_2O$		$KClO_4$		$2CaSO_4\text{-}H_2O$	
Spray-drying water-extraction	HADS				$SO_4^=$					

Study of the Disproportionation of Sodium Thiosulfate by X-Ray Photoelectron Spectroscopy*

X.B. Xu[†] *and S.G. Chang*

Thiosulfates are thermally unstable and decompose to form sulfite and elemental sulfur with heat treatment. The kinetics of disproportionation of thiosulfates has not been investigated, however. This knowledge is needed in the power-plant flue-gas clean-up industry, where thiosulfates can be generated or may be employed as an additive in some flue-gas desulfurization processes.[1]

ACCOMPLISHMENTS DURING FY 1983

The kinetics of the disproportionation of sodium thiosulfate was studied with a photoelectron spectrometer (AEI model ES200). (This method, photoelectron spectroscopy, is referred to as XPS.) Sodium thiosulfate samples were prepared by spraying an aqueous solution of 1% $Na_2S_2O_3$ from a glass nebulizer onto clean aluminum foils (~6 × 12 mm) and then dehydrated by heat treatment in an oven at 338 K for at least 24 hours. The average thickness of the sample material on the aluminum foil was calculated from the total sulfur content as determined by x-ray fluorescence analysis and from the morphology of samples depicted by an ISI model DS-130 scanning electron microscope (SEM). Samples were heated by a resistance heating element in the sample holder under vacuum. The XPS spectrum of the S ($2p_{1/2,3/2}$) region of $Na_2S_2O_3$ samples was taken periodically after the samples had reached a desired temperature. The temperature range studied was 495–548 K. The kinetic data were obtained from the change of XPS spectrum intensity of reduced sulfur (S^{2-}) in $Na_2S_2O_3$ as a function of heating time at a given temperature.

Figure 1 illustrates the use of XPS in monitoring the changes in concentrations of oxidized and reduced sulfur species during the course of the sodium thiosulfate disproportionation. The binding energies of the sulfur $2p_{1/2,3/2}$ electrons of oxidized (S^{6+}) and reduced (S^{2-}) sulfur in sodium thiosulfate are 168.4 and 162.3 eV, respectively. Both types of

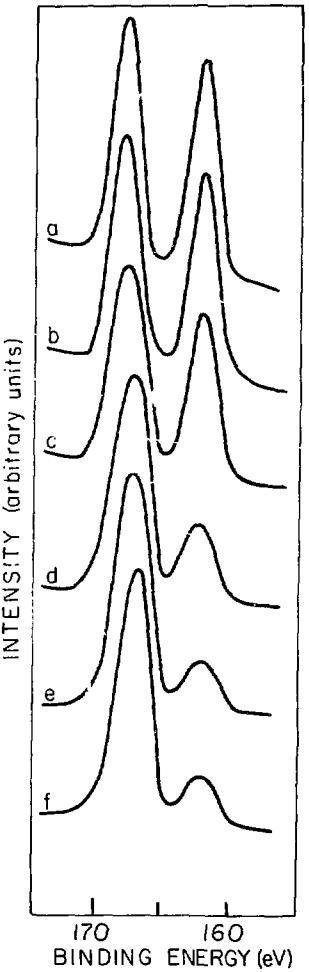

Figure 1. Sulfur (2p) photoelectron spectra of $Na_2S_2O_3$ at 523 K, showing changes in intensity of the reduced sulfur and shifts in binding energy of oxidized sulfur as a function of time of heating; *a*, *b*, *c*, *d*, *e*, and *f* correspond to 0, 3, 6, 11, 15, and 20 minutes of heating, respectively.
(XBL 838-6250)

*This work was supported by the Assistant Secretary for Fossil Energy, Office of Coal Research, Advanced Environment Control Division of the U.S. Department of Energy under Contract No. DE-AC03-76SF00098 through the Pittsburgh Energy Technology Center, Pittsburgh, Pennsylvania.

†On leave from the Institute of Environmental Chemistry, Chinese Academy of Sciences, Beijing, People's Republic of China.

sulfur species show approximately the same intensity (Fig. 1a). XPS intensity of the reduced sulfur decreased along with the heating, as shown in Fig. 1b-f. Whereas the intensity (measured by integrating the peak area) of the oxidized sulfur remains constant, there is a small shift in the binding energy toward the low energy side. We attribute this shift of binding energy to the chemical conversion of $Na_2S_2O_3$ to Na_2SO_3. The binding energy of the sulfur $2p_{1/2,3/2}$ electrons in Na_2SO_3 is 166.7 eV, which is too close to that of oxidized sulfur in $Na_2S_2O_3$ to be resolved with the XPS spectrometer employed for this experiment.

The production of elemental sulfur could not be detected by XPS techniques because of vaporization under the high vacuum and temperature conditions employed. The major sulfur vapor species at temperatures employed in this experiment (495–548 K) is S_2.[2] The disproportionation of thiosulfate can be represented as

$$Na_2S_2O_3 \rightleftharpoons Na_2SO_3 + 1/2S_2 \uparrow$$

The rate equation of a first-order reaction can be expressed as

$$\ln C_o/C = k(t - t_o)$$

where C_o and C are the concentrations of reactant at times t_o and t, respectively, and k is the rate constant. Figure 2 is a typical curve of the plot of ln C_o/C versus t for the disproportionation of sodium thiosulfate. The reactant concentration ratio, C_o/C, was taken as the intensity ratio of the undecomposed reduced sulfur at time t_o to t (normalized to the intensity of the oxidized sulfur), as observed by XPS. This figure suggests that the disproportionation might begin with an induction period (section I), followed by a steady-state regime (section II), and end with a period where the diffusion rate of species from the bulk to the surface seems to be the controlling factor (section III). The duration of the induction period was shorter, and the steady-state disproportionation rate was faster, with the increase in temperature.

The effect of temperature changes on the steady-state disproportionation-decomposition rate constants was studied. When the transition-state theory[3] is applied, the rate constant for the disproportionation of $Na_2S_2O_3$ can be expressed as

$$k \geq (k'T/h)\, e^{S^{\neq}/R}\, e^{-H^{\neq}/RT}$$

where k' and h are the Boltzmann and Planck constants, respectively. The enthalpy and entropy of activation for the disproportionation can be calculated as $H^{\neq} = 26.0$ kcal/mol and $S^{\neq} = -14.9$ e.u. The lower limit for the rate constant was used because in several much thicker sample specimens (average thickness was not determined), we obtained slower disproportionation rates. We attribute this result to the slow heating rate of the samples.

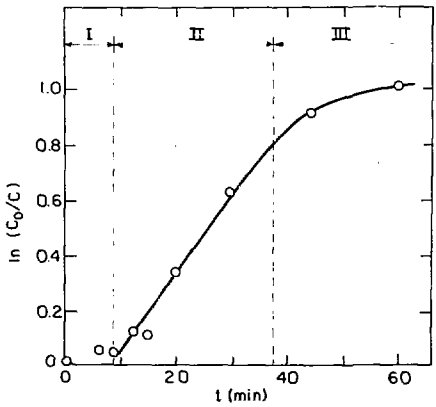

Figure 2. A plot of ln C_o/C as a function of time of heating of $Na_2S_2O_3$ at 498 K. (XBL 838-6248)

PLANNED ACTIVITIES FOR FY 1984

The effect of thiosulfate ion on the reactions involved in a wet flue gas scrubber will be investigated.

REFERENCES

1. Martin, A.E., Ed. (1981), *Emission Control Technology for Industrial Boilers*, Noyes Data Corporation, Park Ridge, N.J.
2. Wiedemeir, H., and Csillag, F. (1980), "The Decomposition and Thermodynamic Properties of SnS_2," *High Temp. Sci. 12*, p. 277.
3. Benson, S. (1960), *The Foundations of Chemical Kinetics*, McGraw-Hill, Inc., New York, p. 225–266.

A High-Pressure, Rapid-Mixing Flow System to Study Synergistic Effects of Metal Ions on S(IV) Oxidation by Raman Spectroscopy*

S. Wolfgang and S. G. Chang

Metal ions in solution can effect changes in the rate of sulfite oxidation by oxygen. Since actual operating flue-gas desulfurization (FGD) systems contain many metal impurities, mixed metal ion systems should be investigated to determine if synergistic effects on the oxidation of sulfite or bisulfite—the S(IV) ions—occur.

ACCOMPLISHMENTS DURING FY 1983

A high-pressure, rapid-mixing flow system has been designed to study this synergism by laser Raman spectroscopy. Because, in general, a concentration of solution species of at least 10^{-2} *M* is necessary to obtain an adequate Raman scattering signal, we must operate at oxygen partial pressures in the vicinity of 10–50 atm, i.e., between roughly 1×10^{-2} and 5×10^{-2} *M* O_2.

A schematic of the rapid-mixing flow system appears in Fig. 1. Aqueous solutions of O_2 and bisulfite (HSO_3^-) are driven from separate feed tanks to a mixer by O_2 and N_2 gas pressure, respectively. Both tanks may contain any combination of dissolved metal ions, including Fe^{3+}, Mn^{2+}, and Cu^{2+}, among others. Flowmeters will be used to measure the flow rate of each feed stream. The progress of the reaction can be followed by Raman scattering of an incident Ar ion laser beam through a quartz window, positioned downstream from the mixer. The spent fluid will be collected in an exhaust tank. The system has been designed for operation under either continuous-flow or stopped-flow conditions.

The system will be constructed primarily from stainless steel, a choice dictated by the high operating pressure, 1500 psi. However, steel surfaces that would be wetted will be lined with an inert substance, thereby preventing the metal from leaching into and reacting with the solution and complicating our investigation of the synergistic effects. Thus, the feed tanks, valves, metal parts of the flow meters and mixer, and the end fittings, which are all stainless steel, will be gold-plated, and flexible Teflon-lined stainless steel hose will transport the fluid from the feed tanks to the observation window. The mixer will be machined out of solid Teflon and encased in a stainless steel housing. A porous Teflon plate will be mounted slightly above the base of each feed tank to aid in dispersing the gas throughout the solution. The top of the feed tank will be a threaded cap that can be readily disassembled for filling with solution. The quartz observation window will be held between two Teflon mounts and sealed with an O-ring. The mounts are inserted into stainless steel flanges, which are then draw-bolted together. The exhaust tank and all tubing downstream from the observation window will be stainless steel.

The dimensions of all components in the system were determined in compliance with the ASME code for pressure vessels. The Teflon-lined stainless steel hoses are ¼-inch nominal size, i.e., 7/32-inch i.d. All stainless steel tubing will be ¼-inch o.d. with a 0.035-inch wall thickness. Two 4-foot-tall 5-inch i.d. steel feed tanks will be constructed to provide a maximum capacity of about 16 liters per tank. Two 6-gallon polyethylene containers will collect the spent fluid.

Turbulence is required to mix the two solutions and to maintain homogeneity in the mixture as it flows from the mixer to the observation window. The mixing chamber is thus designed to increase the fluid velocity and create a vortex. Turbulence in the tube leading from the mixer to the observation window can be achieved at flow rates exceeding 60 L/hr. The flowmeters are useful up to flow rates of about 144 L/hr so that the range for continuous flow measurements is 60–144 L/hr.

PLANNED ACTIVITIES FOR FY 1984

With this setup, we will be able to study the reactions at high concentration conditions and to monitor the concentration of reactants and products *in situ* during the course of reactions. The ratio of the reactants consumed and the relative amounts of sulfate and dithionate produced as a function of reaction conditions will be measured. Attempts will be made to detect the reaction intermediates and obtain a reaction rate law.

*This work was supported by the Electric Power Research Institute through the U.S. Department of Energy under Contract No DE-AC03-76SF00098.

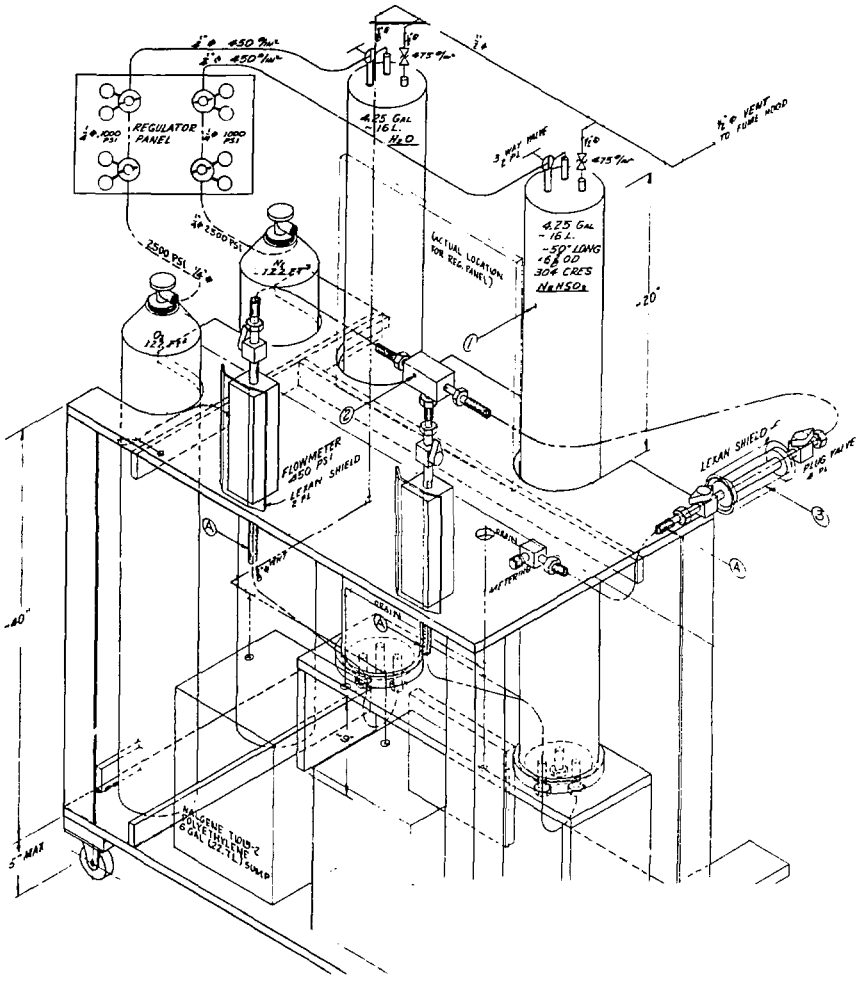

Figure 1. Layout of the high-pressure, rapid-mixing flow system.

(XBL 844-1576)

Aquatic Microcosms for Ecotoxicology*

J. Harte, D. Levy, J. Oldfather, J. Rees, and R. Schneider

As part of the Lawrence Berkeley Laboratory's Lake Ecotoxicology program, this project evaluated—and enhanced—the role of lake microcosms in testing the ecological effects of toxic substances. Microcosm designs and operating procedures were developed and assessed, using as criteria the replicability of the microcosms, the similarity of their chemical and biological conditions to those of natural water bodies, and the simplicity and robustness of these designs and procedures. In addition, the microcosms were applied in a study that provided a realistic context for evaluating their role in ecotoxicology.

ACCOMPLISHMENTS DURING FY 1983

Our research on optimal design and operating procedures focused on two problems. One concerned methods for including benthic sediment cores in freshwater lake microcosms and the other concerned the determination of the optimal level of water turbulence in the pelagic zone of the microcosms. The role of the benthos and of water turbulence has previously been investigated in freshwater lakes and in marine microcosms, but not in freshwater lake microcosms.

Water turbulence is important in limnology because it affects the rate at which suspended particles, including nonmotile plankton, settle out of the water column. It can also influence the distribution of nutrients in the immediate vicinity of organisms. The small depth of microcosms, in comparison to reservoirs and most natural lakes, could result in shorter residence times in the water column for organisms that sink due to gravity. To compensate for this, it has been suggested that greater turbulence may be required in a microcosm than in the lake it is designed to simulate. A theoretical scaling argument also suggests that caution must be exercised when placing benthic materials in microcosms. In particular, the top of the benthos will exert an exaggerated influence on the relatively shallow water column of microcosms unless the surface area of the benthic zone is scaled down appropriately. A systematic series of experiments was therefore carried out to determine optimal design and procedures for including turbulence and benthic materials in freshwater microcosms.

The microcosm application was designed to explore the use of microcosms for hypothesis testing and for developing and validating mathematical models of lake chemistry and biology. In this study, data previously obtained from microcosms in our laboratory were compared with a variety of mathematical models in order to test our hypothesis about decomposer-detritus interactions in freshwater ecosystems. The data were collected by adding various amounts of organic materials to lake microcosms and observing the subsequent changes in inorganic nitrogen and carbon, and in phytoplankton and zooplankton population densities.

Experimental Designs

Microcosm Design Studies

For the research on microcosm design and procedures, microcosm contents, including water, benthic cores, and aquatic organisms associated with both media, were obtained from lakes and ponds in California and Colorado. Both low-elevation hardwater lakes and subalpine softwater lakes and ponds were studied. Each experiment simulated a single water body. Most of the experiments were carried out in a controlled laboratory environment specifically designed and constructed to allow regulation of water temperatures and the day-night light cycle. The only exception was an exploration of the technique of floating microcosms in subalpine ponds. In this technique, the microcosm tank is floated in the natural water body to achieve realistic temperature and light conditions. The method is particularly appropriate for the study of remote water bodies for which the logistics of bringing back large quantities of water to a laboratory are prohibitive.

All microcosms were operated as batch systems, with no flow through to replenish organisms or nutrients. Microcosms of 50 liters volume were used

*This research was supported by the Electric Power Research Institute, the U.S. Environmental Protection Agency, and the U.S. Department of Energy under Contract No. DE-AC03-76SF00098.

for most experiments, particularly those of several months' duration. Four-liter tanks were used for shorter runs and for the subalpine pond studies.

To prevent the build-up of algal wall growth, the contents were transferred periodically to clean containers by a pouring procedure that leaves surface growth behind and transfers all pelagic materials. Standard methods were employed for all chemical and physical measurements and for the taxonomic and population density determinations. Most microcosm treatments were run in triplicate to assess replicability and to provide a base for statistical analysis. In some cases, quadruplicate or duplicate treatments were used.

Turbulence Studies

Our investigation of optimum turbulence rates used microcosms initiated with epilimnionic waters from a San Francisco Bay area reservoir. These microcosms were housed in a controlled-environment facility (to be described later) and were subjected to various magnitudes of water agitation. Agitation rates were measured and quantified in both the reservoir and the microcosms by measuring the rate of dissolution of tethered gypsum blocks. During the experimental runs, plankton population densities and chemical nutrients in the microcosms were compared with those in the reservoir; these parameters defined the realism and replicability of the microcosms.

Benthic Cores

To evaluate benthic microcosms, special cylindrical compartments were designed and constructed. These chambers were built in two sizes (similar height, different diameter) to investigate the influence of benthic surface area on microcosm realism. In one mode of operation, the sediments fill the chambers to within 1 cm of the top; however, screw-on extenders can raise the top about 15 cm above the sediment surface, thus partially shielding the sediments from water agitation. The chambers and extenders can be covered with a removable screw-on cap to allow measurement of sediment-zone oxygen profiles and respiration rates. The chambers were also designed to double as sediment coring devices so that the cores need not be disturbed by transfer from the lake to the microcosms.

Experiments to determine optimum procedures for including benthic cores in microcosms were carried out under two sets of conditions. In one, similar to the turbulence studies, 50-liter microcosms were stocked with water and sediment cores from a nearby reservoir and housed in the LBL microcosm facility. In the second, 4-liter microcosms were stocked with water and sediment cores from a subalpine pond on the western slope of the Colorado Rockies. These microcosms were placed on a wooden structure floating semi-submerged on the pond. In both experiments, chemical and taxonomic variables in the microcosms were compared with those in the parent water bodies.

The Microcosm Facility

Earlier research in our laboratory[1] had established the importance of matching microcosm water temperature to that of the lake being simulated. Achieving this by room air conditioning had proved to be impractical, and a new microcosm facility was therefore designed and constructed.

The facility has two rooms, each capable of containing up to twelve 50-liter tanks. For temperature control, water of the desired temperature flows through copper piping in contact with an outer jacket of water surrounding the microcosm containers. This system provides more precise temperature control, colder temperatures (needed to simulate winter time and subalpine conditions), and less energy consumption than the previous air-controlled coldroom facility. Other features of the new facility include a greater and more uniform illumination intensity before, a clock-regulated illumination schedule, a relatively dust-free environment to reduce the potential for air-borne colonization of the tanks, and a water trap for ammonia in the aeration system to prevent atmospheric NH_3 from entering the microcosm waters.

This controlled-environment facility has proved to be of great value not only in the microcosm assessment studies but also in the subalpine lake acidification experiments, for which water temperatures well below ambient were essential.

Results and Discussion

Turbulence Studies

The experiments designed to assess the effect of various water agitation rates showed that, as measured by gypsum dissolution, this rate must be lower in the microcosms than in the reservoir to optimize realism and replicability.[2] Although this result appears to contradict the theoretical expectation that turbulence should be higher in the microcosms than in deep lakes, experiment and theory can be reconciled by recalling that gypsum blocks suspended in

water will dissolve from both turbulence and laminar flow. Laminar flow is present in reservoirs in the form of large-scale currents, but is relatively absent in the microcosms. Thus, equal rates of gypsum dissolution in the two water bodies correspond to greater turbulence rates in the microcosms. Moreover, the periodic transfer of microcosm contents to clean containers (to prevent wall growth of algae), also serves to resuspend sinking cells in the water column, and this agitation is not measured by the gypsum block method.

The data from these experiments suggest that agitation rate affects plankton dynamics through its influence on grazer populations; higher levels of agitation suppress these grazers, which in turn leads to enhanced phytoplankton populations. The mechanism by which agitation affects grazer populations has not been identified.

Benthic Cores

One of the benthic core assessment studies has demonstrated that the top surface area of the benthic chamber exerts a significant influence on the realism of the planktonic population densities in the overlying water. In one set of replicates, the ratio of the benthic core area to the overlying water volume was set roughly equal to the ratio of lake sediment to lake volume; in another set, the ratio was 10 times larger in the microcosms than in the source reservoir; and in a third set, there were no sediment cores. The planktonic population densities in the first set were statistically indistinguishable from those in the reservoir, while densities in the other two sets generally were not. This is in conformity with theoretical expectations based on scaling laws.

The second benthic core assessment study was carried out in the Galena Lake/Mexican Cut watershed in the Colorado Rockies. Here, the technique of floating microcosm tanks in the natural water body was used. In this study, the benthic chambers were all one size, and the results were compared with controls in which no benthic materials were present. The dominant phytoplankton in the tanks with benthic cores were again statistically indistinguishable from those in the lake, whereas the ones in the controls were not. However, replication was rather poor, so this experiment is not as definitive as the first. The poor replication was judged to result from the considerable spatial heterogeneity of the lake sediments from which the benthic materials were taken.

Microcosm Application

Detritus addition experiments carried out prior to this project investigated the quantitative details of the process by which organic matter stimulates the growth of microbe populations and produces inorganic nutrients by decomposition. Highly replicable and unexpected behavior was observed.[3] In particular, a threshold phenomenon was seen in which inorganic nutrient production was a steeply increasing function of the amount of detritus added when these additions exceeded a critical value. By introducing into a mathematical model of the microbe-detritus-nutrient system the notion of a microbe carrying capacity, and by assuming that microbes utilize for their population growth all inorganic nitrogenous products of decomposition until that capacity is reached, a successful description of the observed phenomena was obtained.[4]

The success of this approach allows a relatively simple procedure for measuring microbial carrying capacities in aquatic systems. Moreover, it makes possible the determination of the ambient and stimulated (by organic additions) rates of decomposition in these waters. Finally, by using the model to analyze the results of experiments in which organic matter *and* a toxic substance are added to a microcosm, practical damage indices measuring the effect of a toxin on decomposition rates and microbial carrying capacities can be extracted.

Summary

The overall conclusion of our research in FY 1983 is that, with the proper operating features incorporated into the experimental design, freshwater lentic microcosms can simulate the chemical and planktonic behavior of lakes and ponds to an extent that is adequate both for ecotoxicological testing and for hypothesis testing of fundamental ecological mechanisms.

PLANNED ACTIVITIES FOR FY 1984

No further work to assess the validity of microcosms is planned. Future work will focus on applications of microcosms to study the effects on aquatic ecosystems of environmental stresses such as acid precipitation, prolonged darkness, and toxic chemicals.

REFERENCES

1. Harte, J., Levy, D., and Rees, J. (1983), "Pelagic Diatom Populations in Lentic Freshwater Microcosms," *Int. Rev. Ges. Hydrobiol. 68*, p. 255.
2. Harte, J. *et al.* (1983), *Realism and Replicability of Freshwater Lentic Microcosms*, LBL-16133, submitted to *Freshwater Biology*.
3. Harte, J., and Levy, D. (1983), "Responses of Lake Waters to Organic Matter Additions," *Hydrobiologia 107*, p. 203.
4. Harte, J. (1982), "Modeling Lake-Water Mineralization Processes," *J. Theor. Biol. 99*, p. 553.

Acid Precipitation and Surface-Water Vulnerability on the Western Slope of the High Colorado Rockies*

J. Harte, G.P. Lockett, R.A. Schneider, H. Michaels, and C. Blanchard

This research is part of a long-term project to investigate the effects of acid precipitation on a sensitive watershed. The watershed has been studied over a 3-year period to date (1980–1983), but data from a 1972 investigation are also available. An advantage of the site is that it contains two drainages, one apparently more vulnerable to acid precipitation than the other, thus providing an opportunity for comparative studies. Alkalinity, pH, anion, and cation measurements for surface-water samples are made regularly, as are censuses of acid-sensitive species.

Findings of the project so far may be summarized as follows: The volume-weighted average pH was 4.61 for summer events, 4.79 for winter events, and 4.74 for the entire 3-year period. Within the watershed, surface-water alkalinities ranged from 20 μeq/L to 900 μeq/L.

ACCOMPLISHMENTS DURING FY 1983

Site Description

Our study site is a remote and relatively pristine high-elevation watershed located in the Elk Mountains of west-central Colorado. The specific site is the Galena Mountain/Mexican Cut Preserve (latitude 39° 01′ 30″ N, longitude 107° 04′ 00″ W), in Gunnison County, Colorado, on land largely owned by the Nature Conservancy. The preserve is a hydrologically self-contained watershed on the eastern side of Galena Mountain. It has never been logged, and there has been no mining for several decades. Galena Mountain is composed of the Morrison and Maroon formations, which include metamorphosed quartzite, siltstone, sandstone, and shale. Near the peak of Galena Mountain and surrounded by it on three sides is Galena Lake, a tarn of approximately 30,000 m^2 in area, 12 m maximum depth, and 3670 m elevation. The terrain surrounding the lake is alpine tundra. The topography below it consists of two shelves (the Mexican Cut). The Lower Cut is open subalpine forest of englemann spruce (*Picea engelmannii*) and subalpine fir (*Abies lasiocarpa*).[1] The Upper Cut is characterized by sparse, dwarfed spruce and fir, or "krummholz." Some outcroppings of limestone occur in the Upper Cut. Ponds are situated in both the Upper and Lower Cuts, which from the time of snow melt until midsummer are connected by small streams, as shown in Fig. 1. As summer progresses, these surface flows dry up.

The Lower Cut contains two parallel drainages separated by a low quartzite ridge. The separation is nearly complete hydrologically, since concentrations of some chemical species vary greatly from one drainage to the other. In particular, alkalinity had a range of 200–350 μeq/L in the drainage that is closer to the Upper Cut and 20–70 μeq/L in the other drainage. An earlier investigation by Dodson[2] showed a wide spectrum of biological and chemical conditions among six of the ponds in the Lower Cut. Four of Dodson's ponds are in the low-alkalinity drainage, and two in the high-alkalinity drainage. For the surface-water measurements of this study, we sampled Dodson's sites plus 23 others, including several in the Lower and Upper Cuts, Galena Lake itself, and its inflow streams.

Methods

Surface-water was collected in 1-liter polyethylene bottles. Rain was collected in plastic

*This work was supported by the Nature Conservancy, the Hewlett Foundation, the Maki Foundation, and the U.S. Department of Energy under Contract No. DE-AC03-76SF00098.

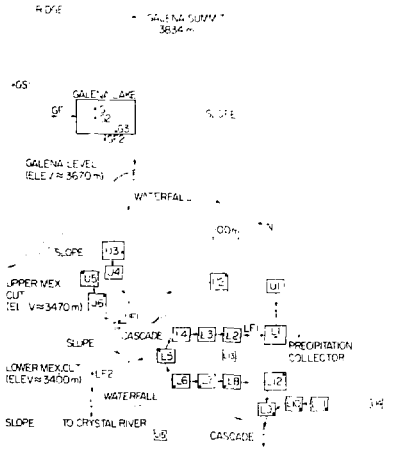

Figure 1. A schematic map of the Galena Mountain/Mexican Cut watershed. Sampling sites are indicated by dots: the lake and ponds by boxes; and connecting streams by lines with arrows in the direction of flow. (XBL 825-674)

buckets (Aerochem Metries) mounted to avoid the collection of rain splash and located in a meadow 20 m from the nearest trees. Snow was collected on a snow board in a meadow near the Rocky Mountain Biological Laboratory, about 10 km southeast of the study site, at an elevation of 2900 m. Rain and snow were collected on an event basis within minutes after each event. (An event is a discrete, more or less continuous precipitation period, such as a storm.) Some events were sampled at subintervals during the event.

The pH of precipitation and surface waters was determined potentiometrically. From July 1980 to May 1981, pH readings were taken while stirring. Subsequently, they were read unstirred. Tests conducted on the type of electrode used in the earlier period demonstrate that stirred measurements are 0–0.1 pH units lower than quiescent readings. While the earlier measurements are thus not strictly comparable to the later ones, the bias is small. The alkalinity of surface-water samples was measured by titrating with a strong acid; endpoints were determined by the Gran method.[3,4] Precipitation pH measurements were usually made within 6 hours after collection and always within 24 hours. Alkalinity and pH of surface waters were generally measured within 6 hours of collection. The precision of pH measurements was $s = 0.06$ pH units. The precision of alkalinity measurements varied with alkalinity, $s = 4.09 + 0.023(\text{alk})$ μeq/L. Commencing in August 1982, the accuracies of pH and alkalinity measurements were checked through the use of dilute strong acid and Na_2CO_3 standards.

Results and Discussion

Table 1 shows averages of the H^+ concentrations over three summer and three winter precipitation seasons. Precipitation occurs as snowfall from about November to May; most of the remainder of the year's precipitation is from thunderstorms in July and August. Data are presented separately for summer and winter because the chemical composition of snowfall may be quite different from that of rain. The difference in location of the summer and winter sampling sites appears unimportant, as judged by some summer measurements made simultaneously at the two sites. All 15 of the precipitation samples with pH ≤ 4.1 are from the first winter (1980–81). In the subsequent two winters, only three events with pH ≤ 4.5 occurred. Precipitation pH figures were high (5.6–6.8) each year during April or May. Mean pH was similar for each summer, with little variation about the mean. All summer average pH readings were lower than the averages for the second and third winters. These data contrast with observations reported elsewhere that the widest pH range occurs in summer.[5]

The seasonal variation described above and further analysis of the precipitation data indicate that the underlying mechanisms controlling precipitation chemistry at this site are complex. Individual event H^+ concentrations correlate poorly with event water volume ($r^2 = 0.08$, $n = 217$) and with the time interval since the last event ($r^2 = 0.02$, $n = 217$). The data thus do not show a simple dilution of acidic materials with increasing storm volume. Nor do the data demonstrate a simple washout effect that might be attributable to frequency of precipitation. These results do not change appreciably if the data of each season are analyzed separately. A plausible contributing factor is airborne dust from the alkaline soils of the Great Basin.[6] Long intervals between storms may allow acidic materials to build up in the atmosphere under some circumstances, and, under other circumstances, the intervals may allow alkaline agents to build up.

Table 2 shows lists average pH and alkalinity at representative surface-water sites in the watershed. At about half the lentic sites, the alkalinity averaged approximately 40 μeq/L throughout the ice-free

Table 1. Precipitation $[H^+]$ averages as pH.

Period	Dates	Number of events	Event average[a] (pH units)	Precipitation amount (cm)[b]	Precipitation weighted average[c] (pH units)
Summer I[d]	7/80	4	4.4		
Winter I	12/80–5/81	35	4.2	28.7	4.3
Summer II	7/81	14	4.64	7.3	4.68
Winter II	11/81–4/82	40	5.11	54.0	5.17
Summer III	6/82–9/82	59	4.50	13.3	4.48
Winter III	11/82–5/83	43	5.10	50.4	5.16
Summer IV	6/83–9/8	32	4.62	20.2	4.69
All summers		105	4.55	40.8	4.61
All winters		118	4.61	133.1	4.79
Entire period	12/80–9/83	223	4.59	173.9	4.74

[a]Event average $= -\log \sum_{i=1}^{N} \frac{[H_i^+]}{N}$, where N = number of events for the time period.

[b]Precipitation amount is the liquid depth of the precipitation contributing to the sample (water equivalent for snowfall).

[c]Precipitation-weighted average =

$$-\log \left\{ \frac{\sum_{i=1}^{N} [H^+]_i (\text{precipitation amount})_i}{\sum_{i=1}^{N} (\text{precipitation amount})_i} \right\}$$

where N = number of events.

[d]Precipitation amounts not measured. Not all events were sampled. This period is not included in the averages.

periods of 1981, 1982, and 1983. This low alkalinity indicates vulnerability to acidification. The highest alkalinities (400–900 μeq/L) in the watershed were found in ponds U5 and U6 (Fig. 1). These ponds are situated near the limestone outcroppings of the Upper Cut, and geological maps indicate the presence of subsurface limestone in the drainage above these ponds. These facts suggest that inflowing ground water in contact with limestone is the source of the alkalinity.

Of particular interest in studying watershed acidification are long-term trends in alkalinity. During summer 1972, Dodson measured alkalinities for six ponds in the Lower Cut.[2,7] Alkalinity measurements for these ponds from 1972, 1982, and 1983 (and 1981 measurements for two of the ponds) are plotted in Fig. 2. An endpoint correction was applied to Dodson's 1972 data[8] to account for the difference in methods of computing alkalinity. We determined alkalinities using Gran functions; Dodson titrated to a fixed pH (5.20). Our alkalinities are generally at or below the levels reported for 1972. Unfortunately, we cannot rule out differences in measurement technique as the source of the difference between our measurements and the earlier data. Furthermore, the annual variations displayed in the more recent years are large. We find the differences between ours and the earlier data suggestive, but cannot conclude that a trend exists in surface-water alkalinity over the 10-year period.

The annual and weekly variations, however, are larger than can be explained by analytical and sampling error. These variations, as well as differences between 1972 and the present, cannot be accounted

Table 2. Surface-water pH and alkalinity.

	Average pH			Average alkalinity (μeq/L)		
Site[a]	1981	1982	1983	1981	1982	1983
L1	7.49	7.20	7.30	222	226	235
L5	7.22	6.84	7.22	205	220	248
L8	6.43	6.18	6.43	39	31	45
L9	6.24	6.24	6.23	25	25	41
L10	6.06	6.15	6.22	59	40	56
L12	6.69	5.34	6.32	28	19	34
LF2	7.43	7.23	7.38	207	199	232
U3	7.53	7.22	7.11	175	118	131
U4		7.22	7.15		132	157
U5	7.72	7.44	7.42	462	445	459
U6	8.10	7.24	7.71		445	691
UF1	7.54	7.22	7.23	332	161	221
G	6.66	6.29	6.51	30	18	31
GF1	6.33	6.12	6.24	15	13	20
GF2	6.46	6.28	6.46	23	18	26

[a]See Fig. 1.

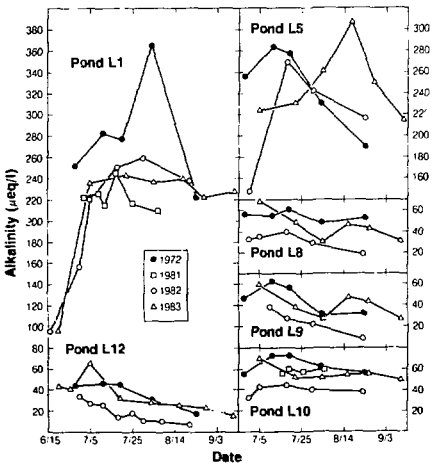

Figure 2. Summer alkalinity data for ponds L1, L5, L8, L9, L10, and L12 for 1972, 1981, 1982, and 1983.
(XBL 8311-4464)

for by processes such as plant succession or soil formation because the time-scale of the variations is too short. Nor can the effects of human land use play a role, since the watershed was never logged and is now used only for research. It is more likely that short-term variability is caused by hydrological factors. The volume of precipitation can cause seasonal changes in alkalinity by varying the hydrologic flushing rate in a watershed.[9] An unusually late snow melt in 1983 and the occurrence of very heavy storms that summer may account for the differences between 1982 and 1983. Biological factors, such as productivity, may also explain part of the weekly variability. In order to separate long-term trends from short-term fluctuations, both a better understanding of the site-specific factors affecting surface-water alkalinity and data covering a longer time span are needed.

An attempt to include biological effects of acidification is also being made. For example, *Ambystoma tigrinum*, a species of salamander inhabiting many of the ponds in the Mexican Cut, is being censused regularly. Since this species belongs to the same genus as the acid-sensitive spotted salamander (*Ambystoma maculatum*) of the Adirondacks,[10] it may serve as a valuable biological indicator of decreasing trends in surface-water pH. Other populations that may serve as useful indicators are cutthroat trout (*Salmo clarki*), lichens living above timberline, and several species of *Daphnia*, including the acid-sensitive *D. pulex*.[11] A discussion of the associations between the *Daphnia* populations and the specific physicochemical conditions in the individual ponds is given by Dodson.[2]

Conclusion

The results reported here establish the occurrence of acid precipitation at the study site. Most surface waters are poorly buffered, and biological species sensitive to acidification are present. This combination of factors indicates that the Galena/Mexican Cut watershed could undergo adverse ecological changes from acid precipitation.

PLANNED ACTIVITIES FOR FY 1984

The baseline monitoring of precipitation and surface-water chemistry will be continued. In addition, a study of the role of nitrogen-fixing lichens in the watershed nitrogen budget will commence. Nitrogen-fixing lichens are sensitive to acidification and it is thus important to establish a baseline against which future impacts can be detected. Finally, numerous studies of the response of

watershed soils and lake sediments to repeated acidification will be conducted in order to obtain rate constants needed for a mathematical model describing the chronology of watershed acidification.

ACKNOWLEDGMENTS

We are grateful to the Rocky Mountain Biological Laboratory for the use of its facilities and to its staff and members for helpful discussions. We are particularly indebted to B. Barr for snow collection and pH measurements. The cooperation of the Nature Conservancy in permitting this research on its land has been vital.

REFERENCES

1. Weber, W.A. (1956), *Rocky Mountain Flora*, 5th edition, Colorado Associated University Press, Boulde., CO.
2. Dodson, S.I. (1982), "Chemical and Biological Limnology of 6 West Central Colorado, U.S.A., Mountain Ponds and Their Susceptibility to Acid Rain," *Am. Midland Nat. 107*, p. 173.
3. Galloway, J.N., Cosby, B.J., Jr., Likens, G.E. (1979), *Limnol. Oceannog. 24*, p. 1161.
4. Gran, G. (1950), *Acta. Chem. Scan.* p. 559.
5. Johannes, A.M., Altwicker, E.R., and Clesceri, N.L. (1981), "Characterization of Acidic Precipitation in the Adirondack Region," Electric Power Research Institute Report EA-1826, Palo Alto, CA.
6. Winkler, E.M. (1976), "Natural Dust and Acid Rain," *Water, Air, Soil Pollut. 6*, p. 295.
7. Dodson, S.I., Department of Zoology, University of Wisconsin, Madison, WI, personal communication.
8. Stumm, W. and Morgan, J.J. (1981), *Aquatic Chemistry*, 2nd edition, Wiley-Interscience, New York, pp. 174–175.
9. Lewis, W.M., and Grant, M.C. (1979), "Relationships Between Stream Discharge and Yield of Dissolved Substances from a Colorado, U.S.A., Mountain Watershed," *Soil Science 128*, p 353.
10. Pough, F.H. (1976), "Acid Precipitation and Embryonic Mortality of Spotted Salamanders, *Ambystoma maculatum*," *Science 192*, p. 68.
11. Davis, P., and Ozborn, G.W. (1969), *Canad. J. Zoology 47*, p. 1173.

Survey of Instrumentation for Environmental Monitoring*

M. Quinby-Hunt, R. McLaughlin, G. Morton, and A. Quintanilha

Technological development has resulted in the generation, transformation, and release of large numbers of substances that constitute health and safety hazards to human beings. Accurate measurement of such products is necessary if corrective or preventive actions are to be taken. For 13 years, the Survey of Instrumentation Monitoring has been an up-to-date source of critical information on instruments for detecting, measuring, and monitoring substances of environmental concern.

The Survey is of great value to industrial and government groups that must spend considerable time and money investigating and selecting techniques and instruments for obtaining reliable data on environmental problems. It provides extensive information both on specific pollutants (sources, pathways, and approaches to control) and on monitoring instruments (principles of operation, problems, detection limits, and interferents). Detailed descriptions of commercially available instruments are also included.

The Survey is in four volumes: *Radiation*, *Water*, *Air*, and *Biomedical Monitoring*.

ACCOMPLISHMENTS DURING FY 1983

Radiation

The *Radiation* volume[1] was published by John Wiley & Sons in April 1983. The instrument notes were completely revised so that the latest information (up to January 1983) could be included for each manufacturer. Final editing and the preparation of an extensive index were also completed. The published edition contained over 1100 pages.

Water

A contract was negotiated with Wiley for publication of the *Water* volume by the end of 1984. Several sections were updated, as follows:

- Nutrient species
- Dissolved gases
- Solids
- Fibrous materials (asbestos)

Several new sections were written:

- Disinfectants
- Halogenated hydrocarbons
- Biomass indicators
- Color, taste, and odor

PLANNED ACTIVITIES FOR FY 1984

Water

The *Water* volume will be completely rewritten and submitted to Wiley by 1 July 1984 for publication later in the year. The book will consist of four major sections: Inorganic, Organics, Biological Parameters, and Physical Parameters. Chapter topics include:

Inorganics

- Salinity, the major ions, and cyanide
- Characteristics of metallic trace elements
- Measurement of metallic trace elements
- Nutrient species
- Dissolved gases
- Disinfectants
- pH, Alkalinity

Organics

- Organic carbon
- Petrochemicals
- Pesticides
- Halogenated hydrocarbons
- Phenolics
- Oil and grease

Biological Parameters

- Biomass indicators
- Coliform bacteria and other microorganisms
- Biochemical and chemical oxygen demand

*This work was supported by the Assistant Secretary for Environment, Office of Health and Environmental Research, Pollutant Characterization and Safety Research Division of the U.S. Department of Energy under Contract No. DE-AC03-76SF00098.

Physical Parameters

Temperature
Turbidity
Solids
Fibrous materials (asbestos)
Color, taste, and odor
Radiation

Instrument notes will be completely revised and expanded to include the latest information (up to May 1984) on instrumentation for environmental monitoring of water.

Air

Contingent on funding, work will begin on rewriting and editing the *Air* volume, with an expected publication date in 1986.

REFERENCE

1. Environmental Instrumentation Survey Group, Lawrence Berkeley Laboratory (1983), *Instrumentation for Environmental Monitoring: Volume 1, Radiation*, John Wiley & Sons, New York.

Application of X-Ray Fluorescence and Neutron Activation Methods for Characterization of an In-Situ Oil Shale Retort*

R.D. Giauque, F. Asaro, H.V. Michel, and L.E. Sindelar

This program was a cooperative effort between Geokinetics, Inc. and the U.S. Department of Energy through Lawrence Berkeley Laboratory. Its primary purpose was to ascertain the technical and economic feasibility of shale oil recovery from the Geokinetics *in-situ* retort process. Additionally, information on the effect of this process on the distribution of minerals and elements was desired. The retort was carried out in an area south of Vernal, Utah, during 1980. A year later, cores were drilled from the region of the retort. Mineral characterizations were carried out at the University of Wyoming under the direction of G.M. Mason. Element characterization studies and statistical analysis of all data were performed at LBL. Additionally, leaching studies were carried out at Colorado State University under the direction of D.B. McWhorter.

ACCOMPLISHMENTS DURING FY 1983

Four cores from the retort region and one reference raw core acquired from the periphery region were used for mineral and element distribution studies. The cores were drilled between 1 and 25 meters below the surface. For these studies, each core was typically sectioned at 0.3-m intervals. The concentrations of 55 elements were determined by either x-ray fluorescence or neutron activation. Mineral and organic carbon, as well as hydrogen, nitrogen, and sulfur were determined elsewhere. Fischer assay oil yields and water content were also determined elsewhere. Eleven naturally occurring minerals and seven high-temperature minerals produced during the retorting process were measured by x-ray diffraction at the University of Wyoming.

Data from each sorted core were divided into three groups corresponding to different zones. A simplified description of these zones has been made by G.M. Mason.[1] They are as follows: Zone ABC—oil shale with little or no heat alteration observable; Zone D—retorted oil shale that was black or sooty and appeared carbonized; and Zone EF—retorted oil shale that underwent substantial heat alteration, appeared tan or light gray in color, and in some cases was from a melt. Weight losses of the major components were calculated for each spent oil-shale core. These components included mineral carbon as CO_2, organic carbon, calcium as CaO, magnesium as MgO, hydrogen, nitrogen, sulfur, and water. Abundances determined for each spent core were compared with the abundances determined for a corresponding depth interval of the reference raw core. The average ratio of the abundances after retorting to that before retorting for 22 elements (elements that were not expected to be significantly lost during the retorting process and that could be determined with a high degree of accuracy) determined the fraction, F, of the core weight that remained after retorting. These average ratios were re-averaged over the entire depth of the zone.

The calculated weight loss (%) for any component, W_f, within a zone is expressed by the equation:

*This work was supported by Geokinetics, Inc. through the U.S. Department of Energy under Contract No. DE-AC03-76SF00098.

$$Wt.\ loss\ (\%)_v = 100(A_{iv} - A_{sv} \times F)$$

where A_{iv} and A_{sv} are the abundances of components v (averaged over the entire zone) for corresponding depth intervals of the raw and spent "retorted" cores, respectively, and F has the same definition given above.

In the highest temperature region of the retort, Zone EF, major component weight losses, WL, and the fraction of the component, FC, in the raw shale lost during retorting are listed in Table 1. The close agreement between the gross weight loss, $100(1-F)$, and the summation of the weight losses of the listed individual components indicates that all major sources of weight loss have been determined. The cores 2, 19, 11, and 10 were taken in a diagonal pattern to the general direction the retort traversed, with core 2 being nearest the beginning of the retort and core 10 being nearest the end of the retort. Table 2 lists similar results for specific trace elements.

The principal phases that were associated in the same zones as determined by statistical analyses are summarized in Table 3. Finally, Table 4 lists the principal phases with which the analyzed elements were determined to be associated.

The above tables list only a fraction of all results determined in these studies; a fuller account will appear in a report being prepared for the Environmental Protection Agency.

Table 1. Weight losses (WL, in percent) of major components and the fraction of these components (FC) lost during retorting for Zone EF.

	Core No.							
	2		19		11		10	
Component	WL	FC	WL	FC	WL	FC	WL	FC
$C_{min}(CO_2)$	18.2	0.90	16.5	0.95	14.9	0.85	11.8	0.65
C_{org}	12.3	1.00	12.7	1.00	11.5	0.90	16.4	0.95
Ca(CaO)	4.9	0.25	3.4	0.20	—[a]	—[a]	1.4	0.10
H	1.6	0.90	1.7	0.90	1.5	0.90	2.1	0.90
Mg(MgO)	1.3	0.20	1.2	0.20	—[a]	—[a]	1.5	0.25
N	0.5	0.90	0.5	0.90	0.4	0.90	0.6	0.90
S	0.2	0.50	0.1	0.20	0.3	0.50	0.3	0.50
Water	(2.0)	+1.90	0.6	0.60	(0.9)	+0.80	(0.3)	+0.30
Summation of weight losses	37%	—	37%	—	—	—	34%	—
Gross weight loss[b]	40%	—	36%	—	28%	—	31%	

[a]Not determined.

[b]Gross weight loss is defined as $100(1-F)$, where F is the fraction of core weight that remained after retorting.

Table 2. *Trace-element concentration losses (WL) and the fraction of the component (FC) lost during retorting for Zone EF.*

Element	Core 2		Core 19		Core 11		Core 10	
	WL (ppm)	*FC*	*WL* (ppm)	*FC*	*WL* (ppm)	*FC*	*WL* (ppm)	*FC*
As	15	0.50	5	0.15	5	0.15	18	0.50
Ba	124	0.20	88	0.15	30	0.05	31	0.05
Mo	5	0.30	4	0.30	—	—	8	0.40
Sb	0.6	0.40	0.0	0.00	—	—	0.7	0.40
Sr	229	0.25	179	0.25	36	0.05	49	0.05
U	1.0	0.25	1.0	0.25	—	—	1.0	0.25
Zn	3	0.05	10	0.20	4	0.10	5	0.10

Table 3. The principal mineral phases that were associated in the same zones; inverse relationships are indicated by parentheses.

Mineral phase	Zones	Mineral phase
Analcime	Raw, ABC, D	Water
	Raw, ABC	K-feldspar, Na-feldspar
Aragonite	—	—
Calcite	All	(K-feldspar)
	Raw, ABC	Oil
Dolomite	Raw, ABC, D	Quartz
	Raw, ABC	K-feldspar
K-feldspar	All	(Calcite)
	Raw, ABC, D	Na-feldspar
	Raw, ABC, EF	Quartz
	Raw, ABC	Analcime, dolomite
Na-feldspar	Raw, ABC, D	K-Feldspar, quartz
	Raw, ABC	Analcime, oil
Pyrite	—	—
Quartz	Raw, ABC, D	Dolomite, Na-feldspar
	Raw, ABC, EF	K-feldspar
	ABC, D	(Water)
Oil	Raw, ABC	Calcite, Na-feldspar
Water	Raw, ABC, D	Analcime
	ABC, D	(Quartz)

Table 4. Mineralogical residence of elements.

Mineral phase	Zones	Associated elements
Analcime	Raw, ABC	As, Ga, Ni, Pb
Aragonite	—	—
Calcite	All	C_{min}, C_{org}, N, Sr
Dolomite	—	—
K-Feldspar	All Raw, ABC, D Raw, D	Rb, Zn Fe, Ga, Nb, Zr Al, Ce, Co, Cr, Cs, Cu, Dy, Eu, Hf, K, La, Mn, Na, Nd, Ni, Pb, S, Sb, Sc, Sm, Ta, Tb, Ti, Y
Na-Feldspar	Raw, ABC	As, C_{org}, Cu, H, Ni, Pb
Pyrite	—	—
Quartz	—	—
Akermanite/Gehlenite	EF	Ba, U
Cristobalite	EF	—
Diopside/Augite	EF	Al, Ce, Co, Cs, Cu, Dy, Eu, Fe, Ga, Hf, La, Lu, Nd, Ni, Rb, Sc, Sm, Ta, Tb, Ti, V, Zr
Monticellite	EF	—
Tridymite	EF	Fe, K, Nb, S, Y, Zn
Oil	Raw, ABC	As, C_{org}, Cu, H, N, Pb
Water	Raw, ABC, D	Ba, Cu, Ni, Pb

PLANNED ACTIVITIES FOR FY 1984

A final report is being prepared at the University of Wyoming at Laramie. Other than proofreading, LBL participation in the project has concluded.

ACKNOWLEDGMENTS

The authors have cooperated with G.M. Mason of the University of Wyoming Research Corporation in these studies. Fischer assays were performed at the Laramie Energy Technology Center. Total carbon, hydrogen, nitrogen, sulfur, inorganic carbon (carbonate) and organic carbon analyses were carried out by Huffman Laboratories, Inc. of Wheat Ridge, Colorado.

REFERENCE

1. Mason, G.M., Giauque, R.D, and McWhorter, D.G. (1984), *Post Burn Characterization of Geokinetics In-Situ Retort*, University of Wyoming Research Corp. Report DOE/LC/RI-83-G, Laramie, Wyoming.

Characterization of Atmospheric Aerosols from the Albuquerque Haze Study Program*

R.D. Giauque and L.E. Sindelar

The area encompassing Albuquerque, New Mexico, is in violation of federal guidelines regarding carbon monoxide emissions. Additionally, visibility is seriously degraded during winter months. Albuquerque is situated at the base of a group of mountains, and atmospheric inversion processes occur over this region. The contribution of various emission sources to the overall problem is unknown. A program requiring the annual inspection of vehicles for compliance with emission standards has been mandated. Although the program will lead to the reduction of carbon monoxide emissions, there is great concern that there will be little improvement in overall visibility. Consequently, an evaluation and understanding of the degree to which various emission sources contribute to the visibility degradation is desired.

ACCOMPLISHMENTS DURING FY 1983

An aerosol characterization experiment was carried out between December 1982 and March 1983. A number of atmospheric variables were measured. Ground stations, tethered balloons, and a helicopter with a suspended sampling system were used. The program included the collection of size-segregated aerosol specimens at three ground-station sites. Specimens were collected at 12-hour intervals using dichotomous aerosol sampling systems. The fine-particle stage collected particles of less than 2.5 microns, while the coarse-particle stage collected particles between 2.5 and 20 microns as well as 10% of the particles smaller than 2.5 microns. Characterization of the particles collected on the fine stage was of primary interest for this program, as it is these particles that reduce visibility.

Approximately 120 size-segregated specimens were collected at each ground station over periods of intensive visibility reduction. Beta-gauge[1] mass determinations were carried out at the Environmental Protection Agency Research Center in Raleigh, North Carolina, under the direction of W. Courtney. The concentrations of thirty elements (Al, Si, S, Cl, K, Ca, Ti, V, Cr, Mn, Fe, Ni, Cu, Zn Ga, Ge, As, Se, Br, Rb, Sr, Zr, Mo, Ag, Cd, Sn, Sb, Cs, Ba, and Pb) were determined by x-ray fluorescence at LBL using an LBL-designed spectrometer[2] that provided secondary excitation radiation.

Pearson correlation coefficients were determined for 15 variables (mass and the elements Al, Si, S, Cl, K, Ca, Ti, Mn, Fe, Zn, Br, Sr, Ba, and Pb) for each site, using fine-particle results. Variables paired with mass which yielded correlation coefficients greater than 0.50 are listed in Table 1. For each site, K has the highest correlation coefficient with mass; it was highest at site ZUNI (a predominantly residential area and the site with the highest visibility reduction) and lowest at site CNDL (an area of mixed residential and industrial development). (Site VLND was a less densely populated residential area than the ZUNI site.) Correlation coefficients for Cl and Zn are slightly lower than for K at each site. The elements K and Cl can serve as tracers of wood combustion.[3] Correlation coefficients for tracers of automotive combustion (Br and Pb) are considerably lower than for the tracers of wood combustion.

All results have been included in a data bank at the Sandia National Laboratory, Albuquerque. Source apportionment calculations are being made for each site so that more definitive results may be ascertained.

Table 1. Pearson correlation coefficients (>0.50) for fine-particle element-concentration results paired with fine-particle masses sampled from three sites in Albuquerque, New Mexico.[a]

Site (no. of pairs)		
ZUNI (64)	VLND (64)	CNDL (56)
K (0.99)	K (0.97)	K (0.82)
Cl (0.99)	Cl (0.94)	Zn (0.82)
Zn (0.94)	Zn (0.84)	Br (0.81)
Br (0.85)	Br (0.79)	Cl (0.29)
Pb (0.79)	Pb (0.72)	Pb (0.78)
Al (0.76)	Al (0.62)	S (0.59)
S (0.52)	—	Al (0.59)

[a]See text for description of sites; K and Cl (highest coefficients) are related to wood combustion, Br and Pb (significantly lower coefficients) to automotive combustion.

*This work was supported by Sandia National Laboratory, through the U.S. Department of Energy under Contract No. DE-AC03-76SF00098.

PLANNED ACTIVITIES FOR FY 1984

This project was concluded during FY 1983.

ACKNOWLEDGMENTS

This program has been carried out under the direction of B. Zak of Sandia National Laboratory and B. Stevens of the Environmental Protection Agency.

REFERENCES

1. Jaklevic, J.M., *et al.* (1980). *Aerosol Analysis for the Regional Air Pollution Study Final Report*, LBL-6497.
2. Jaklevic, J.M., Gatti, R.C., Gouldig, F.S., and Loo, B.W. (1981). "A β-Gauge Method Applied to Aerosol Samples." *Envir. Sci. Tech. 15*, p. 680.
3. Stevens, R.K. (1983). *Analytical Measurements for Use in Source Apportionment Studies to Determine Impact of Wood Burning on Visibility and Fine Particle Mass*, in press, U.S. Environmental Protection Agency Research Center, Research Triangle Park, NC.

The Iridium Anomaly at the End of the Cretaceous*

H.V. Michel, F. Asaro, W. Alvarez, and L.W. Alvarez

The impact theory[1] predicts that significant enrichments of iridium will be found at the Cretaceous-Tertiary (C-T) boundary (65 million years B.P.), wherever it is intact.

A new Ir anomaly (61 nanograms/cm^2) has been found at this boundary in a north central Pacific Ocean deep sea core (DSDP Hole 577B) drilled especially for our project. The position of this anomaly is synchronous in the stratigraphic column within 3 cm of the boundary defined by the extinction of Cretaceous nannoplankton. Very sensitive methods of Ir detection (suitable for running large numbers of samples) have been developed which can measure the background Ir variations. New methods of data interpretation also have been developed which distinguish between Ir peaks due to background and those due to the impact of an extraterrestrial object. The data from Hole 577B confirm a close correlation between the impact of an extraterrestrial object and the extinction of species.

*This work was supported by the Director, Office of Energy Research, Office of Basic Sciences, Division of Engineering, Mathematical and Geosciences of the U.S. Department of Energy under Contract No. DE-AC03-76SF00098, the U.S. National Science Foundation under Grant EAR-81-15858, and the National Aeronautics and Space Administration Ames Research Center under Contract A-71683B.

ACCOMPLISHMENTS DURING FY 1983

Carrier-Free Extraction of Ir

A post-irradiation carrier-free technique for removing the siderophile elements from samples has been developed. The irradiated sample is heated in air to 800°C to drive off CO_2 and H_2O. The 100-mg sample is then mixed with 100 mg basalt, 8 mg graphite powder, and 200 mg powdered iron and placed in a small boron nitride crucible. Several crucibles are placed inside a larger graphite crucible and heated in an inert atmosphere to 1450°C for 60 minutes. The resulting iron ball separates from the silicate phase and contains the siderophile elements scrubbed out of the silicates. About 18% of the Ir is lost in a volatile phase in the furnace exhaust stream. This technique lowers the detection limit for Ir to ~15 parts per trillion (ppt) for one sample per day counting time. If the samples are highly calcareous, four or more can be analyzed simultaneously, lowering the limit of detection to 7 ppt in one day of counting time.

Study of DSDP Hole 577B

Hole 577B recovered the C-T boundary and was sampled for geochemical studies using neutron activation analysis (NAA). It has one core consisting of six sections of undisturbed white to light brown nannofossil ooze.

An iridium anomaly of 61 ng/cm^2 was found in core 1, section 4, within 3 cm of the C-T boundary defined by calcareous nannofossils.[2]

In Fig. 1, the Ir abundance profile is plotted as a function of stratigraphic position. One major peak is

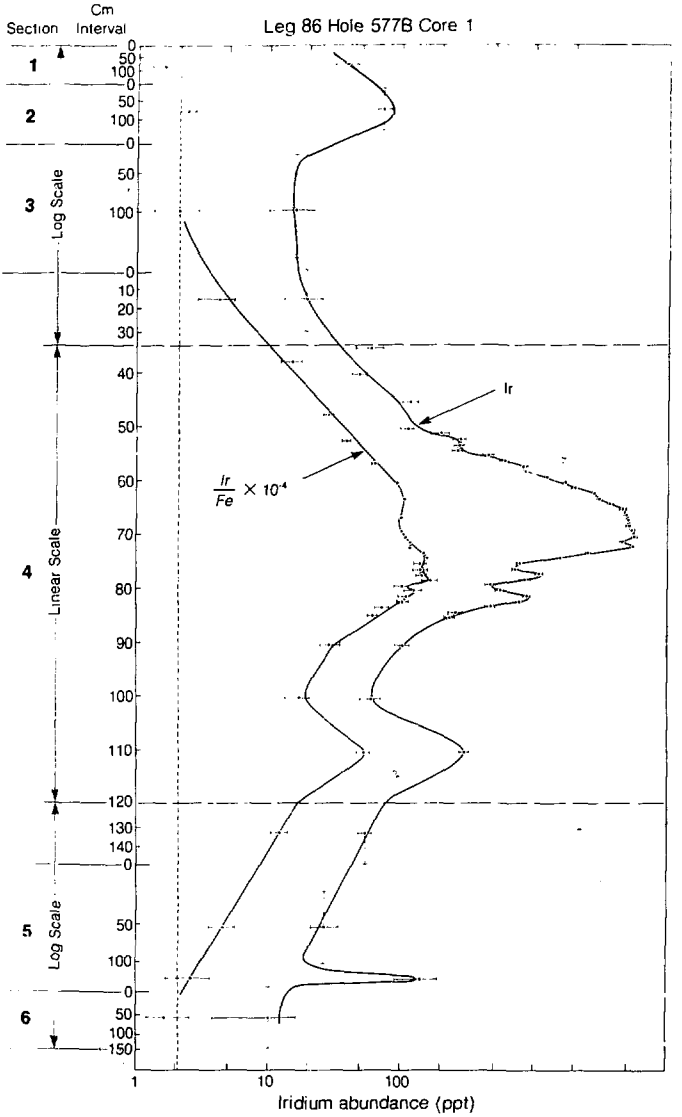

Figure 1. Abundance of iridium and the iridium-iron ratio [(Ir/Fe) × 10^{-4} in ppb] vs. stratigraphic position in hole 577B, core 1. (XBL 8312-4775)

seen, along with five smaller ones. In order to determine which peaks are associated with an impacting meteorite and which with the normal iridium background deriving from meteoritic dust, the following model was used. During a brief interval of geological time, the clay deposition rate in the area of Hole 577B would be approximately constant, as would the rate of Ir deposited from meteoritic dust. The rate of $CaCO_3$ deposition, however, could change as the biological productivity altered or the calcite compensation depth varied. These changes would affect the abundances of clay and iridium, but not their ratios. For the present analysis, iron rather than aluminum is taken as a measure of the clay abundance because Fe is measured with comparably high sensitivity throughout the section studied, while Al is not.

The ratio Ir/Fe (reduced by a factor of 10,000) is shown in Fig. 1. The background value is 2×10^{-8} in both the Cretaceous and Tertiary regions even though the Ir abundance varies by an order of magnitude. Thus, the broad Ir peak in sections 1 and 2 and the relatively sharp peak in section 5 may have been caused simply by changes in the deposition rate of $CaCO_3$. On the other hand, the main Ir peak and the three peaks at 76–77 cm, 81–83 cm, and 110 cm in section 4 have Ir/Fe ratios that are one or two orders of magnitude higher than background and should therefore have a different origin. There is also an elevated tail in section 5 and the lower part of section 4 that is not due to background.

The rise of the main Ir peak is steepest between [illegible] and 73 cm, in close agreement[3] with the C-T boundary at 72 cm defined by nannofossil studies. Such agreement has been found in many marine sections and is an excellent confirmation of the asteroid impact theory. The three peaks below the main peak and the elevated tail, however, should not be primary deposits in Cretaceous sediment if the asteroid impact theory is correct. These peaks and the tail may have been caused by bioturbation (worm burrowing) or by the cutting wire smearing material as it sliced downward through the core. A method of checking these suppositions would be to re-sample the material below the sliced surface. Any contamination due to the slicing procedure is not likely to have penetrated this deeply. Bioturbation is also unlikely to reproduce the observed satellite peaks in such a measurement. Therefore, if the peaks are still observed in a subsequent measurement, another cause is likely. The elevated tail may also have been caused by downward mobility of the Ir subsequent to deposition.

Identity of Bulk Chemistry from Two C-T Boundary Sites

A detailed chemical stratigraphic study was made of the Cretaceous-Tertiary boundary sections in what were two similar marine environments 65 million years ago. These sections are halfway around the world from each other—one in Stevns Klint, Denmark, and the other in the central Pacific Ocean (deep sea drilling core DSDP Hole 465A). If we consider all measured elements (13) whose abundances show a sharp peak (anomaly) in the boundary, the anomalous densities (grams/cm^2) of the elements in the central Pacific boundary layer agree with those from Denmark as well as two independent collections from Denmark agree with each other (Table 1). This is the first time that widely spaced boundary layers have been shown to be chemically identical. The data indicate that the boundary material was thoroughly mixed before dispersal to different parts of the world.

The ratios of abundances of Ir, Ni, Cr, and Co indicate a meteorite component in the mixture (Table 2). The abundance of this component is $10 \pm 3\%$, with the remainder being terrestrial. No mantle component is detected (as determined from the Cr abundance), and an upper limit of 5% can be set on its contribution. The chemistry of the terrestrial component ($\sim$ 90%) in the mixture is consistent with either a basalt or shale, but agrees best with a continental basalt. These data strongly confirm an asteroid or other extraterrestrial impact as the origin of the Cretaceous-Tertiary boundary and suggest that the impact was on basalt. Other workers have also suggested basalt as the impact site,[4] and an oceanic impact has been suggested.[5]

Clay Fraction Mineralogy and Chemistry

Studies (with Miriam Kastner of Scripps Institution of Oceanography) of oxygen-isotope ratios, x-ray diffraction patterns, and rare-earth and major-element abundances in two C-T boundary sediments in different parts of the world (Stevns Klint, Denmark, and Deep Sea Drilling Project Hole 465A in the central Pacific Ocean) strongly suggest that the clay fraction (particles smaller than 2 microns in diameter) is an alteration product of microtektite-like particles[6] which resulted from an asteroid impact 65 million years ago. Like the chemical analysis, this completely independent line of evidence further demonstrates the connection between the C-T boundary layer and the impact of an asteroid (or other large extraterrestrial body).

Table 1. Surface densities of anoxic C-T boundaries.

Element measured	Pacific Ocean	Denmark I	Denmark II
Al[a]	0.435 ± .024	0.463 ± .010	0.571 ± .006
Fe[a]	0.412 ± .031	0.432 ± .024	0.780 ± .006
Na[a]	0.083 ± .016	(0.079 ± .002)	- - -
Ni[b]	4438 ± 437	5788 ± 175	6572 ± 96
Zn[b]	3014 ± 141	5024 ± 117	5113 ± 84
Cr[b]	1755 ± 81	1648 ± 56	2283 ± 34
Co[b]	709 ± 22	713 ± 15	607 ± 4
As[b]	413 ± 40	466 ± 19	588 ± 31
Sb[b]	62 ± 12	41.8 ± 1.9	46.1 ± 1.6
Th[b]	36.1 ± 2.2	33.7 ± 1.9	53.7 ± 1.8
Hf[b]	23.5 ± 1.6	20.3 ± 1.6	29.2 ± .5
Ta[b]	2.69 ± .10	2.71 ± .05	4.15 ± .04
Ir[c]	319 ± 12	336[d]	336 ± 5
Mean ratio:		1.05	1.28
Std. Dev./mean:		±22.5%	±21.9%

[a]Density in g/cm^2.
[b]Density in μg/cm^2.
[c]Density in ng/cm^2.
[d]Normalized to the total Ir abundance found for collection II.

Table 2. Percent meteorite in C-T boundary clay, assuming basalt impact site.

Pair	% Meteorite	Pair	% Meteorite
Al-Ir	7.7	Ta-Ir	10.2
Al-Ni	7.7	Hf-Ir	9.6
Al-Co	7.2	Fe-Ir	9.0
Al-Cr	10.2	Th-Ir	6.9

Mean Meteorite Component:

8 pairs	8.6 ± 1.3%
26 pairs[a]	10.5 ± 2.8%

Upper Limit on Mantle Component: 5%

[a]Total of 13 elements were measured.

Sand-Size Fraction Mineralogy and Chemistry

Another approach whose results support the impact theory deals with the presence of sand-size spherules with unusual chemical and unique mineralogical characteristics.[7] These spheroids have textures similar to those of rapidly crystallized feldspar and mafic silicates. They are interpreted as diagenetically altered microcrystalline spherules of basaltic composition produced by the impact of a large asteroid in a basalt environment at the end of the Cretaceous. They are analogous to the glassy microtektites produced by impact on more siliceous target rocks. Figure 2 shows the Ir and spherule abundances in the Petriccio C-T boundary section.

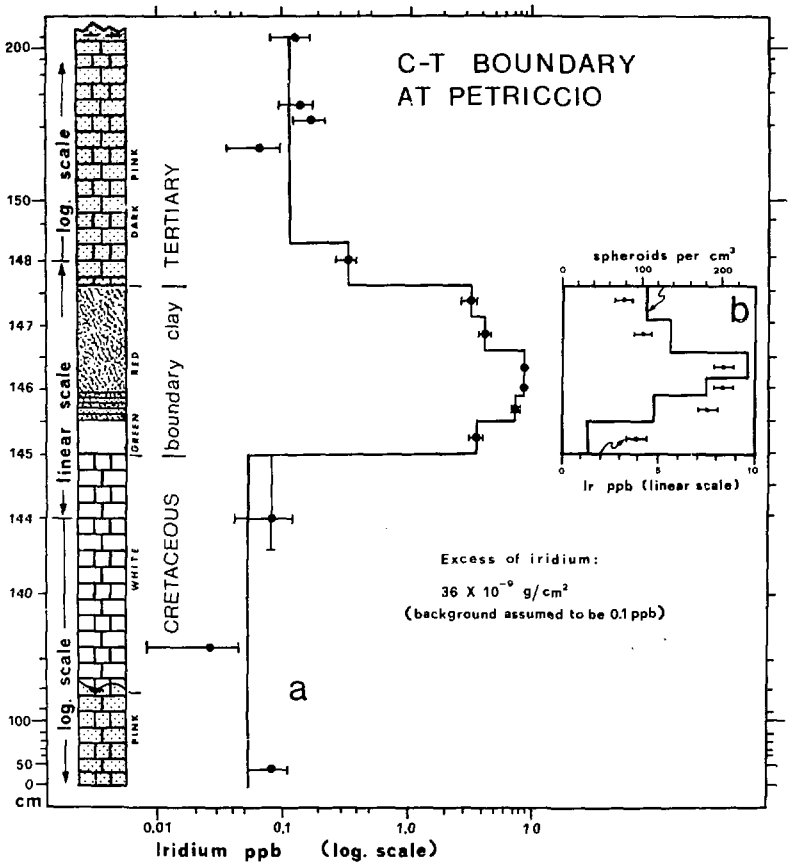

Figure 2. Stratigraphy of Petriccio section across C-T boundary. (a) Lithology and iridium profile; (b) profiles of spherical abundance and iridium (ppb, whole rock) across C-T boundary. A few spheroids are found in ichnofossil burrows immediately below and above the boundary. (XBL 842-571)

PLANNED ACTIVITIES FOR FY 1984

A unique coincidence spectrometer capable of measuring Ir at the 50 ppb level at the rate of 100,000 samples per year is being designed.

Analysis of other extinction boundaries for Ir and other elements will continue.

ACKNOWLEDGMENT

DSDP samples were provided through the assistance of the National Science Foundation.

REFERENCES

1. Alvarez, L.W., Alvarez, W., Asaro, F., and Michel, H.V. (1980). "Extraterrestrial Cause for the Cretaceous-Tertiary Extinctions," *Science 208*, p. 1095.
2. Monechi, S. (1983), personal communication.
3. Asaro, F., Alvarez, L.W., Michel, H.V., and Alvarez, W. (1982), Letter to Editor, *Am. Scientist 70*, p. 567.
4. Gilmore, J.S., Knight, J.D., Ortn, C.J., Pillmore, C.L., and Tschudy, R.H. (1984), "Trace Element Patterns at a Non-Marine Cretaceous-Tertiary Boundary," *Nature 307*, p. 224.
5. Shaw, H.F., and Wasserburg, G J. (1982). ' Age and Provenance of the Target Materials for Tektites and Possible Impactites as Inferred from Sm-Nd and Rb-Sr Systematics," *Earth Planet. Sci. Lett. 60*, p. 155.
6. Kastner, M., Asaro, F Michel, H.V., Alvarez, W. and Alvarez, L.W. (1984), "The Precursor of the Cretaceous-Tertiary Boundary Clays at Stevns Klint, Denmark and DSDP Hole 465A," *Science*, in press.
7. Montanari, A., Hay, R.L., Alvarez, W., Asaro, F., Michel, H.V., Alvarez, L.W., and Smit, J. (1983), "Spheroids at the Cretaceous-Tertiary Boundary are Altered Impact Droplets of Basaltic Composition," *Geology 11*, p. 668.

Building of a Reliable and Generally Useful Data Bank of Mesoamerican Obsidian Sources and Its Application to Ancient Artifacts*

F.H. Stross, F. Asaro, and H.V. Michel

Work in developing precise and cost-effective methods for characterizing obsidian sources and some applications in studying the distribution networks of this valuable commodity in the New World have been reported previously.[1]

Procedures have been worked out for enabling intercomparison of precise, but not necessarily accurate, data in the relevant literature so as to make them generally useful to all workers in the field. This work has now been published.[2]

More emphasis is now being placed on stratigraphic documentation of the obsidian artifacts found during excavation, so that better information is becoming available on the evolution of exchange networks with time. This is obviously a more demanding task and cannot be achieved in all projects.

* This work was supported by the Council on Research and Creative Work of the University of Colorado and the National Science Foundation (through a grant to P.M. Rice, University of Florida, Gainesville, and the University of Texas, San Antonio), and the U.S. Department of Energy under Contract No. DE-AC03-76SF00098

ACCOMPLISHMENTS DURING FY 1983

Petén Project

A project carried out in collaboration with the University of Florida involved analysis of 296 obsidian artifacts from the lakes area of the Department of Petén, Guatemala, by x-ray fluorescence and neutron activation analysis.[3] The obsidian comes from primarily rural/domestic sites, and from periods ranging from the Middle Pre-Classic (*ca.* 800 B.C.) to the Spanish conquest, 1525 A.D. Since no obsidian sources exist in this region of the Maya lowlands, the new, well-documented data on the acquisition and distribution of this important trade item are of considerable interest.

Of the 296 artifacts, provenience of 288 could be reliably established. All but four of these 288 came from the large source areas of El Chayal, Rio Pixcayá, and Ixtepeque, all in Guatemala. Four obsidians had Mexican origins (Pachuca, Tulancingo, and Zacualtipan). Of the obsidians that could not be assigned, five formed a group whose origin we have designated as "Source X." This group is of some interest, since obsidian deriving from a not very distant site in Belize (Colha), analyzed for another project (see below), had the same provenience.

Belize Project

This project, continued over several years in collaboration with Professor T.R. Hester of the University of Texas in San Antonio, recently involved the analysis of obsidian from several sites in Belize, including the well-known site of Colha, and an offshore island, Moho Cay (north), the latter sometimes

referred to as a "port of trade." These sites are about 100 miles northeast from the Peten lakes studied by the University of Florida team. Of the Belize obsidians, 24% came from Rio Pixcayá, 38% from El Chayal, and 24% from Ixtepeque, all well-known large sources in Guatemala. One artifact, excavated in Colha, had the composition of "Source X" mentioned above. One third of the Belize specimens studied are attributed to Pre-Classic dates (900–300 B.C.), the remainder to Late- and Post-Classic periods (*ca.* 9th–11th centuries A.D.). These results are consistent with our earlier studies of Belize obsidian.

Nicaragua Project

A new project, the study of obsidian from Nicaragua, was carried out in collaboration with Professor Payson Sheets of the University of Colorado, Boulder. Since the sparse literature on the subject has suggested export of Nicaraguan obsidian to the northwestern, Maya area, this project is of special interest. However, even the relatively small sample studied so far (chemically and technologically) indicates that this suggestion may not be valid. No Nicaraguan sources to date have yielded obsidian of the quantity, size, and quality required for the "commercial" production of the artifacts traditionally found in Central American sites. The five pebbles found by Sheets in riverbeds and lake shores in Nicaragua all differed in composition from each other, and from the nine artifacts found at an archaeological site named Nindiri. Of the latter group, three came from the Guatemalan source of Ixtepeque; the remaining six formed a homogeneous group of unknown origin, but of a composition that suggests greater affinity to Guatemalan sources than to the Nicaraguan sources represented here.

Pachay Project

In determining the sources of obsidian glass, one of the most recurring problems is the definition of terms, in this case the term "source," itself. Sometimes a deposit consists of, or contains, boulders of a size that immediately identify it as the site of the volcanic activity that produced it, and hence as a primary, geological source. Sometimes there is a region in which unworked pebbles and boulders are copiously imbedded in the local rock or consolidated soil over a considerable area. This, too, is usually designated a primary source. Where the evidence is not as clear-cut—for instance, when the imbedded glass is sparse, or when an appreciable number of pebbles in a riverbed are of similar composition but obviously might have been carried down by the river from some primary deposit—we have spoken of a secondary source, and will continue to do so until a better definition becomes available.

Sometimes a number of geographically distinct outcrops of chemically indistinguishable composition covers sizable areas, on the order of 100 square kilometers, and we then speak of sources in a wider sense, or we may call them source areas. Such an area is that of Chimaltenango, Guatemala, also designated Rio Pixcayá, which has been studied in some detail (see Ref. 2, pp. 327–9). In January 1983, one of the authors (F.H.S.) collected significant amounts of obsidian at one of the Rio Pixcayá deposits by a village named Pachay[4] (the name means "among obsidian"). This village is only a few kilometers by straight line from San Martin Jilotepeque, but is quite difficult of access. Among the copious deposits of unworked obsidian were areas covered with chips, cores, and simple artifacts, indicating the presence of workshops[5] there or in the vicinity.

Samples were collected from all deposits. Analysis by x-ray fluorescence (XRF) on eight samples, including unworked and workshop specimens, showed good agreement with the corresponding values designated "representative Rio Pixcayá."[2] A "short sequence" neutron activation analysis (NAA) on one of the unworked samples also gave very good agreement with "representative Rio Pixcayá" (Table 1A and B).

Pachay, by virtue of the abundance of unworked as well as worked obsidian, can thus be considered a major primary source in the Chimaltenango source area.

Table 1A. X-ray fluorescence analysis of Pachay obsidian.

	Ba	Zr	Rb/Zr	Sr/Zr
Pachay (8 samples)	1033 ± 50	118 ± 3	0.925 ± .052	1.645 ± .055
Reference Rio Pixcayá	1105 ± 32[a]	115 ± 3	1.01 ± .05	1.65 ± .06

[a]NAA value.

Table 1B. Neutron activation analysis of Pachay obsidian.

	Ba	Dy	K (%)	Mn	Na (%)
Pachay (1 sample)	1007 ± 76	...01 ± .13	3.23 ± .28	524 ± 5	2.96 ± .06
Reference Rio Pixcayá	1105 ± 32	2.03 ± .10	3.54 ± .25	521 ± 10	2.94 ± .05

PLANNED ACTIVITIES FOR FY 1984

Cooperative research with other universities will continue, for example, with W.R. Fowler, Jr. at the University of North Dakota on samples from El Mirado, Guatemala, and with T.R. Hester and others on obsidian from the southwestern United States.

REFERENCES

1. Stross, F.H., Asaro, F., and Michel, H.V. (1982), "Precise Characterization of New World Obsidian Sources and the Cost-Effective Determination of Provenience of Selected Artifacts," in *Energy and Environment Division Annual Report, FY 1981*, LBL-13500; p.4-116.
2. Stross, F.H., Sheets, P., Asaro, F., and Michel, H.V. (1983), "Precise Characterization of Guatemalan Obsidian Sources and Source Determination of Artifacts from Quiriguá," *Am. Antiquity 48*, p. 323.
3. Rice, P.M., Michel, H.V., Asaro, F., and Stross, F. (1983), "Provenience Analysis of Obsidians from the Central Peten Lakes, Guatemala," submitted to *Am. Antiquity*.
4. Clark, J. (1981), "Guatemalan Obsidian Sources and Quarries, Additional Notes," *J. of New World Archaeol. 4*(3), p. 1.